Pressure distribution on wing-body-flap configurations at subsonic speed

Bitomsky, Uwe

Award date:
1993

Awarding institution:
University of Bath

PRESSURE DISTRIBUTION ON WING-BODY-FLAP CONFIGURATIONS AT SUBSONIC SPEED

submitted by Uwe Bitomsky

for the degree of PhD

of the University of Bath

1993.

VOLUME 1

Copyright

ProQuest LLC
789 East Eisenhower Parkway
P.O. Box 1346
Ann Arbor, MI 48106-1346

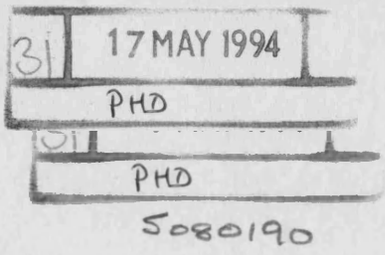

5080190

SUMMARY

Investigations have been undertaken to study the aerodynamic differences between a high wing and a low wing model with and without flaps attached. Pressure tappings were distributed over the entire model, to measure the detailed pressure distribution. Tests were carried out on the model as a whole and on the individual components to obtain the pressure distributions. Surface flow visualisation tests were conducted to aid interpretation of the pressure data.

The pressure distributions for both the high and low wing model were measured and compared. Losses in lift on the low wing model occurred up to one chord in spanwise direction from the wing-body junction due to the fuselage. A mechanism for these losses has been given.

The integrated lift distributions in the spanwise and longitudinal directions were calculated from the pressure distributions. Over the fuselage the lift of the unflapped low wing model was higher than over the high wing model. The mechanism responsible for this has been explained. On the low wing model large lift losses inherent with the pressure losses were observed over the wing at higher angles of attack. The displacement effect of the fuselage led to an upwash near the fuselage which resulted in a premature flow separation near the wing-body junction. This was more pronounced on the low wing model and the reasons for this have been outlined. On the high wing model the flap "carry over" lift over the fuselage, was at least of equal magnitude to the wing lift.

A numerical method was employed to predict the pressure distribution on both high and low wing models. Streamlines derived from this method were compared with those obtained in the flow visualisation tests. Viscous effects greatly affected the pressure distribution but these could not be modelled numerically and discrepancies were noted.

Acknowledgements

I would like to express my sincere thanks to all those who have helped me during me time at Bath. In particular:

Dr. J. F. Henderson for his assistance and guidance given in discussion throughout all stages of this project, and for the accumulation of some of the data

Dr. E. Saliveros and G. Elphick of British Aerospace, Filton, Bristol kindly undertook the numerical analysis

The model was originally funded by SERC G-D-78558.

D. Barker, whose assistance with computing was invaluable

Mr. A. Dando, L. Dudridge, and D. Rushton who prepared the model and lightened my darkest moments in the lab

Dave for his critical comments during writing-up time: Bill, Tim, and Rushard for the accumulation of some of the data: Doug, Maggie, and Reza for their useful comments, tips and hints and who made my time in the office enjoyable

I am indebted to Dr. Anna Hayes, who spent many hours correcting and clarifying my writing

Finally, I would like to thank my parents. Without their help and support this thesis would not have been written.

Table of contents

Nomenclature

A	Cross sectional area of the working section of the wind tunnel	
a_0	Lift slope	
$\bar{c}$	Wing chord	(see Fig. 2.7)
C_l	Local lift coefficient, see Page 34, $C_l \approx C_n$	
$C_L = \frac{L}{\frac{1}{2}\rho V^2 \bar{c}}$	Lift coefficient	
C_n	Local normal coefficient	
$C_p = \frac{p - p_\infty}{\frac{1}{2}\rho V^2}$	Pressure coefficient	
$C_{p\,low}$	Pressure coefficient of the lower surface	
$C_{p\,up}$	Pressure coefficient of the upper surface	
ΔC_p	Pressure coefficient difference	
d	Fuselage diameter	(see Fig. 2.7)
e	Distance between wing chord line and fuselage centreline	
L	Lift	
M	Mach number	
m	Meter	
p	Pressure	
Δp	Pressure difference	
$q = \frac{1}{2}\rho V^2$	Dynamic pressure	
R	Fuselage radius	(see Fig. 2.7)
s	Second	
s	Semi wing span	
Re. no.	Reynolds number (based on wing chord) $= \frac{\rho V \bar{c}}{\mu}$	
V	Free stream velocity	
x	Coordinate in main stream direction.	(see Fig. 2.7)
y	Coordinate horizontally perpendicular to main stream	
z	Coordinate vertically perpendicular to main stream	

α	Angle of attack (relative to chord line and fuselage centre line)	
Γ	Circulation about the wing	
Δ	Difference of a value, e.g. $\Delta\alpha$	
δ	Angle of flap deflection	
ε	Correction factor for the angle of attack	
μ	Viscosity of the air	
φ	Angle of tapping position on the fuselage	(see Fig. 2.15)
ρ	Density of the air	

Subscripts

bottom	Tapping position at the bottom of the fuselage
eff	Effective
i	Induced
low	Lower model surface
max	Maximum value, e.g. $C_{L\,max}$
n	Normal
n	Nose
nR	Normal to the fuselage
ref	Reference
stat	Static
t	Tail
top	Tapping position at the top of the fuselage
up	Upper model surface
w	Wing

1. INTRODUCTION

1.1. General Remarks

The aerodynamics of the individual parts of an airplane are well established and experimental data for the aerodynamic coefficients are widely available. Theoretical analyses have also been developed and applied to predict the aerodynamic behaviour of each part, i.e. the fuselage, wing, nacelle, and the flaps. When the individual parts are assembled into a complete airplane, however, their interference plays a very important role in the formation of the aerodynamic forces. In many cases the magnitude of the interference effects are of the same order as the contribution of the parts to the loads on the airplane (Schlichting, 1979). It is therefore important to investigate these effects so that the additional loads caused by these interactions can be predicted. Theoretical analyses of such interactions have not yet been fully developed to the same depth as those predicting the behaviour of the individual parts and in general are only available for inviscid flow. An experimental investigation of these interference effects is therefore of great interest.

The majority of previous experimental investigations have concentrated on the accumulation of data for lift and drag of wing-body models. Only a few have provided data for both the load distribution along the span and pressure distribution along the length of the fuselage. Even then the pressure data were only acquired at selected spanwise locations on the wing and at positions close to the wing on the fuselage. These data were therefore restricted to the vicinity of the wing-body junction and did not cover the entire model, thus interference effects at a distance from the wing-body junction were not recorded. Empirical data available in the literature on the interference effects of the wing-body junction are therefore limited. No research has been published which has investigated the influence of other components such as the addition of flaps.

The aim of this research program was to provide extensive and comprehensive empirical pressure data for a model consisting of a fuselage, a wing, and flaps in order that their combined effects on the pressure distribution could be investigated in detail.

This present investigation was carried out on a wind tunnel model similar in geometry to modern commuter aircraft such as the DeHaviland Dash 8 or the British Aerospace ATP. These represent two typical configurations in the 40 to 70 seater commuter market.

A fuselage-wing-flaps model was specifically designed to obtain a comprehensive pressure distribution for each part. Each component was tested individually to enable a direct assessment of the interference effects which occurred when the components were assembled together. An investigation of the influence of the flaps on the lift distribution of the fuselage and the wing was included in addition to a detailed analysis of the interference effects of the wing-body junction. The model was also designed in such a way that assembly in either high or low wing configuration was possible. The lift coefficient, C_L, was calculated from the pressure data for all possible combinations. A comparison of the lift distribution with other experimental data obtained from the literature was carried out where feasible. The CFD-code VSAERO (see Chapter 7) was also used to predict numerically the differences in loading between a high and a low wing configuration and to compare surface streamlines calculated by the code with those obtained by means of surface flow visualisation.

1.2. Wing-Body Interference

The aerodynamics of wing-body configurations and the interference effects arising from such combinations have been subject to theoretical and experimental investigations under two main categories:

a) idealised models consisting of a wing attached to a flat surface
and, b) models where a wing was mounted on a fuselage or nacelle.

The flow field around the latter has been described by many researchers one of which, Küchemann (1978), divided the aerodynamic effects into four main areas:

a) Displacement effects
The displacement effect of the wing-body interference generates significant changes to the streamwise velocity distribution at the junction. These induced velocities are a result of the thickness of the wing and the curvature of the intersection lines along the body surface. They are symmetrical for a mid wing combination and a symmetrical airfoil, thus the velocity distribution is symmetrical as well. Therefore, no net lift is produced on the combination. If the wing is set at an angle relative to the fuselage centreline, an asymmetric displacement effect occurs resulting in a lift increment which is related only to the asymmetry of the junction flow. If the wing is cambered the intersection lines between the two wing surfaces and the fuselage are no longer symmetrical with respect to the fuselage. As a result the velocity distribution is also asymmetric, hence the wing-body junction will generate lift, with the appropriate vorticity shed downstream.

b) Lifting effects

The lifting line theory describes the lifting effects associated with wing-body interference as it alters the total lift and lift distribution. Along the junction additional velocities will be induced attributable to the vorticity distribution on both the wing and the fuselage.

Alterations of the spanwise vorticity of the wing and a continuation of this over the body produce velocity increments on the wing and the body, as a result of their close proximity. The chordwise and spanwise load distribution, and hence local velocities are changed considerably in the vicinity of the junction and at a distance from it. This means that, to maintain the loading on the isolated wing, the wing must be cambered and twisted. The carry-over of vorticity implies that the body is lifting which in turn results in further interaction at the wing. If the body is at non-zero angle of attack the resulting upwash at the wing will increase the loading in general, with corresponding increases in the velocity increments at the junction.

c) Non-symmetrical wing locations

Locating the wing at the high or low wing position considerably alters the flow around the junction and at a distance from it. The intersection shapes along the upper and lower surface are not the same and as a consequence the velocity distribution along the junctions differ from one another. Induced velocity increments due to lift are also changed when the wing is located at a distance from the fuselage centreline. The wing vorticity is carried over on to the body in a much more complex way.

d) Viscous effects

The viscous flows result in a development of three-dimensional boundary layers on the fuselage and wing. Boundary layer separation occurs along oblique separation lines at the junction, with trailing vortices shed downstream. The influence of viscous effects are considered to be of equal importance to the other effects in contributing to wing-body interference. If the Reynolds number is relatively low separation lines around the wing-body junction are likely to persist and vorticity is likely to be concentrated and submerged within the viscous region. The viscous region near the junction then loses the properties of a boundary layer altogether, and the pressure field throughout the region will change dramatically from the usual displacement effect produced by ordinary boundary layers. So far, there is no way of calculating this important effect.

Some of these effects have been corroborated by other researchers who have investigated the development of the boundary layer near a wing-body junction in

particular (Kubendran, 1978; Flax and Lawrence, 1951). These experiments were carried out, mainly, on idealised models where a symmetrical wing was attached to a flat wall. On these models the effect of the incoming boundary layer was examined as well as the effects of a fillet in the junction on the development of the boundary layer (Devenport, 1990). Boundary layer control, where the wing-body junction vortex was suppressed by means of suction along the body surface immediately upstream of the wing, was also investigated (Philips, 1992).

Lift carry-over

One aspect which has not been considered hitherto is the exact way in which the wing lift is carried over the fuselage. The strength of the circulation of a line along the span and through the fuselage must be constant unless vorticity is shed into the wake (Weber, 1970). Thus, if the lift does not completely vanish at the wing root a finite amount of circulation, induced by the wing, must exist. On the other hand, the fuselage alone is not able to fulfil the Kutta-condition since the body does not have a well defined sharp trailing edge. In the theoretical case, with constant spanwise circulation, the lift at all locations along the span will be equal, including the locations at the wing-body junction. If the wing circulation is not transferred to the fuselage, a net loss in circulation at the wing-body junction would be expected which would be shed into the wake. As a consequence the lift generated within the wing-body intersection would be less than the lift produced outside this area.

According to Lennertz (1963) the flow about a cylindrical body, at a great distance behind the wing can be found by the use of the free vortices relative to the body surface. He derived the following equation for the lift of a wing-body combination:

$$L = \rho V \Gamma 2s\left(1-\frac{R^2}{s^2+e^2}\right) \qquad 1.2.1.$$

This equation does not differentiate between a high or low wing position since the term for the wing height is quadratic and assumes a constant circulation. Thus, insufficient information is given for the distribution of the circulation along the span to be determined.

Schlichting *et al* (1979) obtained a similar equation for the lift of a fuselage & wing system where the circulation was not assumed to be constant along the span:

$$L = 2\rho V \int_{y=R}^{s} \Gamma(y)\left(1+\frac{R^2}{y^2}\right) dy \qquad 1.2.2.$$

Although this equation does not account for the height of the wing in relation to the fuselage centreline it takes into account the change of circulation along the span but, as Schlichting pointed out, the circulation has to be assumed since an exact distribution is not known.

Boundary layer in the junction

The flow field at a wing-body junction is exposed to three-dimensional interactions between the approaching boundary layer and the pressure field produced by the wing. The approaching boundary layer along the fuselage is not able to withstand the adverse pressure gradient imposed by the wing and will separate ahead of the leading edge before it reaches the stagnation pressure. The structure of the flow in the wing-body junction is almost independent of the boundary layer thickness and the Reynolds number (Devenport, 1990). The thickness of the boundary layer is not affected by the flow in the separated region (East *et al*, 1968).

On the wing the boundary layer is skewed by spanwise pressure gradients as it encounters the fuselage. These gradients turn some of the spanwise boundary layer vorticity into the streamwise direction. The separation lines formed ahead of the wing and the skew-induced streamwise vorticities concentrate close to the wing and become a structure, well known as the horseshoe vortex. The distance of the vortex centre to the wing increases as the vortex trails downstream. The position of the vortex is also significantly influenced by the shape of a fillet between the wing and fuselage. The fillet can even eliminate the leading edge separation and can reduce the skewing of the boundary layer (Devenport, 1992).

These developments are mainly established for mid-wing configurations and for idealised junctions. The vertical and horizontal position of the wing on the fuselage has not, as yet, been considered and previous work has only included experiments for off-centreline wing position. Furthermore, the geometry of the wing such as taper, sweep and camber and the effects thereof have been neglected.

Fuselage and nacelles

In many theoretical approaches the fuselage has been assumed to be infinite in length and of circular cross section. Thus no difference between fuselages and nacelles has been established even though the nacelle bodies are shorter and smaller in diameter. The relative position of nacelles with respect to the wing has not been considered either. For example, sometimes the body of the nacelle might end before the wing trailing edge. Therefore the intersection lines differ not only between the upper and

lower wing surface but might also be curved in the spanwise direction. A theory for the aerodynamic effects arising from the varying shape does not exist, yet. These major differences are pointed out in previous experimental studies only (Boermans, 1983, Küchemann, 1978).

Fairings are often designed to achieve a smooth transition of the surface between the wing and the fuselage. They can reduce the pressure gradients in front of the leading edge and thus eliminate separation. However, a reduced pressure gradient does not necessarily result in lower drag (Maughmer, 1989). In general there are no design rules which govern the layout of a fairing.

1.3. Previous experimental work

Experimental work investigating the problems associated with wing-fuselage combinations covers the past 70 years. During these experiments various parameters such as the wing and/or fuselage shape, wing location with respect to the fuselage, angle of wing chord to fuselage axis, etc. have been examined. The overall performance, in terms of drag and lift, has been investigated on scaled and full scale models (Ross *et al,* 1982) in wind tunnels. In the following sections work relevant to this thesis is introduced in order to provide a better understanding of the problems discussed later.

Among these experiments the geometry of the fairing, or fillet, of wing-fuselage models has been subject to many investigations. Often this geometry has been idealised in the form of a wing attached to a flat wall. The development of the flow close to a wing-body junction has been studied in such idealised models and attempts have also been made to model such flow theoretically. Work which will aid the understanding of the flow behaviour on a wing-fuselage model is introduced and referred to.

The general arrangement of the fuselage and the wing was studied in the earlier part of this century (Prandtl, 1920, Jacobs and Ward, 1935). In particular the location of the wing in relation to the fuselage was examined extensively (see Fig. 1.1 for Prandtl's work). The combination of wing and nacelle is a similar problem and much research has been undertaken in this area. Any relevant work here has also been included in this thesis.

The influence of the shape of the individual parts, in particular, the fairing or fillets for the wing-fuselage junction was examined extensively. Not only has the shape of the junction been considered but also the possibility of changing the boundary conditions

by surface suction close to the junction. Only two research teams have reported experiments with surface suction and the results are presented at the end of this Section.

The majority of work has concentrated on the overall performance of the model in terms of drag and lift. So far only a few investigations have considered the detailed pressure distributions on parts of the model. Furthermore, all work considered the wing and fuselage only; flaps and their effects were neglected in previous investigations.

The discussion of previous work is subdivided into the following Sections: Work on the geometry of the wing is presented in Section 1.3.1., followed by the fuselage geometry in Section 1.3.2.. Investigations on fairings and fillets between a wing and fuselage is dealt with in Section 1.3.3. succeeded by work on other parameters such as surface suction which influence the flow around wing-fuselage combinations (Section 1.3.4.). A short summary in Section 1.3.5. accumulates all of the important and relevant findings.

1.3.1. Wing geometry

The flow around a fuselage is influenced by the presence and by the shape of the wing. The wing geometry is expressed by several parameters, such as the aspect ratio, the profile, sweep, the thickness, and the camber. Even the fact whether a wing is present or not and the influence on the flow over the fuselage has been investigated.

The general flow behaviour of a fuselage with and without wings was analysed by Grosche (1972). He conducted experiments with a slender body at exactly the same Mach number and similar Reynolds number (5×10^5) at angles of attack of $\alpha = 7^o$, 10^o, and 15^o (see Fig. 1.1). He found out that the strength of the vortices which were shed from the forebody of the fuselage was considerably reduced by the presence of the wing. This reduction was mainly due to the downwash from the wing which weakens the cross flow past the body, thus cutting off the influx of boundary layer vorticity into the body vortices.

Wing shape

The influence of the wing shape on the flow field of wing-body combinations has been subject to many experiments. In particular the thickness, the camber, the taper, the nose shape, and the sweep have been investigated. In the following paragraphs an overview of research in this area is given.

Parkin and Klein (1930) carried out a series of experiments with three different airfoils attached to three different fuselages at high, mid, and low wing position (see Fig. 1.2). They concluded that the thicker the wing section and the better the aerodynamic form of the fuselage, the greater the interference between the two. This was also found by Jacobs and Ward (1935) who discovered that airfoils with moderate thickness are most susceptible to adverse interference. They also concluded that a thick tapered wing has favourable drag characteristics owing to the thick, high-drag portion of the wing being shielded by the fuselage. The thick root of the tapered wing results in a more satisfactory form of junction than those resulting from a rectangular wing root. This was evidenced by the fact that the drag increased less rapidly for a low wing configuration. This was also observed by Muttray (1935). During investigations with a low wing combination he showed that the difference in drag between a tapered wing and a tapered wing and fuselage was smaller than for a rectangular counterpart, with the tapered combination performing better at high lift coefficients. He concluded that the fuselage was "smaller" with respect to the wing root for a tapered wing than for a rectangular wing.

These observations for the tapered wing were noted for a cambered wing by Parkin and Klein (1930) too. Furthermore, the maximum lift coefficients of the combination with a cambered airfoil were less affected by the different variables (vertical wing position, fillets, fuselage shape) than the combination with a rectangular wing.

The leading edge profile of a wing is a further parameter which influences the flow in the junction of wing and fuselage. McLellan (1948) conducted an experiment on the effect of the nose profile of the wing on a high wing-nacelle combination at a Re.-number of 3.8×10^6. Part of his work will be included in the discussion of results since that report is one of the few which included pressure data. McLellan measured the overall lift characteristics and he found that drooping the nose section increased the maximum lift up to the value of the wing alone but with more abrupt stall characteristics. The greatest improvement was at an angle of attack of $\alpha = 2.5^{\circ}$. Mehta (1984) investigated the influence of the nose shape on the flow with a model which had an idealised junction at a freestream velocity of the flow of 25 $^{m}/_{s}$. Three wings with different nose bluntness were attached to a flat wall. His results showed that the vortex size and strength was increased with nose bluntness. This was explained by the streamwise vorticity which increased rapidly in a region of low streamwise velocity and high lateral divergence, i.e. maximum bluntness. Furthermore, he showed that the vortex flow will persist up to the trailing edge of the wing with little or no attenuation.

Vertical wing position

Much previous experimental work concentrated on the position of the wing relative to the fuselage. The first published report dates back as far as 1921 in which Prandtl investigated five different vertical positions of the wing. He concluded that the worst location for the wing , in terms of aerodynamic performance, was below the fuselage with a considerable increase in drag. This position is followed by the low wing position where the lower wing surface was tangential to the fuselage surface. The lowest increase in drag was the high wing position followed by the mid wing position. The addition of the fuselage displaced the L/D curve to higher drag values.

Prandtl's (1921) work was followed by some experiments from the Aerodynamische Versuchsanstalt zu Göttingen (1925) which investigated the drag of various nacelle shapes mounted on a wing. The nacelle had the same chord as the wing and consisted of two halves which were mounted either on top or underneath the wing. The results confirmed Prandtl's investigation. With the nacelle mounted underneath the wing the drag increase was significantly less than with the nacelle on top of the wing. The drag increase was less severe at lower lift values. This was also found by Jacobs (1930) who conducted an experiment with nacelles positioned below and on top of a wing. The least drag increase was obtained with the nacelle almost entirely embedded in the wing followed by a nacelle underneath the wing. Increasing the vertical distance between the nacelle chord and wing chord led to lower drag values. Jacobs showed that with equal vertical distance of wing chord to nacelle centreline, the high wing combination had a smaller drag increase than the low wing configuration.

Parkin and Klein (1930) investigated 12 different wing-fuselage combinations. They varied the vertical position of the wing and changed the shape of the fuselage and the wing. On all combinations the low wing configuration had the lowest maximum lift coefficient C_{Lmax}. The maximum lift of the mid wing occurred at a lower angle of attack than for the high wing model, but both combinations had the same value. This was independent of the shape of the fuselage and the wing. This commonality was not observed on the L/D ratio versus angle of attack. The faired high wing model with a fuselage of elliptical cross section had the best L/D ratio over a wide range of angle of attack followed by the mid wing combination. On the configuration with a rectangular fuselage the high wing arrangement again had the best L/D ratio followed by the low wing configuration. The combination with a semi-elliptical fuselage had the same L/D ratio distribution as the model with the elliptical fuselage. However, the curves are much closer over almost the entire range of angle of attack and the peaks do not vary as much as they did for the other two fuselages. Parkin and Klein (1930) explained the

interference effects by a change of effective camber of the wing. The fuselage is surrounded by a system of curved streamlines. If a vertical plane is passed through this system, near the fuselage, the flow in this plane is curvilinear with the curvature bent downwards in the vicinity of the wing. This flow, past the cambered airfoil in effect increases the camber of the airfoil. This can be visualised by picturing the streamlines and airfoil camber as readjusted until the streamlines are straight. The airfoil then becomes deeply cambered. Obviously with the camber being increased the critical angle at which the airfoil stalls is smaller. Had the airfoil been on top of the fuselage, the reverse would have been the case. The streamlines would have been deflected upwards and thus the effective camber of the airfoil near the fuselage decreased.

The general variation of lift and drag versus the distance of the wing chord to body axis was investigated by Ower (1932). He examined 15 different wing positions above and underneath the fuselage. The position of maximum lift was found to be 0.2 chord under the centreline of the body and the lowest lift was observed with the upper wing surface tangential to the lower body surface. At this location the combination had the highest drag. The mid wing configuration was a good compromise of drag and lift.

In their research program on 209 wing-fuselage combinations Jacobs and Ward (1935) investigated the vertical wing position with several profiles (NACA 0012, NACA 4412 and NACA 0018-09). For the NACA 0012 profile in mid wing position the drag curve showed an abrupt increase in drag at $\alpha = 12^{o}$. By lowering the wing this abrupt change smoothed out to higher values of drag at a lower angle of attack. A similar trend was observed for the NACA 4412 profile but at higher drag values. The NACA 0018-09 airfoil showed a sudden increase in drag only for the low wing configuration whereas the remaining combinations had a smooth curve. This abrupt increase in drag corresponded to an incomplete flow breakdown occurring at the leading edge of the wing before the more complete breakdown occurred that determined the maximum lift. This initial breakdown tended to become aggravated so that it spread rapidly over the remaining wing. Associated with this breakdown was a lower maximum lift than for the wing alone, which was not observed for the high wing where the maximum lift was the same for the wing and wing & fuselage. With the high wing configuration the smallest interference was at small angles of attack. This was not the case for the low wing combination where the interference occurred at the high speed range of the lift curve with an interference "burble" occurring before zero lift. Owing to the interference the local angle of attack was increased on the wing sections adjoining the fuselage. The highest drag for the low wing combinations was from a configuration where the wing chord was tangential to the fuselage surface. For this configuration they observed an

increased induced drag associated with a loss of lift over the central portion of the wing in the neighbourhood of the fuselage.

The results of the low wing combination were corroborated by McLellan (1948) who measured a drag increment twice that for the nacelle in higher vertical positions although the low wing combination had the least effect on maximum lift. The highest loss in lift occurred in the high wing position and the mid wing had a slight increment in lift.

Fore and aft position of the wing

The fore and aft position of the wing relative to the fuselage has also been investigated for a mid wing configuration by Jacobs and Ward (1935). The further back the wing was located the earlier a rapid rise in drag occurred. This rise occurred at $\alpha = 12°$ for the wing further back than one chord from the nose. The best position was right at the nose of the fuselage. This result confirmed Schlichting's (1979) tests which showed a decline of maximum lift coefficient as the wing was moved backwards from the fuselage nose. From the point where the wing is about one chord behind the nose the lift curve had a smaller gradient and the curve approached a finite value. McLellan (1948) investigated the effect of the fore and aft wing position in the high wing and nacelle configuration. He concluded that the presence of the nacelle in the most rearward position increased the lift slightly and the most forward position had little effect on the drag but resulted in a higher loss of lift.

The effect of the fore and aft wing position on a low wing model was part of Muttray's (1928) research program. He found that the magnitude of the additional drag was greatly affected by the distance between wing and fuselage nose. With the wing leading edge at 1.5 times the wing chord behind the fuselage nose the fuselage exerted greater lift than the portion of the wing which it replaced. Associated with the higher lift was a higher drag. The fuselage model had a blunt nose which affected the flow at the wing root. This was observed with the wing closer to the nose than half chord.

An investigation of combinations of horizontal and vertical movement of the wing was carried out by Boermans (1983) (see Fig. 1.3). On a model of a Schleicher ASW 19 glider, consisting of a fuselage and wing, he compared the lift and drag of the original position with the performance of the configuration with the wing above and behind the original position. By moving the wing back and up the lift and drag decreased. On a fuselage with a higher tail contraction ratio the results showed that moving the wing back and down increased the lift over a wide range of angle of attack and increased the

drag for angles of attack greater than 3°. For a fuselage with an even higher contraction ratio the benefit of higher lift is over a smaller range of angle of attack associated with an increase in drag.

The effect of wing angle in relation to the fuselage centreline was investigated by Jacobs and Ward (1935) and later by Körner (1972). On both models the wing was located at the mid wing position. Jacobs and Ward changed the angle between wing chord and fuselage centreline from -4° to +8° whereas Körner varied that angle between +3° and +6°. He compared his calculation method (described in Section 1.4) with results from Müller (1970) and plotted the spanwise lift distribution for a Reynolds number of 0.31 x 10^6, based on the wing chord. His results show a higher lift at the wing-body junction than for the combination with the chord parallel to the body centreline. A similar observation was made by Jacobs and Ward who plotted the drag versus angle of attack. Reducing the wing angle led to an increase of drag at lower angles of attack. The rapid increase in drag occurred at an angle of incidence of 16° instead of 12° for the parallel wing. Furthermore, the maximum lift appeared at a lower angle of attack with the wing set at a positive angle. The absolute value was the same for all combinations.

1.3.2. Fuselage geometry

The geometry of the fuselage has been subject to experiments within the framework of wing-fuselage combinations. Within their work parameters such as length, diameter, contraction ratio, height etc. have been investigated. Only a few researchers included pressure data in their results and the majority of work considered the effects on lift and drag only. References including pressure data are included in the Discussion of the Results but those investigating drag and lift performance are discussed in the following paragraphs.

Among those who changed the shape of the fuselage were Muttray (1928, 1935), Parkin and Klein (1930), Jacobs and Ward (1935), and Boermans (1983) who modelled a sailplane. The shape of nacelles and their effects on the flow characteristics was examined by the Aerodynamsiche Versuchsanstalt zu Göttingen (1925), Jacobs (1930), Smith and Smelt (1939), Neely (1945), and Wickens in 1987.

In his first tests Muttray (1928) adapted the shape of the fuselage to the streamlines of the wing for a high-, mid-, and low wing configuration. This resulted in a very small increase in drag over the entire range of angle of attack. In the high lift range (C_L > 1.5) of the lift versus drag curve the low wing configuration had smaller lift values

(C_L = 1.6) than the high wing combination (C_L = 1.65) but both curves exceeded the curve for the wing alone lift (C_L = 1.55). The curves for both configurations maintained the shape of the wing alone curve and did not show a rapid increase in drag as did the results of Jacobs and Ward. In his second series of tests Muttray (1935) changed the shape of the fuselage in a low wing configuration. He attached fuselages in the shape of a triangle, square, diamond, and an inversed triangle to a rectangular wing. The square fuselage showed the least drag increase followed by the triangular shape. The increase in drag of these two arrangements was mainly at the high lift end of the lift curve. This was not the case for the other two combinations where the drag curve was shifted to the right and the rise was considerably higher. He concluded that an acute angle between fuselage and upper wing surface acted like a diffuser with a widening of the area towards the trailing edge of the wing. Thus, the flow had to move against an unusually high adverse pressure gradient.

Parkin and Klein (1930) arranged several vertical wing positions on fuselages with an elliptical cross section, a semi-elliptical section, and a rectangular cross section (see Fig. 1.2). Their results showed a common maximum in the L/D curve for the elliptical and rectangular fuselage in the high wing configuration. In the low wing configuration the rectangular and the semi-elliptical fuselage had the same maximum whereas the maximum for the elliptical fuselage was considerably lower. For the mid wing combination the maximum of the L/D curve was seen for the elliptical fuselage followed by the semi-elliptical section. Similar findings were made by Jacobs and Ward (1935). They changed the fuselage cross section from round to rectangular. As a result the drag was reduced at higher angles of attack and the abrupt increase in drag was absent. For lower angles of attack the drag was almost the same for the two models. Fitting a model of an engine at the nose of the fuselage gave a higher drag over the entire range for the rectangular fuselage.

Boermans (1983) changed the thickness of the fuselage behind the point of maximum height and the contraction ratio of the rear part of the fuselage behind the cockpit of a sailplane model (see Fig. 1.3). His results showed, that by increasing the contraction the drag decreased, particularly at higher lift values. The lift reduction was also less affected by the smaller fuselage. He concluded that the reduction in drag was due to a decrease in the wetted fuselage surface, thus reducing the skin friction. However, if the change in fuselage contraction was too large, the drag increased. He concluded that boundary layer material flowing over the upper surface of the fuselage forebody was accumulated against a subsequent adverse pressure gradient which eventually led to an early separation.

The shape of nacelles has been investigated with the view to improve the aerodynamic performance in combination with a wing. Amongst the first research was that of the Aerodynamische Versuchsanstalt zu Göttingen (1925) which placed a nacelle underneath and on top of a wing with the same chord. They compared models of semi-circular cross section and full circular cross section. Obviously the drag rose with increasing diameter, no matter where the nacelle was located. However, the drag increment was higher for the semi-circular models on top of the wing than for the counterparts underneath the wing. Placing the nacelle below the wing affected the drag curve over the entire range of lift. This was corroborated by Jacobs (1929) who altered the rear shape as well as the vertical positions of the nacelle. Some combinations had a pointed tail whereas others had a vertical "beaver tail" . Those combinations which had a pointed tail were found to have a higher drag than those with a "beaver tail".

Smith and Smelt (1939) investigated a similar design and changed not only the shape of the tail of the nacelle but also the location where the tail ended. The two "beaver tails" were orientated at 90° to each other with the horizontal tail in the same plane as the wing chord. Furthermore, the nose of the nacelle was set at various distances from the leading edge of the wing. With the nose in front of the wing leading edge the horizontal tail showed the highest drag over the entire lift range. A significantly smaller drag, approximately 27%, was observed for the vertical tail with the tail ending at the trailing edge of the wing. Moving the nacelle tail behind the trailing edge reduced the drag by another 5%. Compared with the "beaver tails" the drag measured for the pointed tail with the tail ending at the trailing edge of the wing was much lower; approximately 40% less than the drag for the horizontal "beaver tail".

Neely (1941) made similar observations on his model which consisted of a fuselage & wing and two nacelles on either wing side. The length and the front shape of the nacelles remained constant throughout the tests. The tail shapes were similar to those used by Smith and Smelt (1939). In the extreme case the width of the "beaver tail" was constant over the entire length of the nacelle. All modified inboard nacelles reduced the drag of the model at high lift coefficients but had little effect at low lift coefficients. The horizontal "beaver tail" was less effective than a nacelle where the end was tapered.

1.3.3. Fairing geometry

The effects of the geometry of a fairing or fillet have been investigated as an idealised junction model as well as on wing-fuselage models. The idealised junction has been modelled with a wing mounted on a flat wall and has often been used in theoretical

models and with numerical methods. Relevant work is discussed in section 1.4. The geometry of fairings on wing-fuselage models is more complex and has mainly been used in experimental work.

The shape of the fairing varied according to the different wing-fuselage models. The simplest model was investigated by Gough in 1928. He used a high wing configuration and filled the right-angled combination with fillets of different radius. With a small fillet he observed a drag reduction of 0.7% which was increased to 1.7% by doubling the radius of the fillet.

In 1932 Ower tested 15 different configurations, filling the wing-body junction on either side of the wing, where possible, or just on the upper or lower surface. His results showed that no further drag reduction was gained if the fillet was bigger than 8% of the wing chord, independent of the wing position. For the low wing combination the improvement in terms of drag value was greater than for the high wing configuration. He also observed a similar trend in the gain of lift. No extra lift was obtained if the radius of the fillet exceeded 8% of the wing chord.

Muttray (1935) changed the radius and the length of the fairings on a fuselage of diamond shape making the angle between the upper wing surface and the fuselage 45^{o} (see Fig. 1.4). The fairings remained under the two horizontal edges. A small fillet did not prevent a flow separation at the wing root and as a result of this the drag showed a sharp increase at higher lift values. This sharp rise moved to higher lift values as the radius of the fillet increased. If the fillet was of the "wrong" shape the area acting as a diffuser expanded and the subsequent pressure rise led to a sharp rise in drag at lower lift coefficients. Jacobs and Ward came to the same conclusion in their work in 1935. Furthermore, they deduced that a fairing reduced the wetted area and thus reduced the skin friction drag of the model. On their high wing model they observed a reduction in drag at low lift coefficients only and no reduction at all on the mid wing configuration.

Maughmer (1984) investigated the effect of a fairing on a glider model (see Fig. 1.4). The tests were conducted with two types of fairing at the leading edge of the wing, one of a parabolic form and one a straight edge between the adjacent parts. He found that the parabolic fairing increased the drag by 15% over almost the entire L/D curve. But it was possible to reduce the drag by 3-5% with a straight edge. As the leading edge of the fillet became sharper the performance increased.

The flow around an idealised junction has been analysed recently. Kubendran and Harvey (1986) fitted a wing onto a wind tunnel floor and investigated the effect of leading edge fillet on the flow around the wing and the wind tunnel floor. With the use of fillets they reduced the junction drag at moderate angles of attack. At larger angles of attack and larger fillet they noticed a deterioration of the flow characteristics. By modifying the junction the strength and location of a secondary vortex system was controlled. This displacement was corroborated by Devenport and Simpson (1988 and 1990). In their first report they concluded that a fillet displaced the flow in a manner that increased the "effective" nose radius of the wing (the flow was displaced further outwards). With the wing at an angle of attack the effects of the fillet on the structure of the horseshoe vortex were not altered. In their second series of tests they used a larger fairing in the corner between the wing nose and the tunnel surface upstream. With this fairing the leading edge separation was eliminated and the formation of a horseshoe vortex prevented. Furthermore, the pressure fluctuations were reduced in the vicinity of the appendage.

1.3.4. Other geometry effects

An attempt to control the flow was made by Philips (1990) and Butler and Lawford (1967) via area surface suction in front of the wing-body junction and at the leading edge of the wing. Philips used an area suction in front of an idealised wing-body junction and suppressed the junction vortex almost completely, only a weak vortex remaining. Butler applied leading edge suction on a low wing model with 31^{o} sweep back, with conventional L.E. flaps and full-span T.E. Fowler flaps. In his tests he measured an increase in C_{Lmax} and a reduction in the surface pressure at the leading edge.

1.3.5. Summary of previous investigations

The findings of previous researchers cover a wide range of experiments and test conditions. However, some of the results are reiterated throughout the investigations. Those overall conclusions are summarised in the following paragraphs.

The fairing between the wing and fuselage determines to a great extent the flow behaviour in the junction and furthermore on the surface of the individual parts. A fillet moved the junction vortex further out of the junction onto the wing and changed the size and strength of the vortex. A parabolic shaped fairing at the leading edge of the wing increased the drag, whereas a straight edge fairing reduced the drag slightly (Maughmer, 1989). However, increasing the size of the fairing radii between the wing

and fuselage above 8% of the wing root did not gain any improvement in the flow (Gough, 1928). If the shape of the fairing was such that a diffuser between the wing and the fuselage was formed, then the flow had to overcome an unnecessarily high pressure gradient (Muttray, 1935).

A tapered wing and a cambered wing were less affected by interference effects than a rectangular or symmetrical wing (Jacobs and Ward, 1935; Muttray, 1935). The shape of the wing nose determined the size and the strength of the vortices of the junction between wing and body (Mehta, 1984; Jacobs and Ward, 1935).

Near the leading edge of the wing a concentration of vorticity was formed within the boundary layer, which modified the local static surface pressure (East, 1968). In front of the leading edge two regions of separated flow occurred (Devenport, 1990).

1.4. Previous theoretical work

Theoretical investigations of the aerodynamics of the wing-fuselage combinations can be divided into two main categories:

a) analytical

and b) numerical.

The latter approach has been increasingly employed recently owing to the growing number of computer programs which can now handle the large number of matrices necessary to solve such detailed problems. The interference effects between wing and fuselage were divided into four main areas by Küchemann (1978): a) displacement effects, b) lift effects, c) effects of asymmetry, and d) effects of viscosity (see Section 1.2.). Most theoretical approaches neglect the viscosity effect and consider an inviscid flow only. Details of theoretical investigations that attempt to describe the flow around various wing-fuselage combinations are discussed below.

Theoretical investigations date as far back as 1941 when Multhopp used the method of conformal transformation to calculate the load distribution on the wing and fuselage. Application of this method for a wing and fuselage combination was inherently associated with fuselage shapes mainly of circular or elliptical cross section. Such results are of limited relevance, however, in modern applications where the shape of the body changes along the wing root. However, Multhopp calculated the effect of the fuselage on the sectional lift distribution as follows. The circulation of a section of the wing is:

$$\Gamma = \frac{1}{2} a_0 \alpha_{eff} \bar{c} V \qquad 1.4.1.$$

where α_{eff} is the angle between the local direction of incident flow and the direction of zero lift of the wing section. After applying the Kutta-Joukowski equation and inserting the normal velocity, w_n, via conformal transformation the sectional lift can be written as:

$$\frac{dL}{dy} = \frac{1}{2} \rho V w_n a_0 \bar{c} \qquad 1.4.2.$$

where: $w_n = \alpha_w V + w_{nR} + w_i$

α_w: local angle of attack and hence the angle between the flight path and its direction of zero lift

w_{nR}: additional normal velocity due to the effect of the fuselage

w_i: induced velocity due to the vortex sheet which forms behind the wing

Multhopp simplified the calculation of the lift distribution of a wing with a fuselage to that of an equivalent wing where the effect of the fuselage is partly represented by a variation in the chord distribution and partly by a change in the distribution of the angle of attack.

Zlotnik (1952) developed the method of conformal mapping based on Multhopp's method of conformal transformation. He applied this method to the simplified lifting surface theory, although the author admitted that this was not fully justifiable, since the concept of conformal mapping is based on two dimensions and the concept of lifting surface cannot be reduced to two dimensions. However, Zlotnik did attempt to account for the vertical position of the wing in relation to the fuselage in his calculations. The function which took this position into consideration was squared, thus a distinction between a high and a low wing was not made.

The method of conformal mapping was also used by Arthur in 1984. He based his work on the method of Firmin (1980) who used a small perturbation method to determine the inviscid flow. Arthur concluded that corrections for the wake thickness affect the pressure distribution over most of the upper wing surface. Also, owing to the neglect of the boundary layer of the fuselage the calculated pressures were found to be higher than the experimental results..

In his second approach, where Zlotnik (1952) located horseshoe vortices on the wing and images inside the fuselage, he was limited to combinations where the fuselage diameter was smaller than half the wing chord at the root. Applied to a swept mid-wing configuration the calculations showed a decrease of lift close to the wing-fuselage junction which had not been observed by experiment (Körner (1972)).

A similar concept was used by Weber (1969) who located a single straight vortex line at 90° to the fuselage (see Fig. 1.5). In order to satisfy the boundary conditions of no flow velocity normal to the fuselage surface a source-sink distribution was situated on the fuselage surface. The results were applied only within linear wing theory, thus the interference between wing thickness and lift was ignored. In the results for the spanwise lift distribution she showed an increase in spanwise lift which resulted from the effect of the sectional angle of attack. The lift was also shown to decrease towards the wing-body junction in the same manner as had been observed on the model detailed in this thesis.

In the second investigation Weber (1971) located a source line at exactly the same position as in the first investigation. As before a source distribution was added on the fuselage surface. She also showed that according to first order theory for wing-body combinations the streamwise perturbation velocity in the junction can be reduced by 10 to 20%. However, according to second order theory the reduction is about 60%. This, therefore, categorically showed that all second order terms should be considered in the calculations.

Numerous researchers have used the assumption that an infinitely long cylinder can be used to model the fuselage. Albone (1972) used a transonic small perturbation equation for solving the velocity potential. His calculations for the pressure distribution along the chord showed a reasonable agreement with experimental measurements for angle of attacks of 0° and 1°, but for $\alpha = 2°$ a discrepancy on the upper surface at the junction was observed. The calculated pressure was higher than that obtained experimentally.

With the advance of high speed computers more numerical approaches have been developed over the last twenty years. The revolution was led by A.M.O. Smith and J.L. Hess at the beginning of the 60's. Their method is essentially the core of the panel method where a source distribution is located over the entire model surface. Local regions of separation and reattachment did not invalidate the calculations and compressibility effects were neglected for Mach numbers up to 0.5. The results showed

that the lift distributions were the same for the wind tunnel model and the computer model, but the method was less accurate for three-dimensional bodies than for two-dimensional cases.

Based on this method is the research of Basu (1989), Labrujere (1990) and Körner (1972). All of these researchers changed the original method slightly and used it for different configurations. Some of their results are compared with the data obtained during this present work and are discussed in Chapter 5.

Basu (1989) placed a source and vorticity distribution on the camber surface of the wing and a source distribution on the fuselage surface. Additionally two source lines were located close to the leading edge of the wing. A vorticity distribution was used on the wake surface behind the wing and tail plane. His results showed an overestimation of lift along the entire span. This discrepancy was attributed to viscous effects and wind tunnel interference. Despite this the method gave details of the lift distribution in general and showed local trends which were also observed by experiment.

A source distribution on the model surface was used by Labrujere. Additionally a vortex sheet was used to represent the wake in the case of a lifting wing. The method was applied to a mid wing combination with a rectangular wing. In his calculations the lift over the fuselage was obtained for the cylindrical part of the fuselage only. The method overestimated the lift along the span owing to the neglect of viscous effects. Small details of the spanwise lift distribution which were observed by experiment were also predicted in the computer model.

Körner developed a slightly different approach. The wing was represented by a vortex model which consisted of discrete horseshoe vortices. An infinitely long cylinder modelling the fuselage became a stream surface by mirroring the vortex system of the wing at the fuselage surface and by adding a source-sink distribution on the fuselage surface and a doublet distribution on the axis. This method was applicable to arbitrary wing positions and planforms. In the calculation for the induced velocity due to the fuselage the vertical position of the fuselage was taken into consideration and a distinction between high- and low wing was only made for the fuselage parallel to the uniform flow. For the fuselage at any angle of attack this distinction vanished since the calculation was slightly different. Further details of this method are included in the Discussion of Results (Chapter 5) since some comparison of the spanwise lift distribution was made.

To summarise:
In most cases the body is assumed to be infinitely long and the cross section does not change rapidly along the body axis. Most calculations of the spanwise lift distribution also assume that the flow is non viscous. Clearly, in many cases, this leads to an overestimation of the lift and a higher pressure than that obtained by experiment, particularly at the wing-fuselage junction. Furthermore, most theoretical approaches are restricted to small angles of attack ($\alpha < 3°$), therefore, separation is not taken into account. Some of the numerical methods predict the overall lift distribution, but again the calculated lift is higher than the one obtained experimentally.

1.5. The present investigation

Most of the research of wing-fuselage combinations has so far concentrated on:

a) the development of appropriate theoretical methods in order to predict the lift distribution precisely
b) experiments to investigate the overall performance of such combinations in terms of drag and lift
c) developments of wings in order to reduce the interference effects of the fuselage

Up to the present day no, or little attempt, has been made to investigate in detail the pressure distribution around wing-fuselage configurations. In particular the influence of the flaps has not been investigated nor have flaps been taken into consideration in any of the theories described in the preceding sections.

In order to achieve a better understanding of the interference problems, the influence of the flaps, and the differences between a high wing and a low wing configuration in terms of performance, a detailed experimental study was undertaken in order to provide extensive comparative data for both high and low wing combinations.

In order to be able to examine the mutual effects on the flow of the individual parts the following configurations were tested:

1. Wing alone
2. Wing & flaps
3. Fuselage alone
4. High wing & fuselage
5. Low wing & fuselage
6. High wing & fuselage & flaps
7. Low wing & fuselage & flaps

The following guidelines were adopted in view of previous work and the available facilities:

1) The test model was to be mounted in the 2.1m by 1.5 m working section of the University of Bath wind tunnel (see Fig. 2.3 to 2.6 and Chapter 2.).
2) The pressure data was to be taken over the entire model for a range of angles of attack of $\alpha = 0°$ to 15° and the flap setting should allow a maximum deflection of $\delta = 30°$.
3) The airfoil should incorporate tapping holes where the pressure data was to be taken and their location should allow the detection of local steep gradients in the pressure field.
4) The fuselage should incorporate tappings where the pressure was to be taken and should hold the Scanivalves and the mountings for the wing.
5) The flaps should be of a simple design in order to allow a precise deflection angle and removal without altering the airfoil shape.
6) The design of the model should allow the testing of each individual part alone and in combination without changing the wind tunnel test conditions.
7) The loading on the wing should be as near as possible to the two-dimensional case for the wing alone and wing & flap configuration. This was to eliminate overlapping of wing tip effects onto the wing-fuselage junction effects.
8) The ratio of the fuselage diameter to the wing chord $d/\overline{c}$ was to be equal 1 since it would then represent the design of airliners such as the DeHaviland DHC Dash 8.
9) The design of the fairing between the fuselage and the wing was chosen to be similar for the high and low wing configurations.
10) The model was similar to one used by Rahman-Jami *et al* (1984) in order to compare directly test results.
11) The wing section was to be cambered in order to give positive wing lift at zero wing and fuselage incidence for both a high and low wing configuration with an appropriate fairing shape between fuselage and wing

1.6. A brief guide to the remainder of this thesis

The design considerations of the model will be outlined in detail in Chapter 2. Included in this chapter is a description of the wind tunnel at the University of Bath and a description of the calibration of the working section of that wind tunnel. In addition, the control system for altering the angle of attack is explained.

Information of the instrumentation system used in this study and the computer programs employed to analyse the wind tunnel data are given in Chapter 3. Listings of the computer programs can be found in Appendix A. The calculation of the lift distribution is also outlined in this chapter.

Chapter 4 presents the pressure data obtained during this thesis and the lift distribution calculated from the data over the entire model. Other relevant research results are also presented here.

Chapter 5 includes a detailed discussion and analysis of the data obtained for the individual components. The pressure and lift data are also compared with pressure data obtained by other researchers and differences or similarities are noted.

Conclusions from the discussion of the results will be drawn in Chapter 6.

Chapter 7 gives a brief description of a numerical analysis with which an attempt was made to predict the pressure distribution of both high and low wing models.

Chapter 8 compares the results of the numerical method with photographs taken from surface flow visualisation. Differences will be highlighted and explained.

The conclusions of the numerical method and the flow visualisation will be given in Chapter 9.

A summary of the conclusions of the experiment and those obtained from the flow visualisation tests is given in Chapter 10.

Finally, suggestions for further research programs will be outlined in Chapter 11.

2. APPARATUS

2.1. Wind tunnel

All tests were conducted in the 2.1m by 1.5m aeronautical working section of the dual purpose wind tunnel shown Fig. 2.1. The tunnel was powered by a 170 h.p. motor which drove a 4 bladed fan, 3.05m in diameter. Downstream of the working section was a multi-cell diffuser. The contraction upstream had a ratio of 4:1. The maximum continuous centreline velocity in the high speed aeronautical section is 49 $^{m}/_{s}$. The return duct of the wind tunnel is a 3.7m by 3.05m industrial working section with a maximum centreline velocity of 12.3 $^{m}/_{s}$. The tunnel was operated with the vents in the industrial section open to atmosphere in order to avoid airflow through the vents in the aeronautical section, which were closed. The position of the vents is shown in Fig. 2.1.

2.1.1. Calibration of the working section

Before the series of tests the working section was calibrated by Greenwell, Wood and Bean (1990). The variation of the dynamic pressure with reference to the centreline pressure did not exceed 0.4%. At 40 $^{m}/_{s}$ the level of turbulence with respect to the centreline speed was approximately 0.7%.

Figure 2.2 shows schematically the arrangement of the pressure tappings in the wind tunnel. The reference static pressure tappings (p_{stat}) were located at the ends of the contraction. The reference pressure difference across the contraction (Δp_{ref}) was used to set the tunnel speed. The reference static pressures and the tappings on the model were connected to the Scanivalve system in order to record the pressure differences.

2.2. Model

The model consisted of three major parts: the wing, the fuselage, and the flaps. The wing supported the model in the wind tunnel for the high and low wing configuration, as can be seen in Fig. 2.3. Fig. 2.4 presents the low wing model in the wind tunnel. Fig. 2.5 shows the fuselage alone, supported on struts, in the wind tunnel. The design of the model enabled either the whole model, the wing alone or the fuselage alone to be tested at the same position in the wind tunnel. The boundary conditions under different configurations were therefore the same throughout the series of tests. Fig. 2.6 shows the arrangement of the Scanivalves inside the fuselage for the high wing model.

The dimensions of the high wing model are shown in Fig. 2.7. The ratio of fuselage diameter to wing chord $d/\bar{c}$ = 1.0 was made to be similar to many airliners such as the DHC Dash 8 and also matched the model used by L. Bernstein *et al* (1984). The wing was attached to the centre section of the fuselage in such a way that the chordline was tangential to the fuselage topline. The shaded area in Fig. 2.7 b shows the fairing in plan view. The width is given as the widest part of the fairing. On each wingtip endplates were mounted to reduce tip effects and to simulate a wing of infinite span. These are shown as the dotted line in Fig. 2.7 (a). The thickness of the endplates was 6mm. Also shown in this figure are the coordinates and their origin for the data acquisition. All coordinates were in the same direction for all configurations, as can be seen in the low wing configuration in Fig. 2.8. Fig. 2.8 (b) shows the model from underneath with the fairing as a shaded area. The fairing shape changed slightly according to the configuration, as explained in Section 2.5.. However, the wing was located at exactly the same longitudinal position on the fuselage as for the high wing configuration.

2.3. Wing structure

The wing airfoil section was NACA 23015 There was no twist. The wing was machined from two solid pieces of aluminium (Fig. 2.9) with copper or stainless steel tubes embedded in the surface along the span. The two pieces were held together by bolts which were located across the span. The centre void in the wing accommodated the pressure tubes and electrical connections from the fuselage which were connected outside the wind tunnel to the Scanivalves. A small hole in the middle of the wing upper and lower surfaces provided access for the vinyl pressure tubes. All holes on the surface of the wing where the tubes were embedded, and the screw holes, were filled with epoxy and subsequently smoothed to follow the profile of the wing. The hinges for the flaps were mounted onto the wing. These hinges were left on the wing even when the flaps were not attached. The outer ends of the flaps were supported by endplates fittings.

2.4. Fuselage structure

The fuselage centre section was constructed from rolled aluminium sheet, with the bulkheads to which wooden rotatable nose and tail sections were connected by a rod down the centreline of the fuselage as sketched in Fig. 2.10. A thread at the tail end of the rod and a locking nut allowed the cones to be loosened, rotated and locked in place.

The shapes of the nose and tail portions are given by the following equations:

Nose: $$r_n = 5 \times \sqrt{\frac{x}{29}} \left(0.375 \frac{x^2}{29^2} - 1.25 \frac{x}{29} + 1.875 \right) \qquad 2.4.1.$$

Tail: $$r_t = 5 \times \left(\frac{x^4}{30^4} - 2 \frac{x^3}{30^3} + 2 \frac{x}{30} \right) \qquad 2.4.2.$$

where: x: distance in inches from the fuselage nose or tail respectively

r_n, r_t: radius of the nose and tail at x-location

The above equations are for $x \leq 16$ inches for the nose and $x \leq 20.4$ inches for the tail.

The centre fuselage diameter (and wing chord) was 254 mm (10 inches).

The centre section accommodated the mounting attachment to the wing and had a removable cover to enable easy access. The bulkheads in Fig. 2.10 are shown in more detail in Fig. 2.11 for the fuselage alone configuration. When testing the fuselage alone the supporting rods were fixed in the centre section at the same longitudinal position as the wing quarter chord and at the centre of the fuselage. The design of the rods allowed the use of the same bearings as for the wing at the wind tunnel walls. The centre rod was hollow in order to accommodate the struts and the Scanivalve tubes. The clamp blocks and the centre piece were removed when the wings were attached. For the wing configuration the bulkheads are shown in Fig. 2.12. At the bottom of the bulkheads, spacers were positioned according to the high or low wing configuration. Because of the differing upper and lower profile of the wing the cut out of the fuselage changed as well. Also shown in Fig. 2.12 is the approximate position of the fairing side walls.

Located inside the fuselage were manifolds which are shown in Fig. 2.13. A total of 24 manifolds were used for the centre section of the fuselage. This arrangement allowed the use of up to 7 Scanivalves at the same time thus reducing the testing time. The manifolds consisted of aluminium discs with 9 tubes leading to one chamber from which one tube was connected to a Scanivalve. The 9 tubes were connected to surface pressure orifices on the fuselage which will be described in detail later. In order to prevent leakage the tubes were glued in and additionally sealed with silicone rubber, as shown in Fig. 2.14. After assembly all the connections were proof tested with soapy water with pressure applied at one end.

2.5. Fairings

The fairings between the fuselage and wing were made out of glass fibre and of a similar design to that of a DC Dash 8 airliner, for the high wing configuration. The fairing for the low wing configuration was similar. This was to ensure an almost identical model apart from the wing position. However, owing to the different curvature of the upper and lower wing surface the fairing area behind the wing was designed in such a way that it followed the respective curvature tangentially. The fairing was screwed onto the fuselage after the wing had been mounted. Due to the thickness of the glass fibre small gaps between the fuselage and the fairing were unavoidable. These gaps were sealed with plasticine, so that a smooth junction was achieved.

2.6. Pressure orifices on the fuselage and fairings

The distribution of the pressure tappings over the fuselage is shown in Fig. 2.15. On the wooden and aluminium nose and tail units four rows of pressure tappings separated by 90° were drilled allowing simultaneous measurement of pressure. To cover the whole pressure field the nose and tail cones were rotated by ten degree intervals until the whole 360° were covered. These pressure tappings were in line with those from the centre section which were drilled at every ten degrees around the circumference. Each row consisted of 48 pressure tappings along the length of the fuselage leading to 1728 data points on the fuselage surface. Over the section which coincided with the wing the tappings were located at the same longitudinal position as the chord wise positions on the wing. Due to the presence of the wing no fuselage pressure data is available in the region between 0° and 60° on either side of the centre line of the wing as shown in Fig. 2.15.

Over the fairing the pressure tubes were distributed in line with those on the fuselage as can be seen in Fig. 2.15. The tappings on the side wall of the fairing were located at the extended line of the appropriate tapping on the fuselage surface. Unfortunately the fairing covered some pressure tappings on the wing and fuselage causing some gaps in the surface pressure plot.

2.7. Pressure orifices on the wing

In order to obtain a three-dimensional surface pressure plot the entire wing was covered with pressure orifices as depicted in Fig. 2.16 and 2.17. At selected spanwise locations, holes (N^{o} 73 drill, coball drill for the stainless steel tubes) were drilled leading to a total of 38 rows in order to measure the chordwise pressure across the wing. The holes were drilled perpendicular to the surface, in order to give an accurate

measurement of the static pressure only and not a component of the dynamic pressure. To be able to detect the anticipated rapid changes in the pressure field the distance between the row of holes close to the fuselage was smaller than outside the overlapping area. Furthermore on the part of the wing over the fuselage diameter the tappings were at the same lateral projected position as the 10° fuselage intervals.

A total of 46 pressure tubes were distributed across the chord which are presented in Fig. 2.17. This arrangement led to 1748 data points on the wing. The pressure tubes were sealed at one end and connected to the Scanivalves at the other. Row number 24 was at the centre of the wing and coincided with the 0° and 180° position of the fuselage. Near the leading and trailing edge the tubes were closer together in order to detect changes in those areas. However, not all orifices were used for the wing alone and the wing & flap configuration since a uniform flow field was anticipated.

2.8. Flaps

The model used external flaps with the same profile as the wing (NACA 23015) but with $c_{Flap}/c_{Wing} = 1/3$. The flaps were hinged on the wing and were not retractable. Fig. 2.18 shows the dimension and location of the flap with respect to the wing. The location of the pressure tubes on the flaps is presented in Fig. 2.19. The spanwise locations of the rows of tappings on the flap were in line with those on the wing; thus the pressures to be measured were at exactly the same spanwise location. On each flap the tubes were sealed at the fuselage side and connected to one Scanivalve on the side behind the endplate. The adjustment device and the datum line from which the flap deflection angle was measured was mounted on the endplate. For the wing & flap-configuration, the flap was a single piece with the same span as the wing in order to ensure that there was no spanwise gap in the wing and flap data. For the complete configuration the flap was then cut into two pieces in such a manner that there was no gap in the high wing configuration between the fuselage and the flaps.

2.9. Angle of attack control

During the tests two different control systems for varying the angle of attack were used. Fig. 2.20 shows schematically the arrangement of the fuselage in the wind tunnel. For the fuselage alone the centre rod of the fuselage was connected to a wire which spanned the working section of the wind tunnel behind the model. The wire was coupled to a small wheel winch outside the wind tunnel which was operated by hand. Small markings on the wire were related to the correct angle of attack thus allowing external control while the wind tunnel was running. Additionally a thin extension with a diameter of 1mm was mounted on the centre rod which also gave an indication of the

position on the diffuser just behind the model. Since the wire was exposed to the airstream the accuracy of this system was tested prior to the tests. The system was reliable and highly accurate. An offset of 0.5 mm at the diffuser at an angle of attack of 3° led to an error of 0.58%. The second control system for varying the angle of attack consisted of markings on the endplate of the wing. An indicator above the endplate showed the angle of attack. The indicator and the markings on the endplate are visible in Fig. 2.3 and are schematically shown in Fig. 2.20. A window in the working section allowed an observation of the control setting while testing.

3. INSTRUMENTATION AND DATA ANALYSIS SYSTEM

The experiments were carried out in two series of tests for which two different data acquisition systems were used. A flow chart showing details of the operator input and the control signals is shown in Fig. 3.1. The operator input varied slightly according to the data acquisition system used. Details of the steps required for this input are given in the following sections.

3.1. Data acquisition system

The first series of tests (wing alone, wing & flaps, and high wing combination) was conducted with a total of four Scanivalves, two of which were situated inside the fuselage. In order to cover the entire pressure field of the fuselage, therefore, the fuselage had to be opened and the pressure tubings relocated to the new row where data were due to be taken. Owing to this arrangement the tests were extremely time consuming and the model suffered mechanically from continual reopening. The wing and flap data were each obtained with Scanivalves which were located outside the wind tunnel.

To overcome the problems with the fuselage measurements, manifolds (described in Chapter 2) were designed which were operated via another arrangement of Scanivalves. These utilised a second program "Rigtest 3.5" (Greenwell, 1992) for the second series of tests (fuselage alone and low wing combination). During these experiments a total of seven Scanivalves were employed. Throughout this series of tests all pressure tappings on the centre part of the fuselage were connected to the manifolds which subsequently were connected to the Scanivalves. All rows were covered with sellotape apart from the one where data were due to be taken. This arrangement allowed the fuselage to be kept closed permanently. Details of the acquisition systems are explained in the next paragraph.

The fuselage was equipped with four Scanivalves and the wing with one. Each of the two flaps had another Scanivalve. The arrangement of seven Scanivalves allowed simultaneous data acquisition and significantly reduced the time required in the tunnel. The calibration of the Scanivalves was done through a "wind-off" run prior to each test. During this run the ambient pressure in the tunnel was taken as the reference pressure, thus allowing the pressure on the model to be measured directly as the difference from this ambient pressure. The Scanivalves were built into a rack which also accommodated the transducers which were connected to a data acquisition board

(DT 2821 by Data Translation Inc.). Each new set of data taken for one row was assigned to a datafile which was named by the operator.

The static pressure on the model surface was measured against the reference pressure p_{stat} in the contraction part of the wind tunnel (see Fig. 2.2). This static pressure p_{stat} was actually taken upstream of the working section and had been checked by calibration to match the equivalent free stream static pressure in the test section. The pressure coefficient C_p was then calculated from the differences between these pressures as follows:

$$C_p = \frac{p - p_{stat}}{\frac{1}{2}\rho V^2} \qquad 3.1.1.$$

The calibration factor

$$\frac{1}{2}\rho V^2 = 1.03 \times \Delta p_{ref} \qquad 3.1.2.$$

was introduced, hence

$$C_p = \frac{p - p_{stat}}{1.03 \times \Delta p_{ref}} \qquad 3.1.3.$$

3.2. Data analysis system

Two different analysis programs were used during the tests. The first program was a BASIC program written for this model at the University of Bath by Qereshi (1987). For this program only the listings and no documentation was available. The second program (Greenwell, 1992) was written for multi purpose use at the University and was only slightly modified for this model. The software packages and steps involved are depicted in Fig. 3.2.

3.2.1 BASIC program

The BASIC program provided a complete system from pressure measurements to graphical output of the results and only utilised a total of four Scanivalves. The program was also only written for the high wing configuration. This limitation resulted in gaps on the pressure graphs for the fuselage although data at those points were available. By applying the program for the fuselage alone it was realised, that in combination with a different set of Scanivalves erroneous results (such as a C_p value greater than +1) were produced. Furthermore at locations where no data were available the program inserted a value of 10 for C_p. These values were erased at a later stage in the spreadsheet program. Due to these flaws this program was not used for

subsequent analysis of the data. However, data obtained with this program, in C_p form, for the first series of tests were retained.

It was necessary to convert the data from BASIC into ASCII format in order to pursue the analysis further. A small program was written which read in the data from the BASIC file, converted it and stored the resulting data in a new file (see Appendix A for the listing). The ASCII files consisted of up to 1794 lines adjoining all data in one column. This column was then transformed into a matrix reflecting the tapping grid on individual parts of the model. Some files contained data for the wing as well as data for the flaps, thus a separation of the data into two different files was required. These transformations were conducted within the spreadsheet program AS-EASY-AS (see Appendix A). In order to produce a three dimensional graphical output and perform calculations a further transformation into MS-EXCEL format followed

3.2.2. RIGTEST 3.5

To overcome the problems with the BASIC program a second program "Rigtest 3.5" (Greenwell, 1992) was employed which was more versatile and allowed the connection of a maximum of 7 Scanivalves. The program was written specifically to control the DT 2821 board (see Fig. 3.1), which drove the Scanivalves and provided the user with a menu. The operator had to write a configuration file in accordance with the number of Scanivalves used and required an input of the step length for the pressure recorded and the delay time between each step. Before each new model configuration was tested a fresh configuration file had to be written which included a new file name for the data file.

A series of pilot tests was conducted before the actual test runs were started in order to find the optimum response time for the Scanivalves and in order to detect the lags in the pressure changes due to changes as the angle of attack was increased. The Scanivalves averaged the pressure over 100 samples during a set test time of 0.1s per channel. The delay time between channels was set to 0.2s. Before starting a new test run at a different angle of attack the delay was set to 1 min to allow the air in the tubes to settle. The program provided an on-line screen for all seven Scanivalves so that blocked pipes or leakage's could be detected immediately.

The data were stored in ASCII format, similar to those files converted from the BASIC program. The files consisted of one column and up to 1730 lines, thus again a transformation was necessary. Because data taken simultaneously were stored in one

file, regardless of the individual part of the model, some files had to be fragmented accordingly. The routines within AS-EASY-AS for the rearrangement of the data were similar to those used before. After reorganisation the files were converted into MS-EXCEL format, as described previously, for further analysis, calculations and plots.

3.2.3. Analysis algorithm in MS-EXCEL

After the data were transformed into the format required by this commercial package the co-ordinate system was inserted into the files. The coordinates were determined by the location of the tapping positions on the model as described in Chapter 2. For the wing the span was given as the tapping row and the chord as $^{x}/_{c}$ respectively. The fuselage matrix was arranged in a similar way, but with the tapping row versus the tapping angle φ. An example of the final layout of the desired matrix form is shown in Fig. 3.3.

Once the matrix was established the calculation of C_p was performed by dividing all cells of one column by the first cell of that column, since the reference pressure was stored in that cell. After this computation the data were separated into different files according to the surface where the data originated from. Subsequent calculations were then simple. Pressure differences were derived by subtracting data at appropriate cell positions. The listings can be found in Appendix A. Since the tapping distribution varied between the upper and lower surfaces at the trailing edge the pressure difference was computed only at points with the same chord location.

The numerical integration (see Appendix A) of the lift distribution over the wing and the fuselage was also carried out within this package. At positions where data were not available due to an overlap of two parts of the model, the data were inserted from the appropriate file, e.g. data from the upper surface of the wing were inserted into the fuselage file on the high wing configuration.

Once the calculations were completed the data were imported into the graphic package GRAFTOOL which allowed surface pressure plots and X-Y plots for the lift distribution and pressure difference to be created.

3.3. Lift distribution over the whole configuration

The calculation of the lift distribution over the entire model was executed in two directions. The integration for the wing was made along the chord whereas over the fuselage the integration was in both a lateral and longitudinal direction. Figures 3.4,

3.5 and 3.6 indicate the direction of integration. Since the pressure tappings were located at the same position on both surfaces (upper and lower), regardless of the part of the model, the calculation of C_n by numerical integration was simple. The trapezium rule was applied in the calculation of the local normal coefficient C_n given by Equation 3.3.1.

$$C_n = \int_0^1 (C_{p\,low} - C_{p\,up}) \frac{dx}{\bar{c}} \qquad 3.3.1$$

where $C_{p\,low}$: pressure coefficient on the lower surface
$C_{p\,up}$: pressure coefficient on the upper surface

For the remainder of the text it will be asumed that C_n represents the local lift coefficient given that the cosine of the angle of attack is close to unity.

Fig. 3.4 shows the partition of the wing and the corresponding equations. The lift for an area between two tapping positions was obtained from the sum of pressure coefficients of two adjoining tapping positions on the upper surface and then subsequently subtracted from the corresponding pressure coefficients on the lower surface. The sum for the whole area was then divided by the chord thus leading to a local lift coefficient. This calculation was repeated for all tapping positions resulting in a spanwise lift distribution over the entire wing. At positions where fuselage data were inserted, the distribution of pressure tappings was slightly different and thus, the calculation on that surface was adapted in that area. Fig. 3.5 depicts details of the area where the data were inserted and also shows details of the calculation over the remaining fuselage. Each tapping row on the fuselage at an angle φ corresponded to one tapping position on the wing, for example $\varphi = 60°$ is equivalent to $y/c = 0.433$ on the wing. In order to calculate the local lift coefficient for each tapping angle the length of the individual row varied since the fuselage was tapered. The length of each row was determined by projecting the tapping rows onto the plan view to establish the first and last pressure orifice in that plane. The difference between the lower and upper fuselage surface of each row was subsequently divided by the chord of the wing. Thus, all C_l coefficients were normalised with respect to the wing chord.

The calculation of the lift over the fuselage in a lateral direction was carried out in a similar manner. Fig. 3.6 illustrates the areas used for these calculations. The diameter $d = c$ was held as the constant reference length over the entire fuselage in order to prevent fallacious loadings in the nose and tail region.

3.4. Data validation

In order to check the data obtained during this research and estimate errors which occurred during the tests the pressure data of the wing was compared with a two-dimensional panel method (Obrien, 1993) The calculated lift from the experimental data was also compared with results from Abbott and von Doenhoff (1959).

Figure 3.7 shows the mean, calculated along the span, and one standard deviation for each chordwise tapping position for an angle of attack of $\alpha = 0°$. On the upper wing surface a maximum standard deviation of 0.14 for a mean value of $C_p = - 0.4$ occurred at $^x/_c = 0.05$. However, for the majority of tapping positions the standard deviation was only in the order of 0.02. Included in this graph is the calculated pressure distribution from the panel method. The numerically predicted pressure distribution shows a good agreement with the experimental data over the first 40% of the wing chord. From about $^x/_c = 0.4$ toward the trailing edge the panel method overestimates the pressure. The deviation of the theoretical curve from the mean of the experimental data can be explained by viscous effects which were not taken into account by the inviscid code.

Figure 3.8 depicts the mean and one standard deviation for the lower wing surface. A maximum deviation of 0.18 for a mean value of $C_p = - 0.24$ occurred close to the leading edge at $^x/_c = 0.02$. As for the upper wing surface the numerical data has been included. The panel code calculated a higher pressure along the entire chord. However, the trend of the experimental data is reflected well in the data obtained from the two-dimensional inviscid code.

Figure 3.9 shows the lift coefficient versus angle of attack for the wing alone compared with results from Abbott and von Doenhoff (1959) and the calculated coefficient from the panel method. The graphs from both experiments show a similar flattening of the lift curve at angles of attack of $\alpha \geq 12°$. This clearly shows an approach of the stalling angle of the wing, which is obviously higher for the higher Reynolds number in the tests of Abbott and von Doenhoff. The slope of the lift curve obtained from the panel code remains constant for all angles of attack, which is due to the absence of viscous effects in this method.

Pankhurst and Holder (1965) gave the following equation for a correction of the angle of attack due to the wind tunnel walls:

$$\Delta\alpha = \varepsilon \frac{S}{A} C_L \qquad 3.4.1.$$

The correction factor ε can be found from tables in Pankhurst and Holder (1965) and depends on the shape of the tunnel section and the wing loading. For the wind tunnel of the University of Bath this factor was 0.138. The ratio of the wing area to the cross sectional area of the working section is 0.105. Since the product of these two factors is of such a small magnitude the curve of the corrected values for the angle of attack almost coincides with the curve of the uncorrected values and the maximum difference is for $\alpha = 15°$ where the correction is of + 1.02°.

4. PRESENTATION OF RESULTS

This chapter contains a summary of the results obtained; the discussion of the results is reserved for Chapter 5. The data are presented in two forms: First the original pressure data for all configurations are represented in surface pressure plots (Figs. 4.1 to 4.21). These data are shown for three angle of attacks: α = 0°, 6°, and 12° and for the following flap deflections: δ = 0°, 10°, and 20°. Second the calculated data (C_L and ΔC_p) are illustrated as X-Y plots where data from the literature (Körner, McLellan and Müller) have also been inserted where appropriate (Figs. 4.22 to 4.53). These figures also include angles of attack of α = 3°, 9°, and 15° and a flap angle of δ = 30° for the low wing configuration.

4.1. Original Pressure Data

The original wing data are presented with the wing data first followed by the fuselage data. The figures corresponding to each configuration will be introduced and any erroneous data will be explained. The plots have been arranged such that, where possible, the high wing configuration is always above the low wing configuration, thus allowing a direct comparison between these two arrangements.

4.1.1 Wing data

The wing data are given in the following order: wing alone (Figs. 4.1.), wing & flap configuration (Figs. 4.2 to 4.4), followed by the fuselage & wing configuration (Figs. 4.5 to 4.7). The fuselage & wing & flap configuration is shown in Figs. 4.8 to 4.17. The figures consist of 6 graphs illustrating the pressure distribution on the upper surface of the wing (indicated by subscript "a" and "d" on the plot), followed by the lower surface (subscript "b" and "e") and finally with the difference between the two (subscript "c" and "f"). In order to be able to compare all configurations simultaneously the minimum value for C_p and ΔC_p was set to -8. The x- and y-axes have been normalised with respect to the wing chord. The y-axis starts at y/c = -2.5 which represents the first row of pressure tappings on the port wing. The last row is located at y/c = +2.375; thus the y-axis is asymmetrical. The x-axis represents the chordwise distribution of pressure tappings (see Fig. 4.1).

Small irregularities in the pressure distribution at the leading edge were unavoidable due to blocked holes and dirt inside the pipes. However, these problems did not make a significant difference to the overall pressure field.

Figures 4.1 displays the pressure distribution for the wing alone. Figures 4.2 to 4.4 present the pressure data for the wing & flap model for increasing angles of attack, starting with flaps attached but not deployed. The variations in the grid of the surface plot between the two configurations are due to the number of rows of pressure tappings used.

Figures 4.5, 4.6 and 4.7 show the pressure distribution for the fuselage & wing configuration for $\alpha = 0°$, $\alpha = 6°$ and $\alpha = 12°$, respectively, for both the high and low wing configuration. The gap in the data on the lower wing surface for the high wing configuration (subscript b) and on the upper surface for the low wing configuration (subscript d) was due to the presence of the fuselage. As a result of this, the graphs of the pressure difference over this area show only the pressure data for one surface. On the high wing configuration the first five lines of pressure tappings above the fuselage were covered by the fairing, so that no data were available here. This is illustrated most clearly in Figures 4.6 a and 4.7 a. The same applies to the first five lines on the lower surface of the low wing configuration. For both configurations at the leading edge of the lower surface there was a difference in the pressure between the starboard and port wing. This was due to a small leakage in the tube on the wing.

Figures 4.8 to 4.16 show the pressure distribution for the fuselage & wing & flap configuration. Data are first presented for a constant flap angle, δ, of 0° and an increasing angle of attack, α, and then subsequent graphs illustrate data obtained for varying angles of attack at $\delta = 10°$ and 20°, respectively.

The variation in the trailing edge pressure on both high and low wing configurations on the lower surface and the unevenness on the upper surface on the low wing configuration were due to blocked pipes. At an angle of attack of $\alpha = 12°$ (Fig. 4.10 b, 4.13 b, and 4.16 b) the row of pressure data on the lower surface at $y/c = 0.3$ was due to an error in the data acquisition process within the BASIC program which was not apparent during the testing procedure.

4.1.2 Fuselage data

The data for the fuselage is arranged in a similar way to the wing data. The first Figure 4.17 shows the configuration for the fuselage alone. This is followed by the fuselage & wing configuration in Fig. 4.18 and the fuselage & wing & flaps configuration in Fig. 4.19 to 4.21. These figures show the pressure distribution for an increment in angle of attack, α, while the flap angle, δ, was held constant. Due to the rotation of the fuselage between the high and low wing configuration the origin of the tapping angle φ varies

between the graphs. Nevertheless the graphs are arranged in such a way that a direct comparison is possible. The φ-axis varies according to this rotation as well. The x-axis represents the distribution of pressure tappings along the fuselage. The origin for these tappings coincided with the leading edge of the wing, thus the x- axis starts at $^x/_c$ = - 3.1 and finishes at $^x/_c$ = 4.8. In order to display small pressure changes the z-axis covers a smaller range of values of C_p than in previous graphs (see Section 4.1.1).

The high suction peaks in figure 4.17, representing the fuselage alone, were caused by the supporting rods. The effect of these rods extended up to φ = ± 30°. The small drop in pressure at $^x/_c$ = - 0.5 was due to a small step between the wooden and aluminium part of the fuselage. Data from the fuselage & wing configuration is shown in Figure 4.18. Gaps in these data were due to the location of the wing. For the high wing configuration these are at the edge of the graph between φ = 0° and 60°, and between φ = 0° and 300°. For the low wing configuration they are in the middle (φ = ± 60°) of the graph. Three peaks in the pressure data at the tail of the fuselage on the high wing model were caused by a blocked tube. A step at $^x/_c$ = 0.4 between φ = -120° and -180° was also due to a blocked tube in the low wing configuration. Pressure tappings were fitted on the fairing but nevertheless the entire model could not be covered owing to the use of plasticine as described in Chapter 2. This explains some missing data in the middle of the graphs. The Figures for the fuselage & wing & flap (4.19 to 4.21) are shown in the same order as for the wing, i.e. the flap deflection, δ, is constant while the angle of attack varies, for δ = 0°, 10°, and 20°. The graphs for the high wing configuration and an angle of attack of α = 12° (subscript "c") have three lines of faulty pressure data. These data points are excluded from further discussion since a value of C_p > +1 at low speed is impossible. However, the overall performance for this test condition will be discussed.

4.2. Two- dimensional pressure plots

This section presents the pressure difference between vertical pressure tappings on the upper and lower surface of the model. Empirical results and theoretical analyses from the literature have been included in some figures. The organisation of the figures for the high and low wing configurations is as described previously, with the high wing data above the low wing. Data plotted as two-dimensional graphs of the fuselage concentrate on the pressure above and underneath the fuselage in order to examine the extent of the influence of the wing and flaps on the fuselage pressure. The difference between the two locations was calculated as follows:

$$\Delta C_p = C_{p\,bottom} - C_{p\,top} \qquad 4.2.1$$

where $C_{p\ top}$ pressure coefficient at tapping position $\varphi = 0°$

$C_{p\ bottom}$ pressure coefficient at tapping position $\varphi = 180°$

4.2.1. Fuselage pressure data

The difference in the pressure above and underneath the fuselage is depicted in Figs. 4.22 to 4.26 for a range of angles of attack from $\alpha = 0°$ to $\alpha = 15°$ for all configurations tested. A sketch of the wing has been inserted at the bottom of all plots in order to clarify the location of the pressure tubes. The x-axis is represented in the same form as on the three-dimensional figures. Owing to the distribution of the pressure tappings the vertical axis of the graphs ranges from -1 to +1 for the lift C_L and the pressure difference ΔC_p in order to be able to detect small changes in the flow. A few data points which show the lift on the fuselage over the wing area exceed those vertical limits. In order to validate the results presented in this thesis with those quoted by other workers some data obtained from the literature have been included in Figures 4.27 to 4.29.

Figure 4.22 presents the fuselage alone configuration. The irregularities at the centre of the fuselage are caused by the supporting rods which had a diameter ratio of $d_{rod}/d_{fuselage} = 0.196$. Although the rods were at an angle of 90° to the tapping positions the influence is clearly visible. Figure 4.23 presents the fuselage & wing model at all angles of incidence tested. For the high wing configuration data were also available at $\alpha = 15°$. Figures 4.24 to 4.26 display the fuselage & wing & flap model. No data were available for the high wing with a flap deployment of $\delta = 30°$. Both graphs include the fuselage alone case in order to enable direct comparison of the influence of the wing and flap on the fuselage pressure.

Results from Rahman-Jami and Bernstein (1984) are depicted in Figures 4.27 and 4.28. The model tested was similar to the one described in this thesis apart from an additional tailplane and the lack of fillets between the wing and the fuselage. The Reynolds Number was 0.343×10^6 based on the wing chord. The data show exceptionally good agreement for angles of incidence of $\alpha = 6°$ and 12° over the majority of the fuselage. For $\alpha = 0°$ some differences between the two sets of data can be seen, which are probably due to the lack of fillets on the QMC model (Model used by Rahman Jami and Bernstein).

McLellan (1947) conducted an investigation with a nacelle mounted on a wing. His results are shown in Figure 4.29. The wing consisted of a NACA 65-210 profile where

an ellipsoid type nacelle was situated at several horizontal and vertical positions. The speed range was higher (up to M = 0.7) than that described in this thesis and the design was different with a smaller nacelle length / wing chord ratio. However, the data has been transformed in order to show differences and properties of the individual model.

4.3. Lift distribution

The next two sections present the integrated pressure distribution over the wing and the fuselage. The process of integration has been explained in Chapter 3. In order to further the analysis data, and theory from the literature have also been included. The spanwise lift distribution over the wing was obtained by the chordwise integration of the local pressure distribution. The loading along the fuselage was obtained by integrating the pressure across each local diameter, non-dimensionalised with respect to the wing chord c.

4.3.1 Lift distribution over the wing

An indication of the performance of the various configurations is the lift distribution over the wing, which shows the influence of the fuselage for different arrangements and leads to a measure of the overall performance of a particular configuration. In order to obtain a baseline the wing was tested alone. Figure 4.30 displays the lift for the entire range of angles of attack tested. For the wing & flap model the lift distribution is shown in Fig. 4.31. The range of angle of incidence varies from $\alpha = 0°$ to 15° with flap angles of 0°, 10°, and 20°. Figure 4.32 presents the lift distribution for both high and low wing configurations and for a range of $\alpha = 0°$ to $\alpha = 15°$. For a given angle of incidence the lift over the wing is lower than for the wing alone.

To enable a comparison of the flap influence on the lift distribution of both models (high and low wing) Figures 4.33 to 4.35 are presented. The angle of attack was held constant while the flap deflection varied up to $\delta = 30°$ for the low wing configuration. Figures 4.36 to 4.38 show the development of the lift distribution with increasing angle of attack and constant flap deployment. In these graphs results for $\alpha = 3°$ and 9° have been included. For the low wing model data at $\alpha = 15°$ are also given. The loading on the flaps is depicted as a cross hatched and hatched area above the wing loading curve.

For comparison, other research results have been included in Figures 4.39 to 4.43. In order to show small details the C_l - axis has a different range. As previously cited McLellan (1947) conducted similar tests at Mach numbers varying from 0.15 to 0.7. The corresponding Reynolds number varied from 3.8×10^6 to 13.6×10^6 based on the

wing chord. His data are compared with data previously presented in Fig. 4.32 in Fig. 4.39 to Fig. 4.41 for an angle of incidence of $\alpha = 0°$ to 6°. However, the angles of incidence used in both studies were not exactly the same and data obtained in this study at $\alpha = 3°$ is compared with McLellans work at $\alpha = 2.5°$ and $\alpha = 6°$ with McLellans data at $\alpha = 5°$.

The theory from Körner (1972) has been compared with other data (Müller 1970) in Figure 4.42. It shows the lift difference for two different angles of attack. In order to display small changes the scale on the y-axis has been altered. Included in these graphs is the lift difference of the two corresponding models. Because Körner's theoretical data does not differentiate between a high and a low wing the curve is the same on both graphs. Müller (1970) conducted tests with the wing mounted a quarter diameter above and below the centreline and at a Reynolds number of 0.31×10^6.

4.3.2. Lift distribution over the fuselage

The mathematical analysis for the lift distribution has been explained in detail in Chapter 3. The fuselage was first tested alone to observe changes with the attachment of the wing. Figure 4.44 depicts the lift distribution along the body. The irregularities in the middle of the graphs are due to the supporting rods. The fuselage & wing configuration is shown in Fig. 4.45. Included in both graphs is the test configuration of $\alpha = 15°$. Fig. 4.46 to 4.48 show the comparison of the lift distribution for the fuselage & wing & flap configuration with the fuselage & wing model and the fuselage alone configuration. For the low wing model the flap setting of $\delta = 30°$ is shown. In order to show the lift distribution over the fuselage at a set flap angle with different angles of attack Figures 4.49 to 4.51 are presented. For the low wing model the curves for an angle of incidence of $\alpha = 15°$ have been included.

5. DISCUSSION OF RESULTS

The following chapter discusses the results obtained in order to determine the influence of the parts of the model on the pressure distribution. First the pressure data of the **wing** is discussed starting with the wing alone configuration in Section 5.1 followed by the data from the wing & flap combination (Section 5.2). Section 5.3 examines the fuselage & wing arrangements, after which the fuselage & wing & flap model is considered in Section 5.4.

The surface pressure plots for the **fuselage** are discussed in Sections 5.5 to 5.7, starting with the fuselage alone (Section 5.5). After that the data of the fuselage for the fuselage & wing configurations is examined in Section 5.6, which is followed by the fuselage & wing & flaps combinations in Section 5.7.

In Section 5.3, which deals with both high and low wing configurations, the discussion is concentrated on the high wing arrangement first, succeeded by the examination of the low wing before moving on to the comparison of the two. In order to simplify the analysis of the data, the discussion of the fuselage & wing & flap configurations compares both models (high and low wing) before moving to the next set of graphs. After the original data of wing and fuselage have been examined, the discussion concentrates on the pressure difference between the top and bottom rows of pressure tappings on the simple picture of the fuselage (Section 5.8). This is then followed by an examination of the spanwise lift distribution over the wing (Section 5.9). Last but not least, the longitudinal lift distribution along the fuselage is examined in Section 5.10.

5.1. Wing alone

Common to all graphs of the wing data is the almost constant spanwise loading for each angle of attack indicating that the endplates were effective in suppressing tip effects. The small irregularities at the leading edge (most noticeable in Fig. 4.1 g) were due to dirt inside the pressure tubes of the wing. The grid visible on the surface plots represents the location of the pressure orifices. For the wing alone fewer holes were used and thus the grid differs from other configurations.

Figure 4.1 shows the wing alone configuration. The most prominent feature is the linear change in the pressure coefficient on the upper surface with increasing angle of attack. The pressure at the leading edge of the lower surface changed from $C_p = +1$ ($\alpha = 0°$) to $C_p = -1$ at $\alpha = 12°$. As expected, the stagnation point moved backwards as the angle of attack increases. The pressure at the trailing edge on both surfaces remained

almost constant at $C_p = 0$ with varying angle of incidence. A theoretical value of $C_p = 1$ should be achieved (Kutta-Condition) but because of the boundary layer development that value was not obtained. The pressure difference rose linearly from $\Delta C_p = 0$ for $\alpha = 0°$ to $\Delta C_p = -4.5$ for $\alpha = 12°$ at the leading edge.

5.2. Wing & Flap combination; Wing data

Figure 4.2 to 4.4 present the wing & flap configuration starting with flaps attached but not deployed. On the lower surface (subscript b, e, and h) a more positive pressure can be seen at the trailing edge along the entire span. This increase was higher with increment in flap deflection than with rising angle of attack. This indicates that the gap between the wing and the flap was perhaps slightly too small and that the flap should be located further backwards. However, a value of $C_p = 0$ was not exceeded for similar reasons as stated in the previous paragraph. For $\delta = 20°$ (Fig. 4.4) the pressure distribution are of similar shape for all angles of attack. A similar development can be observed for $\delta = 10°$ (Fig. 4.3). Near the leading edge of the upper surface the pressure for $\alpha = 0°$ and $\delta = 0°$ ($C_p = -1$) (Fig. 4.2 a) decreased steadily to $C_p = -5$ for $\alpha = 12°$ and $\delta = 0°$ (Fig. 4.2 g) this decrement was lower than with increase in flap deflection where the pressure drops to $C_p = -1.5$ for $\alpha = 0°$ and $\delta = 20°$ (Fig. 4.4 a).

A comparison between the wing alone and the wing & flap combination shows that the flaps reduce the pressure near the leading edge of the lower surface from $C_p = -0.75$ (Fig. 4.1 h) to $C_p = -1.75$ (Fig. 4.2 h) for $\alpha = 12°$. Setting the flap to $\delta = 10°$ reduced the pressure on average to $C_p = -3$ and for $\delta = 20°$ to $C_p = -5$. This decrement in pressure was similar near the leading edge of the upper surface (Fig. 4.1 g, 4.3 a, d, g to 4.4 a, d, g). Only small changes are noticeable at the trailing edge on the graphs of the pressure difference. For $\alpha = 0°$ the difference rose from about $\Delta C_p = 0$ (Fig. 4.1 c) to $\Delta C_p = 0.5$ (Fig. 4.2 c) for a flap setting of $\delta = 0°$. This increase was slightly higher for $\alpha = 6°$ (Fig. 4.2 f) and 12° (Fig. 4.2 h). With the flaps at $\delta = 10°$, this rise in pressure difference was similar and a value of $\Delta C_p = 1$ was not exceeded. Increasing the flap angle to $\delta = 20°$ increased the value above $\Delta C_p = 1$, which was already obtained at $\alpha = 0°$. Surprisingly, the step in pressure of the lower surface is not shown on the graphs of the pressure difference.

5.3. Fuselage & Wing configuration; Wing data

The pressure distribution for the fuselage & wing combination is depicted in Fig. 4.5, 4.6, and 4.7. For the lower wing surface, it was noted that the pressure at the leading edge varied significantly between the port and starboard wing, which is clearly visible

in Fig. 4.7 b. By comparing the graphs for the high and the low wing combination, it is noticeable that the surface pressure plots of the high wing model are smoother than for the low wing configuration. An explanation for the difference, and the smoother surface plots, could have been dirt inside the tubings located inside the wing, or leakage in the tubing system. Furthermore, it should be noted that the grid, reflecting the pressure holes on the wing surface, differs from the configurations discussed in Section 5.1 and 5.2, because all pressure orifices on the model were used with the fuselage attached to the wing.

5.3.1. $\alpha = 0°$

On the high wing model the pressure on the upper wing surface was very even across the entire span (Fig. 4.5 a), leading to a constant chordwise pressure gradient. No differences between the area above the fuselage and the remaining wing are noticeable. The suction peak near the leading edge approached a value of $C_p = -1$. The pressure distribution of the lower surface (subscript b) was of equal evenness across the entire span. However, careful examination of Fig. 4.5 a and b reveals a small elevation close to the wing-body junction ($^x/_c \approx 0.1$ and $^y/_c = 0.5$). This was due to an increase in flow velocity due to the displacement of flow by the fuselage. The suction peak is not visible in the pressure difference (Fig. 4.5 c). In the region occupied by the fuselage data present on the upper wing surface were eliminated in the graphs for the pressure difference, in order to avoid confusion, since appropriate data of the fuselage was not inserted in the file for the lower surface data (see Chapter 3).

The flow over the wing on the low wing configuration varied significantly from the flow of the high wing model. Fig. 4.5 d shows lower pressure close to the wing-body junction ($^x/_c \approx 0.05$ and $^y/_c = \pm 0.5$) on the upper wing surface. A velocity increase here, due to the displacement of flow by the fuselage, caused a local pressure reduction. The drop in pressure on the lower surface (Fig. 4.5 e) was also caused by an increase in flow velocity due to displacement effects.

The pressure difference in Fig. 4.5 f does not show the pressure reductions which were observed in the pressure distribution of the individual surfaces. The difference between the upper and lower surfaces was very similar to that observed on the high wing model. However, the peaks at the leading edge were marginally higher on the low wing configuration.

Comparing the two configurations for $\alpha = 0°$ reveals that the suction peaks on the upper surface near the leading edge (Fig. 4.5 a and d) were of similar magnitude and

the chordwise gradients were the same. The same developments in the flow field are also seen on the lower surface.

5.3.2. $\alpha = 6°$

The pressure peaks seen in the wing-body junction at $\alpha = 0°$ (Fig. 4.5 f) are also present at $\alpha = 6°$ (Fig. 4.6 f). A small pressure peak is observed at the leading edge . This peak originates from the upper surface which showed a similar distribution (Fig. 4.6 d) at the leading edge. Owing to a separation bubble on the upper surface between 20% and 40% chord, a flattening of the pressure surface across the entire span can be observed. This separation was probably a result of the relatively low Reynolds-number. The pressure at the leading edge of the lower wing surface (Fig. 4.6 e) bore little resemblance to the pressure at $\alpha = 0°$ showing no peak and having a distribution like that of the wing alone (Fig. 4.1 e), but with slightly lower C_p values.

The even spanwise pressure distribution of the upper wing surface, discussed in the previous paragraph, is no longer visible for $\alpha = 6°$ (Fig. 4.6 a). Here the rise in suction peak can be seen on the "clean" wing ($y/c > \pm 0.5$) and is constant over that part of the wing. The pressure over the area above the fuselage increased to a smaller extent. The difference between this area and the outboard wing caused a change of chordwise pressure gradient over the first 25% of the wing chord. The remaining area of the wing had a common gradient across the span. The influence of the fuselage on the pressure on the lower wing surface (Fig. 4.6 b) was small and led to a smooth surface across the entire wing which is also reflected on the graph of the pressure difference in Fig. 4.6 c. At this angle of attack the pressure difference did not show any disturbances close to the junction and therefore no reduction or increase in pressure occurred. The "effectiveness" of the wing in providing lift was maintained up to $y/c = \pm 0.5$.

For $\alpha = 6°$ a comparison of the pressure difference (Fig. 4.6 c and f) for both configurations indicates that the influence of the fuselage was confined to within its vicinity and did not extend in a spanwise direction. Only the pressure rows next to the fuselage showed small changes compared with those further away. Flow visualisation tests confirmed this, as discussed in Chapter 8.

5.3.3. $\alpha = 12°$

The developments seen for $\alpha = 6°$ were more pronounced for $\alpha = 12°$ (Fig. 4.7 a and b). At the leading edge the difference between the port and starboard wing are clearly visible. These differences are not seen on the pressure difference (Fig. 4.7 c) since the

leading edge data is covered by the remaining surface data. Surprisingly, for both angles of attack, $\alpha = 6°$ and 12°, a reduction in pressure towards the junction is not noticeable on the upper wing surface. Such an increase in suction was expected, due to the upwash of the fuselage in front of the wing and the displacement effects of the fuselage resulting in a higher local angle of attack.

For $\alpha = 12°$ (Fig. 4.7 d to f) the pressure on the upper and lower surfaces differed over the entire wing . On the upper surface (Fig. 4.7 d) the suction peak along the leading edge declined towards the fuselage and had its maximum at approximately $y/c = \pm 2$. At $y/c = -0.7$ a single suction peak can be seen. Owing to a slight flow asymmetry in the wind tunnel this reduction is not noticeable on the starboard wing. However, the peak suggests the starting of a horseshoe vortex which wrapped around the wing-body junction and trailed downstream. The vortex core was displaced outwards from the junction in a spanwise direction, because of the presence of the fairing. Similar observations were made by Devenport (1990) on an idealised model where a wing was attached to a flat wall. Along the wing-body junction ($y/c = \pm 0.5$) the chordwise pressure gradient was very small and the pressure remained almost constant from about quarter chord. This suggests a flow separation starting at about 20% of the wing chord and gradually spreading spanwise up to $y/c = \pm 1.5$; a phenomen which was also observed during the flow visualisation tests (see Chapter 8). The pressure on the lower wing surface in Fig. 4.7 e shows small ripples over the rear part underneath the fuselage. These were caused by a small inaccuracy of the transition between the trailing edge of the wing and the fairing.

The pressure difference in Fig. 4.7 f magnifies these effects and also the effects on the upper surface. Thus a pressure increase at the rear of the wing is clearly visible. At the leading edge the magnitude of the suction peaks varied between the two wing sides which was the combined effect of the variation of pressure at the leading edge on the lower surface (Fig. 4.7 e) and upper wing surface (Fig. 4.7 d).

The difference of the geometry was more evident for an angle of attack of $\alpha = 12°$ (Fig. 4.7). However, the lower wing surface on both configurations showed almost the same pressure distribution (Fig. 4.7 b and e) across the entire span. The major differences were over the upper wing surface (Fig. 4.7 a and d). As a result of a junction vortex, a high suction peak was seen on the low wing model but not on the high wing arrangement, where the vortex was either embedded in the boundary layer or died out (Wickens 1987). The leading edge suction peaks which were almost constant along the span on the high wing model declined towards the fuselage on the low wing

combination. This reduction was caused by the displacement effect of the fuselage which diverted the flow in the outwards direction, a development which was seen in the flow visualisation tests. Furthermore, the magnitude of the peaks is smaller on the low wing model than on the high wing configuration. Separation in the low wing junction happens at about 20% chord, with no reattachment of the flow, leading to a constant pressure coefficient along the chord. This flow phenomena was restricted to the vicinity of the fuselage and did not exceed a spanwise position of $y/c = \pm 0.7$ (Fig. 4.7 d). Further away, between $y/c = \pm 1.0$ and $y/c = \pm 1.3$ the air flowed against a high adverse pressure gradient which eventually led to a separation at the rear of the wing. This was reflected in the almost constant chordwise pressure. Muttray (1941) explained this separation as the result of a form of diffuser which was formed by the fuselage and the wing, where the surface of the wing curved downwards and the fairing between wing and body curved towards the centreline of the fuselage. This half-form of diffuser supported the already existing adverse pressure gradient over the wing leading to an even higher gradient which promoted the flow separation in the junction. This development was obviously only present on the low wing model, because of the higher curvature of the upper wing surface. On the high wing model the pressure on the lower surface decreased towards the trailing edge and therefore counteracted the "diffuser" effect.

By contemplating all graphs it is notable that the general characteristics of the flow for the high wing remained the same independent of the angle of attack. The magnitude of the pressure altered with the angle of attack accordingly, but the distribution across the wing was little influenced by the presence of the fuselage for different angles of incidence. This cannot be said for the low wing configuration where major changes in the pressure distribution developed with increasing angle of attack. Most apparent were those at the leading edge of the wing where the presence of the fuselage led to a reduction in pressure and thus the "effective" span was reduced. Observation during flow visualisation tests showed that this increase was linearly related to the angle of attack and started as early as $\alpha = 3°$.

Such changes are certainly influenced by altering the geometrical conditions of the model, one possibility being the attachment of flaps. The next section discusses the influence of flaps on the flow around the model and compares these results with data discussed in this section.

5.4. Fuselage & Wing & Flaps configuration; Wing data

The pressure distribution for the fuselage & wing & flaps configuration is depicted in Figures 4.8 to 4.16. Figures 4.8 to 4.10 show the pressure distribution for a constant flap angle, δ, but with a varying angle of attack α. Fig. 4.11 to 4.16 show results for varying flap deflection.

5.4.1. $\delta = 0°$

$\alpha = 0°, \delta = 0°$

Fig. 4.8 shows the high and low wing combination with both angles α and δ set to 0°. The pressure surface on the upper wing surface, in Fig. 4.8 a, resembles the surface plot of the high wing & fuselage. A tiny difference in pressure between the starboard and port wing is noted at the trailing edge. This becomes more pronounced in the graph of the pressure difference (Fig. 4.8 c). This difference between the two sides of the model was due to a small offset in flap angle and was observed throughout all tests. The disparity in trailing edge pressure is also evident on the lower surface in Fig. 4.8 b. Owing to blocked orifices at about half chord between y/c = -0.5 and -1.3 a trough can be seen. The pressure at the leading edge of the lower wing surface was similar to the suction peaks of the unflapped model, although, on the port side a slightly higher peak was noticed at the wing-body junction. At the trailing edge the pressure obviously differed from the configuration without the flaps. However, on the starboard side the expected step in pressure at the trailing edge was constant along the span, indicating that the flaps were effective along their entire span. The magnitude of this pressure step was the same as for the wing & flap combination which suggests that the fuselage did not influence the effect of the flaps. This can be explained by the fact that the flaps were restricted at the tips by the endplates and the vertical wall of the fairing, thus no gap between the fuselage and flaps was apparent. The geometry of the wing and the flaps in conjunction with the fuselage was similar to the wing & flap combination but with less span.

The pressure distribution on the upper surface of the low wing model (Fig. 4.8 d) resembles the surface plot for the high wing combination, with slightly higher suction peaks at the leading edge. On the lower surface two distinct spikes are noticeable at the wing-body junction. These peaks indicate a high flow velocity, which was due to displaced flow from underneath the fuselage. Photographs of surface flow visualisation support this (see Chapter 8). Owing to the presence of these peaks the spanwise pressure gradient along the leading edge was higher on the low wing model than on the high wing counterpart.

The pressure difference for both configurations resembled that of the model without flaps. Differences existed at the trailing edge where the flaps caused an increase in the pressure difference, and near the leading edge, where the suction peaks were higher. However, it should be noted that those peaks were lower for the high wing configuration than for the low wing model (Fig. 4.8 c and f). This was due to a marginally lower pressure at the leading edge of the upper surface of the low wing combination.

$\alpha = 6°, \delta = 0°$

Figure 4.9 presents both configurations at an angle of attack of $\alpha = 6°$ and a flap deflection of $\delta = 0°$. On the high wing model the pressure on the upper surface (subscript a) shows a suction peak of approximately $C_p = -2.5$ dropping to approximately $C_p = -0.8$ at the centre above the fuselage. This pressure was the same as for the fuselage & wing combination (Fig. 4.6 a) indicating that the mere presence of the flaps ($\delta = 0°$) did not influence the pressure at the leading edge of the wing over the fuselage area. The suction peaks over the remaining leading edge were higher with the flaps present. At the wing-body junction a tiny peak was present which suggested an increase of flow velocity due to the displacement effects of the fuselage. The pressure on the lower surface (Fig. 4.9 b) shows the influence of the flaps at the trailing edge where a small step appeared. Between 30% and 70% wing chord the surface is flat and close to a value of $C_p = 0$, thus showing a higher gradient over the rear end of the wing where the pressure increased to about $C_p = 0.5$. The pressure difference (subscript c) showed a suction peak which was approximately 20% higher (based on the flapped model) than for the model without flaps. Furthermore a small increase in suction towards the wing-body junction can be seen.

A similar trend can be observed for the low wing combination, where the low pressure peaks near the leading edge rose from $\Delta C_p = 2.8$ (fuselage & wing) to $\Delta C_p = 3.2$ (Fig. 4.9 f). Close examination of the graph reveals a small peak at the wing-body junction. This is more clearly visible on the graph for the upper surface (Fig. 4.9 d), where the pressure of the peak is approximately 7% lower (based on the suction peaks of the outer wing) than that of the remaining wing. Again displacement effects were responsible for this reduction which was not noticeable on the lower surface (Fig. 4.9 e). Here the pressure resembled the one for the high wing model. The discussion of that combination is valid for the low wing model as well.

The comparison of the pressure difference (Fig. 4.9 c and f) showed a reduction in the chordwise gradient on the low wing model between $^x/_c = 0.2$ and $^x/_c = 0.3$. This was

due to the presence of a small separation bubble on the upper wing surface. No such trend can be seen on the high wing model where the chordwise gradient was uniform across the span.

$\alpha = 12°, \delta = 0°$

In Figure 4.10 for $\alpha = 12°$ and $\delta = 0°$ the pressure plot for the lower wing surface on the high wing model (subscript b) shows an irregularity at ($y/c = -0.5$) due to a blocked tube. This has been excluded from the discussion. Owing to blocked pipes inside the wing the leading edge pressure showed significant discrepancies between the port and starboard wing. These are also visible on the low wing model (subscript e). However, the overall characteristic of the pressure, and the magnitude thereof, on that wing surface were very similar on both configurations. This was not the case for the upper wing surface, depicted in Fig. 4.10 a and d. The high wing model shows a constant chordwise gradient up to $y/c = \pm 0.5$. This gradient was also present over the rear 50% of the wing above the fuselage. Forward of this point the gradient changed, leading to a c_p of -1.2, slightly above the value for the unflapped model. Outside the fuselage area the suction peaks were almost constant up to the wing-body junction at $y/c = \pm 0.5$, thus showing little influence of the fuselage. This was not observed for the low wing combination, where the negative pressure near the leading edge was gradually reduced towards the fuselage to about 50% of the magnitude over the "clean" wing. Close to the wing-body junction ($y/c = \pm 0.5$) the pressure shows a separation zone, which leads to an area of equal pressure. This was particularly visible on the port side where the pressure orifices were closer together. The magnitude of this pressure was the same as for the model without flaps. The suction peak caused by a vortex was not observed for this combination. One reason for this might be that the location of the suction lay between the pressure orifices and therefore was not detected.

By comparing the pressure difference of the two configurations in Figure 4.10 c and f it can be seen that the magnitude of the suction peaks is up to 50% higher on the high wing model than on the low wing arrangement. Furthermore, the influence of the fuselage was much more visible on the low wing combination. Since the lower surfaces of both configurations showed a similar pressure distribution, the differences in wing loading clearly came from the upper wing surface. As expected, the chordwise pressure gradient was larger with the flaps attached than for the model without flaps.

5.4.2. $\delta = 10°$

$\alpha = 0°, \delta = 10°$

The pressure distribution for both configurations, with the flaps set to $\delta = 10°$, is shown in Fig. 4.11 to 4.13, starting with an angle of attack of $\alpha = 0°$. For both high and low wing configurations the graphs for the lower wing surface generally show a similar distribution apart from the peaks in the wing-body junction. Here, on the low wing model the pressure was approximately 40% of that of the high wing combination (based on the low wing data). However, the chordwise gradient along the junction and the rest of the wing was the same for both models. This is also evident on the upper surface with only marginally lower C_p values over the entire surface for the low wing model (Fig. 4.11 a and d). At the leading edge of the low wing model two suction peaks were apparent which were not as pronounced on the high wing combination. Again displacement flows, and the effect thereof, were responsible for the reduction in pressure. Since the increase in velocity was present on both wing surfaces of the low wing model it would be expected that this effect would be seen on both surfaces of the high wing configuration. However, the displacement effects appear to be more pronounced on the low wing model since the pressure peaks were higher. The graphs for the pressure difference show a slightly higher chordwise gradient for the low wing model than for the high wing combination, because of higher suction peaks at the leading edge.

$\alpha = 6°, \delta = 10°$

The characteristics for the configurations at an angle of attack of $\alpha = 6°$ and a flap setting of $\delta = 10°$ (Fig. 4.12) are similar to those where the flap was deflected at $\delta = 0°$ (Fig. 4.13). Naturally the pressure was lower but the overall pressure distribution was the same. On the high wing model the pressure at the leading edge above the fuselage dropped from $C_p = -0.8$ (Fig. 4.9 a) to $C_p = -1$ (Fig. 4.12 a), indicating that the flaps had an influence here. At the trailing edge only a marginal reduction in pressure was observed at the centre of the wing ($y/c = 0$) which suggests a stronger cross flow over the fuselage caused by the flaps.

$\alpha = 12°, \delta = 10°$

The influence of the flaps was also observed for $\alpha = 12°$ in Fig. 4.13. For the high wing model (subscript c) the pressure difference over the fuselage increased with flap deflection (compare with Fig. 4.10 c). As expected, the decrement in pressure was higher with increment in angle of attack than with increment in flap deflection. However, the trends on the lower surface (Fig. 4.13 b and e) remained the same as for $\alpha = 6°$. On the upper surface (subscripts a and d) the suction peaks for the high wing

model remained constant along the span and the pressure is obviously lower than for the same configuration with δ =0°. For the low wing model the pressure at the wing-body junction ($y/c = \pm 0.5$) remained constant ($C_p \approx -3$) with increment in flap deflection whereas an increase in negative pressure further out from the fuselage was visible, thus leading to a higher gradient along the span at the leading edge. Moreover, the pressure at about $y/c = \pm 2$ was lower than for the high wing model, a development which is not so pronounced at $\delta = 0°$.

5.4.3. $\delta = 20°$

$\alpha = 0°, \delta = 20°$

Three lines of faulty data can be seen on the graphs for the high wing model with a flap setting of $\delta = 20°$ in Figure 4.14. Two in the plot for the upper wing surface at $y/c = -1$ and 0.4, and one for the lower surface at $y/c = -0.7$. These led to troughs in the plot of the pressure difference and were not characteristic for this configuration. Unfortunately, they give the impression that the pressure surface on the upper wing surface on the high wing model was less smooth than for lower angle of attack. However, the pressure distribution resembled the one for $\delta = 10°$. The graph of the pressure difference (Fig. 4.14 c) shows two peaks at the wing-body junction which were not observed with the flaps set at a lower angle with the model at the same angle of attack. Those peaks are also present on all graphs for the low wing model which show a similar pressure pattern as for a flap deflection of $\delta = 10°$. The graphs of the pressure difference for both configurations show a similar pressure distribution, with suction peaks at the leading edge of equal magnitude. The spikes at the wing-body junction on the low wing model at smaller flap angle are still visible, but less prominent. This indicates an interaction between the pressure field induced by the flaps and the pressure distribution caused by the fuselage.

$\alpha = 6°, \delta = 20°$

The trends noted for a flap deflection of $\delta = 10°$ and an angle of attack of $\alpha = 6°$ were similar with an increment of flap deflection to 20°. Figure 4.15 b and e show the same pressure distribution on the lower surface as in Fig. 4.12. Equivalent tendencies were observed on the upper surface with the exception of a line of faulty data. Accordingly the pressure difference (Fig. 4.15 c and f) for both configurations showed parallels to those with a lower flap deflection. The negative pressure at $x/c \approx 0.1$ was approximately 10% higher (based on the low wing data) for the high wing arrangement than for the low wing model. This difference was mainly caused by the variation in pressure on the lower surface.

$\alpha = 12°, \delta = 20°$

Figure 4.16 shows the pressure distribution for $\alpha = 12°$ and a flap angle of $\delta = 20°$. The pressure at the leading edge above the fuselage of the high wing model (subscript a) was almost twice as low as for the unflapped combination (see Fig. 4.7 a) and 2.5 times lower over the remaining wing. This distribution shows that the reduced pressure at the wing leading edge induced by the flaps was carried over on the fuselage, but with lower values. For the low wing configuration (subscript d) the pressure at the leading edge was higher and only a few peaks show a high suction. On the lower surface the pressure distribution was similar to that for a lower flap setting with different values. Not surprisingly, the difference in the pressure (Fig. 4.16 c and f) was similar to those for a lower flap deflection.

5.4.4. Summary

To summarise the alteration of the pressure distribution with changing angle of attack and flap setting for both configurations: the rise in angle of attack led to higher differences in pressure than an increment in flap deflection. This rise of the pressure difference is linear both with increment in flap setting and increase in angle of attack. However, the increase in pressure difference with flap setting was higher on the high wing model than on the low wing combination. The reason behind this development is the gap between the flaps and the fuselage on the low wing model. Since the ends of the flaps were beneath the fuselage and not restricted by any fairing, a tip vortex can develop which in turn reduced the effect of the flaps on the pressure distribution of the wing.

The general pressure pattern was common on both models at low angles of attack. The influence of the fuselage on the magnitude of the pressure field was the same for both combinations. For larger angles ($\alpha > 9°$) the influence of the fuselage affected the pressure distribution more on the low wing model than on the high wing arrangement. Since approximately two thirds of the lift was provided by the upper wing surface the effect of the flow displacement caused by the fuselage was more severe on the upper wing surface than on the lower surface. The separation of flow on the rear part of the upper surface led to a higher pressure difference over that area which in turn provided a higher lift. This was, however, counteracted by the fact that the suction peaks at the leading edge were significantly smaller than for the high wing model. This decline reduced the overall lift performance of the low wing model.

The pressure distribution over the wing as well as that of the fuselage has to be considered in the overall performance of a wing-fuselage combination. The next section discusses the data obtained over the fuselage.

5.5. Fuselage alone

In the graphs for the fuselage alone (Fig. 4.17 a to c) a small drop in pressure in front of the wing position is observed, which was due to a small step between the wooden and aluminium centre section of the fuselage. The pressure spikes in the middle of the graphs are due to the rods which supported the fuselage in the wind tunnel. Behind this area a trough at $^{x}/_{c} = 1$ and between $\varphi = 300°$ and 180° can be seen. This was due to a blocked pipe in the data acquisition system. The most distinct feature of these graphs is the linearity of the pressure drop at the tail and the rise in pressure at the nose, due to an increase in angle of attack. At the bottom of the fuselage ($\varphi = 180°$ and $^{x}/_{c} = -3.1$) the pressure rose from about $C_p = 0.4$ for $\alpha = 0°$ to $C_p = 0.8$, $\alpha = 12°$. At this angle the tail of the fuselage showed an elevation which approximately approached a value of $C_p = - 0.3$, following the shape of the rear end of the body. The pressure at a tapping angle of $\varphi = \pm 30°$ between $^{x}/_{c} = - 1$ and $^{x}/_{c} = 1$ did not change with increment in angle of attack, apart from the area where the supporting rods affected the pressure.

5.6. Fuselage & Wing; Fuselage data

In order to investigate the influence of the wing on the pressure field of the fuselage the wing was first attached to the body in the high wing position, followed by the low wing arrangement. The differences are discussed in the following section. The fairing was considered to be part of the fuselage, thus data obtained over the fairing is included in this part of the discussion. The arrangement of the graphs in Figures 4.18 to 4.21 again allows a direct comparison of the two configurations, with the plots for the high wing model above the graphs for the low wing combination. On the high wing graphs a set of faulty data points which appear at the end of the fuselage are ignored in the discussion. This was also the case for data points on the low wing graphs at approximately $^{x}/_{c} = - 1.1$ and between $\varphi = - 180°$ and - 60°.

The most noticeable feature on the high wing model is the change in pressure at the wing-body junction (Fig. 4.18 a to c). On these graphs, between $^{x}/_{c} = 0$ and 1, the pressure curves, which bend upwards to a minimum of $C_p = - 0.3$ ($\alpha = 0°$), change to curves which bend downwards to $C_p = 0.4$ for $\alpha = 12°$. This can be explained by an increase in pressure on the lower wing surface, due to an increment in angle of attack, causing an increase in the pressure on the fuselage beneath the wing. In the region just

ahead of the wing the flow runs against an adverse pressure gradient which can lead to separation before it reaches the stagnation point, thus the value of the stagnation pressure ($C_p = 1$) is not approached (Devenport, 1990). The circumferential gradient over the area underneath the wing was linear and the pressure at $\varphi = 180°$ was still affected by the presence of the wing. Details of the effects on the pressure caused by the wing are discussed in Section 5.8.

Locating the wing underneath the fuselage changed the pressure field significantly over an area close to the junction. Fig. 4.18 d to f depict the development of the pressure distribution with increasing angle of attack. In the junction ($^x/_c = 0$ to $^x/_c = 1$) the pressure followed a similar curve as seen on the high wing model, but with a negative pressure for all angles of attack ($C_p = -0.2$ for $\alpha = 0°$ to $C_p = -0.7$ for $\alpha = 12°$). This suction was caused by the negative pressure field of the wing which led to a higher circumferential gradient over an area which was the same width as the wing chord. Furthermore, the area behind the wing, between $^x/_c = 1$ and $^x/_c = 2$ and $\varphi = \pm 90°$, showed a higher longitudinal gradient with an increment in angle of attack than on the high wing. The pressure over the tail region ($^x/_c > 2$) did not change to the same extent as over the forebody of the fuselage.

A comparison of the high and low wing model shows a slightly different development of the pressure field over the forebody. At approximately $\varphi = \pm 90°$, between $^x/_c = -3$ and $^x/_c = 0$, on the high wing combination, an adverse pressure gradient towards the wing-body junction was present, whereas the low wing model showed a favourable pressure gradient. This pattern is clearly visible in Fig. 4.18 b and e for $\alpha = 6°$ and is even more pronounced in Fig. 4.18 e and f for $\alpha = 12°$. These gradients were a result of the two different pressure fields of the wing. On the high wing model the fuselage was exposed to the underside of the wing, thus a positive pressure was predominant. On the low wing model the body was subjected to the upper wing surface where a negative pressure was present. Since the pressure on the upper wing surface approached higher numerical values than the lower surface the effect is larger on the low wing combination.

The pressure at the nose varies between the high wing and low wing configuration. The general form of the surface plot at the nose suggests that the influence of the wing on the pressure over the forebody was similar in magnitude for both configurations. Labrujere (1989) corroborates these results with tests conducted on a model with the wing in midwing position at $\alpha = 6°$ and a Reynolds number of 0.65×10^6. Six rows of pressure tappings were located at several circumferential positions. Among these, one

row was directly above and one was directly underneath the wing. The pressure distribution along these rows was similar to the pressure in the wing-body junction for both high and low wing models. Comparison of the pressure beneath and above Labrujere's wing with the pressure distribution below the high wing and above the low wing revealed a similar pressure gradient just ahead of the wing. A difference occurred behind the trailing edge of the wing, which was due to the lack of a fairing on Labrujere's model.

The magnitude of the wing influence on the fuselage pressure can be perceived by comparing Fig. 4.17 and 4.18. At the nose, both wings led to a higher circumferential gradient with lower pressures at the top and higher pressures at the bottom of the fuselage. One chord ahead of the leading edge the pressure pattern of the high wing model resembled the one for the fuselage alone, but with higher values at a given position. On the low wing the pattern was the reverse of that of the high wing model.

For the low wing combination the large negative values in the junction are a clear indication of displaced flow, which has been accelerated around the obstacle (the wing). This displacement effect was of much smaller proportion on the high wing model, since only a few negative pressure peaks were visible, which were smaller than those observed on the other two models.

The influence of the wing on the pressure distribution of the afterbody can readily be seen for the case of $\alpha = 12°$ (Fig. 4.18 c and f). At the top of the fuselage an increase in pressure was noticeable on both combinations. The influence at the bottom was not clearly evident and is discussed in detail in Section 5.8.

Apart from the wing, other aircraft components which are not necessarily directly attached to the fuselage influence the pressure distribution over the body. The following section examines the influence of flaps on both high and low wing configurations and compares the results with the fuselage & wing model.

5.7. Fuselage & Wing & Flaps; Fuselage data

The discussion concentrates first on the fuselage & high wing & flap combination before examining the low wing arrangement, which is followed by a comparison of the two. This is carried out for each angle of attack, first with the flap deflection held constant, before proceeding to the discussion of the flaps set at higher angles. On the graphs for the high wing arrangement (Fig. 4.19 c) three lines of faulty data exist at an

angle of attack of $\alpha = 12°$. These lines and a step on the low wing combination at $^x/_c$ = 0.4 between $\varphi = -180°$ and $-60°$ have been excluded from the discussion.

5.7.1. $\delta = 0°$

With the flaps attached to the wing but not deflected the pressure distribution of the high wing model (Fig. 4.19 a to c) was very similar to the fuselage & wing configuration (Fig. 4.18 a to c). However, small differences between the two combinations are noticeable, in particular between $^x/_c = 1$ and 1.5 at $\varphi = 70°$ and 290° on the high wing model. This is especially visible on graphs (a) and (b), where the flaps reduced the pressure on the fuselage slightly. This influence was restricted to close proximity to the flaps. The reduction in pressure can be explained by the high flow velocity between the wing and the flaps, leading to a negative pressure at the leading edge of the flaps which was carried over onto the fuselage.

The effect of the flaps on the low wing model (Fig. 4.19 d to f) is observed between $^x/_c$ = 1 and 1.5 at $\varphi = \pm 60°$. A small reduction in pressure can be seen for $\alpha = 0°$. This gradually increased to a value of $C_p = -0.8$, as seen in Fig. 4.19 f. Here, a second series of peaks, which almost reached the same values as those caused by the wing, is clearly visible, extending the area of high suction towards the rear of the fuselage. The flaps acted here as a second airfoil which was attached to the body. These peaks were followed by a steep adverse pressure gradient which eventually led to a pressure field like that of the fuselage & wing combination.

Although Fig. 4.19 c for the high wing combination is distorted, the peaks seen on the low wing model cannot be observed. The upper surfaces of the flaps were tangential to the upper surface of the fairing, thus their influence was smaller. The lower surface of the flaps did not exert the same pressure on the body and therefore their influence was significantly lower at a flap deflection of $\delta = 0°$. At lower angles of attack the flaps on the high wing model (Fig. 4.19 b) induced an increase in pressure at the leading edge of the wing ,which in turn increased the pressure on the fuselage thus resulting in a higher adverse pressure gradient ahead of the leading edge of the wing than on the configuration without the flaps attached (Fig. 4.18 b). At $\alpha = 0°$ (Fig 4.18 a and Fig. 4.19 a) the presence of the flaps reduced the suction pressure close to the wing-body junction thus decreasing the adverse pressure gradient. The opposite case existed for the low wing model. By comparing Fig. 4.18 e and 4.19 e a rise in the pressure gradient can be observed. Again, the high suction peaks on the wing, increased by the presence of the flaps, were carried over onto the fuselage. The influence of the flaps

was not restricted in the circumferential direction and also affected the pressure at the top and bottom of the fuselage on both configurations.

5.7.2. $\delta = 10°$

The pressure field over both combinations with the flaps set at an angle of $\delta = 10°$ is depicted in Fig. 4.20. At $\alpha = 0°$ the pressure in the wing-body junction of the high wing model (subscript a) shows smaller suction peaks than the model with the flaps attached but not deflected. Furthermore, at positions where the flaps were located ($^x/_c$ = 1 to 1.5 and $\varphi = 70°$ and 290°) the pressure was positive, something which was not observed for the fuselage & wing model nor for the model with the flaps attached but not deflected. At $\alpha = 6°$ (Fig. 4.20 b) the effect of the flaps is clearly visible just ahead of the wing where the pressure gradient has increased. The positive pressure underneath the wing caused by the positive pressure field of the wing was more pronounced with the flaps deflected. Close examination of Fig. 4.20 b reveals that the pressure reduction on top of the fuselage increased as the flaps were deflected further. At $^x/_c = 1$ and $\varphi = 0°$ the pressure decreases from $C_p = -0.2$ for $\delta = 0°$ (Fig. 4.19 b) to $C_p = -0.4$ for $\delta = 10°$ (Fig. 4.20 b), thus the flaps influenced the pressure field not only via the wing but also, directly, at other locations which were not in the immediate vicinity of the flaps.

The development of the pressure distribution at an angle of attack of $\alpha = 12°$ (Fig. 4.20 c) was similar to $\alpha = 6°$, with obviously higher values of C_p. Owing to the faulty lines of data the surface plot does not reveal any details and the discussion has been confined to the wing-body junction where a sharp increase in pressure is noticeable.

Fig 4.20 d to f depict the pressure distribution for the low wing combination at a flap setting of $\delta = 10°$. At $\alpha = 0°$ the reduction in pressure at the wing-body junction is clearly visible. The area over which the reduction occurred was extended longitudinally and led to a trough at approximately $^x/_c = 1.7$. Ahead of the wing the flaps caused an increase in the adverse pressure gradient, as can be seen at $^x/_c = -0.3$. This development is clearly visible in the graph for $\alpha = 6°$ (subscript e), where sharp irregularities in the wing-body junction indicate a flow field which has separation and vortices present. These pressure peaks are followed by a trough, where the pressure increased, before a further elevation over the rear of the fuselage between $\varphi = \pm 90°$. This elevation can also be seen for $\alpha = 12°$ (Fig. 4.20 f), but the form of the relief is not as pronounced as was seen for the fuselage alone model (Fig. 4.17).

A comparison of the two combinations indicates that the flaps had a much greater influence on the low wing model than on the high wing configuration. However, this influence seemed to be restricted to the part of the fuselage adjacent to the wing. This was illustrated throughout all angles of attack. Not only the pressure in the junction was affected by the presence of the flaps, however, but also the pressure at the opposite side, i.e. at the top of the low wing model and the bottom of the high wing arrangement. Along the entire length of the fuselage at $\varphi = \pm 180°$ on the low wing and $\varphi = 0°$ on the high wing model the pressure values were different from those of the unflapped model.

5.7.3. $\delta = 20°$

Both configurations are presented with the flaps set at $\delta = 20°$ in Fig. 4.21. Setting the flaps at such an angle magnified the change of the pressure field discussed so far. However, since the graph for the high wing model at $\alpha = 12°$ (subscript c) does not include the lines of faulty data, the discussion concentrates on this configuration and the low wing counterpart. Between $^{x}/_{c} = 0$ and 1 the pressure peaks were more prominent on the low wing model than on the high wing combination. This led to a different longitudinal pressure gradient ahead of the wing. More importantly the pressure on the low wing model was negative whereas the pressure on the high wing configuration was positive. These configurations show clearly the effect of the flaps in increasing the camber of the wing, and the fact that the sidewalls of the fuselage were exposed to either the negative pressure or positive pressure, depending on the configuration.

A comparison of all combinations with an increment in flap deflection and rise in angle of attack, shows a linear change of the pressure distribution over the fuselage. The pressure changes on the wing, induced by the flaps, increased the adverse pressure gradient ahead of the wing on the high wing model and also increased the favourable gradient on the low wing model. However, the development on the low wing appeared to be more extreme, showing a larger influence of the wing and the flaps on the pressure distribution over the fuselage in the vicinity of the wing. Small vortices were shed from the flap tip and trail downstream along the fuselage, because of a gap between the fuselage and the flaps, when set at $\delta = 10°$ and 20°. The effect of these vortices cannot be seen on the surface plots for the low wing model, as the fuselage afterbody decreased in diameter and thus "curved away" from the path of the vortices. As a result the pressure field over the afterbody was similar to that of the high wing combination.

At the nose of the fuselage the changes were similar for both configurations with slightly lower pressure values for the low wing model. The variation of the flow field ahead of the wing, which was induced by the wing and the flaps, was responsible for the lower values. The pressure field induced by the wing determines the pressure distribution of the fuselage, not only in the immediate vicinity, but at least one chord ahead of the leading edge of the wing and one chord behind the trailing edge of the flaps and also as far as the nose and the tail of the fuselage. The effect of the wing and the flaps was not restricted in the circumferential direction. Observations made by Sandahl and Vollo (1947) who investigated the pressure distribution over a fuselage attached to a wing and a stabiliser corroborate these results. Their graphs showed the same longitudinal pressure distribution although the chord line of the wing of their model was not aligned with the top of the fuselage.

5.8. Pressure difference between top and bottom of the fuselage

In order to view in more simple manner the effect of the wing and its location on the pressure field of the fuselage, the difference in the pressure at the top and the bottom tappings ($\varphi = 0°$ and 180°) was calculated. Before calculating the pressure difference, the pressure data of the appropriate wing surface were inserted at the appropriate location on the fuselage, i.e. the data along the centreline of the upper wing surface of the high wing model was inserted in the row at $\varphi = 0°$, and for the low wing model the data of the lower wing surface were inserted in the appropriate position. The data were inserted over the entire length of the chord. When considering the fuselage alone configuration the support rods were attached at the sides of the body, so an implantation of data was not necessary. However, the graphs show some irregularities owing to the presence of the support rods . At the bottom of these graphs the position of the wing is indicated by a small sketch.

5.8.1. Fuselage alone

Figure 4.22 depicts data for the fuselage alone configuration. It clearly shows the linear reduction in pressure at the nose. A small step between $^x/_c = -3$ and - 2.7 was probably due to a defect in the acquisition system. Another distinct feature are the tapping positions at $^x/_c = 1.9$ and at $^x/_c = - 0.5$ where all graphs go through the same points. Behind $^x/_c = 1.9$ the pressure difference increased but was not linear in increment with angle of attack. A distinct step between $\alpha = 3°$ and 6° is noticeable. Above this angle of attack the rise in pressure difference was very small. Since the fuselage was tapered from approximately this position backwards the increase in the difference originated mainly from the lower surface. At larger angles of attack the body acted like a crude

airfoil, where the flow over the top part separates and the flow beneath the fuselage was accelerated, leading to a negative pressure. A comparison of the pressure at $\varphi = 0°$ (top of fuselage), for various α, revealed an almost constant distribution over the tail. At the bottom ($\varphi = 180°$) the pressure was reduced with increment in angle of attack, thus an acceleration around the body took place. Sandahl and Vollo (1947) did not find an increase in loading over the rear of the body and they concluded that boundary layer effects were responsible for this, however, they did not give details of the way in which the boundary layer affected the flow.

Since the presence of the wing determined the wake of the flow, any changes to the flow field close to the afterbody should be visible on the graphs for the fuselage & wing combinations. These are discussed next.

5.8.2. Fuselage & Wing

Fig. 4.23 presents the pressure difference of the high wing configuration above the low wing model. The point of common pressure difference ΔC_p at the rear of the body was pushed backwards for the fuselage & wing combination. For the high wing model this point was located at $^x/_c = 2.9$ and for the low wing at $^x/_c = 2.7$. The pressure after this point developed differently for the high and low wing. The peak of maximum pressure lay at $^x/_c = 4.0$ for the high wing configuration and at $^x/_c = 3.6$ for the fuselage & low wing. The magnitude of these peaks was approximately the same for both models. Small irregularities at $^x/_c = 2.7$ and 3.3 can be seen on both models which were due to blocked pipes inside the fuselage.

At the nose the pressure difference was significantly different for the two configurations. The pressure peaks for the high wing model were slightly lower than for the low wing arrangement. However, the peaks for $\alpha = 15°$ exceed the axes chosen for the graphs for both models. Between $^x/_c = -3.1$ and -2.1 a steeper gradient from the nose towards the wing is visible for the high wing configuration, leading to a region where the pressure difference was constant along the fuselage. From about $^x/_c = -1$ up to the leading edge of the wing the difference in pressure shows two sets of curves. The distinction occurs between an angle of attack of $\alpha = 6°$ and 9°. Up to $\alpha = 6°$ the curves are bent downwards resulting in a trough just ahead of the wing. Examination of the pressure plot at $\varphi = 0°$ (top of the fuselage) revealed that the pressure increased just ahead of the wing whereas beneath the fuselage ($\varphi = 180°$) a constant pressure was observed. The curvature of the fairing was responsible for the increased pressure. A fairing geometry such as that seen on the Dornier DO 328 is likely to avoid such a pressure rise, since this fairing is extended up to the nose of the fuselage leading to a

careful blending of the wing. The accelerated flow over the wing resulted in an extremely low pressure over the wing. As the angle of attack was increased the high negative pressure of the wing dominated the flow just in front of the wing and therefore the trough diminished with increment in angle of attack.

On the low wing model the development of the pressure in front of the wing differed significantly from the high wing combination. Between $^{x}/_{c}$ = - 1.5 and the leading edge of the wing the pressure curves are inclined towards the wing. Apart from one or two irregularities the increment in pressure difference was linear with the rise in angle of attack. This clearly indicates that the low wing exerted a higher loading on the fuselage in front of the wing leading edge than on the high wing model. Analysis of the pressure data on top of the fuselage suggests that the wing influenced the flow field around the entire fuselage by reducing the pressure ahead of the area where the wing was situated, something which was not observed on the high wing model. There, the pressure underneath the body increased steadily with an increment in angle of attack.

For both models a completely different distribution was observed over the part of the fuselage where the wing was located. On the high wing model the pressure peaked to a maximum value of $\Delta C_p = 1.43$ for $\alpha = 12°$ at about quarter chord of the wing and then gradually decreased towards the tail. The peak of the low wing configuration was at the leading edge of the wing approaching a value of $\Delta C_p = 0.45$. The pressure difference then dropped before another negative peak at the trailing edge was reached. The negative pressure difference was a result of the negative pressure on the lower wing surface at small angles of incidence. Results of Labrujere (1989) agree with this pressure distribution. The peaks at the trailing edge and the irregularities on the high wing model were due to blocked pressure tubes.

Between $^{x}/_{c}$ = -0.1 and $^{x}/_{c}$ = + 2.1 the pressure pattern again differed significantly between the low and high wing models. On the latter the pressure difference was higher for a given configuration than for the low wing model. Furthermore, the difference on the low wing model was almost constant over this region. The differences originated from a variation in pressure at the top of the fuselage in the high wing combination, and at the bottom of the fuselage on the low wing model. This variation was greater on the high wing configuration and can be explained by the shape of the fairing. The fairing surface behind the wing was designed is such a way that it followed the slope of the respective wing surface, i.e. upper surface on the high wing model and lower surface on the low wing. Thus only a small portion of the surface behind the wing was round due to the fuselage. The wing chord was effectively "extended". For

this reason the curves on the high wing configuration followed the overall trend, and therefore the variation was higher whereas smaller changes were present on the low wing combination.

5.8.3. Fuselage & Wing & Flaps

The influence of the flaps on the pressure at the top and bottom of the fuselage, at various angles of attack, is shown in Figure's 4.24 to 4.26. Included in these graphs are the curves for the fuselage alone and the fuselage & wing combination, in order to be able to make direct comparisons. For the high wing configuration the maximum flap angle was $\delta = 20°$, and therefore a comparison with the low wing configuration with a flap setting of $\delta = 30°$ is not possible.

5.8.3.1. $\alpha = 0°$

Both combinations are depicted in Figure 4.24 at an angle of attack of $\alpha = 0°$. The decrease in pressure difference on the high wing model along the entire length of the fuselage was linear with an increase of flap angle, a development which is also noticeable on the low wing configuration. As expected, the main difference occurred over the area where the wing was located. On the high wing, the increment in pressure difference between the fuselage & wing model and the configuration with the flaps at $\delta = 0°$ over the wing area was zero, apart from a higher suction peak at the leading edge. A similar development can be seen on the low wing combination. Here, the difference in pressure across the wing zone was positive for the fuselage & wing and for flap angles up to $\delta = 10°$. Again, the positive pressure on the lower surface was responsible for this. The second peaks at the trailing edge of the wing were caused by the flaps, where a high negative pressure on the upper surface resulted in a similar pressure distribution to the one for the main wing.

At the rear of the fuselage the two configurations are different in the sign of the pressure difference. On the high wing model the difference was negative whereas on the low wing combination a positive difference can be seen. Here, a step between the models without the flaps attached and the fuselage & wing & flap configuration is noticeable. However, the pressure appeared to be independent of the flap setting since the magnitude did not change with flap angle. The influence was reduced since the flaps were located underneath the fuselage. This is clearly not the case for the high wing model, where the flaps were adjacent to the fuselage and the influence remained up to the tail of the fuselage.

5.8.3.2. $\alpha = 6°$

At an angle of attack of $\alpha = 6°$ (Fig. 4.25) the magnitude of the pressure difference at the nose was the same for both configurations. On the high wing combination the curve for the model with the flaps deflected exceeded the limits of the graph and approached a maximum value of $\Delta C_p = 1.76$ for a flap setting of $\delta = 20°$. Compared with the high wing model the growth of the pressure difference on the low wing arrangement was less extreme and the minimum values were significantly lower. Another notable feature on the low wing was the greater distance between the curves for the fuselage alone and fuselage & wing over the front half of the fuselage, indicating that the influence of the wing was much larger than on the high wing model. By comparing the two graphs it is clear that the curves on the high wing are evenly spread whereas the curves for the low wing are closer together and rise as a bunch. This has also been observed for the unflapped configuration (see Fig. 4.23). The pressure distribution on the respective surfaces were responsible for this dissimilarity. On the low wing model the pressure at the bottom of the fuselage increased marginally and on the top the pressure decreased. Over this section of the fuselage ($^x/_c = 1$ and 2) the pressure remained constant, i.e. no longitudinal pressure gradient was observed. This was not the case for the high wing model, where a gradient was present on both surfaces, which was obviously reflected in the pressure difference. From this figure it appeared that the flaps had a larger influence on the pressure at the top and bottom of the fuselage for the high wing configuration.

5.8.3.3. $\alpha = 12°$

The trends described in the previous paragraph were also observed for an angle of incidence of $\alpha = 12°$ (Fig. 4.26). On the low wing the pressure difference between $^x/_c = 1$ and $^x/_c = 2$ was less than that for a smaller α, which was not the case for the high wing model. Also the pressure difference over the area where the wing was located did not increase but remained almost constant. In front of the wing there was a modest increase in the pressure difference. This was also noted for the high wing, where the difference rapidly increased towards the wing leading edge. Over the wing a maximum value of $\Delta C_p = 2.25$ occurred for the configuration with the flaps deflected at $\delta = 20°$. Behind the wing a higher pressure difference for all cases was observed which gradually reduced towards the tail where all curves converged.

As can be seen from these graphs (Fig. 4.24 to 4.26) the influence of the flaps was higher on the high wing model than on the low wing arrangement. This can be explained by the proximity of the flaps, which were adjacent to the fuselage in the high

wing configuration. On the low wing model the flaps were situated below the fuselage and therefore showed a reduced influence. With the flaps deployed at $\delta = 10°$ and 20° small vortices were observed which emanated from the flap tip and trailed downstream underneath the body. The influence of these vortices was small, since the fuselage was tapered and curved away from the track of the vortices. The expected loss on the wing pressure at the leading edge was recovered by the displacement effect of the fuselage.

5.8.3.4. Comparison with other researchers

Bernstein (1984) conducted tests on a geometrically similar, but smaller, high wing model, without flaps. His results are compared with data obtained during this research in Fig. 4.27 and 4.28. Figure 4.27 depicts the pressure difference between the top and bottom of the fuselage at an angle of attack of 0° and 6°. Towards the end of the fuselage the curve shows higher differences at $\alpha = 6°$, because of a tailplane fitted on Bernstein's model. This is more pronounced at $\alpha = 12°$ (Fig. 4.28). Unfortunately, no data was available over the wing section on Bernstein's model and thus a gap appears in the graph. The dissimilarities just ahead and behind the wing were due to the lack of a fairing on Bernstein's model. The majority of the data, however, show an excellent agreement which suggests that the pressure distribution was independent of the size of the model, as might be hoped, but there still exists the possibility of Reynolds number effects when going to full scale aircraft.

McLellan (1947) conducted experiments with a nacelle mounted on a wing (Fig. 5.1). His results for two angles of attack ($\alpha = 0°$ and 2.5°) are shown in Figure 4.30. The wing consisted of a NACA 65-210 profile, to which an ellipsoid type nacelle was attached at several horizontal and vertical positions. On the high wing model the nacelle topline was tangential to the wing chord line. The speed range was higher (up to Mach 0.7) and the design was different with a smaller nacelle length/wing chord ratio. However, the data have been transformed in order to compare properties of the individual models. The pressure difference over the wing area exhibited a similar distribution to the data obtained in this project. The gradient over the wing was obviously different according to the different wing section. For $\alpha = 0°$ and 2.5° the curves behind the wing show a similar trend seen on Bernstein's model. McLellan had no fairing mounted, thus the same trend with higher ΔC_p values appears. Over the remaining tail the curves are in good agreement. The two graphs show a different distribution at the nose for $\alpha = 0°$ and 2.5° respectively. This dissimilarity is accounted for by the different design of the body. The nacelle of McLellan's model was much more slender with a shorter forebody and a nose of smaller radius.

5.9. Spanwise lift distribution - integrated loadings

The wing was first tested alone in order to obtain the pressure distribution as well as the lift characteristics. The spanwise lift distribution was calculated from the pressure distribution by chordwise integration. The spanwise lift distribution for the wing alone is presented in Fig. 4.30 followed by the wing & flap configuration in Figure 4.31. The fuselage & wing configuration is shown in Fig. 4.32 with the data for the high wing above that for the low wing model. Finally the combinations with the flaps attached are presented in Fig. 4.33 to 4.38. Figures 4.39 to 4.43 compare data obtained during this research with other test results and theory.

On all graphs the hatched and cross-hatched areas show the loading over the flaps. For the low wing model the hatched areas have been designated to certain angles of attack in order to make a distinction.

5.9.1. Wing with and without flaps

Figure 4.30 displays the lift for the wing over the entire range of angles of attack. As can be seen, the lift was spread evenly over the entire span which indicated that the endplates provided good two-dimensional loading on the wing. A fluctuation was noted at $\alpha = 15°$, close to the centre of the wing which was probably attributable to separation and a local vortex close to the stall. Abbott and von Doenhoff (1959) measured a similar stalling angle of $\alpha = 15°$ at a Reynolds number of 2.6×10^6. All curves in Fig 4.30 show a small inclination from left to right. This could have resulted from a small change in the flow incidence across the test section, although it is not so pronounced in Fig. 4.31 which shows the wing & flap with a flap deployment of $\delta = 0°$. The hatched area depicts the loading over the flaps which shows less lift with the flaps attached. The pressure difference over the flap was much smaller than for the wing. The close proximity of the flap to the wing was responsible for this where the pressure field of the wing strongly influenced the pressure field of the flap. For $\alpha = 15°$ the trough in the lift distribution at $^x/_c = 0.5$ was deeper than for the wing alone configuration. This reduction in lift grew as the flap angle increased, as seen in Figure 4.31, which shows also the wing & flap for $\delta = 10°$ and 20°. It should be noted, however, that the increment in lift with increasing angle of attack was fairly linear apart from the step between $\alpha = 12°$ and 15° indicating a flattening of the lift curve.

The flaps produced lift over the entire range of angles of attack despite the reduction of lift over the wing, indicating that the flaps were not stalled at 15°. The comparison

between $\delta = 10°$ and 20° shows the linear increment of flap lift throughout the tested range of angles of attack.

5.9.2. Fuselage & Wing

Data from the pressure distributions along the length of the fuselage was inserted into the data files for the wing at appropriate spanwise positions in order to calculate the overall spanwise lift distribution. Figure 4.32 presents the lift distribution for both configurations (high and low wing), for a range of $\alpha = 0°$ to $\alpha = 15°$. The lift distribution over the wing changed significantly when a fuselage was mounted either on top or underneath the wing. A discussion of these results is given next.

5.9.2.1. High wing

On the high wing model the lift remained constant up to the wing-body junction where a dramatic drop in lift appeared. The increment in lift over the wing varied linearly in steps of approximately $\Delta C_L = 0.3$ up to $\alpha = 12°$. For $\alpha = 15°$ the lift decreased near the wing-body junction, which was due to the high angle of attack close to the stall angle of the wing. Over the fuselage the lift was lower and for $\alpha < 3°$ negative lift was present. This can be explained by a reduction of the circulation of the wing, which was not carried over the fuselage, thus implying that wing-body junction vortices were shed into the wake (Weber, 1970). It should be noted that the fuselage was not able to fulfil the Kutta condition since there was no sharp trailing edge. Over the centre of the fuselage lift peaks with magnitudes equal to or higher than the lift over the wing were observed. This suggested that small vortices were shed from the upper half of the fuselage. This was also indicated by a small reduction in pressure at tapping positions of $\varphi = 60°$ and 300° along the forebody (Fig. 4.18). The vortices shed from the wing-body junction trailed along the upper half of the fuselage afterbody and therefore affected any vortices emanating from the rear fuselage body, thus lower lift was observed here than for the low wing configuration.

5.9.2.2. Low wing

The lift distribution over the wing on the low wing model consisted of two regions: The first for angles of attack lower than $\alpha = 6°$ and the second above that "margin". Up to this angle the lift was constant along the span, up to the wing-body junction. The curves resembled those for the high wing, with marginally higher values of C_L for the low wing combination. Above $\alpha = 6°$ the lift was highest at the most outboard position and then gradually decreased toward the wing-body junction. This was particularly

visible on the starboard wing. On the port wing a single peak was noted which was due to the suction peak created on that wing at higher angles of attack. In the junction a sharp drop of lift was observed. This occurred at the edge of the fuselage where the contribution towards the lift was small and the lift was mainly produced by the wing. At about $y/c = \pm 0.3$ two spikes in the lift appeared. These corresponded to a tapping angle of $\varphi = \pm 130°$ where lower C_p values on the fuselage forebody were observed (Fig. 4.18 f). Again, these indicated that small vortices on the upper half of the fuselage produce lift. For small angles of attack ($\alpha < 6°$) the lift over the fuselage was of equal magnitude to the lift produced by the equivalent portion of the wing alone. For higher angles of incidence the lift over the fuselage was higher than the lift over the outboard wing, which suggested that the lift loss occurring over the wing close to the fuselage was partly recovered by the fuselage.

5.9.2.3. Comparison- high and low wing

In comparison with the high wing configuration the values for the lift over the wing of the low wing model (Fig. 4.32) were smaller for larger angles of attack, $\alpha > 9°$, which was not the case for the lift over the centre of the fuselage, where lower values were noted for the high wing model. However, the effect of the fuselage was more pronounced on the wing of the low wing model where a steady reduction in the lift up to $y/c = \pm 1.5$ was visible. Although a higher value for the pressure difference over the rear of the wing was observed on the low wing model (Fig. 4.7), leading to higher circulation and thus higher sectional lift, the low suction peaks at the leading edge counteracted this higher lift. As a consequence the sectional lift in this region was less than that for the high wing configuration. At low angles of incidence ($\alpha < 6°$) the low wing configuration showed a more uniform lift distribution across the entire wing. This suggested that the inherent drag was lower than that of the high wing model; a result which was obtained in measurements by Jacobs and Ward (1935). For $\alpha = 0°$ the lift of the low wing configuration was of similar magnitude to that of the wing alone. This was not the case for the high wing model due to the trough over the fuselage. For higher angles of incidence the overall lift of the high wing model seemed to be higher than for the wing alone leading to a slightly higher slope of the C_L versus α curve. Owing to the large lift loss over the wing at higher angles of attack ($\alpha > 12°$) the lift slope of the low wing model would presumably be lower than that for the wing alone; a result which Parkin and Klein (1930) also derived from measurements.

5.9.3. Fuselage & Wing & Flaps; α constant, δ varied

5.9.3.1. $\alpha = 0°$

Figure 4.33 shows data for the fuselage & wing & flaps model for $\alpha = 0°$ and various flap settings. In order to see the differences between the basic fuselage & wing configuration and the flapped models, the lift of this combination has been included in both graphs for the high and low wing model.

On the high wing model a significant increase in lift over the fuselage can be seen. This increase was already present with the flaps attached but not deflected. This clearly shows that the increase in lift over the wing induced by the flaps was carried over the fuselage. Furthermore, the almost constant lift distribution across the wing indicates that the flaps were effective in inducing a higher loading on the wing at all angles of flap deflection. The increase in lift over the fuselage with rise in flap angle was of the same magnitude as over the wing itself.

The loading over the flaps at $\delta = 0°$ was negative for the same reason given in Section 5.9.1. Thus the total lift over the wing was lower than the induced lift over the wing. For higher flap angles the flap showed a constant loading across the span, which was not observed on the low wing model. On this configuration the flap loading decreased towards the fuselage, indicating a tip effect and the development of tip vortices, which were also observed during flow visualisation tests.

The lift distribution for the low wing configuration differed significantly from the one for the high wing model. The major differences appeared over the fuselage, where the lift was lower for all flap deflections. This clearly indicates that the additional lift induced by the flaps on the wing was not fully carried over the fuselage. The location of the flaps with the chord line beneath the fuselage was probably responsible. Thus, any lift over the fuselage was caused by the lower wing surface and the upper fuselage surface only. On the starboard side between $y/c = 0.5$ and 0.7 a small peak in the lift in the wing-body junction is noted for all angles of incidence; a feature which has also been observed on mid wing configurations (Müller, 1970). Details of that configuration are discussed at a later stage (Fig. 4.42). The difference between the port and starboard wing have been attributed to a slight flow angle gradient in the wind tunnel, and an offset in flap deflection.

By comparing the two combinations it is noted that the lift over the wing was higher for the high wing configuration than for the low wing model. A flap deflection of 30°

on the low wing combination did not produce the same lift as a flap setting of 20° on the high wing model. The effectiveness of the flaps was higher on the high wing combination due to the design of the model as explained above. The higher lift over the fuselage of the high wing model suggests that the circulation of the wing is carried over the fuselage in a more effective way than on the low wing model for which the fuselage cannot recover any loss occurring in the wing-body junction.

5.9.3.2. $\alpha = 6°$

The flow developments for $\alpha = 6°$, depicted in Fig. 4.34, resembled those discussed for $\alpha = 0°$. The linearity in lift increment over the wing of the high wing combination was remarkable. Over the fuselage the lift was spread more across the body than for $\alpha = 0°$ and a small drop in lift was only noted close to the wing-body junction. However, the lift curve for a flap deflection of $\delta = 0°$ and 10° was higher than for the wing & flap model, suggesting that the overall lift was higher. For $\delta = 20°$ the lift was of equal magnitude as for the wing & flap configuration. This indicates that the lift slope was at least the same, if not higher for the model with the fuselage attached.

The steady rise in lift was also present on the low wing model apart from that with the flap setting of $\delta = 30°$, where only a little extra lift was gained. This was also the case for the centre of the fuselage where no increase in lift was observed for a rise in flap deflection from $\delta = 20°$ to 30°. This clearly shows that the influence of the flaps was reduced and that the increment in wing loading due to the higher flap deflection was small. As a consequence the carry over lift was small too. For $\delta \leq 10°$ the centre of the fuselage showed the same lift as for the wing, which indicated that part of the lift loss near the junction was recovered over the remaining fuselage. For higher flap deflections the lost lift was not recovered by the fuselage.

The increase in flap loading on the low wing model between $\delta = 20°$ and 30° was smaller than the increment between $\delta = 10°$ and 20° which indicated that the flaps were probably stalled at $\delta = 20°$. A reduction in flap loading on the low wing model was clearly visible despite irregularities on the port wing close to the wing-body junction.

5.9.3.3. $\alpha = 12°$

The lift distribution of both configurations for $\alpha = 12°$ is depicted in Fig. 4.35. For the high wing model the pattern changed due to irregularities observed in the pressure data (Fig. 4.19 d, 4.20 d, and 4.21 d). A subtle difference was noted between $y/c = -0.5$ and -1 where the lift for $\delta = 10°$ and 20° decreased slightly toward the fuselage. The

increase in lift remained linear for an increment in flap deflection. The difference in lift over the wing between the fuselage & wing and the model with the flaps attached (δ = 0°) was approximately ΔC_L = 0.5. This was less than for the low wing arrangement, where the difference outboard on the wing averaged about ΔC_L = 0.7. The increment in lift, due to an increased flap angle, was smaller on the low wing model than on the high wing combination. Furthermore, a flap setting of δ = 20° on the high wing model achieved a C_L of about 2.5, a value which was not achieved on the low wing configuration even with a flap angle of δ = 30°, apart from on the outboard side on the starboard wing. This, and the fact that the lift was constant along the span, suggests that the flaps were much more effective on the high wing combination. This was also reflected in the higher lift over the fuselage for the flapped model compared to that for the unflapped configuration. The reason for such effective flaps was the fact that they were closely confined by the endplates and the fuselage, which suppressed the formation of tip vortices, thus producing a higher "effective" flap span. Vortices were observed for flap angles of δ = 20° and 30° during flow visualisation tests on the low wing model. However, at α = 12° the displacement and cross flow effects of the fuselage dominated the development of the lift distribution, thus vortex effects were not visible. At lower angles of incidence the port wing showed a reduction in lift close to the wing-body junction which might have been caused by the vortices. An offset in the flap angle could be responsible for the fact that the reduced lift was only noticeable on one side of the wing.

The lift over the fuselage of the low wing model was lower than that for the high wing counterpart. The minima near the wing-body junction appeared to be almost independent of the angle of attack and of the flap angle. On the unflapped model and with a flap deflection of 10° the lift peaks near the centre of the fuselage exceeded the lift of the wing, indicating a lift recovery over the fuselage. This was not the case for higher flap angles, where only small lift increments were observed. The lift in this area was lower than that for the high wing model, which suggests that the carry over lift of the high wing model was higher than the vortex lift of the fuselage forebody of the low wing configuration.

A reduction in flap loading can be seen on the starboard wing where for δ = 20° the lift was reduced up to a spanwise location of y/c = 1. At this point all curves for δ = 20° and 30° show a sharp kink and the lift drops toward the fuselage. This was also the case for the lift over the flaps which indicated that the displacement effects seen on the wing were also present on the flaps. This reduction was not observed on the high wing

model, indicating a higher flap loading for a given flap deflection than on the low wing model.

To provide an overview of the lift distribution for a given flap deployment and increasing in angle of incidence Figures 4.36 to 4.38 are given. The graphs for the high wing configuration exclude curves for $\alpha = 15°$, since no pressure measurements were taken.

5.9.4. Fuselage & Wing & Flaps; δ constant, α varied

Figure 4.36 exhibits the lift distribution for a flap angle of $\delta = 0°$. The increase in lift over the high wing was linear with an increment in α. The lift carried over the fuselage was almost of the same magnitude as the lift produced by the equivalent area of the wing. The rise in lift over the wing was constant for an angle up to $\alpha = 9°$. The increase between $\alpha = 9°$ and $\alpha = 12°$ was smaller but was also discernible, as can also be seen in the bottom figure. Here, the development of the lift distribution was also linear up to $\alpha = 9°$. At this angle, and for higher angles of attack, a peak appeared at the left wing-body junction which was due to the suction peak observed on the surface plots for the upper wing surface. On the starboard wing the lift increased slightly between $y/c = 0.7$ and 0.5 and was observed up to $\alpha = 9°$. Again, this offset was due to a small incidence gradient across the test section in the wind tunnel and a misalignment of the flaps. At higher angles ($\alpha > 9°$) the lift decreased towards the fuselage from about $y/c = \pm 2$, indicating the extent of the displacement effects caused by the fuselage.

The lift distribution over the fuselage varied with increasing angle of attack for both high and low wing configurations. On the high wing model the peak near the centre, observed for $\alpha = 0°$ and 3°, changed to two peaks at higher angles of attack. The opposite was the case for the low wing model, where a peak at the centre occurred for $\alpha > 6°$. At lower angles the lift was evenly spread across the fuselage, apart from the minima near the wing-body junction. The increase in lift over the fuselage was linear with increase in angle of attack for both high and low wing configurations, with the exception of the smaller increment between $\alpha = 12°$ and 15° for the low wing model. The lower lift of the wing and the lower carry over lift inherent with the wing lift were responsible for this effect.

The loading over the flaps varied between the two models. On the high wing model the flaps showed a negative loading for angles of $\alpha \leq 6°$ and positive loading for $\alpha = 9°$ and 12°. The loading was very small but constant across the span. This was not the

case on the flaps of the low wing model where the lift decreased slightly towards the fuselage. No extra flap loading was observed for $\alpha = 3°$ and 6° which indicated that the flaps were probably operating at angles of attack close to zero lift.

The lift distribution for the high wing model for $\delta = 10°$ resembled that for $\delta = 0°$ and can be seen in Figure 4.37. Here, the lift for $\alpha = 0°$ showed a similar distribution and was of roughly the same magnitude as for $\alpha = 3°$ with $\delta = 0°$. The increment in lift over the fuselage, ΔC_L, was about 0.4 between each angle of attack. This value was higher than for the low wing model, presented in the bottom graph, where the step is only $\Delta C_L = 0.2$ over the fuselage area, again indicating that the flaps were more effective on the high wing model for all angles of incidence. Over the fuselage of the low wing model the lift increment for $\alpha > 6°$ was smaller than for lower angles of incidence, which indicates a reduction of the effectiveness of the flaps.

Erratic behaviour on the port wing of the low wing combination is seen at $\alpha = 9°$, with peaks at the wing-body junction and also spread out further onto the wing. On the starboard wing the lift for $\alpha = 15°$ fell below the lift for $\alpha = 12°$, suggesting that the wing was stalled. Furthermore, the curves declined from about $y/c = \pm 2$ indicating that only the outer half of the wing provided lift whilst the inner half was affected by the presence of the fuselage.

The flaps of the high wing configuration showed an almost constant loading for $\alpha \leq 6°$ and an increased loading for higher angles. This was also the case for the low wing configuration apart from $\alpha = 15°$ where the flap loading was smaller than for 12°. This indicated that the disturbed flow over the wing affected the flow over the flaps in a negative way and as a result less lift was produced. On the low wing model a small reduction of the loading towards the fuselage can be seen for all angles of attack, suggesting less effective span of the flaps.

The disorder seen in Fig. 4.37 is more prominent in Figure 4.38 for a flap deployment of $\delta = 20°$. The lift distribution on the low wing model was irregular from $\alpha = 9°$ upwards, with peaks on the port wing. The lift for $\alpha = 12°$ and 15° was of almost equal value on the port wing and was below values for $\alpha = 6°$ at some spanwise locations. On the starboard side of the fuselage a small peak close to the junction appeared for α up to 6°, due to the presence of tip vortices. No such elevation was visible on the high wing model. A subtle reduction can be seen there between the junction and $y/c = \pm 1.5$. Nevertheless, the lift was generally higher than on the low wing configuration. This was particularly the case over the fuselage where a greater increment than on the low

wing arrangement was noted. The minima in the wing-body junction were of the same magnitude for all flap angles and all angles of attack, indicating an independence of both parameters. This can be explained by the fact that the pressure tappings were very close to the junction where the contribution towards the lift was very small. The lift over the fuselage was higher for the high wing model for all configurations, clearly showing a better mechanism by which the lift of the wing was carried over the fuselage.

The flaps of the high wing model show a higher loading than the low wing model for a given angle of attack, and were thus more effective. This higher loading was also reflected in the higher lift over the fuselage, indicating a better carry-over lift system than on the low wing model.

Common to all graphs of the low wing configuration was the loss in lift over the wing for high angles of incidence ($\alpha > 9°$). The reason for this reduction was a strong crossflow emanating from the wing-body junction, seen in the flow visualisation tests. An additional upwash along the sides of the fuselage was present, which increased the angle of attack of the wing and the lift in the junction. This crossflow and the upwash on the fuselage were more pronounced on the low wing than on the high wing model and resulted in a higher sectional lift near the wing-body junction, which was particularly noticeable for small angles of attack ($\alpha < 6°$) (Fig. 4.32). However, at larger angles of incidence this flow led to an earlier separation over the rear of the wing on the low wing model resulting in higher values of ΔC_p. At the same time the suction peaks at the leading edge were reduced, so that the overall lift was decreased.

5.9.5. Comparison with other researchers

Many researchers (e.g. Körner, 1972; Müller, 1970) included only the area of the fuselage which had the same length as the wing chord for the calculation of the spanwise lift distribution of a wing & fuselage combination or for their tests. In order to make comparison the results presented here show only the spanwise lift distribution which includes that part of the fuselage which was either above or underneath the wing, i.e. the nose and the tail have been neglected.

McLellan (1947) conducted a similar series of tests. His data are compared in Fig. 4.39 to 4.41 for an angle of incidence of $\alpha = 0°$ and 3° respectively. A true comparison is difficult because of the different airfoil section (NACA 65-210, see Fig. 5.1) and a higher Reynolds number of 3.8×10^6 in McLellan's tests. However, general trends of the lift distribution have been analysed. Both configurations are depicted in Fig. 4.39 for an angle of attack of $\alpha = 0°$. On the low wing model the lift increase in the wing-

body junction is clearly visible. On the high wing combination the lift on McLellan's model decreased towards the junction with a minimum at $y/c = \pm 0.5$. McLellan attributed this to the accelerated flow underneath the wing which then led to lower pressure there, a development which was also present on the upper wing surface when the nacelle was mounted above the wing. The displacement effects encountered on the model used in this research seem not to be so pronounced on McLellan's model, probably due to the smaller nacelle body and the smaller ratio of nacelle diameter to wing chord. However, the lift distribution at higher angles of incidence (Fig. 4.40 and 4.41) showed the same features.

The lift distribution on the low wing model remained constant for higher angles of attack, as depicted in Fig. 4.40 and 4.41. It should be noted that on McLellan's model the drop in lift over the fuselage increased as the angle of incidence rose. This was not visible on the high wing configuration. There, the step between $y/c = 0$ and 0.5 remained constant. Again the low drag shape of the nacelle suggests this independence.

The theory from Körner (1972) is compared with other results (Müller, 1970) in Figure 4.42 and 4.43. Included in these graphs is the lift difference of the two corresponding models at angles of attack of $\alpha = 0°$ and 3°. The graphs show the lift difference between the two different angles of attack. In order to display small changes the scale on the y-axis has been altered. Because Körner´s theory does not distinguish between a high and a low wing the curve is the same on both graphs. In the equation in Chapter 1 (1.2.1.) the distance between the wing chord line and the fuselage centreline is accounted for by a quadratic term which eliminates the distinction between a high and low wing. Müller conducted tests with the wing mounted a quarter diameter from the centreline at a Re.-No. of 0.31×10^6 (see Fig. 5.2). In Fig. 4.42 Müller's data show an increase in lift close to the wing-body junction. This rise is higher on the low wing model, probably due to displacement effects of the fuselage which led to an increase in the local angle of attack. Moreover, these curves also show a steeper gradient for the low wing configuration than for the high wing at the junction. Owing to the finite wing the lift curves decreases towards the wing tips. However, the lift distribution close to the junction resembled that for the corresponding model tested in this project. For the high wing configuration an increase in lift difference is noticeable at both angles of attack. This is not so emphasised in the graphs for the individual angle (see Fig. 4.39 and 4.40) where the distribution is very similar. On the graphs for the low wing combination in Fig. 4.42 and 4.43 the difference remains constant for the starboard wing. The reduction in lift difference on the port wing is attributable to the faulty data as outlined earlier in this Chapter.

Figure 4.43 depicts the lift difference for a larger distance of the wing from the fuselage centreline. The wing on Müller's model is at a distance of 1.25 of the fuselage diameter from the centreline. Körner's theory also applies to this position. In order to show the general trend of the lift distribution, data from appropriate models have been inserted. The elevation in the wing-body junction, seen Figure 4.42, is not as pronounced and varies only slightly between the two configurations, indicating a smaller displacement effect of the fuselage, since the vertical distance between the fuselage centreline and wing chord was increased. Müller observed a drop in the lift over the fuselage for both configurations with a slightly higher step on the low wing model, a development which was also present on the low wing model tested during this research. The theory of Körner shows only a small reduction in the lift difference.

5.10. Longitudinal lift distribution over the fuselage

The longitudinal lift distribution over the fuselage is shown in Figures 4.44 to 4.51. The calculation of the lift was performed by integration across the diameter at each longitudinal station, taking into account the taper of the fuselage. On the configurations where the wing was present appropriate data were inserted into the fuselage files as described in Chapter 3. Irregularities occurred in the middle of the curves for the fuselage alone configuration owing to the presence of support rods and these are excluded from the discussion.

This section represents a more comprehensive study of the fuselage lift than that presented in the simple presentation of Section 5.8..

5.10.1. Fuselage alone

Figure 4.44 shows the lift distribution for the fuselage alone for various angles of attack. On the forebody at about x/c = - 2.7 a small plateau appears on all curves followed by a step. This is attributed to a faulty data point. Since the nose cone was rotated in order to obtain the pressure around 360° this fault is present throughout the circumferential pressure field, and is thus reflected in the lift distribution. The change of lift at the nose is linear with increasing angle of attack up to a point where the influence of the rods dominate the distribution. Apart from the erroneous peaks mentioned previously all curves rise towards x/c = 0.25, the position where the rods were attached. The extent of the influence of the rods is surprisingly large since the diameter ratio, $d_{rod}/d_{fuselage}$, was only 0.196.

The lift distribution over the rear shows a download which is smaller than the upload over the front, owing to viscosity affecting the flow over the inclined fuselage in such a way that the pressure on the tail section is reduced (see Fig. 4.19) (Schlichting, 1979). The reduction in lift with increasing angle of incidence is smaller for $\alpha > 9°$, which again, is an effect of viscosity.

5.10.2. Fuselage & Wing

The development of lift with increment in angle of attack for the fuselage & wing configuration is depicted in Figure 4.45. On the high wing model data from the upper wing surface were inserted on the appropriate fuselage area, thus providing a high lift over the wing zone. The general lift distribution is similar to that plotted by Schlichting (1979) for a mid-wing configuration. His theoretical curve for a non-zero angle of attack shows an upload from the nose to the trailing edge of the wing with a peak at the leading edge. At the trailing edge the sign of the lift changes and a modest download is present over the rear of the fuselage. This lift distribution is consistent with a local angle of attack distribution which shows an upwash ahead of the wing and a downwash from the trailing edge backwards. Over the area where the wing was located the local angle of attack is considered to be zero. Such a theoretical approach cannot be considered to be sufficient in order to be able to explain the differences observed here, since the lift over the wing area shows an increment with rise in angle of incidence. This is particularly the case for the low wing configuration, where a completely different distribution was observed.

Just in front of and behind the high wing a modest download was observed which was due to the fairing. Here, the pressure on the upper fuselage surface was positive which led to a negative pressure difference, hence negative lift. However, the lift increased steadily with each increment in angle of incidence. At the nose, the small step previously seen on the fuselage alone is still present but not so pronounced. The download over the rear part of the fuselage in this configuration is slightly less than on the fuselage alone and appears over a smaller area between $^{x}/_{c} = 2.7$ and 4.5. At $^{x}/_{c} = 2.8$ a point exists where all curves show the same lift coefficient. This point is further back at $^{x}/_{c} = 3.1$ for the low wing configuration, depicted in the bottom graph. In front of this point, up to the trailing edge of the wing, the lift coefficient is very similar for all angles of attack except for $\alpha = 0°$. For this angle the lift over the wing is negative, owing to the lower pressure on the underside of the wing compared to that at top of the fuselage. There the pressure was almost constant across the area above the wing section, whereas the pressure on the lower wing surface increased towards the trailing edge. A rise in lift towards the trailing edge was therefore observed. The same pattern

was noticeable for $\alpha = 3°$, where again, the pressure difference was negative, hence producing negative lift. At higher angles the pattern changed and the lift was positive. The effect of the fairing is visible ahead of the wing, where it led to a modest upload before the wing contributed to higher values of lift. At the nose the lift was larger than for the high wing model, thus indicating that the effect of the wing was not confined to its immediate vicinity. Furthermore, a comparison with data from the fuselage alone configuration shows that the load at the tail was higher with the wing attached: a feature which was also observed on the high wing combination, but not to the same extent. Sandahl and Vollo (1947) using a high wing model, stated that the influence of the wing extends to about one chord in front and behind the wing. The present results on both high and low wing configuration show that this is not the case. The presence of the wing led to an increase in lift on both models but with a different distribution along the length. On the high wing combination the increase in lift occurred mainly over the area of the wing and also approximately two chords ahead of the leading edge and one chord behind the trailing edge. On the low wing configuration the lift at the nose was affected by the wing resulting in an approximately 8% higher lift, based on the value for the fuselage alone. The higher lift over the remaining length was more spread along the fuselage than on the high wing combination.

5.10.3. Fuselage & Wing & Flaps; α constant, δ varied

Figs. 4.46 to 4.48 show the lift along the fuselage for various flap settings at a constant angle of attack. To enable a comparison between all combinations the lift distribution for the fuselage alone and fuselage & wing configuration have been included. Compared with the fuselage & wing model the general lift distribution remained unaltered when the flaps were attached.

5.10.3.1. $\alpha = 0°$

Fig. 4.46 depicts all configurations for an angle of incidence of $\alpha = 0°$. On the low wing model the rise in lift was linear with an increment in flap deployment. This effect was largest just behind the wing and faded out towards the tail. Ahead of the leading edge the lift increased linearly apart from the fuselage & wing to the fuselage & wing & flaps combination with 10° flap deflection, where the step is slightly smaller.

On the low wing configuration the increase in lift with rise in flap deflection was again linear, but the step was smaller than on the high wing arrangement. At the rear end of the fuselage the increment was almost negligible. Between the end and the trailing edge of the wing the lift was higher than on the high wing counterpart. In particular between

$^{x}/_{c}$ = 1 and 2 where an upload was experienced compared with a download on the high wing model. The shape of the fairing promoted such a lift distribution, since positive pressures were measured on the upper fuselage surface which were larger than those on the lower surface, hence leading to a negative pressure difference. In this region, a second increase is perceptible for the combinations with the flaps attached. This suggests that the lift induced by the flaps was carried over the fuselage. The lift induced by the flaps on the high wing model was carried over in a different manner and resulted in higher peaks at the leading edge of the wing. Another increase was discernible in front of the wing. The magnitude of the lift fore and aft of the wing was approximately the same for a given flap setting. The contribution of the flaps towards the lift decreased from about $^{x}/_{c}$ = 3.3 towards the front, where all curves show the same values independent of the flap angle.

5.10.3.2. $\alpha = 6°$

This is also observed for an angle of attack of $\alpha = 6°$ as shown in Figure 4.47. Here the curves for the fuselage & low wing and fuselage & low wing & flaps are very similar from about $^{x}/_{c}$ = 3.7 backwards. The magnitude of lift over the rear end is smaller for higher angles of incidence. Behind the wing the second rise is not very pronounced, but the lift is larger than for $\alpha = 0°$. The shape of the curve suggests that the wing and flaps were acting together as a unit. The lift in front of the wing was marginally higher than behind the trailing edge. The high suction peaks on the wing, which are induced by the flaps were responsible for this. These peaks induced a lower pressure on top of the fuselage (see Fig. 4.25), thus a higher lift. The influence of the flaps towards the nose decreased with distance from the leading edge. The lift distribution along the fuselage suggests that the influence of the flaps was confined to the vicinity of the wing and approximately one chord fore and aft of the wing.

The lift distribution on the high wing model resembled that for $\alpha = 0°$. Higher lift was observed at the nose which was a function of the increased angle of incidence. The influence of the flaps remained, however, and at $^{x}/_{c}$ = - 3.1 only the curves show the same magnitude in lift. An upload is discernible just ahead of the wing as well as behind the wing. The influence of the flaps also remained over the rear end, where the lift was the same for all flap deflections at $^{x}/_{c}$ = 4.5. Comparing both graphs reveals that the step between the fuselage alone and the fuselage with the wing attached was larger on the low wing model than for the high wing combination, indicating that the lift carried over was distributed more along the fuselage and not concentrated in the vicinity of the wing. Considering the area underneath the curves for a given angle of incidence, it

appears that the overall lift of the fuselage of the low wing model is higher than that of the high wing combination.

5.10.3.3. $\alpha = 12°$

This simple judgement is not so straightforward for $\alpha = 12°$, where both configurations are depicted in Fig. 4.48. Over the wing area, the curves for the high wing combination exceed the vertical limits of the graphs, thus a visual "comparison" is impossible. On these graphs the influence of the flaps over the rear of the fuselage is discernible up to tail, where only the last two data points show equal lift for all configurations. Between the end of the fuselage and $^{x}/_{c} = 3.3$ the lift was negative for all configurations, but the download was reduced compared with the fuselage alone. The influence of the flaps was also noticeable towards the front where the curves between $^{x}/_{c} = -1.5$ and -2.9 show a small increase in lift with increment in flap angle.

A similar distribution over the front of the fuselage can be seen on the low wing model, where the curve for the fuselage & wing exceeds the curves for the model with the flaps attached. This is attributed to the large separation area on the upper wing surface and therefore less effective flaps: a fact which also effects the lift over the rear of the fuselage, where the curves for the flapped model are of the same magnitude if not less than for the unflapped, from about $^{x}/_{c} = 1.9$ backwards. Over the area where the wing is located the flaps double the lift compared with the fuselage & wing combination.

5.10.4. Fuselage & Wing & Flaps; δ constant, α varied

Figures 4.49 to 5.51 show the fuselage performance at a set flap angle with different angles of attack. For the low wing model the curves for an angle of incidence of $\alpha = 15°$ have been included. Common to all graphs are two points at the rear of the fuselage: at $^{x}/_{c} = 3$ for the high wing and $^{x}/_{c} = 2.7$ for the low wing configuration. At these locations the lift appears to be independent of the angle of attack.

5.10.4.1. $\delta = 0°$

Figure 4.49 presents both configurations for a flap deflection of $\delta = 0°$. The increment in lift on the high wing model was linear with increasing angle of attack. The angle of attack at $\alpha = 6°$ appears to be a boundary at which the load close to the wing and over the rear of the fuselage changes sign. A distinct download is visible in front and behind the wing and an upload is seen over the tail. No negative lift is discernible on the low wing model, apart from over the tail for $\alpha = 12°$ and $15°$. Over the rear of the fuselage

no increase in lift is noticeable for an increment in angle of attack from 12° to 15°. Between $^{x}/_{c}$ = 1.7 and 2.5 the curves are close together and a gain in lift is only marginal.

5.10.4.2. $\delta = 10°$

Setting the flaps to an angle of $\delta = 10°$ changed the magnitude of the lift, but not the distribution along the fuselage, as can be seen in Fig. 4.50. The high wing model shows a higher download at the tail than the low wing configuration. The negative lift over the wing area of the low wing model, which was observed for $\delta = 0°$, is not present any more and the lift is positive for all angles of incidence.

5.10.4.3. $\delta = 20°$

Raising the flap deflection to an angle of 20°, depicted in Fig. 4.51, led to almost equal lift over the rear of the fuselage on the low wing model. Between $^{x}/_{c}$ = 1.9 and 2.9 the curves differ only marginally and a distinction is only possible for the tail region which is attributed to the rise in incidence. At the nose and over the wing the increment in lift was more pronounced and irregularities appeared only at the trailing edge of the wing. This clearly shows that the influence of the flaps at that angle is only close to the wing.

This is also the case for the high wing arrangement where the curves are close together behind the trailing edge. A download for $\alpha = 9°$ and 12° is visible at the tail and at the leading edge as well for $\alpha = 12°$. Between $^{x}/_{c}$ = 1.3 and 2.3 the lines are more spread than on the low wing model which suggests that the influence of the flaps was larger in that area and remained linear with increasing angle of attack.

Common to all graphs is the higher upload at the nose on the low wing combination. In some cases it was almost twice as high than on the high wing counterpart. Furthermore, the download at the tail was lower on the low wing model than on the high wing combination. Outside the area where the wing was located the lift on the low wing configuration was higher than on the high wing. Over the wing the lift on the high wing model approached a maximum value of $C_L = 2.3$ for $\alpha = 12°$.

6. CONCLUSIONS FROM THE EXPERIMENTAL RESULTS

The aims of this research were (i) to examine the influence of the wing position with respect to the fuselage centreline on the pressure distribution of the individual parts, (ii) to investigate the influence of flaps on the pressure distribution, (iii) to provide extensive data for the pressure distributions of fuselage-wing-flap combinations in both high and low wing arrangement, and (iv) to calculate the lift distribution along the fuselage length and along the span of the wing. Pressure measurements of the individual model components were carried out, in order to investigate the interference effects caused when the parts were assembled together. Pressure orifices provided a good means of detecting small changes in the flow around surfaces. The following sections summarise these effects on the pressure distribution of the wing, followed by those for the fuselage. Finally, changes in the lift distribution of the wing and the fuselage are analysed.

The surface plots of the pressure distribution of the wing revealed that the endplates, mounted at each wing tip, were very effective in simulating a wing of infinite span. It has been shown that the reduction in pressure of the upper wing surface and the increase on the lower wing surface was linear with increasing angle of attack and/or increasing flap deflection. The pressure distribution illustrated small changes in the surface flow very well. A separation bubble, for example, observed during the flow visualisation tests, was also noticeable on the surface pressure plots.

6.1. High wing model

On the high wing model the spanwise pressure distribution was constant along the span for all angles of attack and for all flap angles, indicating that the influence of the fuselage was confined to its immediate vicinity. This was attributed to an unchanged geometry of the upper wing surface. Furthermore, the wing-body fairing achieved a smooth transition between the two components, which led to a moderate pressure gradient over the fairing, thus moderate changes in the flow velocity.

Above the fuselage the pressure on the upper wing surface decreased linearly with incidence and flap deflection, but with a smaller magnitude than over the remaining wing. The mechanism which determined the magnitude is still not fully solved, since no theory has been established which predicts the pressure distribution accurately in that area.

The pressure distribution on the fuselage was affected by the presence of the wing. The effect extended along the entire length and was not confined to the immediate vicinity of the wing. On the high wing configuration an adverse pressure gradient ahead of the wing was observed. This gradient increased with increasing incidence as well as with flap deflection. The adverse pressure gradient was caused by the positive pressure of the lower wing surface and by the inherent gradient on the fuselage surface. Owing to the fairing the gradient was moderate and the pressure did not approach the stagnation pressure.

6.2. Low wing model

This was not the case on the low wing model, where strong pressure gradients near the wing-body junction occurred. These led to separation on the upper wing surface at higher angles of attack ($\alpha > 9°$). The negative pressure of the upper wing surface accelerated the flow and therefore promoted any crossflow originating from the fuselage.

At higher angles of attack, $\alpha > 9°$, the pressure on the upper wing surface gradually increased toward the wing root resulting in a corresponding loss of lift in that area. Again, displacement effects of the fuselage were responsible for this, these resulted in an increase in the local angle of incidence. The higher incidence led to a premature separation at the wing-body junction, with constant chordwise pressure gradient on the upper wing surface in the separated area.

With the flaps attached the pressure distribution remained the same, only the magnitude of the changes varied. The change in pressure was higher on the high wing configuration than on the low wing counterpart. This can be explained by the reduced effect of the flaps on the low wing combination. When the flaps were deployed, a gap between the fuselage and the flaps appeared. As a result flap-tip vortices were produced, which reduced the effectiveness of the flaps.

On the fuselage of the low wing model a favourable pressure gradient was observed in front of the wing. This gradient was steeper than that of the high wing combination. This can be explained by the displaced flow which had to travel from the lower side of the fuselage up and over the wing, where a relatively large negative pressure was present. The high negative pressure also affected the pressure on the fuselage sidewalls, more so than the positive pressure of the lower wing surface on the high wing model.

The flaps magnify the pressure distribution due to the presence of the wing, leading to even lower pressures on the fuselage sidewalls. The pressure difference between the top and bottom of the fuselage showed higher values for the high wing configuration, indicating that the flaps were more effective here. The geometrical arrangement of the flaps explains this. On the high wing model the flaps were restricted by the endplates and the fuselage sidewalls at either side, hence a tip vortex was prevented and the induced pressure on the wing was constant along the span.

The lift was calculated from the pressure distributions, leading to the spanwise lift distributions and longitudinal lift distributions along the fuselage. The spanwise lift showed for low angles of incidence ($\alpha \leq 6°$) equal or higher lift on the low wing configuration than that for the high wing model. The displacement effects of the fuselage led to higher angles of incidence near the wing-body junction, resulting in higher lift, which spread out onto the remaining wing. The lift over the fuselage area was higher for the low wing arrangement, since the low pressures on the upper fuselage surface were higher in magnitude than the pressure on the lower fuselage surface for the high wing model.

For incidence of $\alpha > 9°$ large lift losses over the wing were observed on the low wing model. These losses extended up to one chord in spanwise direction and reduced significantly the efficiency of the wing. Again, the displacement effect of the fuselage was responsible for the strong crossflow on the upper wing surface. Further out on the wing the lift for the high wing model was higher than that for the low wing combination, which indicated that the effect of the fuselage is not confined to its vicinity.

The spanwise lift distribution varied with the flaps attached. Over the fuselage area the lift of the high wing model was higher than that for the corresponding low wing configuration. This can be explained by the higher negative pressure of the upper wing surface, which was induced by the flaps. This negative pressure was carried over the fuselage, thus creating higher lift. The lift over the outboard wing was also higher for all high wing combinations. Again, the higher efficiency of the flaps was responsible for this. The flaps induced a pressure which was higher in magnitude on the wing along the entire flap span. Additionally, the displacement effect of the fuselage was smaller than on the low wing model. These differences are not covered by any theory, which is used to calculate the spanwise lift distribution. However, the mechanism by which the lift is carried over the fuselage must vary between high and low wing configurations, otherwise there would be no difference between the two models.

The lateral lift distribution of the fuselage on the flapped low wing model changed very little. The flaps affected the lift in their vicinity and only marginal changes were observed for the fore- and aft body. The location of the flaps and the change of the pressure distribution on the upper wing surface resulted in a smaller influence of the flaps on this model. The effect of the flaps was higher on the high wing configuration, where an increase in lift almost along the entire fuselage was observed. The influence of the flaps decreased linearly with increasing distance from the flaps.

To summarise, the main conclusions obtained from this research are:

1. The pressure distribution of the upper wing surface of the high wing was less affected by the presence of the fuselage, than that of the low wing.
2. The low wing produced large suction peaks on the sidewalls of the fuselage.
3. The interference effect of the wing extended to the whole of the fuselage.
4. The flaps were more effective on the high wing model in providing higher lift.
5. The flaps promoted the already existing pressure gradients on both models.
6. A fairing can reduce steep pressure gradients ahead of the wing leading edge.
7. At low angles of attack the lift over the wing of the low wing model was equal to or higher than that of the high wing counterpart.
8. The displacement effects of the fuselage caused large areas of separation on the upper wing surface of the low wing model, resulting in large lift losses at higher angles of incidence.

As discussed in Chapter 1, no theoretical analysis can accurately predict the pressure and lift distribution on individual parts of an aircraft. Factors such as the presence and design of a fairing, the presence of flaps and the aerodynamic interference effects of these parts have not been taken into account. The only attempt to take account of a non-mid wing position was by Körner (1972). Unfortunately though, his theory could not distinguish between high and low wing position.

Previous experimental research programs have only investigated the total lift and drag of wing-fuselage combinations. Again, the interference effects on individual components have rarely been considered and the effects of the flaps have never been taken into account.

7. A BRIEF DESCRIPTION OF THE CFD-CODE

An attempt was made to predict the flow structure of both high and low wing configuration with a Computer Fluid Dynamic-Code (CFD-Code). This computation was conducted by the kind cooperation of the Aerodynamics Engineering department of British Aerospace Airbus Ltd, Filton, Bristol, UK. The geometry of both models was fed into the VSAERO panel method code, developed by AMI, Redmond, Washington, U.S.A.. The program was designed to calculate pressure distribution and aerodynamic loads for arbitrary bodies at low to average subsonic speeds (M = 0.8), was thought to be capable of handling through-gap flows, such as those present between a wing and high-lift devices in deployed form, i.e. flaps and slats.

For the geometry input the model was separated into three components, i.e. the body, the wing, and the flaps. The geometry of the fairing was measured from the model and then transferred into the code. However, in order to achieve a uniform and continuous surface curvature and to enable an even distribution of panels, the geometry of the fairings was slightly altered. Figure 7.1 depicts the two panelled models used for the numerical computation. No attempt was made to model the endplates at each wing tip because of restrictive panelling techniques between a multi-component high-lift model and a flat plate. The restrictions of the panel method also led to 5mm gap between the fuselage and the flaps on both configurations. Further modifications included the introduction of an additional spanwise panel for both wing and flaps in order to obtain a two-dimensional loading outboard on the wing and flaps. The size of the panel was determined by trial and error until the pressure data agreed with those obtained in the wind tunnel test. The addition of the panels on either side of the wing tips led to an initial aspect ratio of 22.

During initial test runs it was noted that a disagreement occurred between the wing loading of the experiment and the numerical prediction for the same configuration. Therefore, the numerical model was changed in order to account for these discrepancies. Although the pressure peaks on the upper wing surface increased with a rise in aspect ratio, the flap pressure remained constant and the negative pressure of the upper wing side was over-predicted. The higher suction peaks on the flaps resulted in a higher loading on the wing. To reduce the loading and to bring the calculated pressure data in agreement with the measured data the aspect ratio was reduced to 15.2. This did not result in the desired reduction of the wing pressure and instead the flap angle was reduced and the aspect ratio retained. Figure 7.3 presents the flap angles used in the CFD-code. For example the panel model used a flap deflection of $\delta_p = 15°$ for a

geometric flap setting of $\delta = 20°$. The ratio of geometric flap deflection and the flap angle used by the computer model is depicted in Figure 7.4.

An example of the chordwise pressure distribution obtained with these modifications is shown in Fig. 7.5. The agreement at the leading edge between the measured data for $\delta = 20°$ and the calculated data for $\delta = 15°$ and an aspect ratio of 22 is good. Towards the trailing edge differences in the pressure between the computer model and the tested data are noted. These discrepancies were attributed to insufficient modelling of viscous effects over the rear part of the wing, and particularly over the flaps (Reynolds number = 230,000, based on the flap chord).

8. EXPERIMENTAL DATA COMPARED WITH CFD-CODE

The CFD-code VSAERO belongs to a group of methods where the basic panel has a source or doublet of constant strength. The surface of each panel is planar. The grid is constructed of rectangular panels where the control point is at the centre. The control point is the location where the normal vector pointing in the outward direction is anchored. This is the location where all coefficients such as C_p, C_l and the velocity are calculated. The wake is modelled by a wake relaxation method, where the initial wake geometry is specified by the programmer, after which several wake grid planes are established, perpendicular to the freestream. Several iterations are conducted before the flow field is finally modelled. Details of the algorithm and the modelling technique are given by Katz and Plotkin (1991).

The discussion of the results is concentrated on streamline plots provided by BAe and photographs of the surface flow visualisation. VSAERO was not able to provide the pressure distribution in the same format as the experimental results obtained. All Figures show the flow over the wing-body junction from either underneath the model or slightly above it. Thus, the wing flow on the appropriate wing surface is visible. The flow in the junction is not clearly seen but the structure of the streamlines is distinct.

Figure 8.1 depicts the streamlines for the flapped model at an angle of attack of 0° and a flap deflection of 15°. The streamlines on the high wing model showed a concentration over the wing area where the spanwise distance between the lines was reduced. Ahead of the wing-body junction the lines were slightly bent towards the centre of the wing. At the junction two distinct lines were visible where the top line continued over the wing and the bottom line diverted under the wing. The top line followed the wing shape and stayed on the fairing behind the wing before turning upwards towards the centre of the fuselage merging with the rest of the upper streamlines. At the sidewall of the fairing a group of streamlines appeared from underneath the wing which bent upwards and stopped at the sharp corner of the fairing. Below these lines, at about mid-height of the fuselage, a bunch of streaks were visible which remained straight from about half a chord in front of the leading edge up to approximately the position where the fuselage tapered.

The concentration of streamlines at the centre of the wing was not so pronounced on the low wing model. The lines were much more spread across the wing and only accumulated towards the junction. This bunch carried over to the fuselage and deflected upwards merging with the streamlines from the sidewalls of the body. The group of streamlines over the wing in the junction stayed together and merged with

those coming from underneath the wing. Behind the wing a small downward deflection of the lines was noticeable.

The flow structure on the high wing configuration for $\alpha = 6°$ was generally similar to that for $\alpha = 0°$ (Fig. 8.2). In front of the wing the streamlines were more inclined owing to the higher angle of attack. The lines behind the wing were slightly more curved upwards for the same reason. Over the centre part of the wing the streamlines were closer together than for the lower incidence. The straight lines at the height of the fairing corner, which were observed for $\alpha = 0°$ are now shorter and the upward movement started at about 60% of the fuselage length.

On the low wing combination the streamlines at the wing centre remained almost unaltered at higher angle of attack. The major differences were visible behind the wing where the upwards deflection was more and occurred at a position further forwards. Ahead of the wing the streamlines from underneath the fuselage are bent upwards and then followed the curvature over the wing. Just behind the wing the merger point was visible. Streamlines from underneath the wing and those from above the wing merged at about half a chord behind the trailing edge, slightly above the wing chord line.

At $\alpha = 12°$ the concentration of streamlines above the fuselage on the high wing model was clear (Fig. 8.3). The streamlines from almost the entire upper forebody amalgamated ahead of the wing and remained together up to the end of the fuselage. Near the wing-body junction the streamlines were tilted up- and backwards before joining those which curved upwards at about one chord ahead of the leading edge. These formed a second bundle of lines either side of the centre above the wing-fuselage junction. Underneath the wing the streamlines remained constant along a given fuselage height and curved towards the tail over the last 30% of the fuselage.

The developments of the flow on the low wing combination at $\alpha = 6°$ were more distinct than for an incidence of 12°. Over the forebody, a concentration of streamlines was clearly visible. This bundle divided approximately three-quarters of a wing chord ahead of the leading edge into two main streams. About 75% of these lines are diverted over the wing and only a small proportion remained underneath. These two groups merged at about half a chord behind the trailing edge before flowing onto the upper half of the fuselage.

More lines in the wing-body junction were deflected by the wing on the low wing model than by the wing on the high wing model. At lower incidence ($\alpha = 0°$) the

degree to which the streamlines turned upwards appeared to be higher on the low wing configuration. The extent of deflection upstream of the leading edge was also higher. The high degree of deflection induced by the wing indicated a much higher displacement effect on the low wing configuration than on the high wing counterpart.

In order to compare the numerical results with the wind tunnel tests oil surface flow visualisation tests were performed. For these tests the model was rolled by 90° in the tunnel, to put the wings horizontal. The position of the wings in the tunnel was the same, independent of the model configuration.

Fluorescent lights in the corner of the wind tunnel were used as the light source in order to avoid reflections which might have occurred from a flash gun. The colour of the model surface needed to be black for the flow visualisation tests. The fuselage on the high wing model was thus painted black and the wing and flaps were covered with sticky back plastic. However, this caused difficulties with the flow visualisation since the surface consisted of two different roughnesses, which led to different behaviour of the mixture on the model parts. The mixture used for the flow visualisation consisted of 30% oleic acid, 40% paraffin, and 30% titanium dioxide. Owing to the absorbency of the wooden parts of the fuselage on the high wing model this mixture changed slightly during the wind tunnel tests. The entire low wing model was covered with sticky black plastic during the second series of tests, in order to overcome the difficulties encountered in the first series. In order to follow the high curvature of the parts of the model such as the fairing, the plastic needed to be cut into small pieces. Unfortunately, some of these pieces came loose during the tests which also led to an uneven surface. This led to specific flow patterns seen in the photographs which were obviously not present during the pressure tests.

The photographs of the surface flow visualisation are depicted in Figures 8.4 to 8.12. Only a few typical photographs are shown owing to the enormous amount of different configurations tested and the limited space in this thesis. For comparison the flow in the wing-fuselage junction was observed from two different view angles. Some of the photographs for the low wing model were taken while the tunnel was running, thus the entire model is visible which gives a clear overview of the flow developments.

Fig. 8.4 (a) depicts the junction of the unflapped high wing model and Fig. 8.4 (b) the comparable low wing configuration for $\alpha = 0°$. On the high wing model a line of accumulated titanium dioxide is visible at about half of the fuselage height. This line was deflected downwards from the forebody and several streamlines merged into this

accumulation just ahead the leading edge of the wing. Above this line a series of streamlines is noticeable which was displaced by the wing, as can be seen by the curve of these lines in front of the leading edge. These streamlines were deflected downwards along the fuselage. The shape of the fairing promoted this development and prevented a flow separation like that observed by Devenport (1990). The general structure of the surface flow indicated an attached but turbulent flow due to the roughness of the surface.

The flow over the low wing model showed a different pattern. The streamlines above the wing were deflected upwards by the wing. Towards the trailing edge the curves bent down reaching to the same level on the fuselage as they were in front of the wing. Streamlines from the upper front part of the fuselage turned down and followed the pattern. The pattern above and in front of the wing shows that the streamlines were deflected out from the centreline and then upwards along the side of the fuselage.

Figure 8.5 (a) and (b) present the same configurations and locations on the models for $\alpha = 12°$. On the high wing model Fig. 8.5 (a) the line at half height of the fuselage was not so pronounced any more but the locations were almost the same. In front of the wing the streamlines were more inclined due to the higher incidence. Underneath the wing the lines were straight and not turned downwards. As for $\alpha = 6°$ the flow appeared to be attached but turbulent. The relative "smoothness" is also reflected on the surface pressure plots (see Fig. 4.20 c).

The photograph for the low wing model Fig. 8.5 (b) shows the rear end of the fuselage and part of the wing. On the fuselage three main streams converged into a spiral focus at about half chord at the middle height of the fuselage. This spiral focus was also observed by Wickens (1987), but further forward on the fuselage. At this position high negative pressure peaks were noticed (see Fig. 4.20 f). This focus of separation was characterised by streamlines which spiral inwards into the centre at which a vortex core arose and streamed downwind (Wickens, 1987). This flow structure was already visible at an angle of attack of $\alpha = 9°$ (not shown here).

A possible interpretation of the surface flow is depicted in Figure 8.6. On the high wing configuration streamlines merged together ahead of the fairing and formed a vortex, which was probably weak, since the fairing achieved a smooth curvature between wing and fuselage. The interpretation of the low wing combination is based on the observations of Wickens (1987), who observed similar spiral foci on a high wing model, but further ahead of the wing. At the centre of the focus a vortex filament

emerged, which trailed downstream. Obviously the strength, height, and shape of the filament can not be determined from the surface flow.

The next set of photographs shown is for an angle of incidence of $\alpha = 0°$ and a flap setting of $\delta = 20°$ for the high wing model and $\delta = 30°$ for the low wing configuration(Fig. 8.7). The mixture for the surface flow of the high wing model varied during the tests, resulting in a less clearly visible pattern on the model. However, the general flow structure was still detectable and was similar to the one for the unflapped model. In front of the wing the streamlines curved down from the upper part of the fuselage but an accumulation line is not visible. This could be due to the high viscosity of the mixture. At the trailing edge of the wing the influence of the flaps was clearly visible, since the streamlines were deflected downwards. The general flow pattern indicated an attached flow.

The flow on the low wing combination showed an upward deflection of the streamlines ahead of the wing, followed by a downward curvature over the wing. This downward pattern remained over almost the entire afterbody, where an accumulation of titanium dioxide was visible at the bottom. Here the streamlines from the lower fuselage side, and the those described above, merged and formed a line which remained up to the tail. Over the wing area the influence of the wing was visible up to the top of the fuselage.

Figure 8.8 (a) depicts both configurations at an angle of incidence of 12° and a flap deflection of 20°. In front of the high wing pockets of accumulated titanium dioxide are visible, which were due to the sticky back plastic patches. However, the flow pattern in this region was still visible. Owing to the high incidence the streamlines were bent upwards towards the leading edge of the wing. At the junction a few lines formed around the leading edge and eventually led into a line which extended from about half chord to the tail of the fuselage. Close to the flaps, a bunch of streamlines can be seen which was deflected downwards by the flaps before levelling out and curving upwards to the top of the fuselage. Owing to the fairing a clear line of separation at the wing-body junction was not noticeable, indicating that the fairing achieved a smooth transition from the fuselage surface to the upper wing surface.

The flow pattern on the low wing model Fig. 8.8 (b) was dominated by the spiral focus above the wing at approximately half the fuselage height. The streamlines ahead of this focus inclined towards it independent of the original location. This clearly showed a much higher deflection on the forebody than on the high wing model. The flow at the top of the fuselage was drawn into this focus which affected the flow at the top, up to

one chord behind the trailing edge. The vertical position of this focus was independent of the flap deflection and changed only with the attachment of the flaps and with the incidence. However, the centre of the focus rose as the angle of incidence increased. The fore and aft position was independent of incidence, flap attachment and deflection. Behind the spiral focus an area of reversed flow was visible. This was not observed for $\alpha < 6°$ nor for the unflapped model (Fig. 8.5). The area was approximately the same for small flap deflections. This suggested a limited influence of the flaps, probably due to their low position underneath the fuselage. From the focus a line emerged where titanium dioxide accumulated, owing to flow from underneath and above merging together at this height and extending the line up to the tail of the fuselage. The first half of this line changed with incidence corresponding to the position of the centre of the focus. This influence died out further downstream and the second half of the line was independent of the angle of attack and the flap setting.

Figure 8.9 shows a drawing of a possible interpretation of the flow further away from the surface. The drawings are an extension of Wickens work (1987) who undertook extensive flow visualisation tests on a nacelle-wing combination. On the wing two lines appeared which separated regions of the surface flow. Similar lines were observed by Devenport (1990) on a wall with a wing attached. He stated that these lines indicated two regions of different shear stress, with higher stress close to the wing-body junction and lower stress further away. He assumed that large scale unstable turbulent structures of the flow are responsible for the two regions. This cannot be corroborated, since no stress measurements were undertaken during this study.

Figures 8.10 to 8.12 are given in order to enable an examination of the surface flow on the wing. The photograph for the high wing model show the upper wing surface above the fuselage (Fig. 8.10). The angles of attack are 6° and 12° respectively and the flaps were set to 20° and 30° respectively. At the centre of the wing trailing edge an accumulation of pigments can be seen. This was due to the curvature of the fuselage and the straight surface of the fairing. Leading into this accumulation were two lines which emerged from the forebody of the fuselage and trailed over the wing. These lines were probably vortex sheets which developed on the upper fuselage surface. At α = 12° the lines were distorted towards the port wing. This distortion was due to the combined effects of the offset in the flap angle and the small incidence gradient in the wind tunnel.

Figure 8.11 shows the upper wing surface of the unflapped low wing model with the fuselage at the left hand side of the photographs. The angles of attack were 6° and 12°.

Close to the leading edge a deposit of flow visualisation material is visible, which indicates the existence of a separation bubble. This was also noticed on the surface pressure plots (Fig. 4.8 and 4.9). However, the flow was dominated by the large areas of separation adjacent to the fuselage. This area showed up in the pressure plots as a region where the pressure remained constant along the chord. At $\alpha = 12°$ the region extended to approximately one chord in the spanwise direction. In both cases a vortex was seen which clearly indicated that the flow could no longer be considered as two-dimensional but is actually three dimensional. From the centre of the vortex a vortex filament emerged which probably formed a vortex with the filament emanating from the fuselage. In the junction, however, further material can be seen which confirmed the pressure data and suggested a separation here.

The lower wing surface of the low wing configuration is depicted in the top photograph of Figure 8.12. The model was at an angle of attack of $\alpha = 6°$ and the flaps were not attached. The surface flow shows streamlines which remained almost unaltered over the wing area. Over the rear part of the fairing the streamlines curved slightly outwards, something which was more pronounced at $\alpha = 12°$. No distinct lines like those seen on the high wing model (Fig. 8.10) are visible.

The bottom photograph depicts the lower wing surface underneath the fuselage at an angle of attack of 12° and a flap setting of 10°. This picture reflects the flow over the fuselage for all configurations since the flow pattern remained the same throughout the tests. In front of the fairing the streamlines, which were further outside from the centre line, were deflected out- and upwards over the wing. The streamlines at the centre, ahead of the leading edge, were parallel to the centreline of the fuselage and diverted only towards the rear end, squeezed between the flaps and then up the sidewalls of the fuselage.

9. CONCLUSIONS FROM CFD-CODE / FLOW VISUALISATION

The aim of utilising a CFD-code was to investigate whether an inviscid numerical approach can predict the pressure distribution of a complex model correctly. In order to obtain a first impression, streamlines, which were produced by the computer model, were compared with photographs of the surface flow of configurations studied in this project.

The streamlines on the front of the fuselage agreed with those obtained in flow visualisation tests for low angles of incidence.. The observed deflection of the flow near the wing was reflected in the computer model. This deflection varied between the high and the low wing configuration. For both high and low wing combinations the numerical model did not predict the flow pattern near the wing-body junction correctly. This was due to viscous effects, which can be of the same magnitude as displacement effects (Küchemann, 1978). The unsatisfactory modelling of the junction flow led also to a disagreement between the streamlines and observed flow patterns over the rear of the fuselage.

The geometrical model was incorrect due to difficulties encountered in the panel method. A gap between the wing and the fuselage which was present in the CFD-code led to no or only a small influence of the flaps on the flow over the fuselage. This, and the fact that the flap deflection had to be reduced in order to obtain a similar wing loading of the tested model, led to further inaccuracy in the prediction of the flow.

On the grounds of these disagreements and the lack of modelling of the viscous effects, which are considered essential, a further analysis of the calculated pressure data was not pursued.

10. SUMMARY OF CONCLUSIONS

This chapter combines the conclusions drawn from the experimental work with the conclusions from the surface flow visualisation tests. The method of surface flow visualisation was a good aid for the interpretation of the pressure data and made the understanding of the flow phenomena around the entire model easier. In particular, changes in the pressure distribution, such as unexpected constant chordwise pressures, were corroborated by examination of the flow visualisation results.

The main conclusions from this project were:

1. The lift over the fuselage was higher on the unflapped low wing model compared with the high wing model due to high suction peaks on the upper half of the fuselage.
2. On the high wing model the flaps increased the lift over the fuselage to the same magnitude as over the wing, indicating a better mechanism by which the lift was carried over the fuselage.
3. Large lift losses over the wing at higher angles of incidence ($\alpha \geq 9°$) occurred on the low wing model, owing to the displacement effects of the fuselage.
4. The design of the fairing is of importance, since a good fairing can reduce root vortices and therefore make the wing more effective in providing lift.
5. At low angles of attack the lift was of equal magnitude on both high and low wing model.
6. The flaps were more effective on the high wing model and the lift was higher than for the low wing model at equal angles of flap deflection.
7. The flaps maintained the existing pressure distribution of each model and only increased the magnitude of the pressure.
8. The surface flow visualisation provided a good means of making changes in the flow clearly visible.
9. The surface flow visualisation corroborated the pressure distribution over the entire model.

11. FURTHER RESEARCH

The pressure distribution around fuselage-wing-flap configurations has been dealt with comprehensively in this study. However, results have indicated a need for further studies investigating the wing-body-flap interference and associated changes in the pressure field over the entire aircraft.

It is suggested that such research should be extended to include configurations with a symmetrical wing section. Any lift arising from such a combination at $\alpha = 0°$ would be likely to be a result of interference effects, since any lift arising at that incidence could be a result of a wing-body junction lift.. The low wing was exposed to large angles of attack at the wing root in this study. It would be worthwhile investigating the spanwise pressure and lift distribution with a twisted wing where the incidence at the wing root would be reduced.

At large angles of attack the flow visualisation on the low wing model revealed a crossflow in spanwise direction up to a distance of one chord from the wing-body junction. The wing endplates would then lead to a nozzle effect over the remaining wing. It would be of benefit to investigate the effect of increasing the wing span in order to minimise this effect on the wing.

Modern fairings are designed such that the wing surface is partly covered, i.e. the area underneath the fuselage is flat. The fairings on both high and low wing models were very similar in design, where one wing surface was not covered. It is therefore suggested that the effect of a different design should be investigated. Furthermore, a larger fairing with a smooth transition from the fuselage sidewall to the wing leading edge should be considered, in order to study the effect on the lift distribution at the wing root. Furthermore, the effects of different corner radii between the fuselage sidewalls and the wing surface could be examined in this connection.

The surface flow visualisation utilised in this project provided a good means of understanding the surface flow. However, to obtain a more comprehensive view of the off-surface flow, tests conducted in a water tank with orifices for coloured dye located at several spanwise locations and longitudinal positions on the fuselage would be of enormous benefit. These tests should be supported by velocity measurements of the flow away from the surface, in order to examine the extent of possible vortices shed from the forebody and the wing-body junction.

12. REFERENCES

Abbott, I. H., Von Doenhoff, A. E.
Theory of wing sections; Dover Publications; New York 1959

Albone, C. M., Hall, M. C., Gaynor, J.
Numerical solutions for transonic flows past wing-body combinations; RAE Tech. Rep.

Anderson, J. D.
Fundamentals of aerodynamics; McGraw-Hill Inc.,1985

Basu, B. C., Singh, N., Aikat, S.
Incompressible potential flow about complete aircraft configurations
Aeronautical Journal, Paper No. 1653, Nov. 1989

Becker, J. V., Lloyd, H.L.,
High-speed tests of a model twin-engine low-wing transport airplane; NACA R 750, Feb. 1940

Bernstein, L., Rahman-Jami, M.
Steady sideslip effects on wing-body combinations
Queen Mary College ER- 1005, July 1984

Boermans, L.M.M., Terleth, D.C.
Wind tunnel tests of eight sailplane wing-fuselage combinations
Delft University of Technology; OSTIV Congress New Mexico 1983

Bore, C. L.
High wing or low: Factors affecting the choice; ARC 34329, Jan. 1972

Butler, S. F. J. & Lawford, J. A.
Low speed wind tunnel tests on a wing-fuselage model with area suction through perforations at the leading edge flap; RAE TR 67153, July 1967

Devenport, W. J., Agarwal, N.K., Dewitz, M.B., Simpson, R.L., Poddar, K.
Effects of a fillet on the flow past a wing-body junction
AIAA Journal, Vol. 28, No. 12, Dec. 1990

Devenport, W.J., Simpson, R.L., Dewitz, M., Agarwal, N.
Effects of a leading-edge fillet on the flow past an appendage-body junction
AIAA Journal, Vol. 30, No. 9, Sept. 1992

East, L. F., Hoxey, R. P.
Boundary layer effects in an idealized wing-body junction at low speed
RAE TR 68161, July 1968

Flax, A. H., Lawrence, H.R.
The aerodynamics of low-aspect-ratio wings and wing-body combinations
Third Anglo-American Aeronautical Conference 1951

Flax, A. H.
Integral relations in the linearized theory of wing-body interference
Journ. Aero. Science, Vol. 20, No. 483, 1953

Furlong, G.C., Fitzpatrick, J.E.
Effects of Mach number and Reynolds number on the maximum lift coefficient of a wing of NACA 230-series airfoil sections; NACA TN 1299, 1947

Glauert, H.
The elements of aerofoil and airscrew theory; Cambridge Press, 1959

Gough, M.N.
The effect of fillets between wing and fuselage on the drag and propulsive efficiency of an airplane; NACA TN 299, Oct. 1928

Greenwell, D.I., Bean, D.E., Wood, N.J.
Calibration of the high-speed working section of the 7' x 5' wind tunnel
School of Mechanical Engineering, University of Bath, Rep. No. 49/1992, July 1992

Greenwell, D.I.
RIGTEST 3.5 User Guide, Wind Tunnel Data Acquisition Program, School of Mechanical Engineering Report, 50/ 1991, University of Bath, February 1991

Grosche, F. R.
Wind tunnel investigation of the vortex system near an inclined body of revolution with and without wings; DFVLR- AVA Report

Hancock, G. J., Javed, M.A.
Some numerical studies of wing-body combinations
Queen Mary College EP-1060, Nov. 1983

Hazarika, N:
An efficient inverse method for the design of blended wing-body configurations
Institute of Technology, Georgia; PhD. Thesis 1989; NHH 89-04811

Hess, J. L. & Smith, A.M.O.
Calculation of potential flow about arbitrary three-dimensional bodies
McDonnell-Douglas Rep. MDC-J 0545, 1962

Jacobs, E. N
The drag and interference of a nacelle in the presence of a wing
NACA TN 320, Oct. 1929

Jacobs, E.N., Ward, K.E.
Interference of wing and fuselage from tests of 209 combinations in the N.A.C.A. variable density tunnel, NACA Report 540, 1935

Katz, J., Plotkin, A.
Low-speed aerodynamics; McGraw-Hill, Inc., 1991

Körner, H.
Berechnung der potentialtheoretischen Strömung um Flügel-Rumpf-Kombinationen und Vergleich mit Messungen;
Zeitschrift für Flugwissenschaften, VOL 20, No. 9, 1972

Kubendran, L. R. et al
Juncture flow control using leading-edge fillets; AIAA Paper 85-4097, Oct. 1985

Kudendran, L. R. et al
Turbulent flow around a wing/fuselage- type juncture
AIAA Journal Vol. 24, No. 9, Sept. 1986

Küchemann, D.
Some remarks on the interference between a swept wing and a fuselage
RAE Report

Labrujere, Th. E., Loeve, W., Slooff, J.W.
An approximate method for the calculation of the pressure distribution on wing-body combinations at subcritical speeds; AGARD CP 35, 1953

Lawrence, H. R.
The aerodynamic characteristics of low aspect ratio wing-body combinations in steady subsonic flow; Jour, of Aero. Science, Aug. 1953

Lennertz, J.
Influence of the airplane body on the wings; Aerodynamic theory, Vol III & IV;
edited by Durand, W.; Dover Publications, New York 1934

Maughmer, M., Hallman, D., Ruszkowski, R., Chappel, G., Waitz, I.
Experimental investigation of wing/fuselage integration geometries
Jour. Aircraft, Vol. 26, No. 8, Aug. 1989

McLellan, C.H., Cangelosi, J. I.
Effects of nacelle position on Wing-Nacelle interference; NACA TN 1593, Nov. 1947

McMahon, H.,
Mean velocities and Reynolds stresses upstream of a simulated wing-fuselage junture
NASA CR 3695, June 1983

Mehta, R. D.
Effect of wing nose shape on the flow in a wing/body junction
Aeronautical Jour., Dec. 1984

Multhopp, H.
Aerodynamics of the fuselage; Luftfahrtforschung Vol. 18, No. 2/3 1941

Muttray, H.
Untersuchungen über die Beeinflussung des Tragflügels eines Tiefdeckers durch den Rumpf; Luftfahrtforschung, June 1928

Muttray, H.
Die aerodynamische Zusammenführung von Tragflügel und Rumpf
Zeit. f. Luftfahrtforschung, 1933

Neely, R.H., Fairbanks, R.W., Conner, D.W.
Effects of wing and nacelle modifications on drag and wake characteristics of a bomber type airplane model; NACA ARR No. L5J05, Dec. 1941

Ober, S.
Some studies on the aerodynamic effect of the gap between airplane wings and fuselages; NACA TN 327, June 1929

Obrien, J.
Private communications, June 1993

Ower, E.
Some aspects of the mutual interference between parts of aircraft
ARC R & M No. 1480, June 1932

Pankhurst, R. C., Holder, D. W.
Wind-tunnel technique, 1965, Pitman & Sons Ltd

Parkin, J. H., Klein, G. J.
The interference between the body and wings of aircraft
RAS Paper 229, January 1930

Pepper, P.M.
Minimum induced drag in wing-fuselage interference; NACA TN 812, Sep. 1941

Philips, D. B., Cimbala, J.M., Treaster, A.L.
Suppression of the wing-body junction vortex by body surface suction
Jour. Aircraft, Vol. 29, No. 1, Feb. 1992

Prandtl, L.
Effects of varying relative vertical position of wing and fuselage
NACA TN 75, Dec. 1921

Quereshi, M.
BASIC program listings, 1987

Redecker,G., Ahmed, S.R., Jordan, H.L.
Computation of pressure distribution on the DFVLR wing-body model by the panel method; DFVLR Bericht 80-02, 1980

Ross, J. C., Vogel, J. M., Corsiglia, V. R.
Full-scal wind-tunnel study of wing-fuselage interaction and comparison with paneling method, AIAA Journal Vol. 25, No. 10, Sept. 1982

Sandahl, C.A., Vollo, S.D.
Wind tunnel investigation of the air load distribution on two combinations of lifting surface and fuselage; NACA TN 1295, Feb. 1947

Schlichting, H.
Aerodynamics of the mutual influence of aircraft parts
RAE Library Translation No. 275, 1948

Schlichting, H., Truckenbrodt, E
Aerodynamics of the airplane; McGraw-Hill Book Company; New York, USA, 1979

Schlichting, H., Ludwig, H., Wedemeyer, E.
Auftriebsverteilung an schlanken Flügel- Rumpf- Kombinationen bei abgelöster Strömung; Bereicht 251 73 A 32, Feb. 1974

Shabaka, I. M. M. A., Bradshaw, P.
Turbulent flow measurements on an idealized wing/body junction
AIAA Journal, Vol. 19, No. 2, Feb. 1981

Smelt, M.A. & Smith, A.G. & Smith, F.
The installation of an engine nacelle on a wing; ARC R & M 2406, Nov. 1939

Spreiter, J. R.
Aerodynamic properties of slender wing-body combinations at subsonic, transonic, and supersonic speeds; NACA TN 1662, July 1948

Stanbrook, A.
Experimental Observation of Vortices in Wing-Body Junctions
R.A.E. Report 2589. Nov. 1957

Weber, J., Joyce, M.G.
Interference problems on wing-fuselage combinations in inviscid incompressible flow
RAE TR 74073; RAE TR 69130; RAE TR 71179; RAE TR 73189; RAE TR 73190
(1970-1973)

Wickens, R. H.
Viscous three-dimensional flow separations from high-wing propeller-turbine nacelle models; AGARD CP 1984

Zlotnik, M., Diedrich, F.W.
Theoretical calculation of the effect of the fuselage on the soanwise lift distribution on a wing; NACA RM L51J19

Zlotnik, M., Robinson, S.W.
A simplified mathematical model for calcuating aerodynamic loading and downwash for wing-fuselage combinations woth wings of arbitrary plan form; NACA TN 3057, Nov. 1952

APPENDIX A

```
program confile;

  const
    Title = 'Convert Files';

  var
    infile, outfile :text;
    k           :string[14];    {Character to be read in}
    ch          :char;          {To allow 1char at a time to be read}
    tempstr       :string[10];
    fname         :string[30];    {Current filename }
    a_i         :integer;  {Angle of attack indicated at pos 7 + 8}
    s_i         :integer;  {Spanwise position indicated at pos 5 + 6}
    a_s         :string[6];
    s_s         :string[8];



begin

    writeln('Program running');
    writeln;

    k :='';
    fname := '';

    a_i:=0;
      repeat
        str (a_i,a_s);

        s_i:=0;

        repeat
          str (s_i,s_s);
          if length(s_s) < 2 then s_s:= '0' + s_s;
          if length(a_s) < 2 then a_s:= '0' + a_s;

          fname := 'c:\scratch\fl00' + s_s + a_s;
          writeln('Opening file : ',fname);
          writeln;

          assign(infile, fname + '.txt');
          reset (infile);
          assign (outfile, fname + '.xl');
          rewrite (outfile);
```

13.1 Listing for the conversion of BASIC files into ASCII files

```
        readln(infile,k);  (* Read 1st line comment *)
        writeln(k);
        writeln(outfile,k);

        while not eoln (infile) do  (* now read chars *)
          begin
           tempstr:='';
            repeat
              read (infile,ch);
              if ch <> chr(32) then tempstr:=tempstr + ch;
            until ch = chr (32);
           read (infile,ch);      (* read and scrap 2nd space *)
           writeln (tempstr);
           writeln(outfile,tempstr);
          end;

        writeln ('Closing File : ', fname);
        writeln;

        close (infile);
        close (outfile);

        s_i:=succ(s_i);
      until s_i >0;

      a_i:=a_i+3;

    until a_i >3;

    writeln ('Program Finished');
    writeln;

end.
```

13.1 Listing for the conversion of BASIC files into ASCII files

=SELECT('C:\BASIC\FH00_00.WK1'!$A$49:$A$96)	=SELECT("R673C1:R720C1")
=COPY()	=COPY()
=SELECT("R1C2")	=SELECT("R1C15")
=PASTE()	=PASTE()
=SELECT("R97C1:R144C1")	=SELECT("R721C1:R768C1")
=COPY()	=COPY()
=SELECT("R1C3")	=SELECT("R1C16")
=PASTE()	=PASTE()
=SELECT("R145C1:R192C1")	=SELECT("R769C1:R816c1")
=COPY()	=COPY()
=SELECT("R1C4")	=SELECT("R1C17")
=PASTE()	=PASTE()
=SELECT("R193C1:R240C1")	=SELECT("R817C1:R864C1")
=COPY()	=COPY()
=SELECT("R1C5")	=SELECT("R1C18")
=PASTE()	=PASTE()
=SELECT("R241C1:R288C1")	=SELECT("R865C1:R912C1")
=COPY()	=COPY()
=SELECT("R1C6")	=SELECT("R1C19")
=PASTE()	=PASTE()
=SELECT("R289C1:R336C1")	=SELECT("R913C1:R960C1")
=COPY()	=COPY()
=SELECT("R1C7")	=SELECT("R1C20")
=PASTE()	=PASTE()
=SELECT("R337C1:R384C1")	=SELECT("R961C1:r1008C1")
=COPY()	=COPY()
=SELECT("R1C8")	=SELECT("R1C21")
=PASTE()	=PASTE()
=SELECT("R385C1:R432C1")	=SELECT("R1009C1:R1056C1")
=COPY()	=COPY()
=SELECT("R1C9")	=SELECT("R1C22")
=PASTE()	=PASTE()
=SELECT("R433C1:R480C1")	=SELECT("R1057C1:R1104C1")
=COPY()	=COPY()
=SELECT("R1C10")	=SELECT("R1C23")
=PASTE()	=PASTE()
=SELECT("R481C1:R528C1")	=SELECT("R1105C1:R1152C1")
=COPY()	=COPY()
=SELECT("R1C11")	=SELECT("R1C24")
=PASTE()	=PASTE()
=SELECT("R529C1:r576C1")	=SELECT("R1153C1:R1200C1")
=COPY()	=COPY()
=SELECT("R1C12")	=SELECT("R1C25")
=PASTE()	=PASTE()
=SELECT("R577C1:R624C1")	=SELECT("R1201C1:R1248c1")
=COPY()	=COPY()
=SELECT("R1C13")	=SELECT("R1C26")
=PASTE()	=PASTE()
=SELECT("R625C1:R672C1")	=SELECT("R1249C1:R1296C1")
=COPY()	=COPY()
=SELECT("R1C14")	=SELECT("R1C27")
=PASTE()	=PASTE()

13.2 Listing for the conversion of BASIC data into MS-EXCEL format

```
=SELECT("R1297C1:R1344C1")
=COPY()
=SELECT("R1C28")
=PASTE()
=SELECT("R1345C1:R1392C1")
=COPY()
=SELECT("R1C29")
=PASTE()
=SELECT("R1393C1:R1440C1")
=COPY()
=SELECT("R1C30")
=PASTE()
=SELECT("R1441C1:R1488C1")
=COPY()
=SELECT("R1C31")
=PASTE()
=SELECT("R1489C1:R1536c1")
=COPY()
=SELECT("R1C32")
=PASTE()
=SELECT("R1537C1:R1584C1")
=COPY()
=SELECT("R1C33")
=PASTE()
=SELECT("R1585C1:R1632C1")
=COPY()
=SELECT("R1C34")
=PASTE()
=SELECT("R1633C1:R1680C1")
=COPY()
=SELECT("R1C35")
=PASTE()
=SELECT("R1681C1:R1728C1")
=COPY()
=SELECT("R1C35")
=PASTE()
=SAVE.AS("FH00_00.WK1";5;"";FALSE)
=CLOSE()
=RETURN()
```

13.2 Listing for the conversion of BASIC data into MS-EXCEL format

```
#fm~~~wfx00100~{rt}
#fm~~~wfx00200~{rt}
#fm~~~wfx00300~{rt}
#fm~~~wfx00400~{rt}
#fm~~~wfx00500~{rt}
#fm~~~wfx00600~{rt}
#fm~~~wfx00700~{rt}
#fm~~~wfx00800~{rt}
#fm~~~wfx00900~{rt}
#fitffx01000.xl~{rt}
#fitffx01100.xl~{rt}
#fitffx01200.xl~{rt}
#fitffx01300.xl~{rt}
#fitffx01400.xl~{rt}
#fitffx01500.xl~{rt}
#fitffx01600.xl~{rt}
#fitffx01700.xl~{rt}
#fitffx01800.xl~{rt}
#fitffx01900.xl~{rt}
#fitffx02000.xl~{rt}
#fitffx02100.xl~{rt}
#fitffx02200.xl~{rt}
#fitffx02300.xl~{rt}
#fitffx02400.xl~{rt}
#fitffx02500.xl~{rt}
#fitffx02600.xl~{rt}
#fitffx02700.xl~{rt}
#fitffx02800.xl~{rt}
#fitffx02900.xl~{rt}
#fitffx03000.xl~{rt}
#fitffx03100.xl~{rt}
#fitffx03200.xl~{rt}
#fitffx03300.xl~{rt}
#fitffx03400.xl~{rt}
#fitffx03500.xl~{rt}
#fitffx03600.xl~{rt}
#fitffx03700.xl~{rt}
#fitffx03800.xl~{rt}
```

13.3. Listing for the conversion of RIGTEST files into MS-EXCEL files

```
=FOR.CELL("cell_i";'C:\THESIS\WFX215EX.WK1'!$A$1:$A$47;)
= FORMULA(cell_i/850,322/1,039755;cell_i)
=NEXT()
=FOR.CELL("cell_i";'C:\THESIS\WFX215EX.WK1'!$B$1:$B$47;)
= FORMULA(cell_i/843,281/1,039755;cell_i)
=NEXT()
=FOR.CELL("cell_i";'C:\THESIS\WFX215EX.WK1'!$C$1:$C$47;)
= FORMULA(cell_i/849,434/1,039755;cell_i)
=NEXT()
=FOR.CELL("cell_i";'C:\THESIS\WFX215EX.WK1'!$D$1:$D$47;)
= FORMULA(cell_i/850,938/1,039755;cell_i)
=NEXT()
=FOR.CELL("cell_i";'C:\THESIS\WFX215EX.WK1'!$E$1:$E$47;)
= FORMULA(cell_i/843,691/1,039755;cell_i)
=NEXT()
=FOR.CELL("cell_i";'C:\THESIS\WFX215EX.WK1'!$F$1:$F$47;)
= FORMULA(cell_i/850,186/1,039755;cell_i)
=NEXT()
=FOR.CELL("cell_i";'C:\THESIS\WFX215EX.WK1'!$G$1:$G$47;)
= FORMULA(cell_i/849,912/1,039755;cell_i)
=NEXT()
=FOR.CELL("cell_i";'C:\THESIS\WFX215EX.WK1'!$H$1:$H$47;)
= FORMULA(cell_i/854,15/1,039755;cell_i)
=NEXT()
=FOR.CELL("cell_i";'C:\THESIS\WFX215EX.WK1'!$I$1:$I$47;)
= FORMULA(cell_i/857,5/1,039755;cell_i)
=NEXT()
=FOR.CELL("cell_i";'C:\THESIS\WFX215EX.WK1'!$J$1:$J$47;)
= FORMULA(cell_i/895,508/1,039755;cell_i)
=NEXT()
=FOR.CELL("cell_i";'C:\THESIS\WFX215EX.WK1'!$K$1:$K$47;)
= FORMULA(cell_i/886,211/1,039755;cell_i)
=NEXT()
=FOR.CELL("cell_i";'C:\THESIS\WFX215EX.WK1'!$L$1:$L$47;)
= FORMULA(cell_i/870,967/1,039755;cell_i)
=NEXT()
=FOR.CELL("cell_i";'C:\THESIS\WFX215EX.WK1'!$M$1:$M$47;)
= FORMULA(cell_i/880,674/1,039755;cell_i)
=NEXT()
=FOR.CELL("cell_i";'C:\THESIS\WFX215EX.WK1'!$N$1:$N$47;)
= FORMULA(cell_i/857,842/1,039755;cell_i)
=NEXT()
=FOR.CELL("cell_i";'C:\THESIS\WFX215EX.WK1'!$O$1:$O$47;)
= FORMULA(cell_i/881,289/1,039755;cell_i)
=NEXT()
=FOR.CELL("cell_i";'C:\THESIS\WFX215EX.WK1'!$P$1:$P$47;)
= FORMULA(cell_i/847,451/1,039755;cell_i)
=NEXT()
=FOR.CELL("cell_i";'C:\THESIS\WFX215EX.WK1'!$Q$1:$Q$47;)
= FORMULA(cell_i/893,252/1,039755;cell_i)
=NEXT()
=FOR.CELL("cell_i";'C:\THESIS\WFX215EX.WK1'!$R$1:$R$47;)
= FORMULA(cell_i/860,098/1,039755;cell_i)
=NEXT()
```

13.4 Listing for the calculation of Cp

```
=FOR.CELL("cell_i";'C:\THESIS\WFX215EX.WK1'!$S$1:$S$47;)
= FORMULA(cell_i/885,049/1,039755;cell_i)
=NEXT()
=FOR.CELL("cell_i";'C:\THESIS\WFX215EX.WK1'!$T$1:$T$47;)
= FORMULA(cell_i/900,635/1,039755;cell_i)
=NEXT()
=FOR.CELL("cell_i";'C:\THESIS\WFX215EX.WK1'!$U$1:$U$47;)
= FORMULA(cell_i/878,555/1,039755;cell_i)
=NEXT()
=FOR.CELL("cell_i";'C:\THESIS\WFX215EX.WK1'!$V$1:$V$47;)
= FORMULA(cell_i/877,256/1,039755;cell_i)
=NEXT()
=FOR.CELL("cell_i";'C:\THESIS\WFX215EX.WK1'!$W$1:$W$47;)
= FORMULA(cell_i/869,121/1,039755;cell_i)
=NEXT()
=FOR.CELL("cell_i";'C:\THESIS\WFX215EX.WK1'!$X$1:$X$47;)
= FORMULA(cell_i/873,975/1,039755;cell_i)
=NEXT()
=FOR.CELL("cell_i";'C:\THESIS\WFX215EX.WK1'!$Y$1:$Y$47;)
= FORMULA(cell_i/905,625/1,039755;cell_i)
=NEXT()
=FOR.CELL("cell_i";'C:\THESIS\WFX215EX.WK1'!$Z$1:$Z$47;)
= FORMULA(cell_i/867,891/1,039755;cell_i)
=NEXT()
=FOR.CELL("cell_i";'C:\THESIS\WFX215EX.WK1'!$AA$1:$AA$47;)
= FORMULA(cell_i/869,463/1,039755;cell_i)
=NEXT()
=FOR.CELL("cell_i";'C:\THESIS\WFX215EX.WK1'!$AB$1:$AB$47;)
= FORMULA(cell_i/859,346/1,039755;cell_i)
=NEXT()
=FOR.CELL("cell_i";'C:\THESIS\WFX215EX.WK1'!$AC$1:$AC$47;)
= FORMULA(cell_i/883,818/1,039755;cell_i)
=NEXT()
=FOR.CELL("cell_i";'C:\THESIS\WFX215EX.WK1'!$AD$1:$AD$47;)
= FORMULA(cell_i/899,062/1,039755;cell_i)
=NEXT()
=FOR.CELL("cell_i";'C:\THESIS\WFX215EX.WK1'!$AE$1:$AE$47;)
= FORMULA(cell_i/890,312/1,039755;cell_i)
=NEXT()
=FOR.CELL("cell_i";'C:\THESIS\WFX215EX.WK1'!$AF$1:$AF$47;)
= FORMULA(cell_i/905,967/1,039755;cell_i)
=NEXT()
=FOR.CELL("cell_i";'C:\THESIS\WFX215EX.WK1'!$AG$1:$AG$47;)
= FORMULA(cell_i/886,348/1,039755;cell_i)
=NEXT()
=FOR.CELL("cell_i";'C:\THESIS\WFX215EX.WK1'!$AH$1:$AH$47;)
= FORMULA(cell_i/881,494/1,039755;cell_i)
=NEXT()
=FOR.CELL("cell_i";'C:\THESIS\WFX215EX.WK1'!$AI$1:$AI$47;)
= FORMULA(cell_i/879,854/1,039755;cell_i)
=NEXT()
=FOR.CELL("cell_i";'C:\THESIS\WFX215EX.WK1'!$AJ$1:$AJ$47;)
= FORMULA(cell_i/893,73/1,039755;cell_i)
=NEXT()
```

13.4 Listing for the calculation of Cp

```
=FOR.CELL("cell_i";'C:\THESIS\WFX215EX.WK1'!$AK$1:$AK$47;)
= FORMULA(cell_i/887,92/1,039755;cell_i)
=NEXT()
=FOR.CELL("cell_i";'C:\THESIS\WFX215EX.WK1'!$AL$1:$AL$47;)
= FORMULA(cell_i/878,691/1,039755;cell_i)
=NEXT()
=RETURN()
```

13.4 Listing for the calculation of Cp

```
=OPEN("WFX315EX.WK1")
=SELECT("R1C1")
=INSERT(4)
=SELECT("R2C1")
=FORMULA("1")
=SELECT("R2C1:R47C1")
=DATA.SERIES(2;1;1;1)
=SELECT("R1C2")
=FORMULA("1")
=SELECT("R1C2:R1C39")
=DATA.SERIES(1;1;1;1)
=SELECT("R10C17:R14C17,R4C18:R22C18";"R4C18")
=SELECT("R10C17:R14C17,R4C18:R22C18,R2C19:R28C31";"R2C19")
=SELECT("R10C17:R14C17,R4C18:R22C18,R2C19:R28C31,R3C32:R22C32";"R3C32")
=CLEAR(3)
=SELECT("R23C1:R47C39")
=COPY()
=NEW(1)
=PASTE()
=SAVE.AS("WFL315GT.WK1";5;"";FALSE)
=CLOSE()
=CLEAR(3)
=SAVE.AS("wfu315gt.WK1";5;"";FALSE)
=CLOSE()
=RETURN()
```

13.5 Listing for the separation of the data for the upper and lower wing surface

=OPEN("WFL000HW.DIF")	=SELECT("R2C1:R26C1";"R19C1")
=SELECT("R1C1:R38C25")	=FORMULA("0.8")
=COPY()	=SELECT("R2C1:R26C1";"R20C1")
=SELECT("R40C1")	=FORMULA("0.85")
=PASTE.SPECIAL(3;1;FALSE;TRUE)	=SELECT("R2C1:R26C1";"R21C1")
=COPY()	=FORMULA("0.85")
=SELECT("R1C1")	=SELECT("R2C1:R26C1";"R22C1")
=PASTE()	=FORMULA("0.875")
=SELECT("R31C1:R64C38")	=SELECT("R2C1:R26C1";"R23C1")
=CLEAR(3)	=FORMULA("0.9")
=SELECT("R1C1")	=SELECT("R2C1:R26C1";"R24C1")
=INSERT(3)	=FORMULA("0.925")
=INSERT(4)	=SELECT("R2C1:R26C1";"R25C1")
=SELECT("R2C1:R26C1")	=FORMULA("0.95")
=FORMULA("0.002")	=SELECT("R2C1:R26C1";"R26C1")
=SELECT("R2C1:R26C1";"R3C1")	=FORMULA("0.975")
=FORMULA("0.009")	=SELECT("R2C1:R26C1")
=SELECT("R2C1:R26C1";"R4C1")	=SELECT("R21C1")
=FORMULA("0.02")	=FORMULA("0.825")
=SELECT("R2C1:R26C1";"R5C1")	=SELECT("R1C2:R1C39")
=FORMULA("0.034")	=DATA.SERIES(1;1;1;1)
=SELECT("R2C1:R26C1";"R6C1")	=FORMULA("1")
=FORMULA("0.05")	=SELECT("R1C2:R1C39";"R1C3")
=SELECT("R2C1:R26C1";"R7C1")	=DATA.SERIES(1;1;1;1)
=FORMULA("0.075")	=SAVE.AS("WFL000HW.WK1";5;"";FALSE
=SELECT("R2C1:R26C1";"R8C1")	=CLOSE()
=FORMULA("0.1")	=RETURN()
=SELECT("R2C1:R26C1";"R9C1")	
=FORMULA("0.15")	
=SELECT("R2C1:R26C1";"R10C1")	
=FORMULA("0.2")	
=SELECT("R2C1:R26C1";"R11C1")	
=FORMULA("0.25")	
=SELECT("R2C1:R26C1";"R12C1")	
=FORMULA("0.35")	
=SELECT("R2C1:R26C1";"R13C1")	
=FORMULA("0.45")	
=SELECT("R2C1:R26C1";"R14C1")	
=FORMULA("0.55")	
=SELECT("R2C1:R26C1";"R15C1")	
=FORMULA("0.6")	
=SELECT("R2C1:R26C1";"R16C1")	
=FORMULA("0.65")	
=SELECT("R2C1:R26C1";"R17C1")	
=FORMULA("0.7")	
=SELECT("R2C1:R26C1";"R18C1")	
=FORMULA("0.75")	

13.6 Listing for the insertion of the coordinates on the wing files

```
=OPEN("FFX206LS.WK1")
=SELECT("R1C1")
=INSERT(3)
=FORMULA("190")
=SELECT("R1C1:R1C8")
=DATA.SERIES(1;1;1;10;260)
=SELECT("R1C9")
=FORMULA("100")
=SELECT("R1C9:R1C17")
=DATA.SERIES(1;1;1;10)
=SELECT("R15C1")
=INSERT(4)
=SELECT("R2C1:R12C1,R13C1";"R13C1")
=FORMULA("")
=SELECT("R2C1:R13C1")
=FORMULA("0.004")
=SELECT("R2C1:R13C1";"R3C1")
=FORMULA("0.09")
=SELECT("R2C1:R13C1";"R4C1")
=FORMULA("0.16")
=SELECT("R2C1:R13C1";"R5C1")
=FORMULA("0.21")
=SELECT("R2C1:R13C1";"R6C1")
=FORMULA("0.28")
=SELECT("R2C1:R13C1";"R7C1")
=FORMULA("0.4")
=SELECT("R2C1:R13C1";"R8C1")
=FORMULA("0.52")
=SELECT("R2C1:R13C1";"R9C1")
=FORMULA("0.64")
=SELECT("R2C1:R13C1";"R10C1")
=FORMULA("0.76")
=SELECT("R2C1:R13C1";"R11C1")
=FORMULA("0.85")
=SELECT("R2C1:R13C1";"R12C1")
=FORMULA("0.9")
=SELECT("R2C1:R13C1";"R13C1")
=FORMULA("0.95")
=SELECT("R15C2:R26C2")
=FORMULA("=6.35*(R[-13]C+R[-12]C)")
=SELECT("R15C2:R26C2";"R16C2")
=FORMULA("=8.89*(R[-13]C+R[-12]C)")
=SELECT("R15C2:R26C2";"R17C2")
=FORMULA("=6.35*(R[-13]C+R[-12]C)")
=SELECT("R15C2:R26C2";"R18C2")
=FORMULA("8.89*(b5+b6)")
=SELECT("R18C2")
=FORMULA("=8.89*(R[-13]C+R[-12]C)")
=SELECT("R19C2")
=FORMULA("=15.24*(R[-13]C+2*(R[-12]C+R[-11]C+R[-10]C)+R[-9]C)")
=SELECT("R20C2")
=FORMULA("=11.43*(R[-10]C*R[-9]C)")
```

13.7 Listing for the chordwise calculation of the lift over the fuselage and insertion of coordinates

```
=SELECT("R20C2")
=FORMULA("=11.43*(R[-10]C+R[-9]C)")
=SELECT("R21C2")
=FORMULA("=6.35*(R[-10]C+2*R[-9]C+R[-8]C)")
=SELECT("R15C2:R21C18")
=FILL.RIGHT()
=SELECT("R23C2")
=FORMULA("=SUM(R[-8]C,R[-7]C,R[-6]C,R[-5]C,R[-4]C,R[-3]C,R[-2]C)")
=SELECT("R23C2:R23C18")
=FILL.RIGHT()
=COPY()
=NEW(1)
=PASTE.LINK()
=SAVE.AS("FFX206LC.WK1";5;"";FALSE)
=CLOSE()
=SAVE.AS("FFX206LS.WK1";5;"";FALSE)
=CLOSE()
=RETURN()
```

13.7 Listing for the chordwise calculation of the lift over the fuselage and insertion of coordinates

```
=OPEN("WFLX15LW.WK1")
=SELECT("R8C19:R11C19,R13C19:R14C19,R16C19,R18C19";"R18C19")
=COPY()
=OPEN("FWXX15LW.WK1")
=SELECT("R19C14")
=PASTE()
=ACTIVATE("WFLX15LW.WK1")
=SELECT("R8C21:R11C29")
=SELECT("R8C21:R11C29,R13C21:R14C29";"R13C21")
=SELECT("R8C21:R11C29,R13C21:R14C29,R16C21:R16C29";"R16C21")
=SELECT("R8C21:R11C29,R13C21:R14C29,R16C21:R16C29,R18C21:R18C29";"R18C21")
=SELECT("R8C21:R11C29,R13C21:R14C29,R16C21:R16C29,R18C21:R18C29,R21C21:R21C29";"R21C21")
=SELECT("R8C21:R11C29,R13C21:R14C29,R16C21:R16C29,R18C21:R18C29,R21C21:R21C29,R23C21:R23C29";"R23C21")
=SELECT("R8C21:R11C29,R13C21:R14C29,R16C21:R16C29,R18C21:R18C29,R21C21:R21C29,R23C21:R23C29,R25C21:R25C29";"R25C21")
=COPY()
=ACTIVATE("FWXX15LW.WK1")
=SELECT("R19C16")
=PASTE.LINK()
=ACTIVATE("WFLX15LW.WK1")
=SELECT("R8C31:R11C31,R13C31:R14C31,R16C31,R18C31";"R18C31")
=COPY()
=ACTIVATE("FWXX15LW.WK1")
=SELECT("R19C26")
=PASTE.LINK()
=SAVE.AS("FWXX15LW.WK1";5;"";FALSE)
=CLOSE()
=CLOSE()
=RETURN()
```

13.8 Listing for the insertion of wing data into fuselage files

=OPEN("FWXx15hw.WK1")	=ACTIVATE("WWL015hw.WK1")
=SELECT("R17C13:R17C25")	=SELECT("R20C19")
=COPY()	=PASTE()
=OPEN("WWL015hw.WK1")	=ACTIVATE("FWXx15hw.WK1")
=SELECT("R4C19")	=SELECT("R27C13:R27C25")
=PASTE()	=COPY()
=ACTIVATE("FWXx15hw.WK1")	=ACTIVATE("WWL015hw.WK1")
=SELECT("R18C13:R18C25")	=SELECT("R22C19")
=COPY()	=PASTE()
=ACTIVATE("WWL015hw.WK1")	=ACTIVATE("FWXx15hw.WK1")
=SELECT("R7C19")	=SELECT("R28C13:R28C25")
=PASTE()	=COPY()
=ACTIVATE("FWXx15hw.WK1")	=ACTIVATE("WWL015hw.WK1")
=SELECT("R19C13:R19C25")	=SELECT("R24c19")
=COPY()	=PASTE()
=ACTIVATE("WWL015hw.WK1")	=SAVE.AS("WWL015hw.WK1";5;"";FALSE)
=ACTIVATE("FWXx15hw.WK1")	=CLOSE()
=SELECT("R18C13:R22C25")	=CLOSE()
=COPY()	=RETURN()
=ACTIVATE("WWL015hw.WK1")	
=SELECT("R7C19")	
=PASTE()	
=ACTIVATE("FWXx15hw.WK1")	
=SELECT("R23C13:R23C25")	
=COPY()	
=ACTIVATE("WWL015hw.WK1")	
=SELECT("R13C19")	
=PASTE()	
=ACTIVATE("FWXx15hw.WK1")	
=SELECT("R24C13:R24C25")	
=COPY()	
=ACTIVATE("WWL015hw.WK1")	
=SELECT("R15C19")	
=PASTE()	
=ACTIVATE("FWXx15hw.WK1")	
=SELECT("R25C13:R25C25")	
=COPY()	
=ACTIVATE("WWL015hw.WK1")	
=SELECT("R17C19")	
=PASTE()	
=ACTIVATE("FWXx15hw.WK1")	
=SELECT("R26C13:R26C25")	
=COPY()	

13.9 Listing for the insertion of fuselage data into wing files

=OPEN("wfl212lw.WK1")	=OPEN("wfd212lw.WK1")
=SELECT("r27c1:r36c39")	=SELECT("R19")
=CLEAR()	=EDIT.DELETE(2)
=OPEN("wfu212lw.WK1")	=SELECT("R20")
=SELECT("R2c1:R22C39")	=EDIT.DELETE(2)
=COPY()	=SELECT("R21")
=ACTIVATE("wfl212lw.WK1")	=EDIT.DELETE(2)
=SELECT("R27C1")	=SELECT("r22")
=PASTE()	=EDIT.DELETE(2)
=SELECT("R47C1:R47C39")	=SELECT("r1")
=CUT()	=INSERT(3)
=SELECT("R50C1")	=OPEN("WFX1H0HC.WK1")
=PASTE()	=SELECT("R1C1:R38C1")
=SELECT("R46C1:R46C39")	=COPY()
=CUT()	=ACTIVATE("wfd212lw.WK1")
=SELECT("R48C1")	=SELECT("R1C2:R1C39")
=PASTE()	=PASTE.SPECIAL(1;1;FALSE;TRUE)
=SELECT("R45C1:R45C39")	=SAVE.AS("wfd212lw.WK1";5;"";FALSE)
=CUT()	=CLOSE()
=SELECT("R46C1")	=CLOSE()
=PASTE()	=RETURN()
=SELECT("R53C2")	
=FORMULA("=R[-52]C-R[-26]C")	
=SELECT("R53C2:R53C39")	
=FILL.RIGHT()	
=SELECT("R53C2:R79C39")	
=FILL.DOWN()	
=SELECT("R27C1:R52C1")	
=COPY()	
=SELECT("R53C1")	
=PASTE()	
=SELECT("R53C1:R77C39")	
=COPY()	
=NEW(1)	
=PASTE.LINK()	
=SAVE.AS("wfd212lw.WK1";5;"";FALSE)	
=CLOSE()	
=CLOSE()	
=CLOSE()	

13.10 Listing for the calculation of the pressure difference on the wing

Calculation of the lift on the upper wing surface

```
=OPEN("wfu300lW.WK1")
=SELECT("R24C2")
=FORMULA("=(0.889*(R[-22]C+R[-21]C))")
=SELECT("R25C2")
=FORMULA("=1.397*(R[-22]C+R[-21]C)")
=SELECT("R26C2")
=FORMULA("=1.778*(R[-22]C+R[-21]C)")
=SELECT("R27C2")
=FORMULA("=2.032*(R[-22]C+R[-21]C)")
=SELECT("R28C2")
=FORMULA("=3.175*(R[-22]C+2*R[-21]C+R[-20]C)")
=SELECT("R29C2")
=FORMULA("=6.35*(R[-21]C+2*(R[-20]C+R[-19]C)+R[-18]C)")
=SELECT("R30C2")
=FORMULA("=12.7*(R[-19]C+2*(R[-18]C+R[-17]C)+R[-16]C)")
=SELECT("R31C2")
=FORMULA("=6.35*(R[-17]C+2*(R[-16]C+R[-15]C+R[-14]C+R[-13]C+R[-12]C+R[-11]C+R[-10]C)+R[-9]C)")
=SELECT("R33C2")
=FORMULA("=SUM(R[-9]C,R[-8]C,R[-7]C,R[-6]C,R[-5]C,R[-4]C,R[-3]C,R[-2]C)")
=SELECT("R24C2:R33C18,r24c32:r33c39")
=FILL.RIGHT()
=SELECT("R24C19")
=FORMULA("=6.35*(R[-19]C+R[-16]C)")
=SELECT("R25C19")
=FORMULA("=8.89*(R[-17]C+R[-16]C)")
=SELECT("R26C19")
=FORMULA("=6.35*(R[-17]C+R[-16]C)")
=SELECT("R27C19")
```

13.11 Listing for the lift calculation on the wing surface

```
=FORMULA("=8.89*(R[-17]C+R[-16]C)")
=SELECT("R28C19")
=FORMULA("=15.24*(R[-17]C+2*(R[-16]C+R[-14]C+R[-12]C)+R[-10]C)")
=SELECT("R29C19")
=FORMULA("=11.43*(R[-11]C+R[-9]C)")
=SELECT("R30C19")
=FORMULA("=6.35*(R[-10]C+2*R[-9]C+R[-8]C)")
=SELECT("R33C19")
=FORMULA("=SUM(R[-9]C,R[-8]C,R[-7]C,R[-6]C,R[-5]C,R[-4]C,R[-3]C,R[-2]C)")
=SELECT("R24C19:R33C31")
=FILL.RIGHT()
=SELECT("r24c2:r33c39")
=COPY()
=NEW(1)
=PASTE.LINK()
=SAVE.AS("wfu300ll.WK1";5;"";FALSE)
=CLOSE()
=CLOSE()
=RETURN()
```

Calculation of the lift on the lower wing surface

```
=OPEN("wwl003hw.WK1")
=SELECT("R27C2")
=FORMULA("=0.889*(R[-26]C+R[-25]C)")
=SELECT("R28C2")
=FORMULA("=1.397*(R[-26]C+R[-25]C)")
```

13.11 Listing for the lift calculation on the wing surface

```
=SELECT("R29C2")
=FORMULA("=1.778*(R[-26]C+R[-25]C)")
=SELECT("R30C2")
=FORMULA("=2.032*(R[-26]C+R[-25]C)")
=SELECT("R31C2")
=FORMULA("=3.175*(R[-26]C+2*R[-25]C+R[-24]C)")
=SELECT("R32C2")
=FORMULA("=6.35*(R[-25]C+2*(R[-24]C+R[-23]C)+R[-22]C)")
=SELECT("R33C2")
=FORMULA("=12.7*(R[-23]C+2*(R[-22]C+R[-21]C)+R[-20]C)")
=SELECT("R34C2")
=FORMULA("=6.35*(R[-21]C+2*(R[-20]C+R[-19]C+R[-18]C+R[-17]C+R[-16]C+R[-14]C+R[-12]C)+R[-10]C)")
=SELECT("R36C2")
=FORMULA("=SUM(R[-9]C,R[-8]C,R[-7]C,R[-6]C,R[-5]C,R[-4]C,R[-3]C,R[-2]C)")
=SELECT("R27C2:R36C39")
=FILL.RIGHT()
=COPY()
=NEW(1)
=PASTE.LINK()
=SAVE.AS("wwl003hl.WK1";5;"";FALSE)
=CLOSE()
=CLOSE()
=RETURN()
```

13.11 Listing for the lift calculation on the wing surface

```
=OPEN("Fwxx15HW.WK1")
=SELECT("R51C2")
=FORMULA("=21.39/2*(R[-49]C+R[-49]C[1])")
=SELECT("R51C3")
=FORMULA("=20.06/2*(R[-49]C+R[-49]C[1])")
=SELECT("R51C4")
=FORMULA("=18.13/2*(R[-49]C+R[-49]C[1])")
=SELECT("R51C5")
=FORMULA("=15.66/2*(R[-49]C+R[-49]C[1])")
=SELECT("R51C6")
=FORMULA("=12.71/2*(R[-49]C+R[-49]C[1])")
=SELECT("R51C7")
=FORMULA("=9.34/2*(R[-49]C+R[-49]C[1])")
=SELECT("R51C8")
=FORMULA("=5.73/2*(R[-49]C+R[-49]C[1])")
=SELECT("R51C9")
=FORMULA("=1.93/2*(R[-49]C+R[-49]C[1])")
=SELECT("R51C10")
=FORMULA("=1.93/2*(R[-49]C+R[-49]C[1])")
=SELECT("R51C11")
=FORMULA("=5.73/2*(R[-49]C+R[-49]C[1])")
=SELECT("R51C12")
=FORMULA("=9.34/2*(R[-49]C+R[-49]C[1])")
=SELECT("R51C13")
=FORMULA("=12.71/2*(R[-49]C+R[-49]C[1])")
=SELECT("R51C14")
=FORMULA("=15.66/2*(R[-49]C+R[-49]C[1])")
=SELECT("R51C15")
=FORMULA("=18.13/2*(R[-49]C+R[-49]C[1])")
=SELECT("R51C16")
=FORMULA("=20.06/2*(R[-49]C+R[-49]C[-1])")
=SELECT("R51C16")
=FORMULA("=20.06/2*(R[-49]C+R[-49]C[1])")
=SELECT("R51C17")
=FORMULA("=21.29/2*(R[-49]C+R[-49]C[1])")
=SELECT("R51C18")
=FORMULA("=22.05/2*(R[-49]C+R[-49]C[1])")
=SELECT("R51C19")
=FORMULA("=22.05/2*(R[-49]C+R[-49]C[1])")
=SELECT("R51C20")
=FORMULA("=21.39/2*(R[-49]C+R[-49]C[1])")
=SELECT("R51C21")
=FORMULA("=20.06/2*(R[-49]C+R[-49]C[1])")
=SELECT("R51C22")
=FORMULA("=18.13/2*(R[-49]C+R[-49]C[1])")
=SELECT("R51C23")
=FORMULA("=15.66/2*(R[-49]C+R[-49]C[1])")
=SELECT("R51C24")
=FORMULA("=12.71/2*(R[-49]C+R[-49]C[1])")
=SELECT("R51C25")
=FORMULA("=9.34/2*(R[-49]C+R[-49]C[1])")
=SELECT("R51C26")
=FORMULA("=5.73/2*(R[-49]C+R[-49]C[1])")
=SELECT("R51C27")
```

13.12 Listing for the lift calculation over the fuselage

```
=FORMULA("=1.93/2*(R[-49]C+R[-49]C[1])")
=SELECT("R51C28")
=FORMULA("=1.93/2*(R[-49]C+R[-49]C[1])")
=SELECT("R51C29")
=FORMULA("=5.73/2*(R[-49]C+R[-49]C[1])")
=SELECT("R51C30")
=FORMULA("=9.34/2*(R[-49]C+R[-49]C[1])")
=SELECT("R51C31")
=FORMULA("=12.71/2*(R[-49]C+R[-49]C[1])")
=SELECT("R51C32")
=FORMULA("=15.66/2*(R[-49]C+R[-49]C[1])")
=SELECT("R51C33")
=FORMULA("=18.13/2*(R[-49]C+R[-49]C[1])")
=SELECT("R51C34")
=FORMULA("=20.06/2*(R[-49]C+R[-49]C[1])")
=SELECT("R51C35")
=FORMULA("=21.39/2*(R[-49]C+R[-49]C[1])")
=SELECT("R51C36")
=FORMULA("=22.05/2*(R[-49]C+R[-49]C[1])")
=SELECT("R51C37")
=FORMULA("=22.05/2*(R[-49]C+R[-49]C[-35])")
=SELECT("R51C2:R98C37")
=FILL.DOWN()
=COPY()
=NEW(1)
=PASTE.LINK()
=SELECT("R1C38")
=CANCEL.COPY()
=FORMULA("=RC[-29]+RC[-28]+RC[-26]+RC[-25]+RC[-24]+RC[-23]+RC[-22]+RC[-21]+RC[-
=SELECT("R1C39")
=FORMULA("=RC[-38]+RC[-37]+RC[-36]+RC[-35]+RC[-34]+RC[-33]+RC[-32]+RC[-31]+RC[-
=SELECT("R1C40")
=FORMULA("=(RC[-2]-RC[-1])/254")
=SELECT("R1C38:R48C40")
=FILL.DOWN()
=SELECT("R1C40:R48C40")
=COPY()
=NEW(1)
=PASTE.LINK()
=SAVE.AS("Fwxxh5LC.WK1";5;"";FALSE)
=CLOSE()
=SAVE.AS("Fwxxh5LL.WK1";5;"";FALSE)
=CLOSE()
=SAVE.AS("Fwxx15HW.WK1";5;"";FALSE)
=CLOSE()
=RETURN()
```

13.12 Listing for the lift calculation over the fuselage

PRESSURE DISTRIBUTION ON WING-BODY-FLAP CONFIGURATIONS AT SUBSONIC SPEED

submitted by Uwe Bitomsky

for the degree of PhD

of the University of Bath

1993.

VOLUME 2

Copyright

1. LIST OF TABLES

2. LIST OF FIGURES

Tapping	x/d	
1	-3.1	
2	-3.06	
3	-3.0	
4	-2.92	
5	-2.72	
6	-2.65	
7	-2.35	
8	-2.05	
9	-1.75	
10	-1.45	
11	-0.85	
12	-0.55	
13	-0.25	
14	-0.1	
15	-0.001	Leading edge of the wing
16	0.004	
17	0.09	
18	0.16	
19	0.21	
20	0.27	
21	0.4	
22	0.52	
23	0.64	
24	0.76	
25	0.85	
26	0.9	
27	0.95	
28	1.0	Trailing edge of the wing

Tapping	x/d
29	1.05
30	1.1
31	1.15
32	1.2
36	1.6
37	1.9
38	2.2
39	2.5
40	2.8
41	3.1
42	3.4
43	3.7
44	4.0
45	4.3
46	4.5
47	4.7
48	4.8

Table 2.1 Pressure tappings along the fuselage

Tapping	y/c	
1	-2.5	
2	-2.375	
3	-2.25	
4	-2.0	
5	-1.75	
6	-1.5	
7	-1.25	
8	-1.05	
9	-0.85	
10	-0.75	
11	-0.65	
12	-0.6	
13	-0.55	
14	-0.525	
15	-0.5	
16	-0.4924	
17	-0.4698	
18	-0.433	Edge of the area partly covered by the fuselage
19	-0.383	
20	-0.3214	
21	-0.25	
22	-0.171	
23	-0.0868	
24	0	Centreline of the wing and fuselage
25	0.0868	
26	0.171	
27	0.25	
28	0.3214	
29	0.383	
30	0.433	Edge of the area partly covered by the fuselage
31	0.4698	
32	0.4924	
33	0.5	
34	0.65	
35	1.05	
36	1.5	
37	2.0	
38	2.375	

Table 2.2 Spanwise location of pressure tappings on the wing

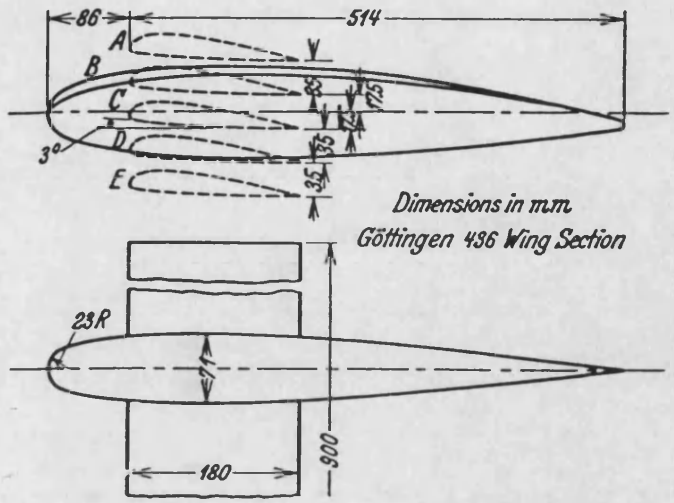

Various wing position tested by Prandtl (1920)

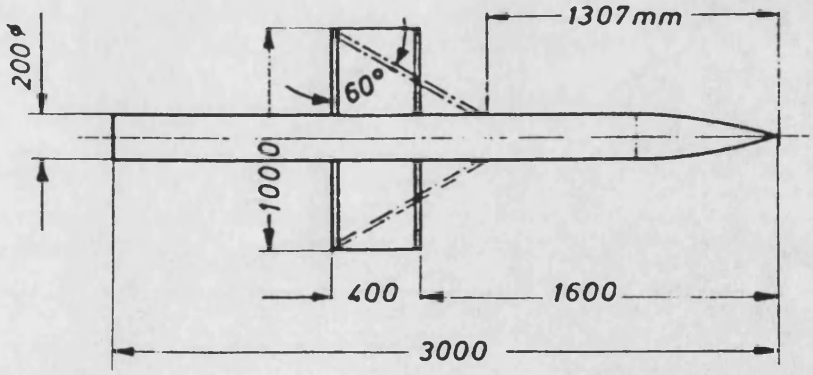

Fuselage model with and without wings tested by Grosche (1972)

Fig. 1.1 Models of Grosche and Prandtl

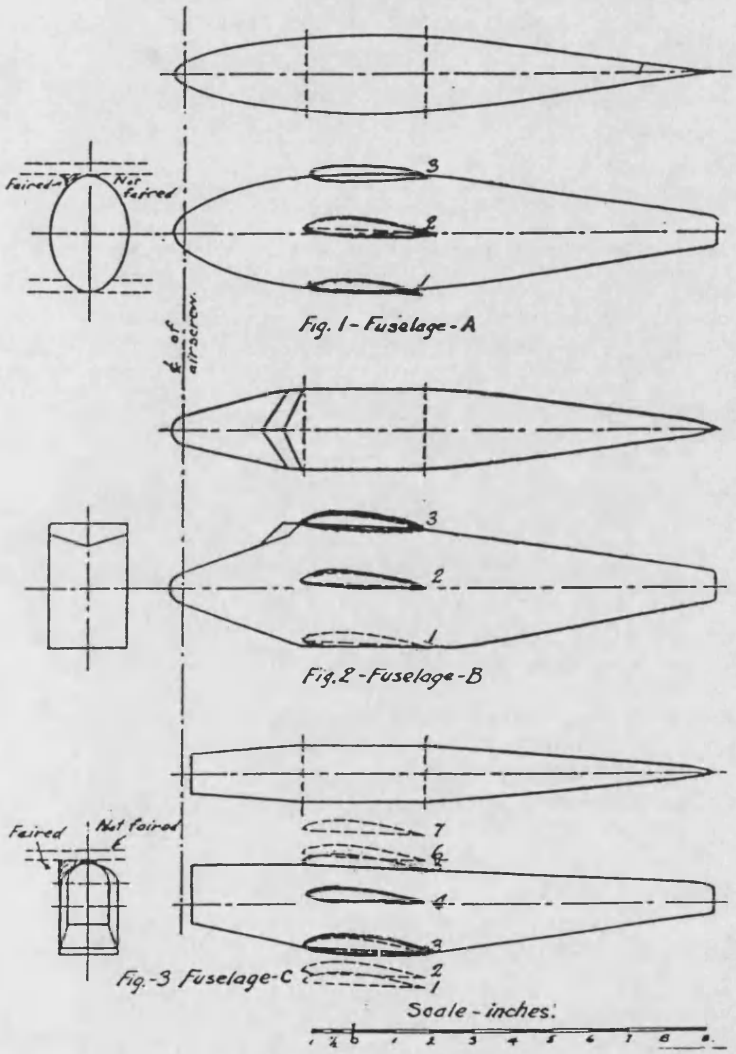

Fig. 1.2 Models of various fuselage shapes tested by Parkin and Klein (1935)

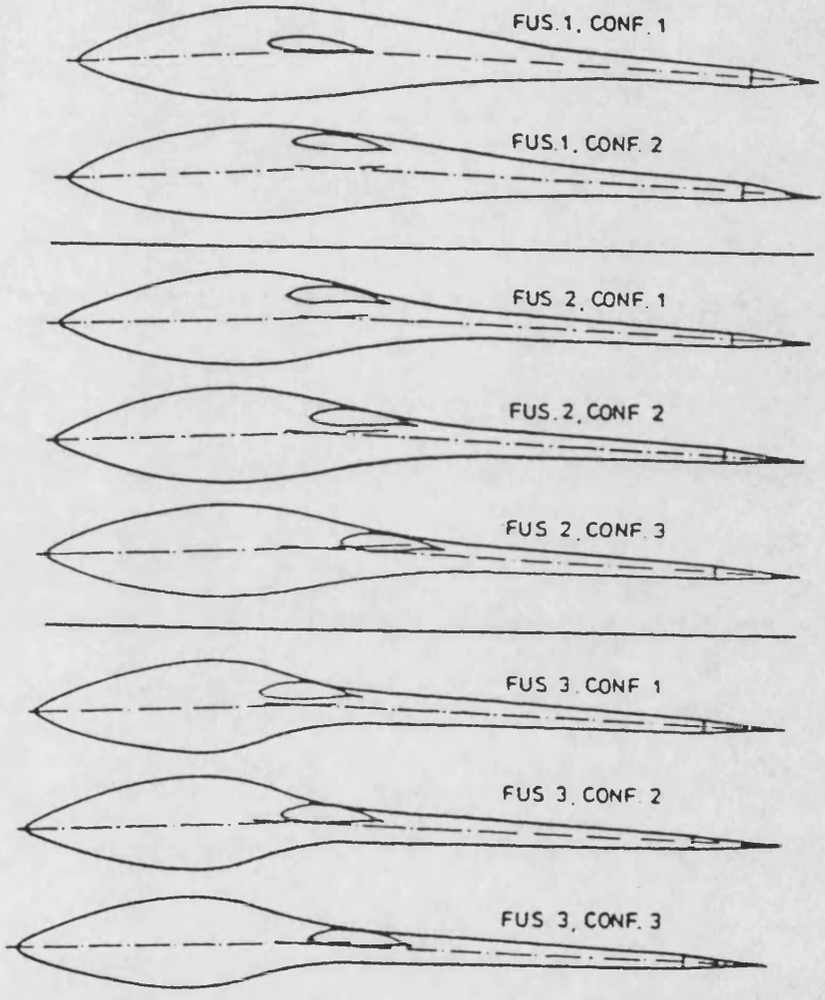

Fig. 1.3 Models of various fuselage shapes, after Boermans (1983)

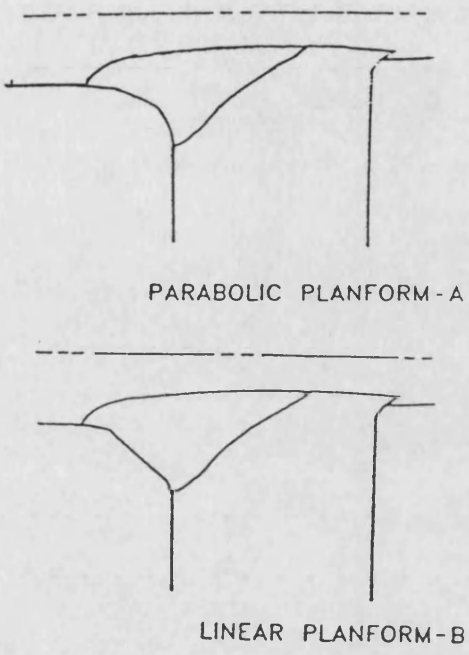

Wing fillet of two planforms tested by Maughmer (1984)

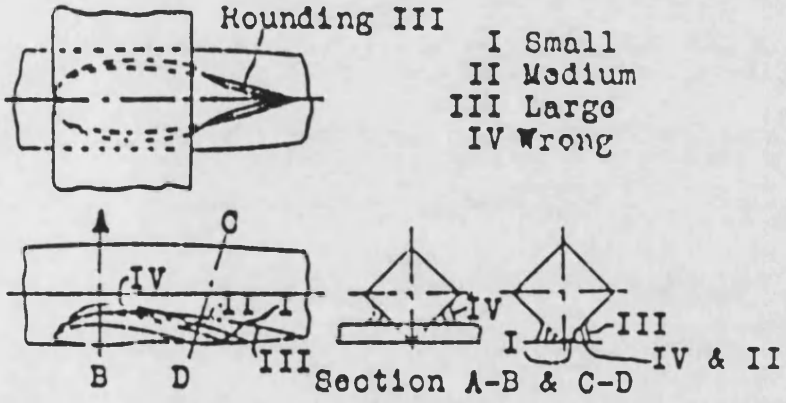

Various fairing shapes tested by Muttray (1928)

Fig. 1.4 Models of Maughmer and Muttray

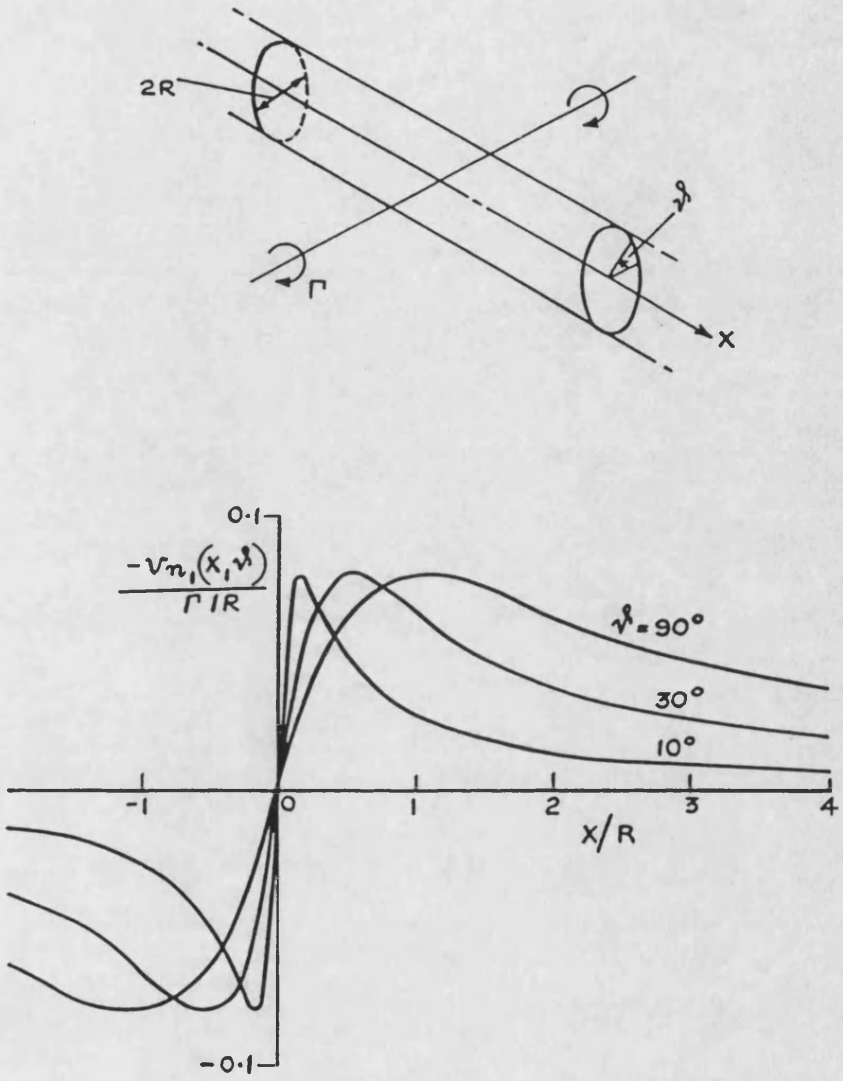

Fig. 1.5 Lifting line, and induced normal velocity distribution on the fuselage, after Weber (1969)

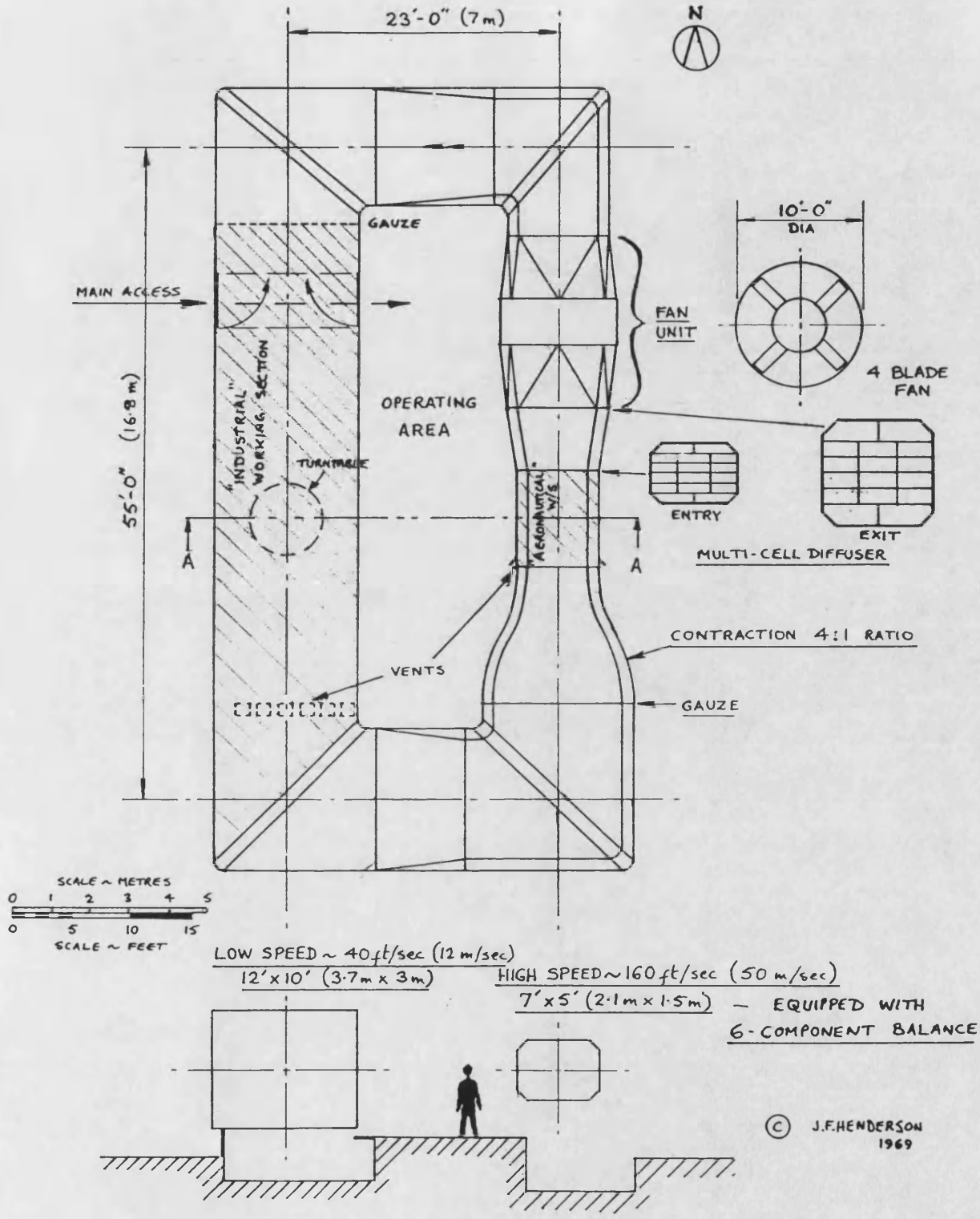

SECTION A-A SHOWING THE TWO WORKING SECTIONS, EITHER OF WHICH MAY BE OPERATED AT AMBIENT PRESSURE, AS REQUIRED

Fig. 2.1 **Layout of the large dual purpose wind tunnel, School of Mechanical Engineering, University of Bath**

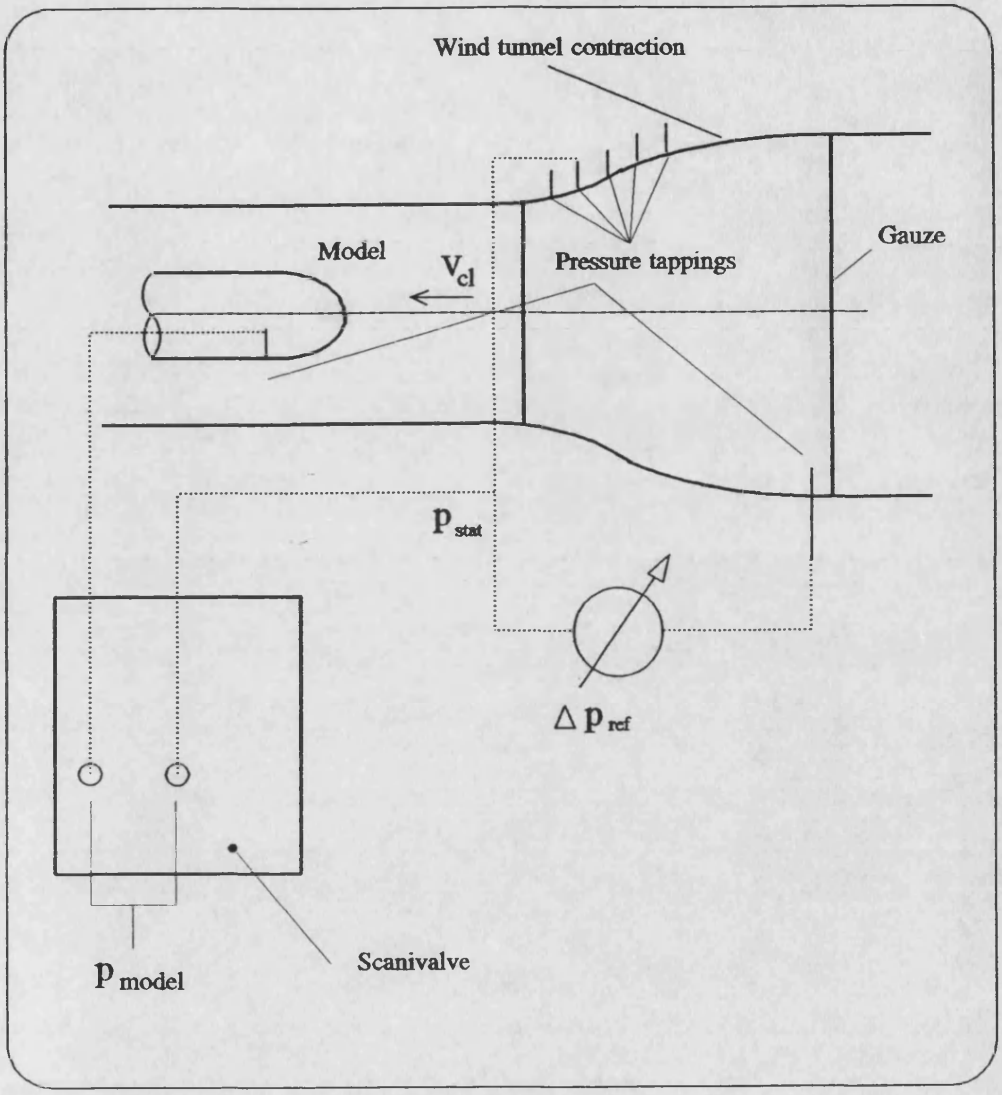

Fig. 2.2 Pressure tappings in the wind tunnel

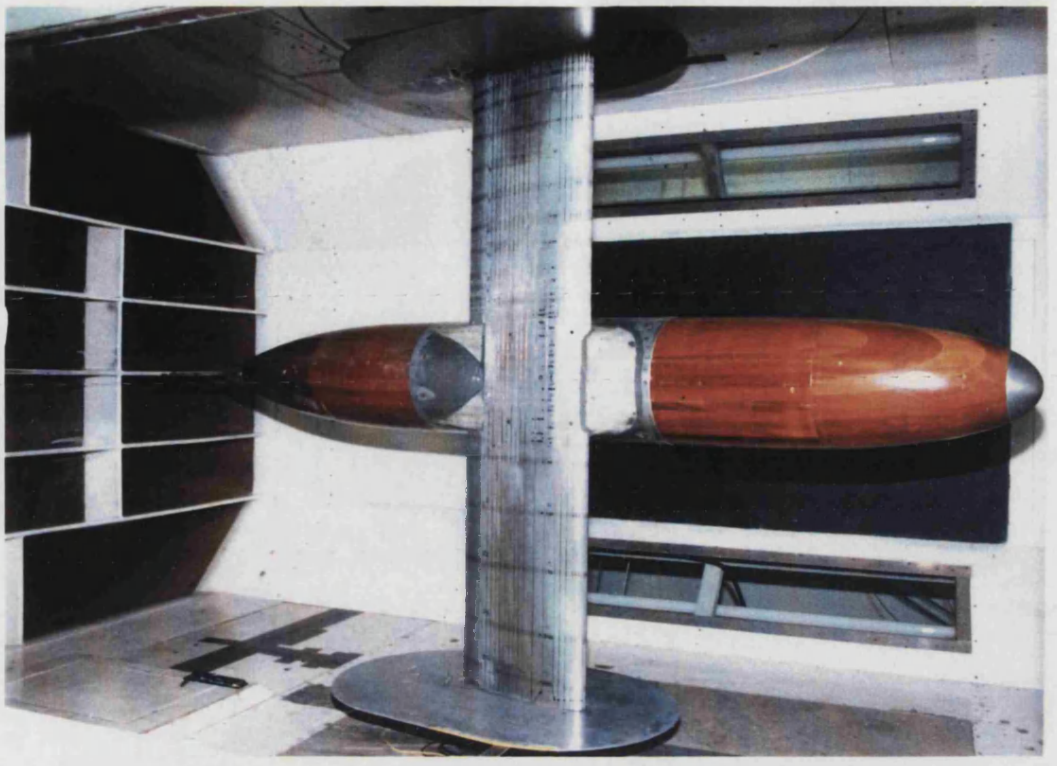

Fig. 2.3 High wing model in the wind tunnel

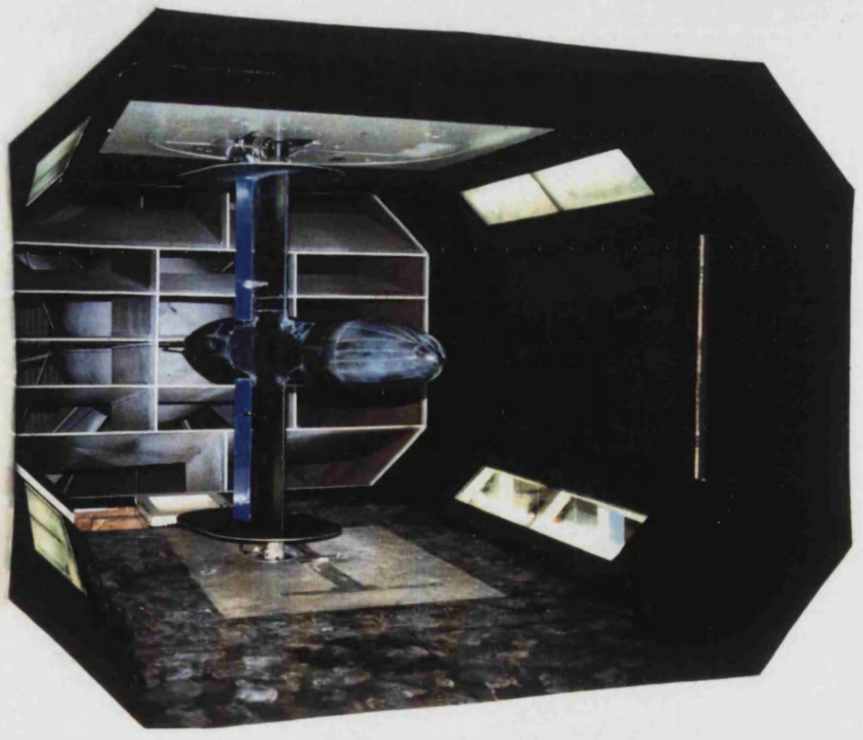

Fig. 2.4 Low wing model in the wind tunnel

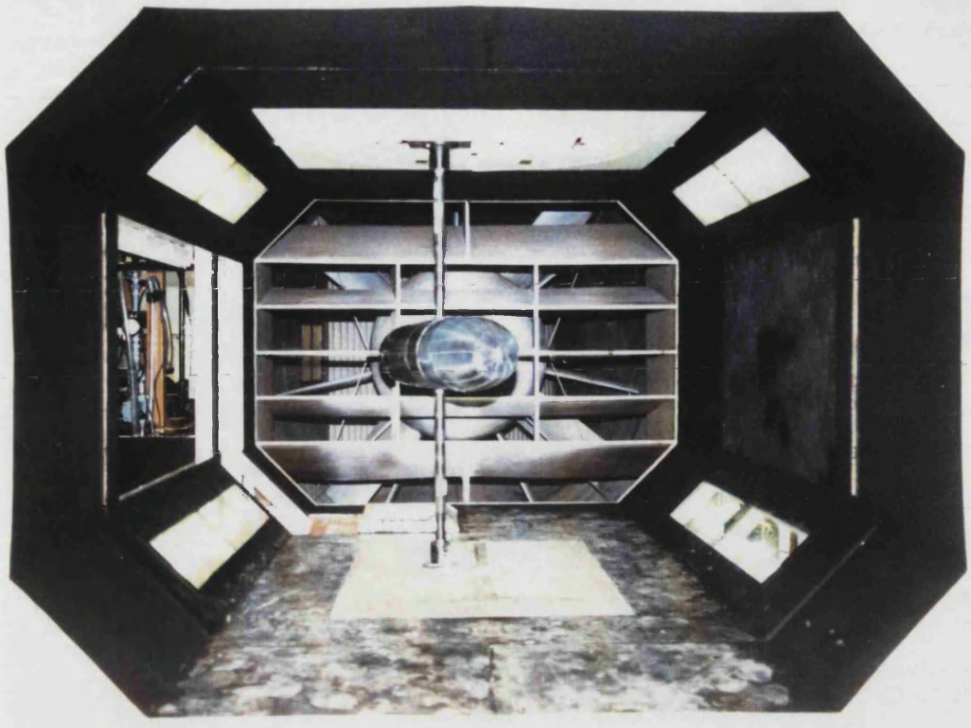

Fig. 2.5 Fuselage alone in the wind tunnel

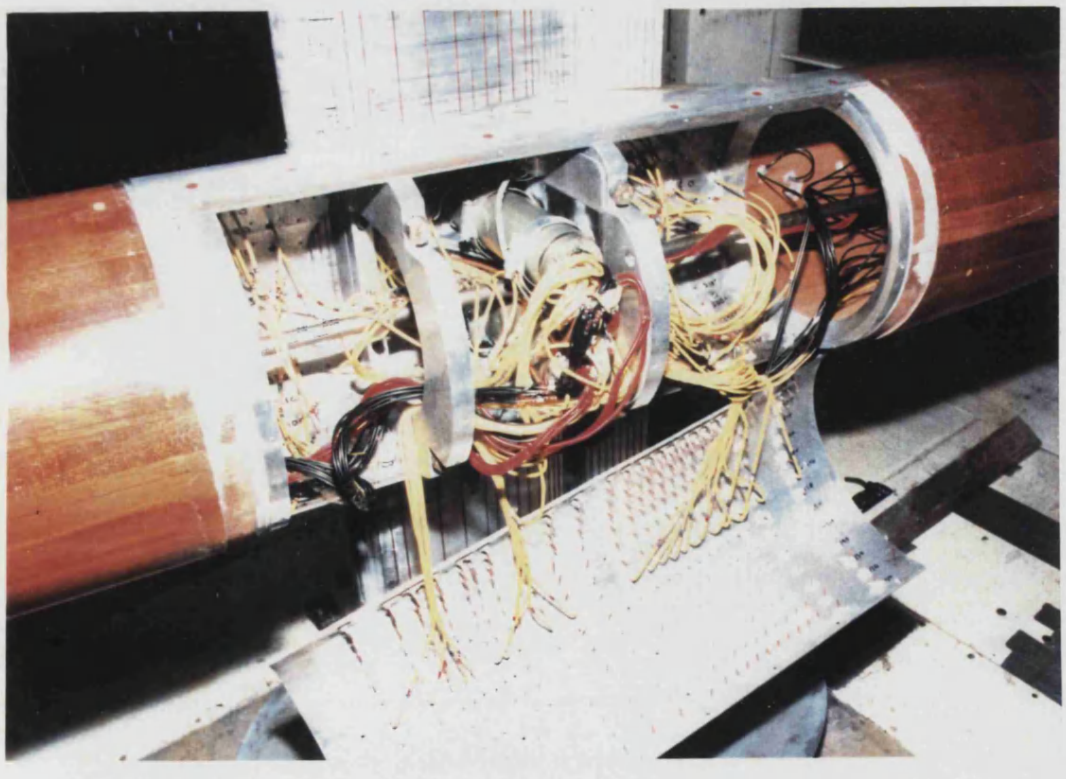

Fig. 2.6 Scanivalve arrangement inside the fuselage (high wing model only)

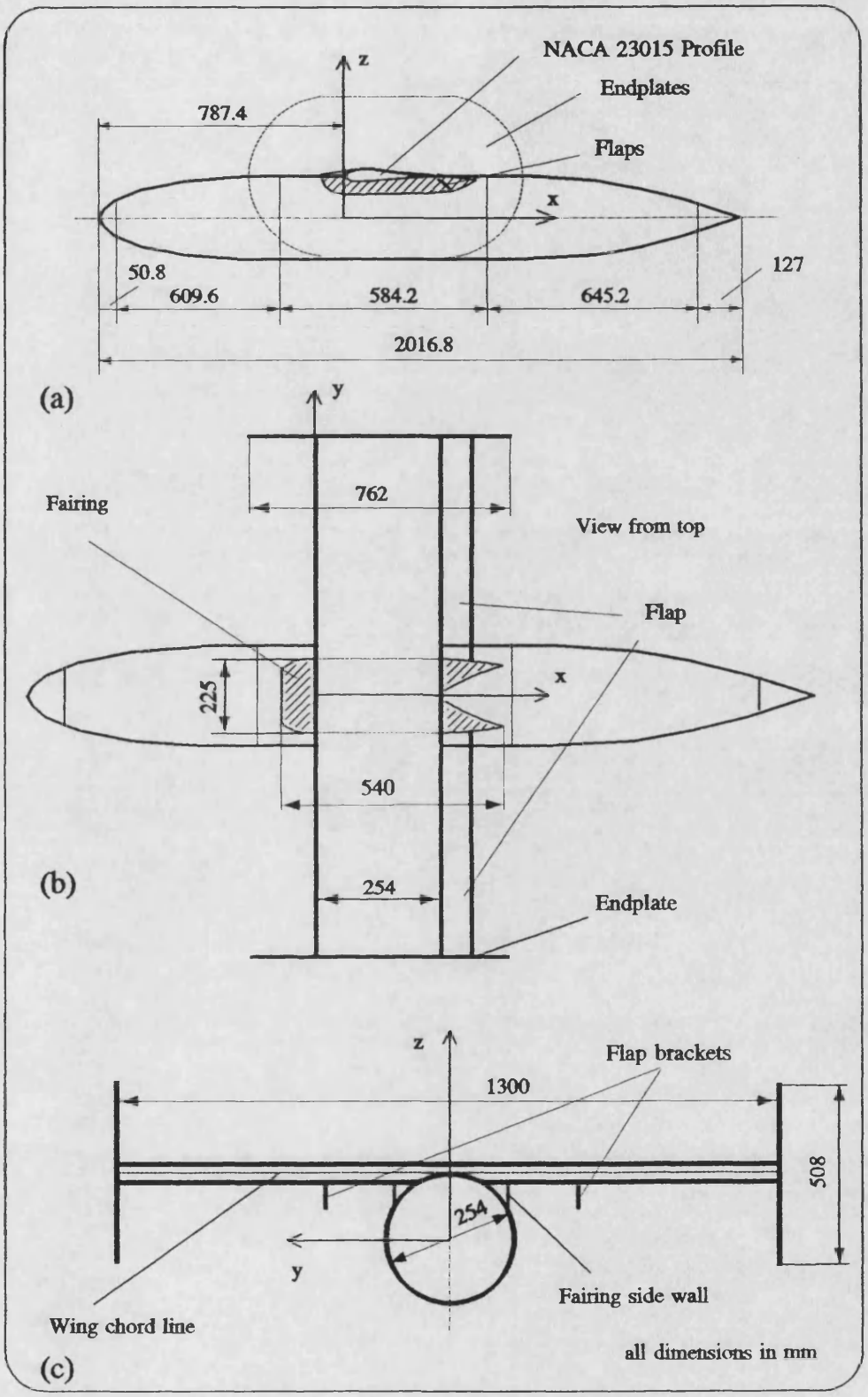

Fig. 2.7 Dimensions of the high wing model

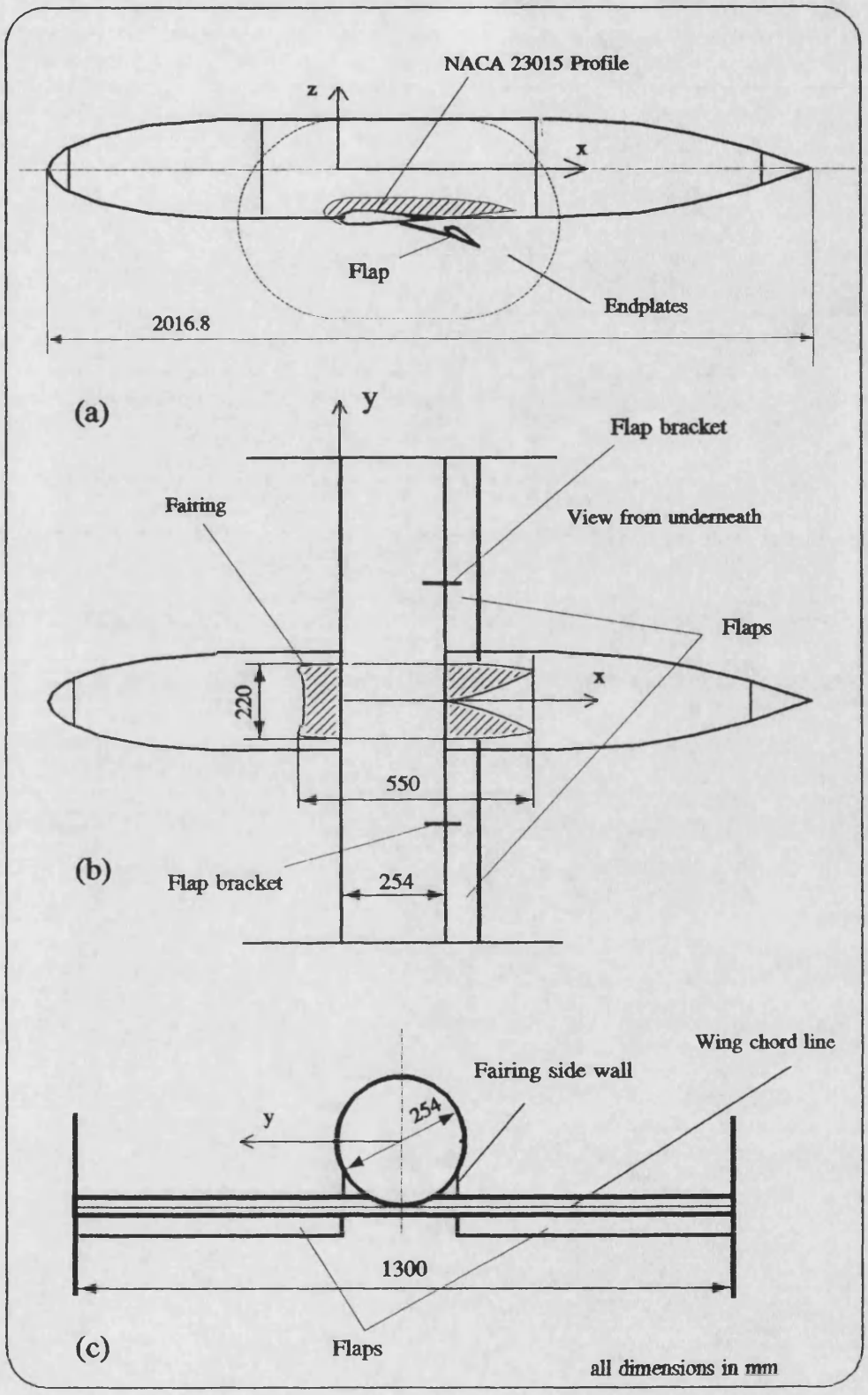

Fig. 2.8 Dimensions of the low wing model

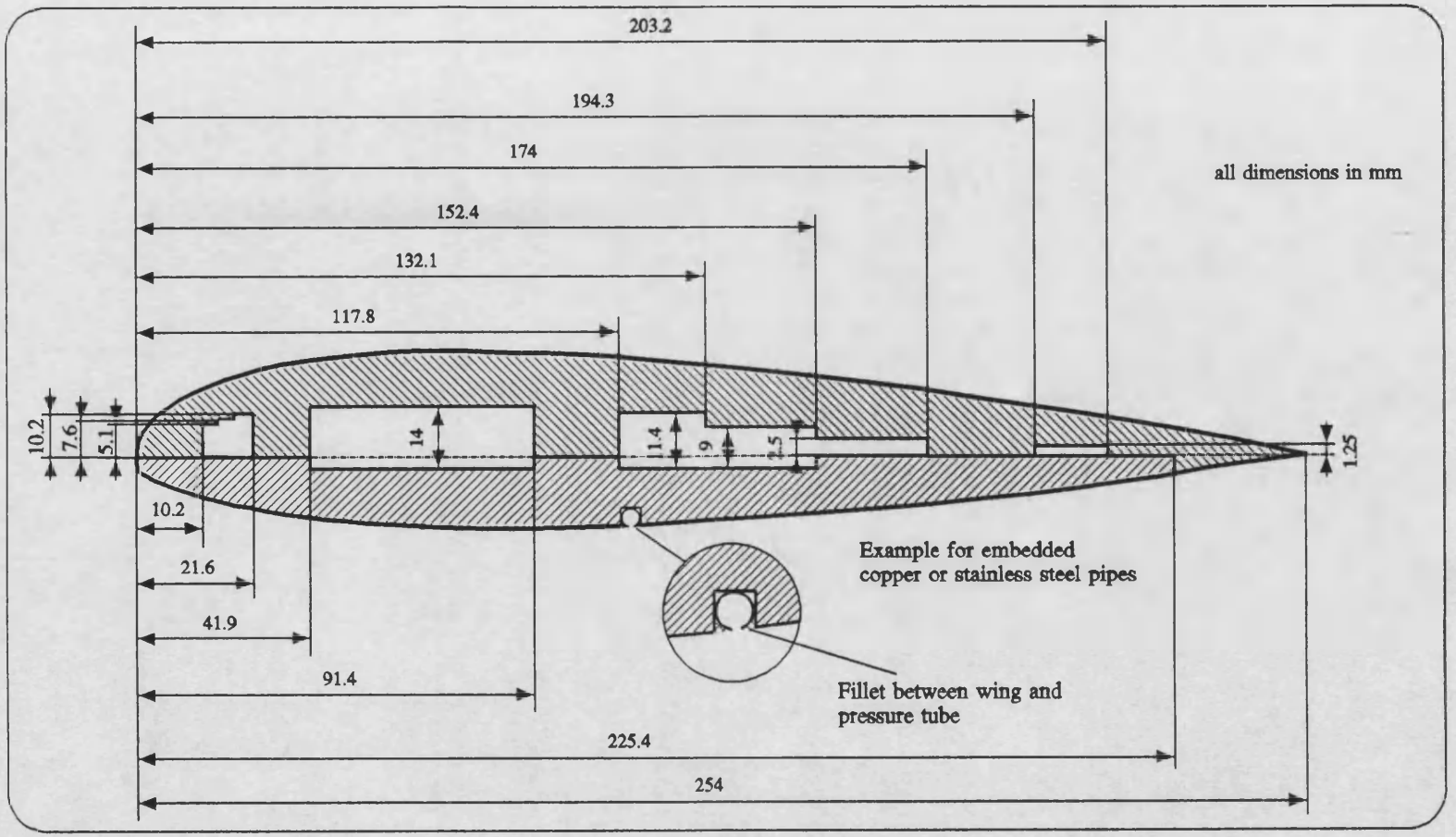

Fig. 2.9 Wing structure

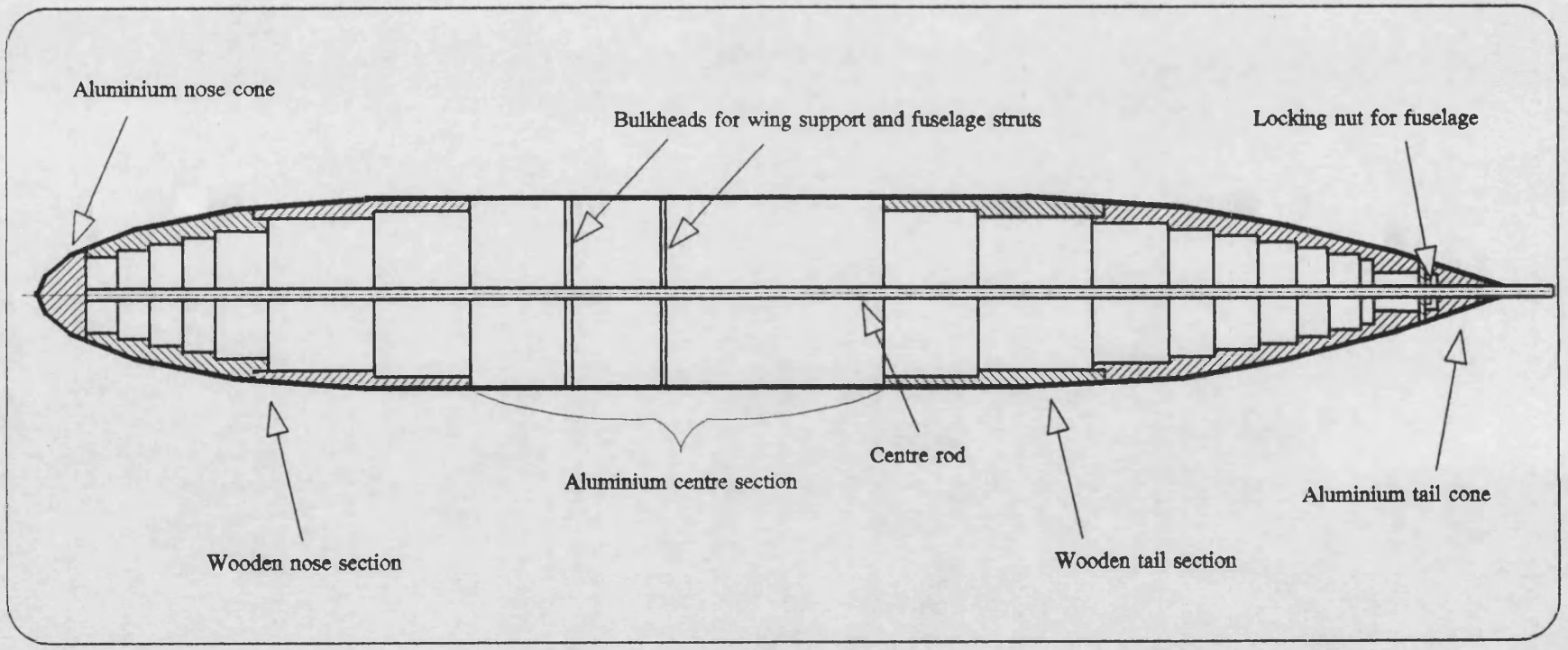

Fig. 2.10 Fuselage structure including bulkheads for wing or struts mounting

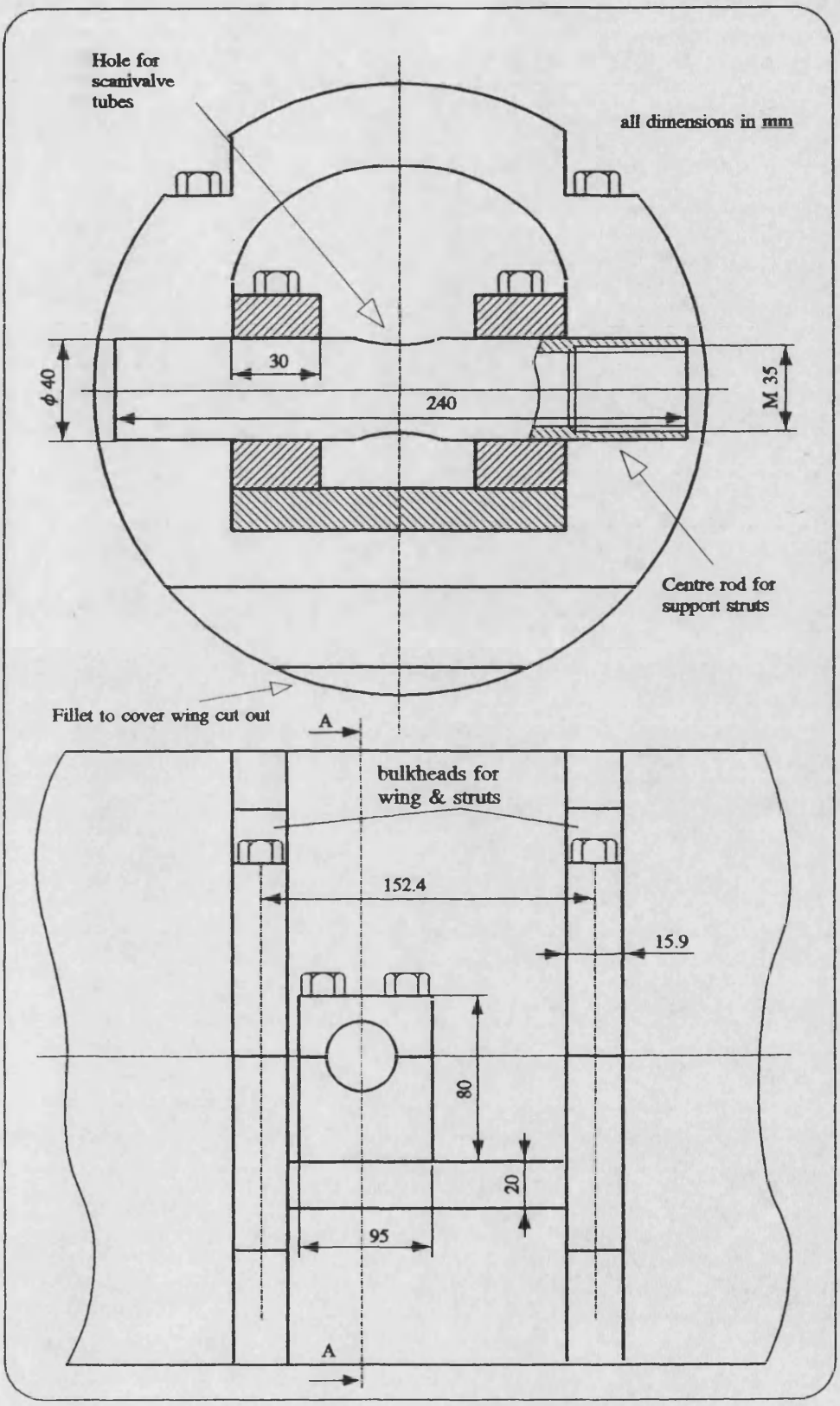

Fig. 2.11 Fuselage structure for support struts (for Fuselage alone)

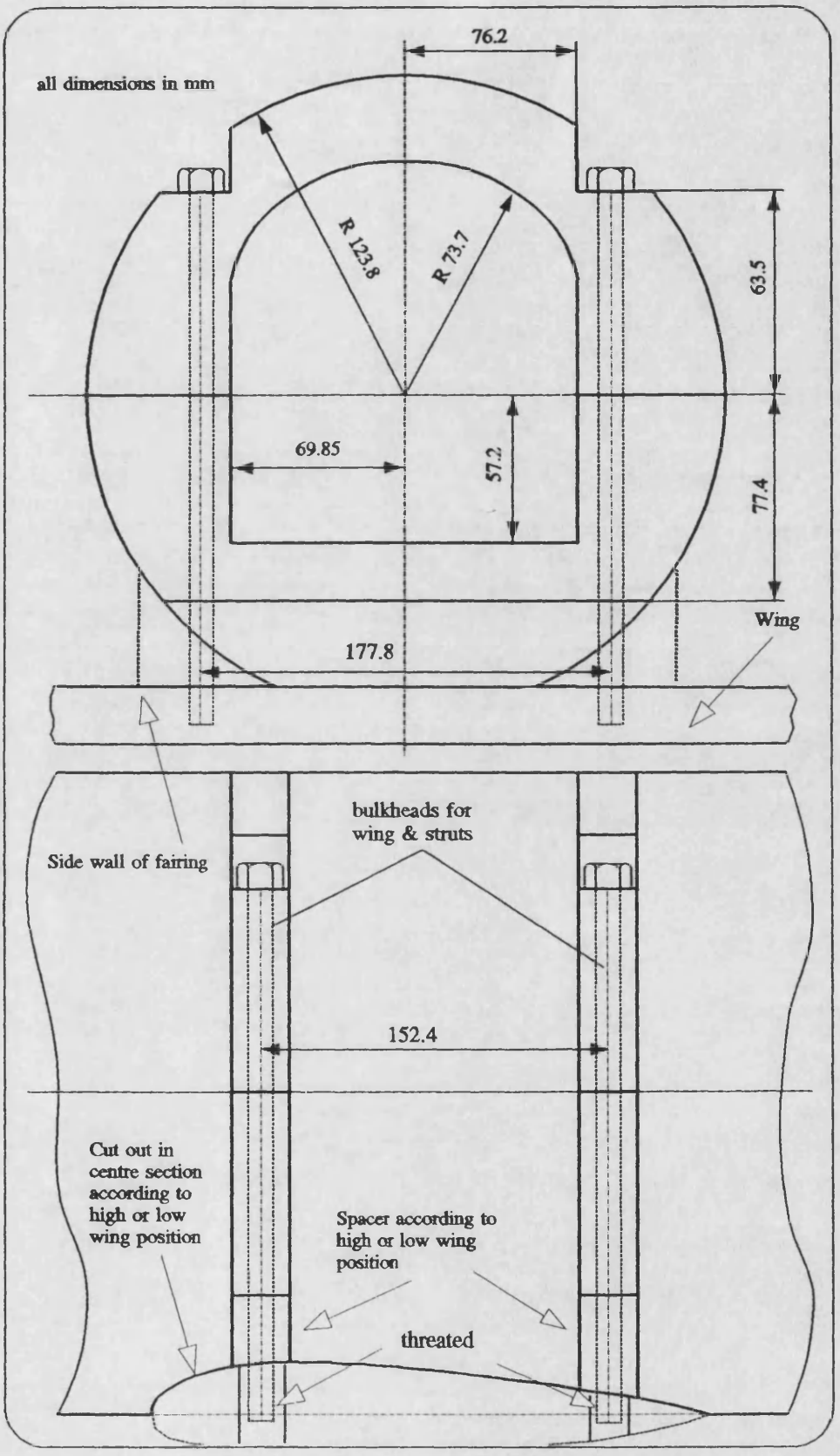

Fig. 2.12 Fuselage structure and wing bulkheads

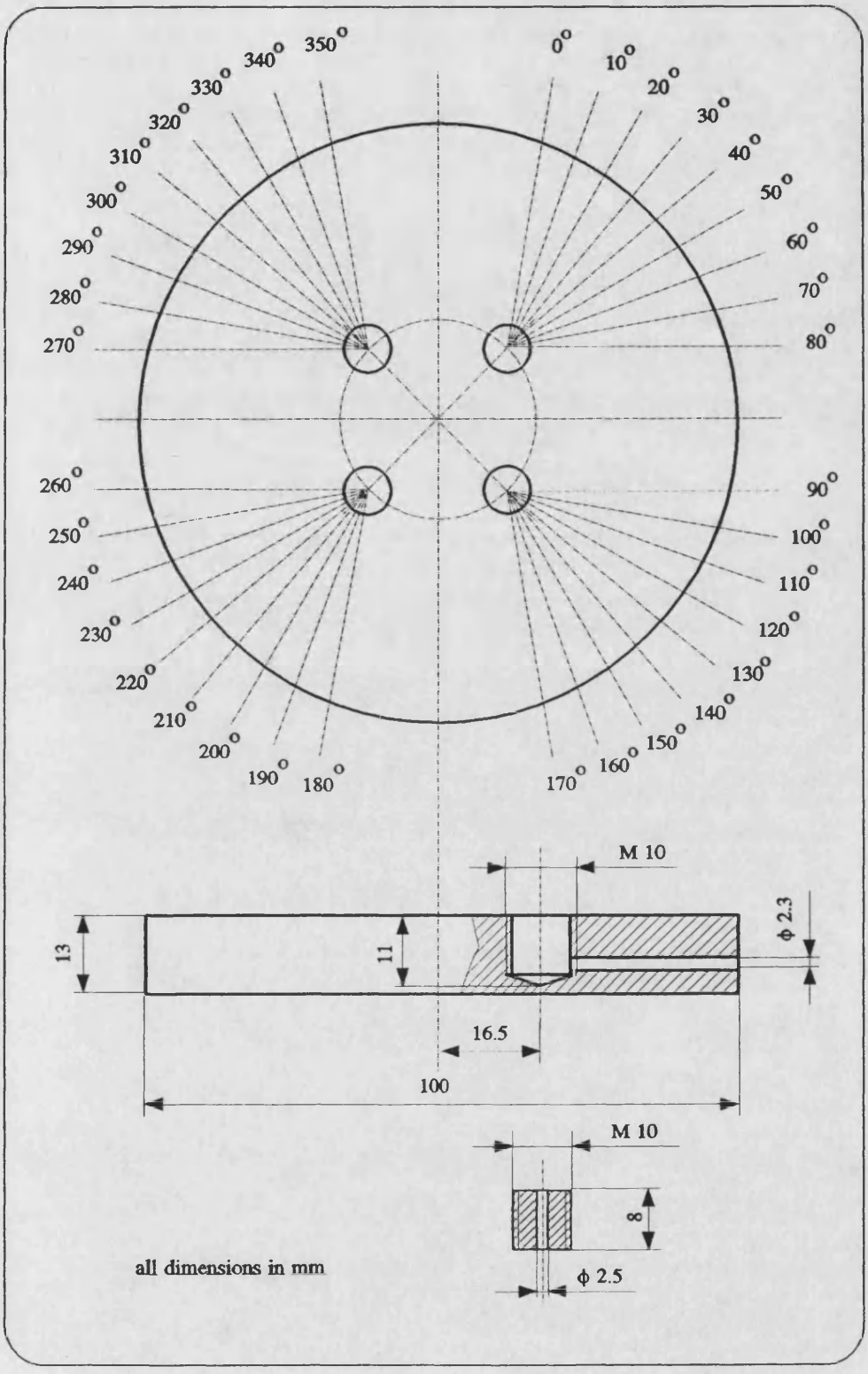

Fig. 2.13 Manifold for pressure tube connection

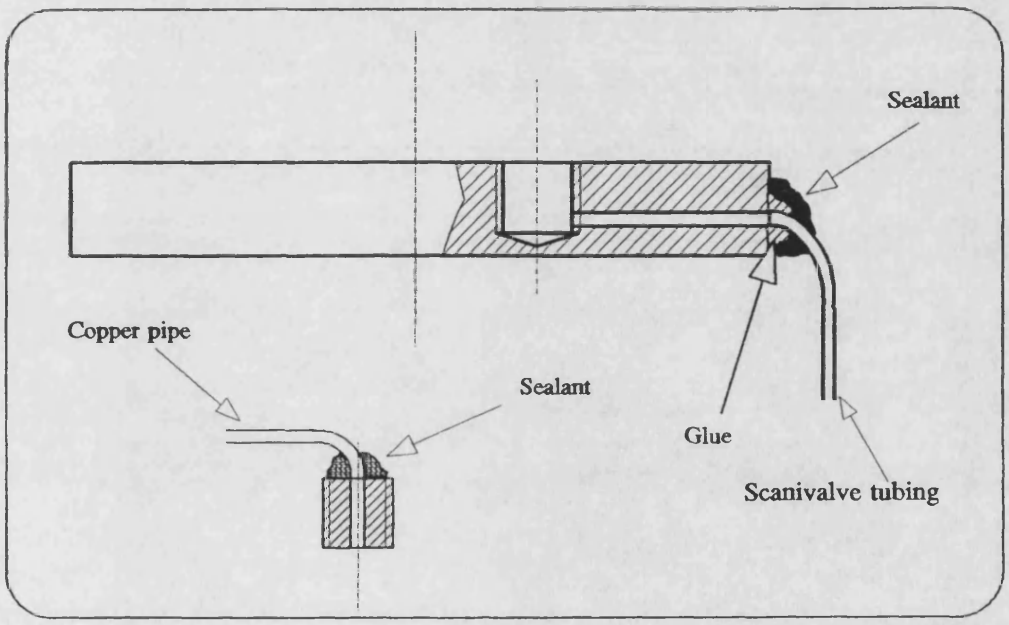

Fig. 2.14 Manifold sealing

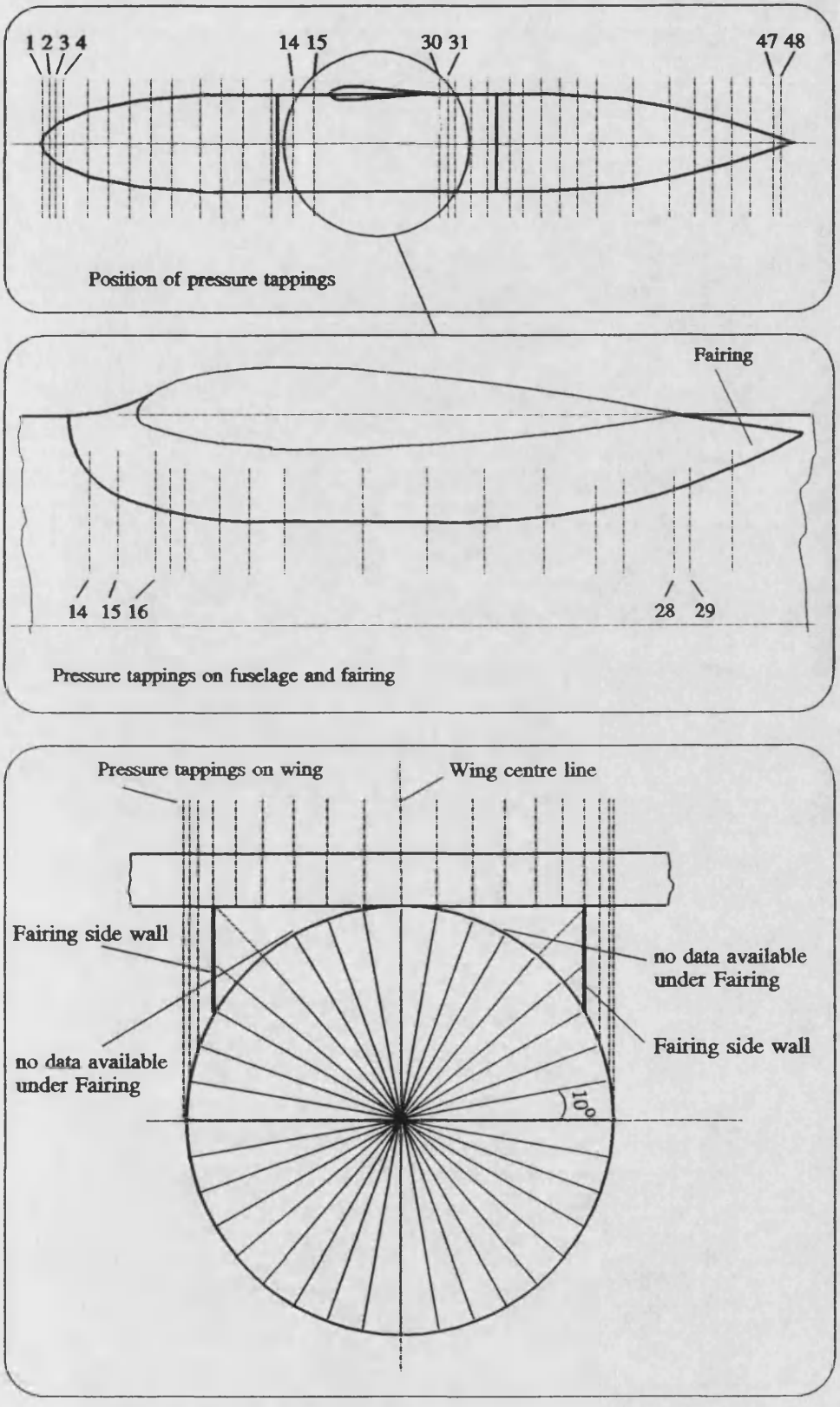

Fig. 2.15 Pressure tappings on the fuselage and fairing

(for locations see Table 2.1)

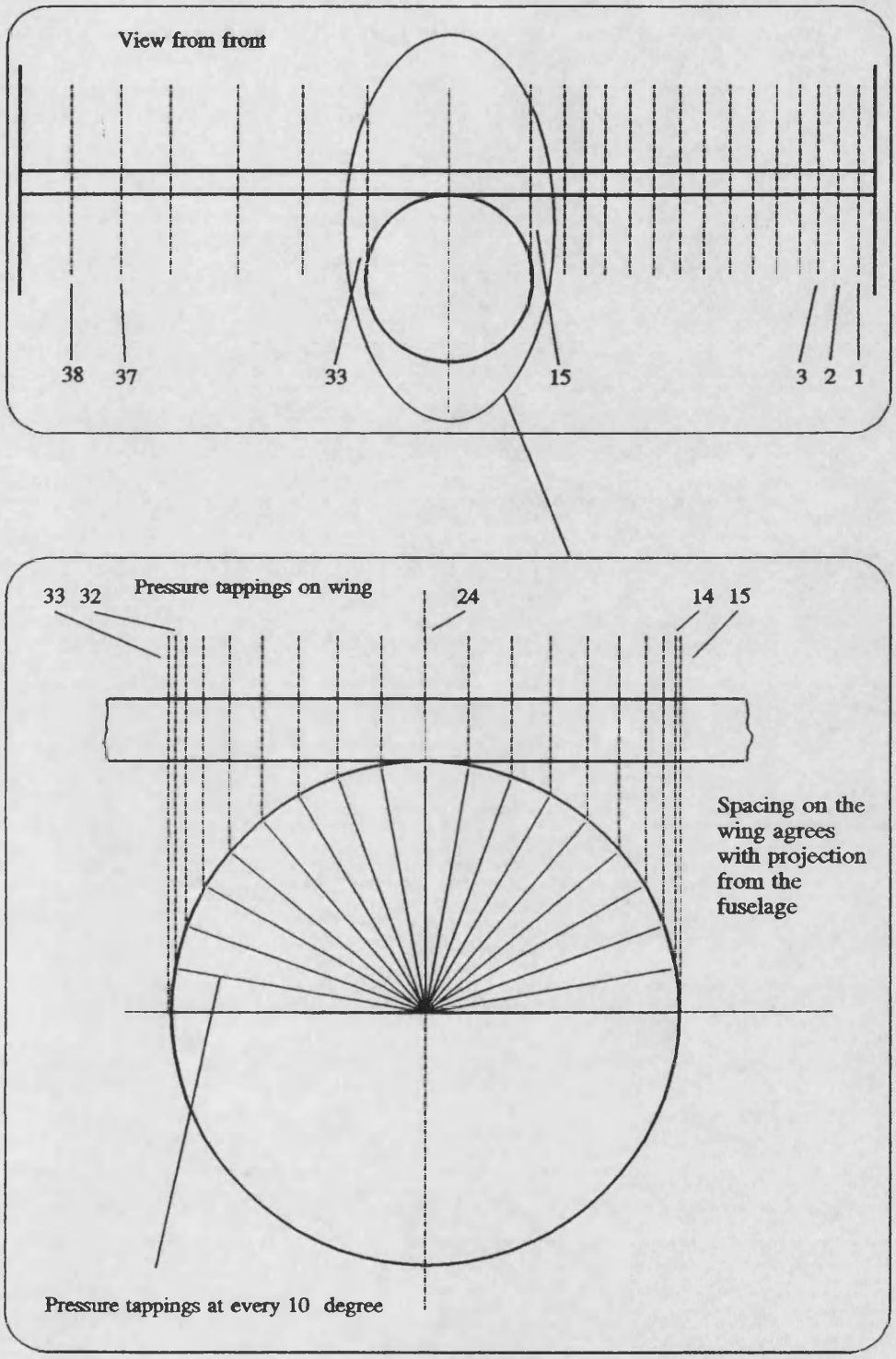

Fig. 2.16 Pressure tappings on the wing

(for locations see Table 2.2)

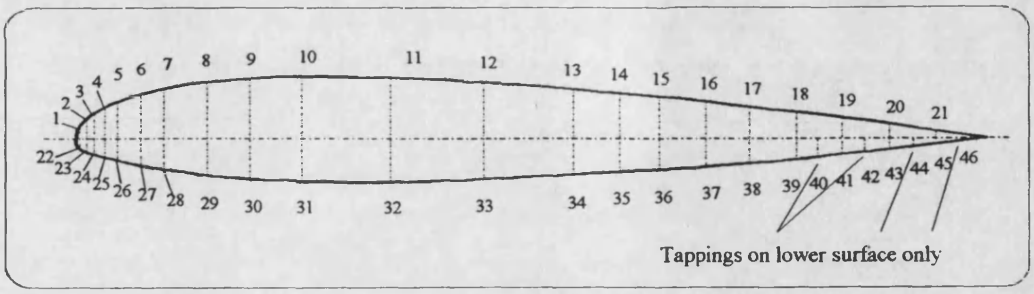

Upper Surface Tapping	x/c	Lower Surface Tapping
1	0.002	22
2	0.009	23
3	0.02	24
4	0.034	25
5	0.05	26
6	0.075	27
7	0.1	28
8	0.15	29
9	0.2	30
10	0.25	31
11	0.35	32
12	0.45	33
13	0.55	34
14	0.6	35
15	0.65	36
16	0.7	37
17	0.75	38
18	0.8	39
	0.825	40
19	0.85	41
	0.875	42
20	0.9	43
	0.925	44
21	0.95	45
	0.975	46

Fig. 2.17 Chordwise pressure tappings on the wing

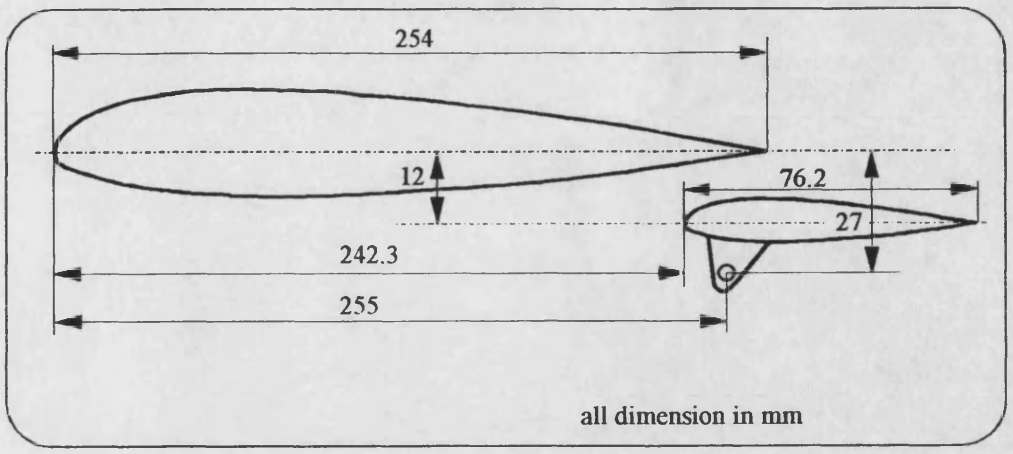

Fig. 2.18 Flap position relative to wing

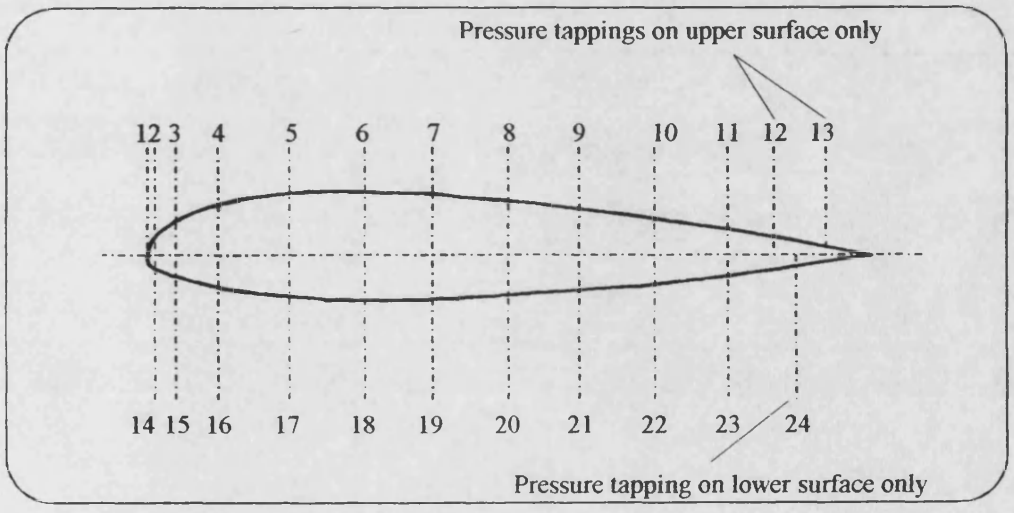

Tapping	x/c	Tapping	x/c
1	0.001		
2	0.01	14	0.01
3	0.04	15	0.04
4	0.1	16	0.1
5	0.2	17	0.2
6	0.3	18	0.3
7	0.4	19	0.4
8	0.5	20	0.5
9	0.6	21	0.6
10	0.7	22	0.7
11	0.8	23	0.8
12	0.86		
		24	0.895
13	0.934		

Fig. 2.19 Chordwise pressure tappings on the flaps

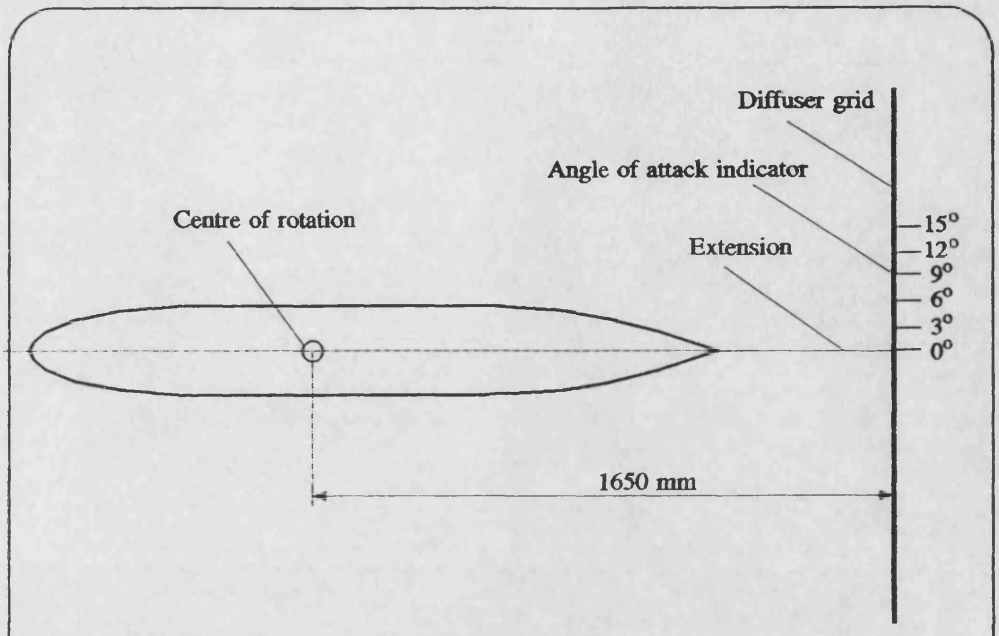

Angle of attack setting system for fuselage alone

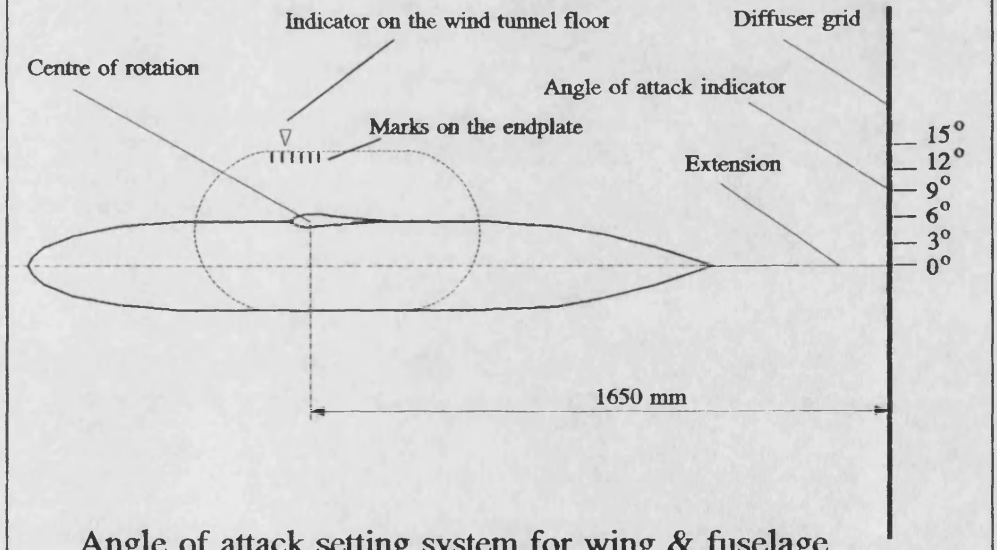

Angle of attack setting system for wing & fuselage

Fig. 2.20 Angle of attack setting system

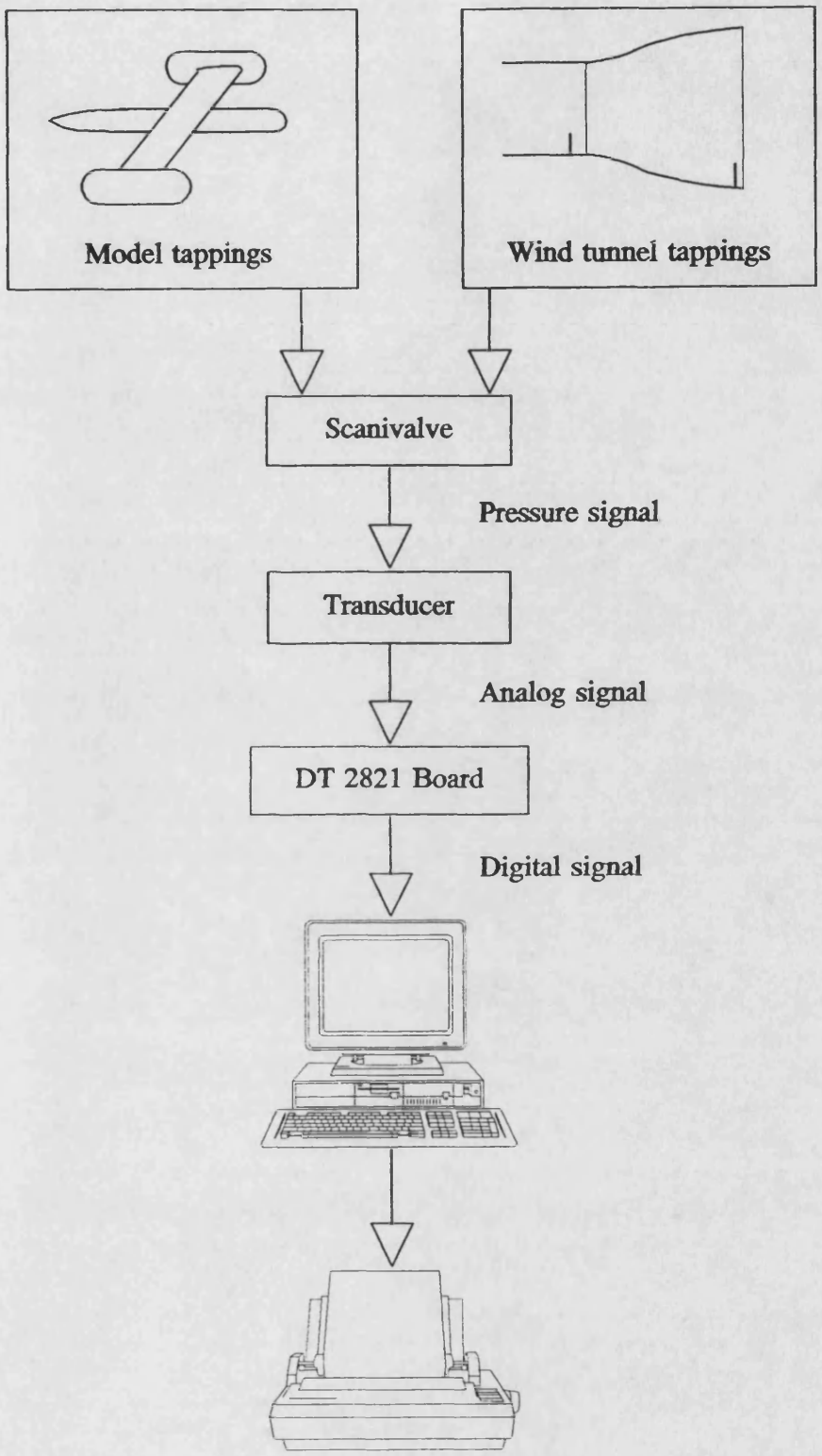

Fig. 3.1 Flow diagram for data signal

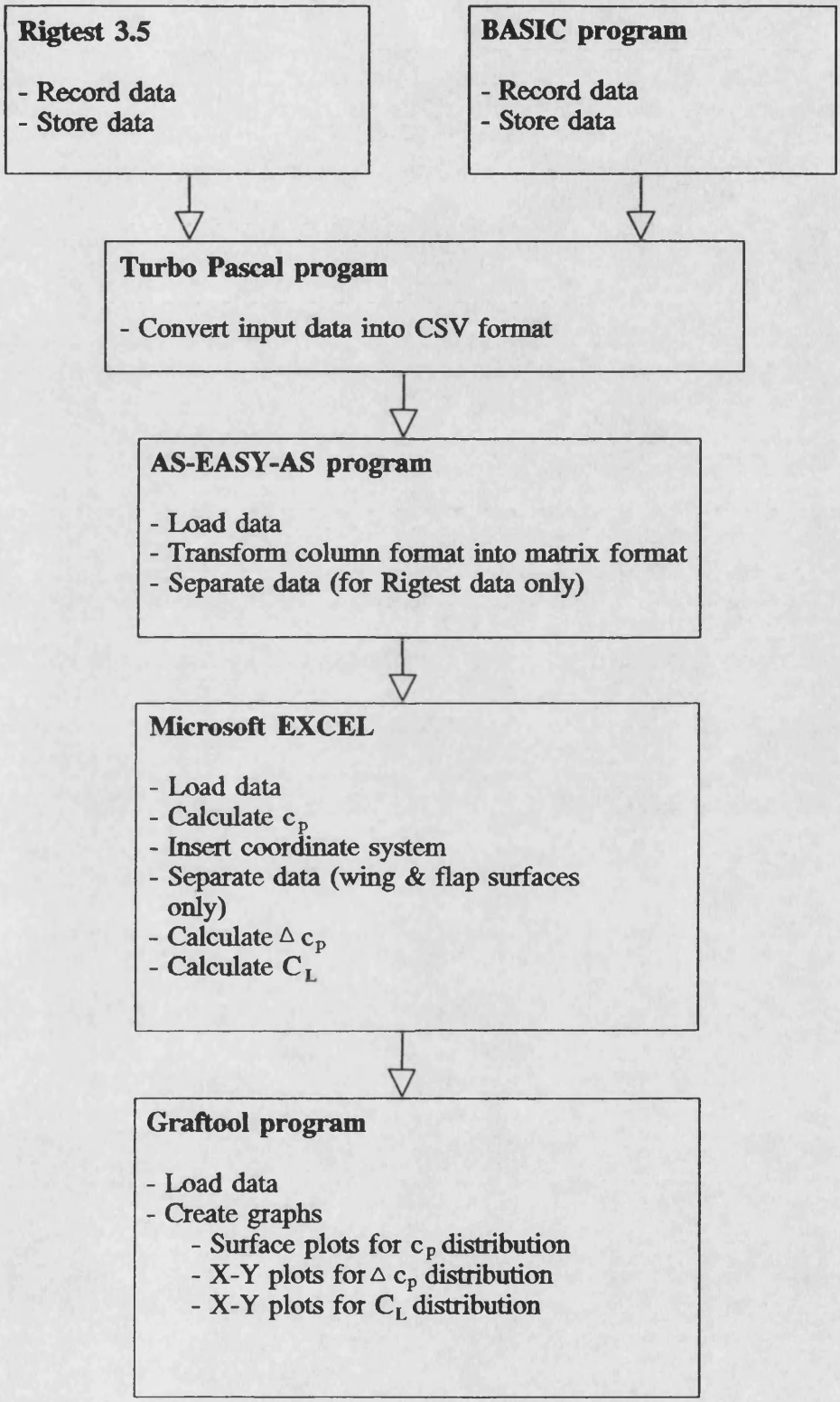

Fig. 3.2 Flow chart for data acquisition

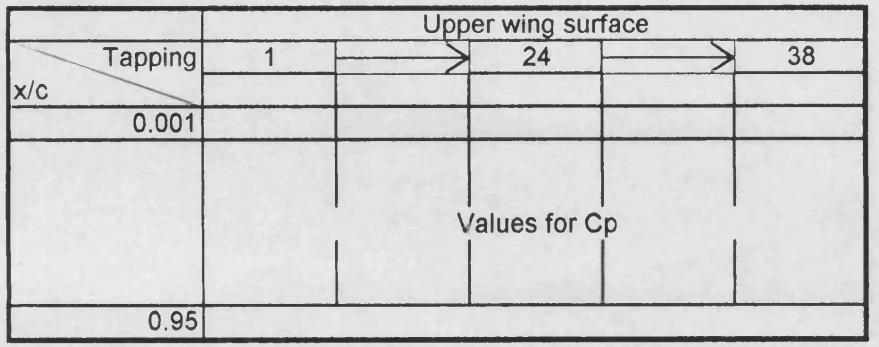

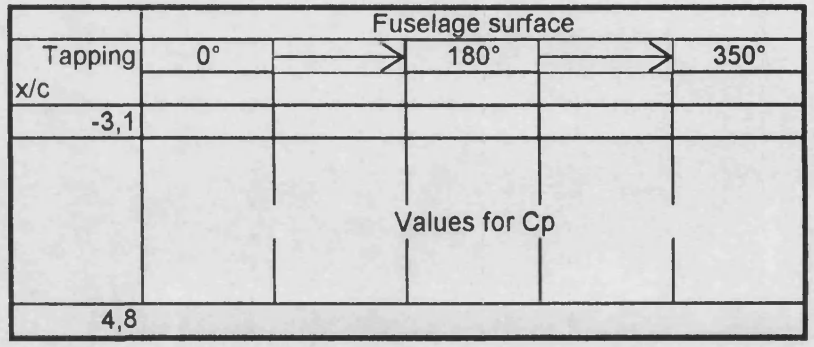

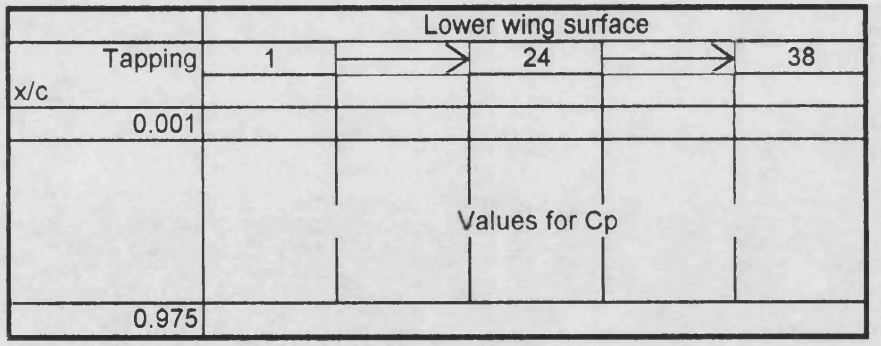

Fig 3.3 Matrix for pressure coefficients on wing and fuselage surface

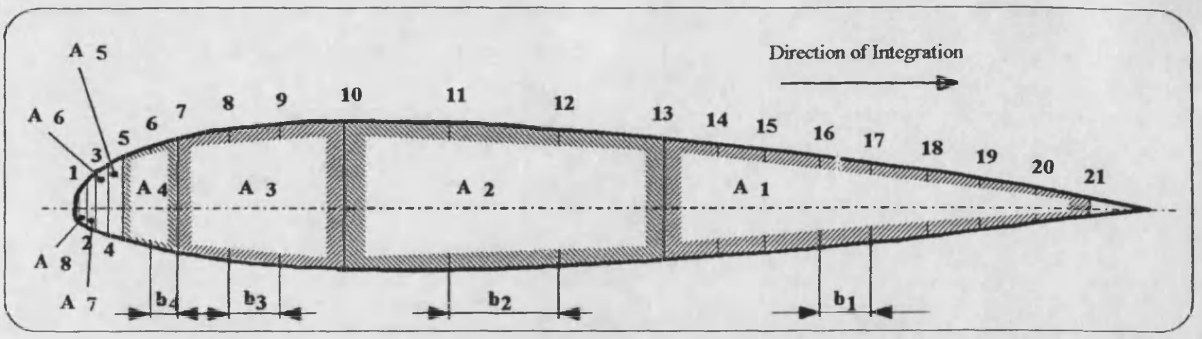

$$A_1 = \frac{b_1}{2}\left(c_{p13} + 2 \times \left(c_{p14} + c_{p15} + c_{p16} + c_{p17} + c_{p18} + c_{p19} + c_{p20}\right) + c_{p21}\right)$$

$$A_2 = \frac{b_2}{2}\left(c_{p10} + 2 \times \left(c_{p11} + c_{p12}\right) + c_{p13}\right)$$

$$A_3 = \frac{b_3}{2}\left(c_{p7} + 2 \times \left(c_{p8} + c_{p9}\right) + c_{p10}\right)$$

$$A_4 = \frac{b_4}{2}\left(c_{p5} + 2 \times c_{p6} + c_{p7}\right)$$

$$A_5 = \frac{b_5}{2}\left(c_{p4} + c_{p5}\right)$$

$$A_6 = \frac{b_6}{2}\left(c_{p3} + c_{p4}\right)$$

$$A_7 = \frac{b_7}{2}\left(c_{p2} + c_{p3}\right)$$

$$A_8 = \frac{b_8}{2}\left(c_{p1} + c_{p2}\right)$$

$$c_l = \frac{1}{c}\sum_{i=1}^{8} A_i$$

Fig. 3.4 Chordwise C_L calculation over wing and flap

continued -->

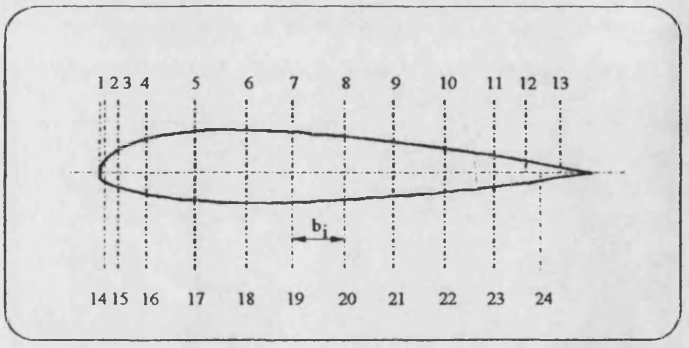

for upper flap surface

$$A_1 = \frac{b_1}{2}\left(c_{p1} + c_{p2}\right)$$
$$A_2 = \frac{b_2}{2}\left(c_{p2} + c_{p3}\right)$$
$$A_3 = \frac{b_3}{2}\left(c_{p3} + c_{p4}\right)$$
$$A_4 = \frac{b_4}{2}\left(c_{p4} + c_{p5}\right)$$
$$A_5 = \frac{b_5}{2}\left(c_{p5} + c_{p6}\right)$$
$$A_6 = \frac{b_6}{2}\left(c_{p6} + c_{p7}\right)$$
$$A_7 = \frac{b_7}{2}\left(c_{p7} + c_{p8}\right)$$
$$A_8 = \frac{b_8}{2}\left(c_{p8} + c_{p9}\right)$$
$$A_9 = \frac{b_9}{2}\left(c_{p9} + c_{p10}\right)$$
$$A_{10} = \frac{b_{10}}{2}\left(c_{p10} + c_{p11}\right)$$
$$A_{11} = \frac{b_{11}}{2}\left(c_{p11} + c_{p12}\right)$$
$$A_{12} = \frac{b_{12}}{2}\left(c_{p12} + c_{p13}\right)$$

for lower flap surface

$$A_1 = \frac{b_1}{2}\left(c_{p1} + c_{p14}\right)$$
$$A_2 = \frac{b_2}{2}\left(c_{p14} + c_{p15}\right)$$
$$A_3 = \frac{b_3}{2}\left(c_{p15} + c_{p16}\right)$$
$$A_4 = \frac{b_4}{2}\left(c_{p16} + c_{p17}\right)$$
$$A_5 = \frac{b_5}{2}\left(c_{p17} + c_{p18}\right)$$
$$A_6 = \frac{b_6}{2}\left(c_{p18} + c_{p19}\right)$$
$$A_7 = \frac{b_7}{2}\left(c_{p19} + c_{p20}\right)$$
$$A_8 = \frac{b_8}{2}\left(c_{p20} + c_{p21}\right)$$
$$A_9 = \frac{b_9}{2}\left(c_{p21} + c_{p22}\right)$$
$$A_{10} = \frac{b_{10}}{2}\left(c_{p22} + c_{p23}\right)$$
$$A_{11} = \frac{b_{23}}{2}\left(c_{p23} + c_{p24}\right)$$

$$c_l = \frac{1}{c}\sum_{i=1}^{12} A_{lower\ surface} - A_{upper\ surface}$$

Fig. 3.4 cont. Chordwise C_L calculation over wing and flap

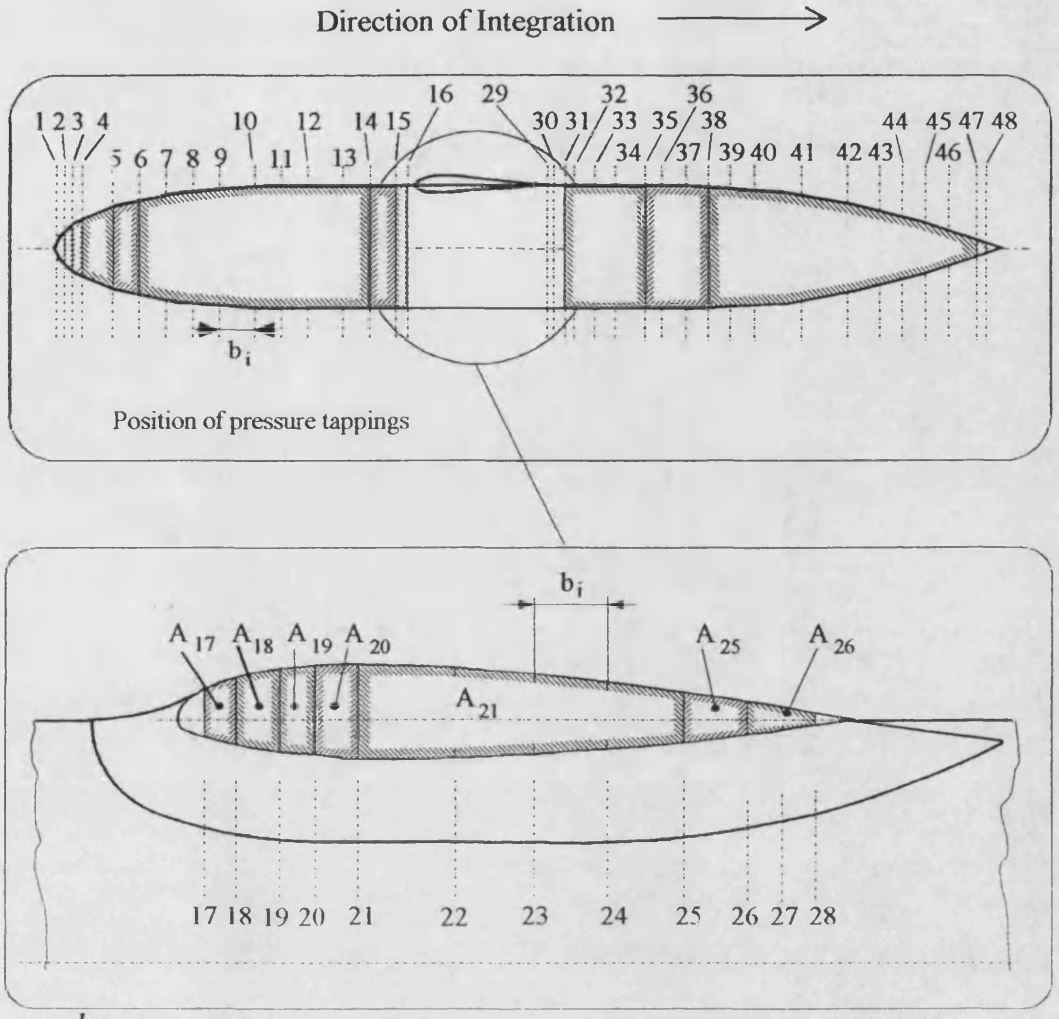

$$A_1 = \frac{b_1}{2}\left(c_{p1} + c_{p2}\right)$$

$$A_2 = \frac{b_2}{2}\left(c_{p2} + c_{p3}\right)$$

$$A_3 = \frac{b_3}{2}\left(c_{p3} + c_{p4}\right)$$

$$A_4 = \frac{b_4}{2}\left(c_{p4} + c_{p5}\right)$$

$$A_5 = \frac{b_5}{2}\left(c_{p5} + c_{p6}\right)$$

$$A_6 = \frac{b_6}{2}\left(c_{p6} + 2 \times \left(c_{p7} + c_{p8} + c_{p9} + c_{p10} + c_{p11} + c_{p12} + c_{p13}\right) + c_{p14}\right)$$

$$A_{14} = \frac{b_{14}}{2}\left(c_{p14} + c_{p15}\right)$$

$$A_{15} = \frac{b_{15}}{2}\left(c_{p15} + c_{p16}\right)$$

$$A_{16} = \frac{b_{16}}{2}\left(c_{p16} + c_{p17}\right)$$

Fig. 3.5 Longitudinal C_L calculation over the fuselage **continued -->**

$$A_{17} = \frac{b_{17}}{2}\left(c_{p17} + c_{p18}\right)$$

$$A_{18} = \frac{b_{18}}{2}\left(c_{p18} + c_{p19}\right)$$

$$A_{19} = \frac{b_{19}}{2}\left(c_{p19} + c_{p20}\right)$$

$$A_{20} = \frac{b_{20}}{2}\left(c_{p20} + c_{p21}\right)$$

$$A_{21} = \frac{b_{21}}{2}\left(c_{p21} + 2 \times \left(c_{p22} + c_{22} + c_{p23} + c_{p24}\right) + c_{p25}\right)$$

$$A_{25} = \frac{b_{25}}{2}\left(c_{p25} + c_{p26}\right)$$

$$A_{26} = \frac{b_{26}}{2}\left(c_{p26} + 2 \times c_{p27} + c_{p28}\right)$$

$$A_{28} = \frac{b_{28}}{2}\left(c_{p28} + 2 \times c_{p29} + c_{p30}\right)$$

$$A_{30} = \frac{b_{30}}{2}\left(c_{p30} + c_{p31}\right)$$

$$A_{31} = \frac{b_{31}}{2}\left(c_{p31} + 2 \times \left(c_{p32} + c_{33} + c_{p34}\right) + c_{p35}\right)$$

$$A_{35} = \frac{b_{35}}{2}\left(c_{p35} + 2 \times \left(c_{p36} + c_{37}\right) + c_{p38}\right)$$

$$A_{38} = \frac{b_{38}}{2}\left(c_{p38} + 2 \times \left(c_{p39} + c_{p40} + c_{p41} + c_{p42} + c_{p43} + c_{p44} + c_{p45} + c_{p46}\right) + c_{p47}\right)$$

$$A_{47} = \frac{b_{47}}{2}\left(c_{p47} + c_{p48}\right)$$

$$C_l = \frac{1}{c}\sum_{i=1}^{47} A_i$$

where:

$$b_6 = b_7 = b_8 = b_9 = b_{10} = b_{11} = b_{12} = b_{13}$$
$$b_{21} = b_{22} = b_{23} = b_{24}$$
$$b_{26} = b_{27}$$
$$b_{28} = b_{29}$$
$$b_{31} = b_{32} = b_{33} = b_{34}$$
$$b_{35} = b_{36} = b_{37}$$
$$b_{38} = b_{39} = b_{40} = b_{41} = b_{42} = b_{43} = b_{44} = b_{45} = b_{46}$$

Fig. 3.5 cont. Longitudinal C_L calculation over the fuselage

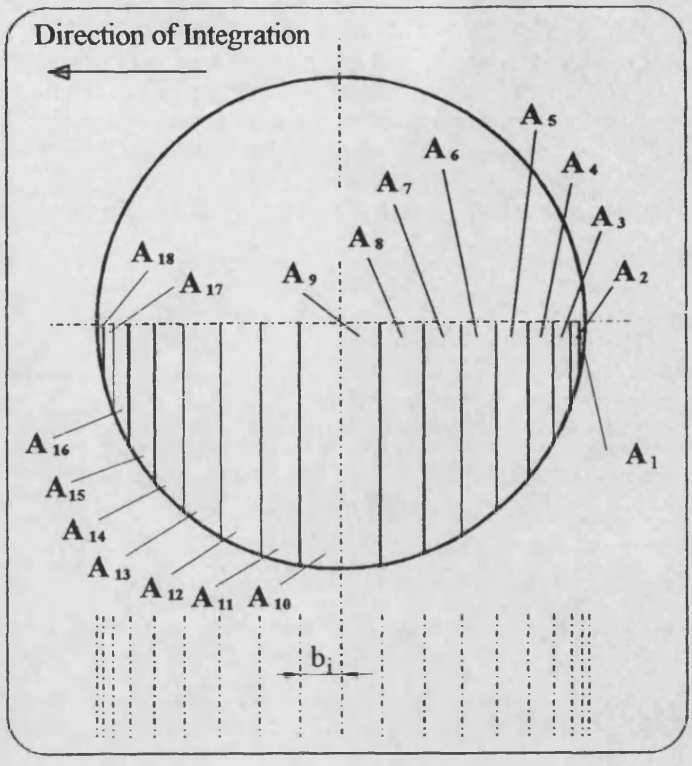

$$A_1 = A_{18} = \frac{b_1}{2}\left(c_{p270} + c_{p260}\right) \qquad A_6 = A_{13} = \frac{b_6}{2}\left(c_{p220} + c_{p210}\right)$$

$$A_2 = A_{17} = \frac{b_2}{2}\left(c_{p260} + c_{p250}\right) \qquad A_7 = A_{12} = \frac{b_7}{2}\left(c_{p210} + c_{p200}\right)$$

$$A_3 = A_{16} = \frac{b_3}{2}\left(c_{p250} + c_{p240}\right) \qquad A_8 = A_{11} = \frac{b_8}{2}\left(c_{p200} + c_{p190}\right)$$

$$A_4 = A_{15} = \frac{b_4}{2}\left(c_{p240} + c_{p230}\right) \qquad A_9 = A_{10} = \frac{b_9}{2}\left(c_{p190} + c_{p180}\right)$$

$$A_5 = A_{14} = \frac{b_5}{2}\left(c_{p230} + c_{p220}\right)$$

$$C_l = \frac{1}{c}\sum_{i=1}^{18} A_i$$

Fig. 3.6 Cross sectional C_L calculation over fuselage

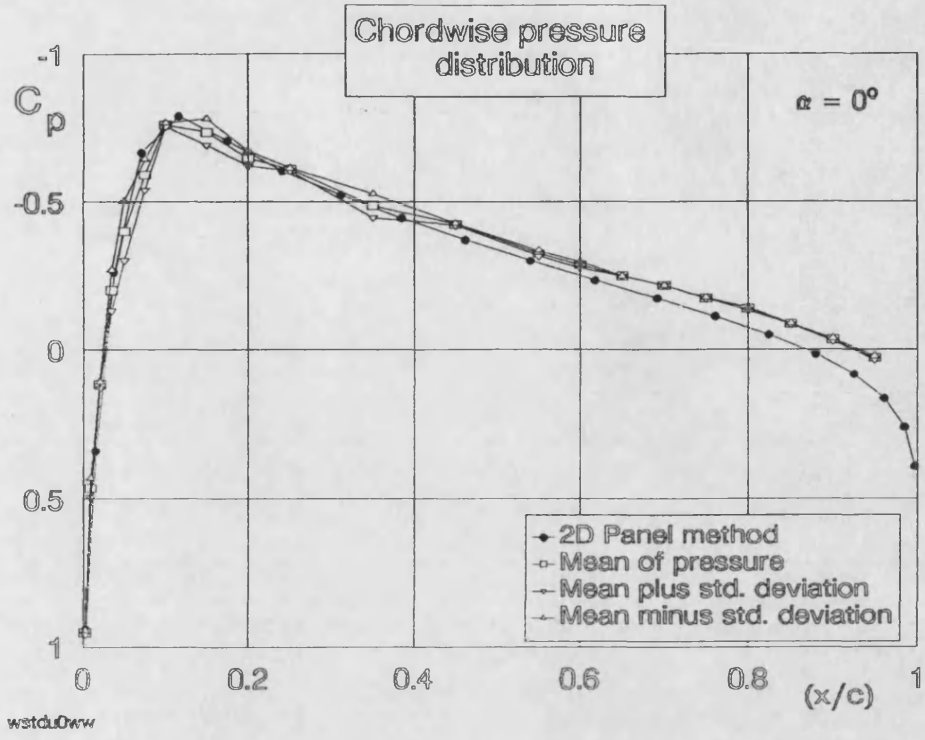

Fig. 3.7 **Mean of chordwise pressure distribution of upper wing surface compared with 2D panel method, (Obrien, 1993)**

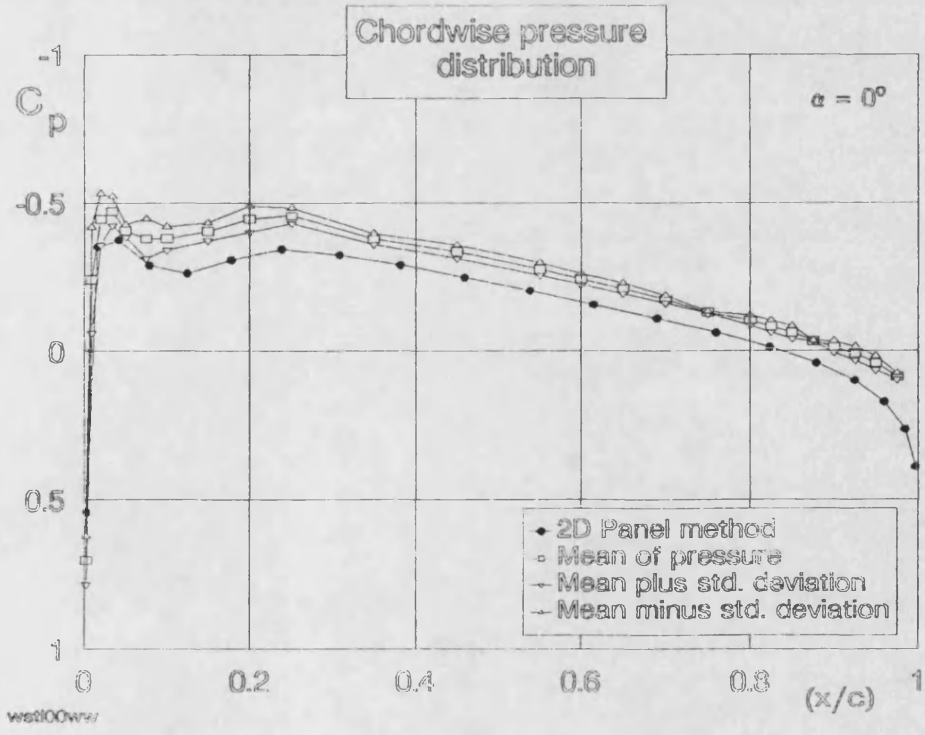

Fig. 3.8 **Mean of chordwise pressure distribution of lower wing surface compared with 2D panel method, (Obrien, 1993)**

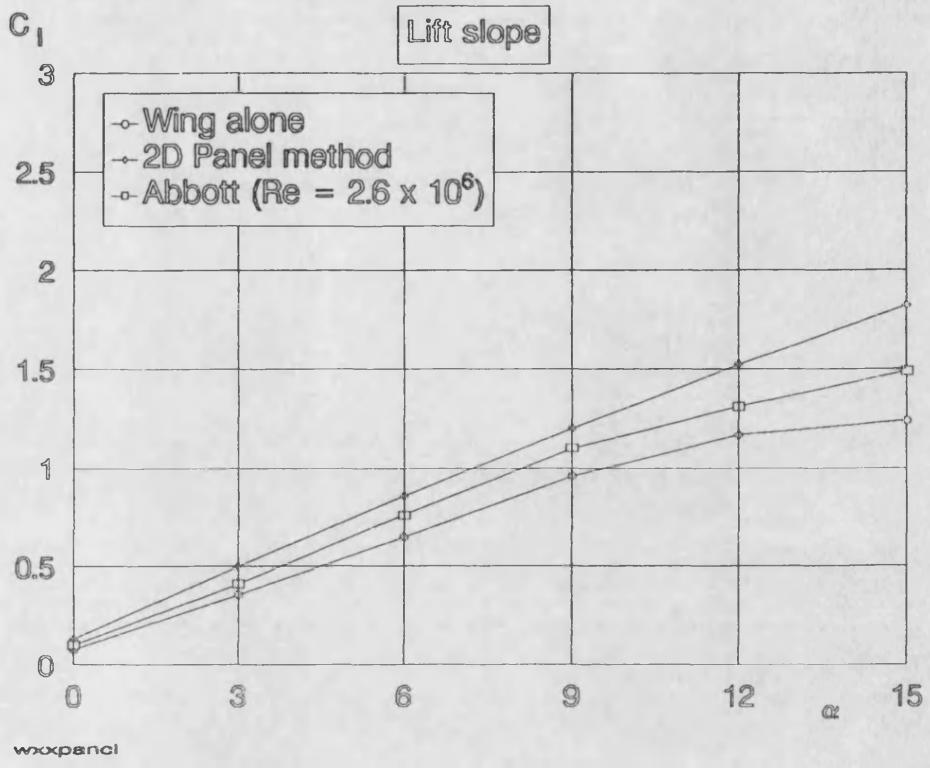

Fig. 3.9 **Lift slope of wing alone, compared with 2D panel method (Obrien, 1993) and Abbott and von Doenhoff (1959)**

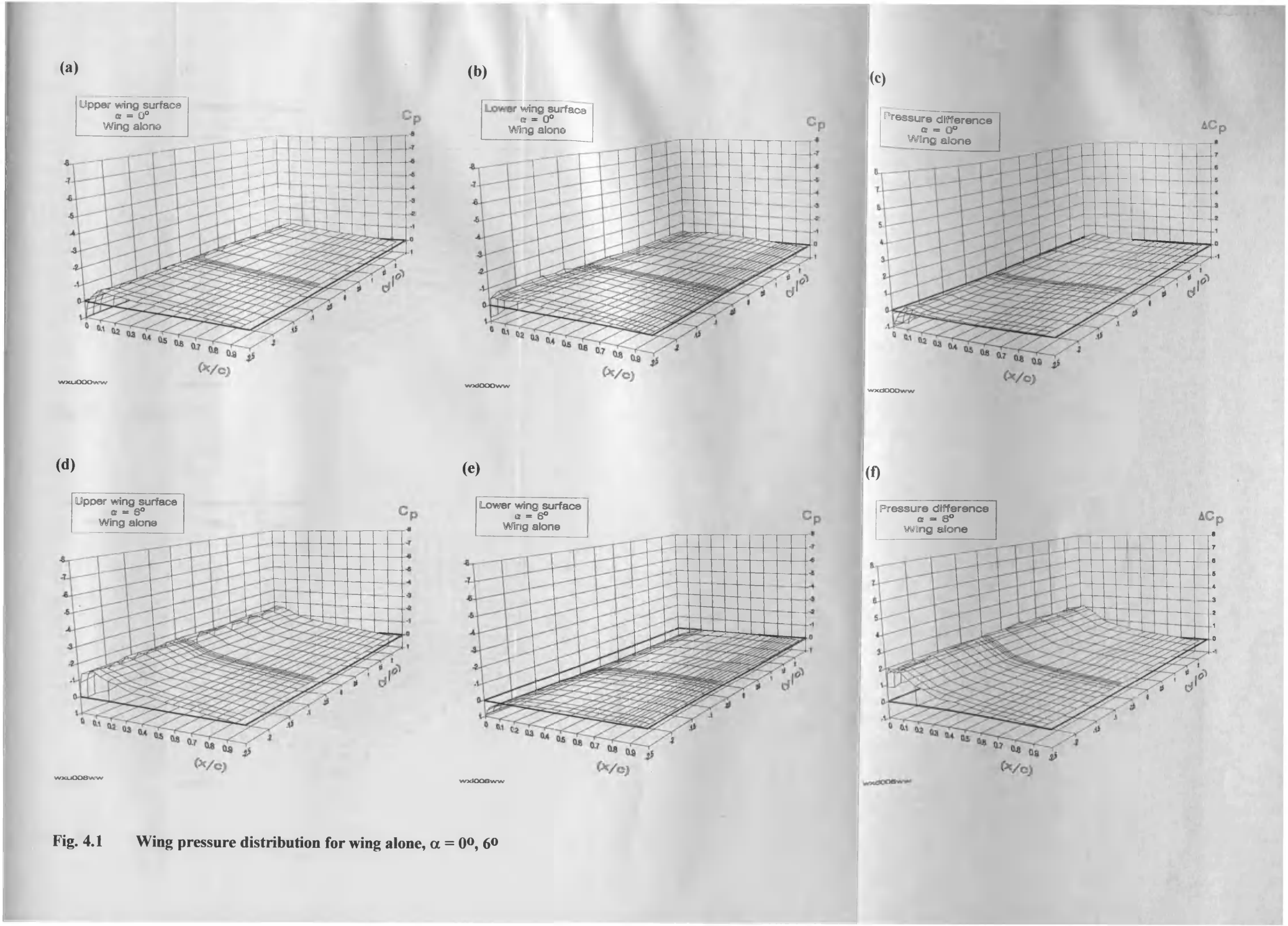

Fig. 4.1 **Wing pressure distribution for wing alone, $\alpha = 0^o, 6^o$**

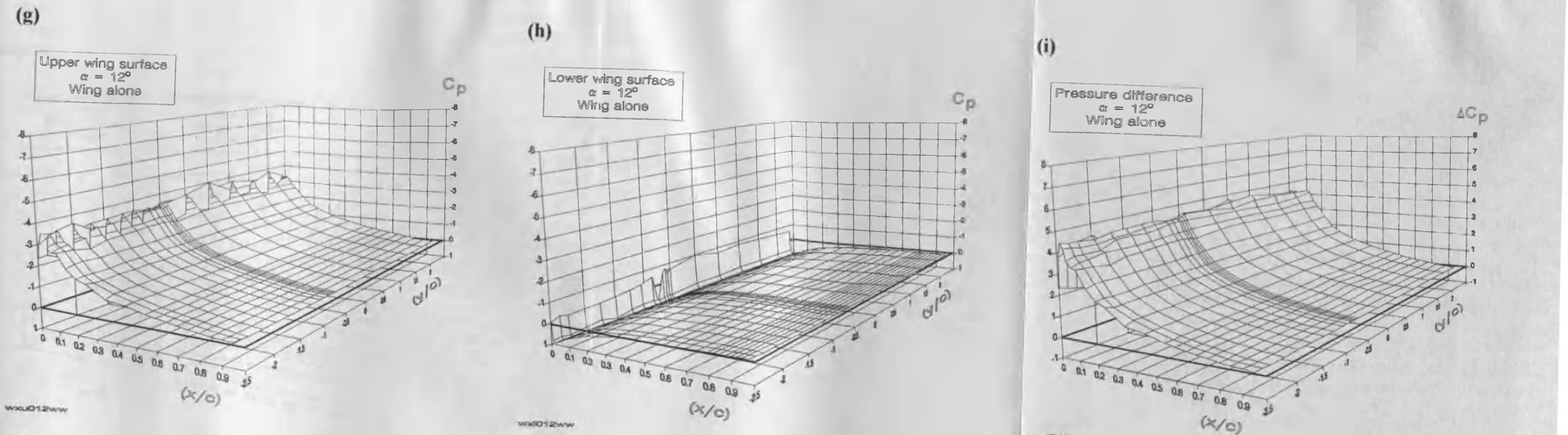

Fig. 4.1 **Wing pressure distribution for wing alone, $\alpha = 12°$**

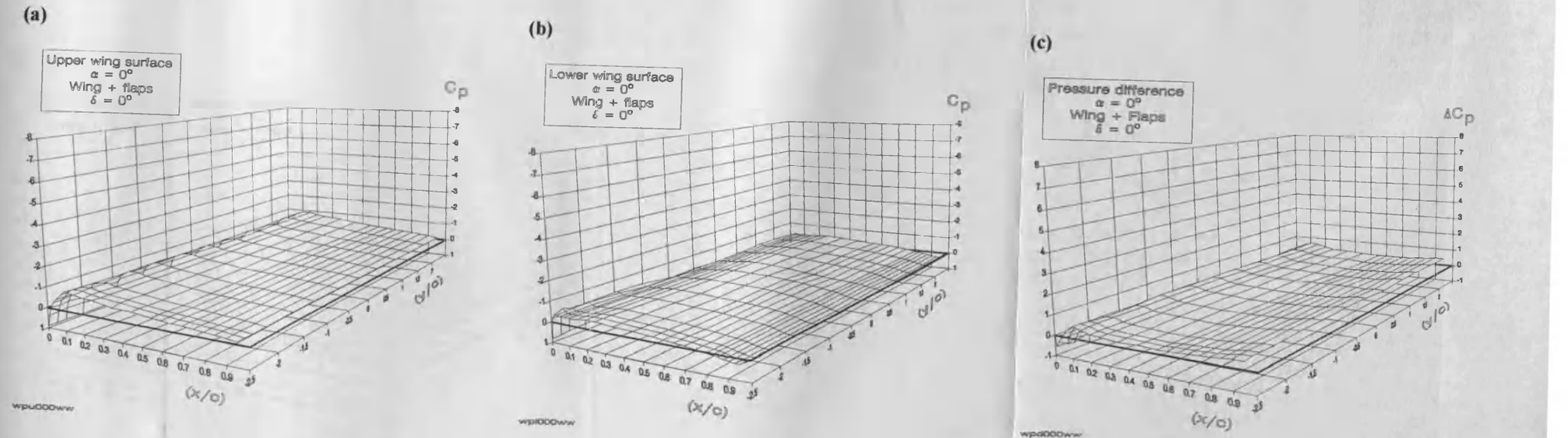

Fig. 4.2 **Wing pressure distribution for wing & flaps, $\alpha = 0^o$, $\delta = 0^o$**

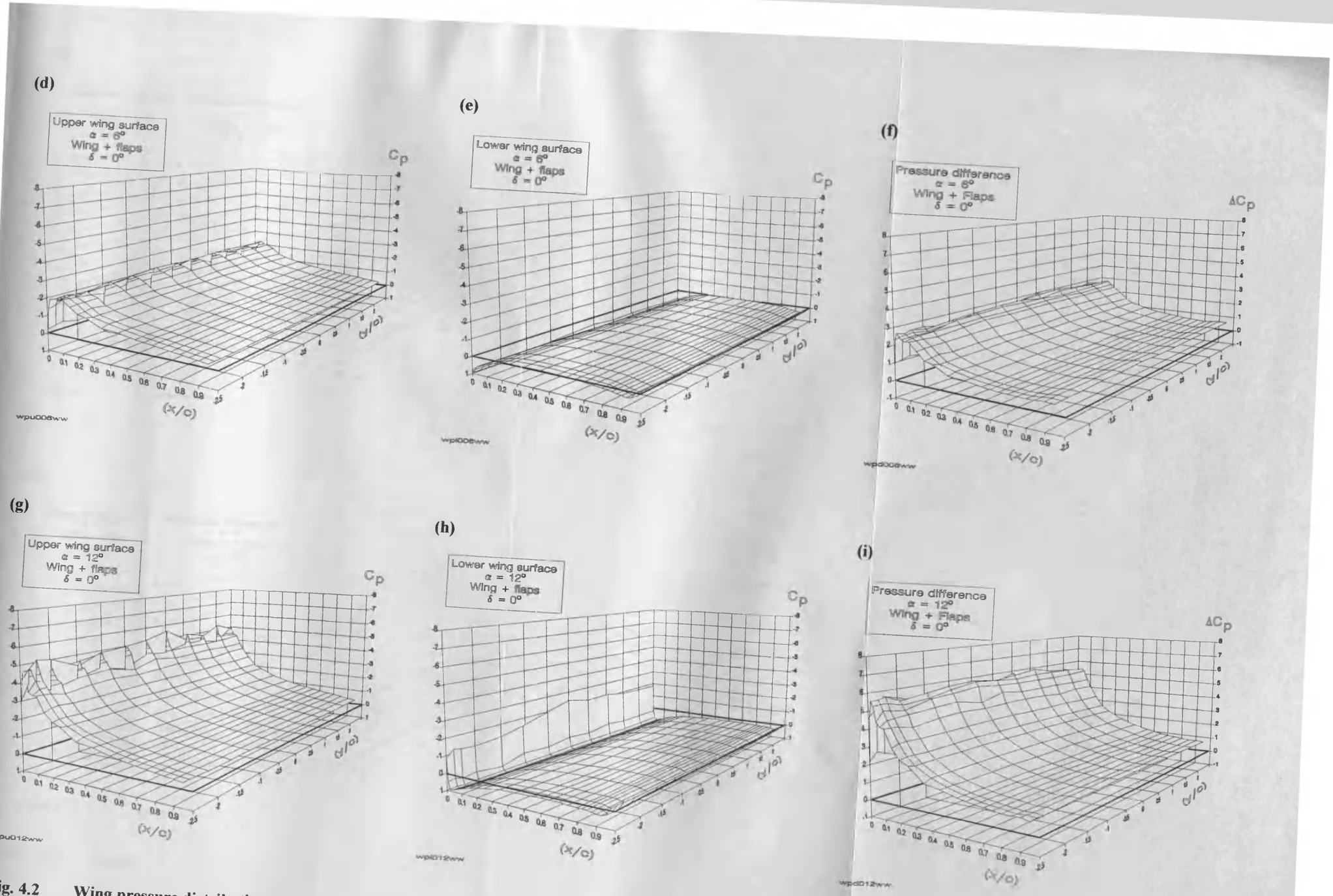

Fig. 4.2 **Wing pressure distribution for wing & flaps, $\alpha = 6^o, 12^o; \delta = 0^o$**

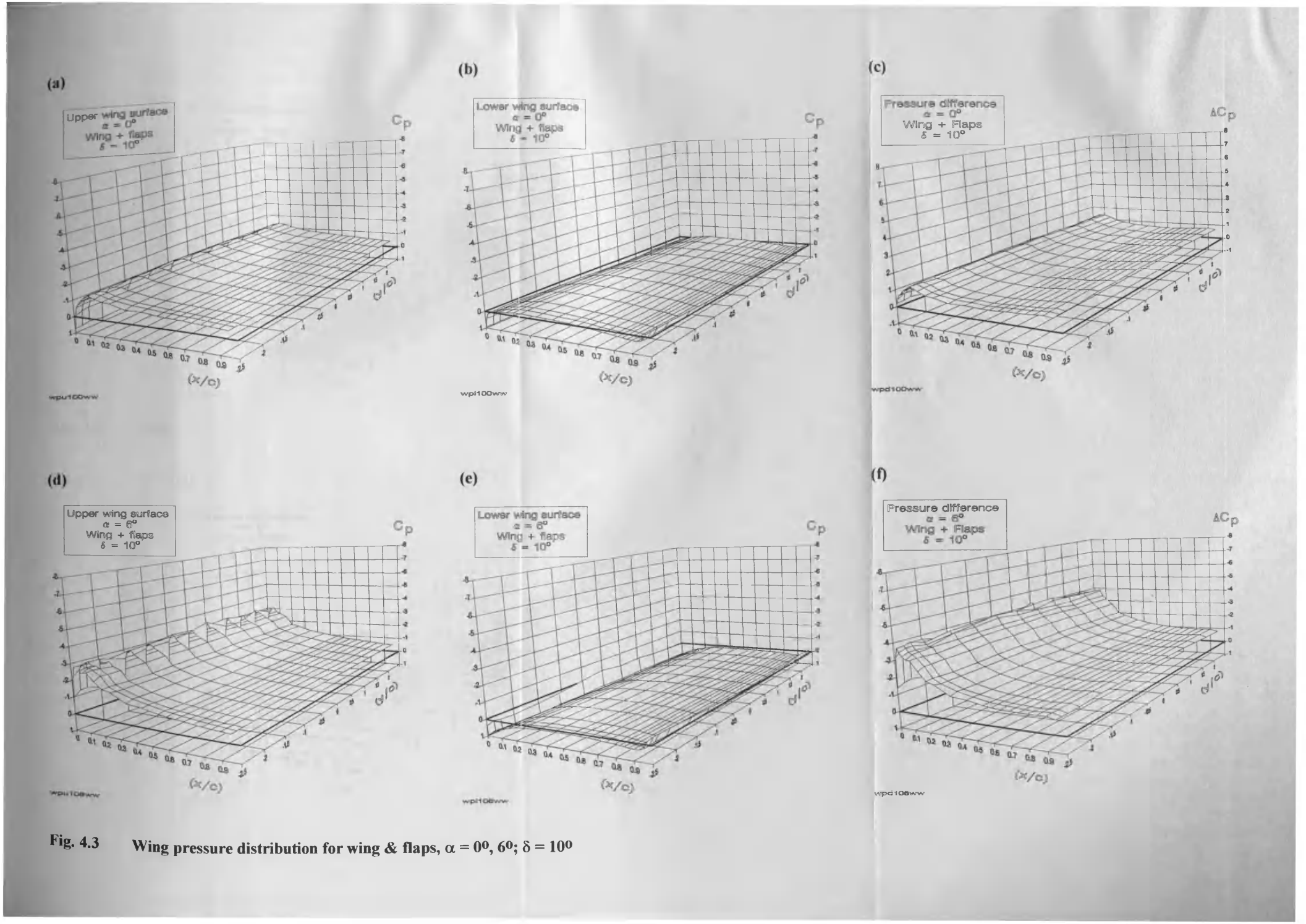

Fig. 4.3 **Wing pressure distribution for wing & flaps, $\alpha = 0^0, 6^0$; $\delta = 10^0$**

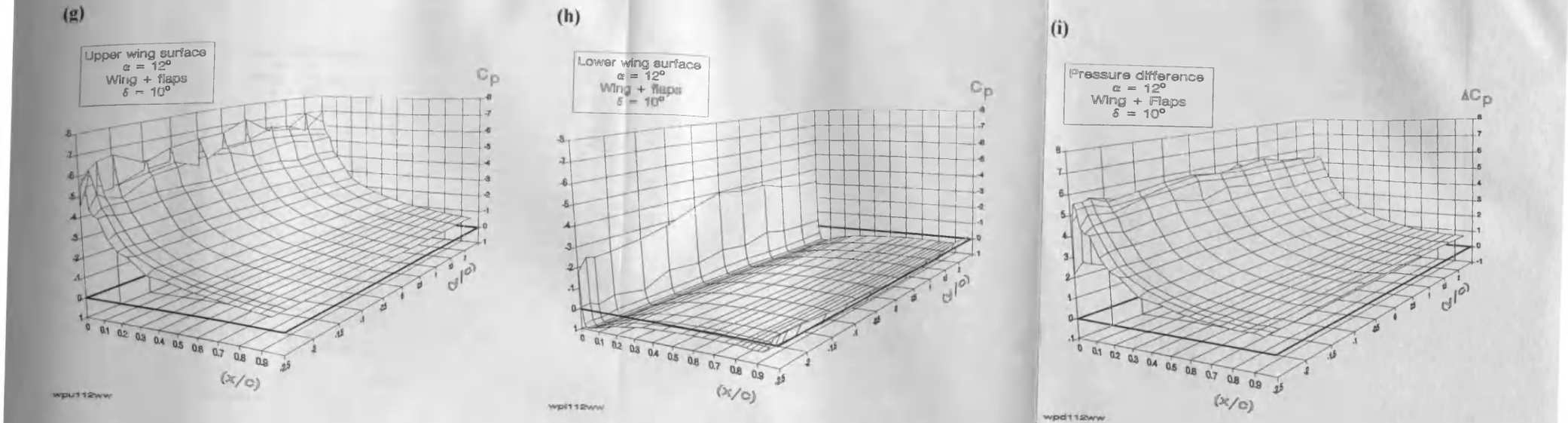

Fig. 4.3 **Wing pressure distribution for wing & flaps, $\alpha = 12^o$, $\delta = 10^o$**

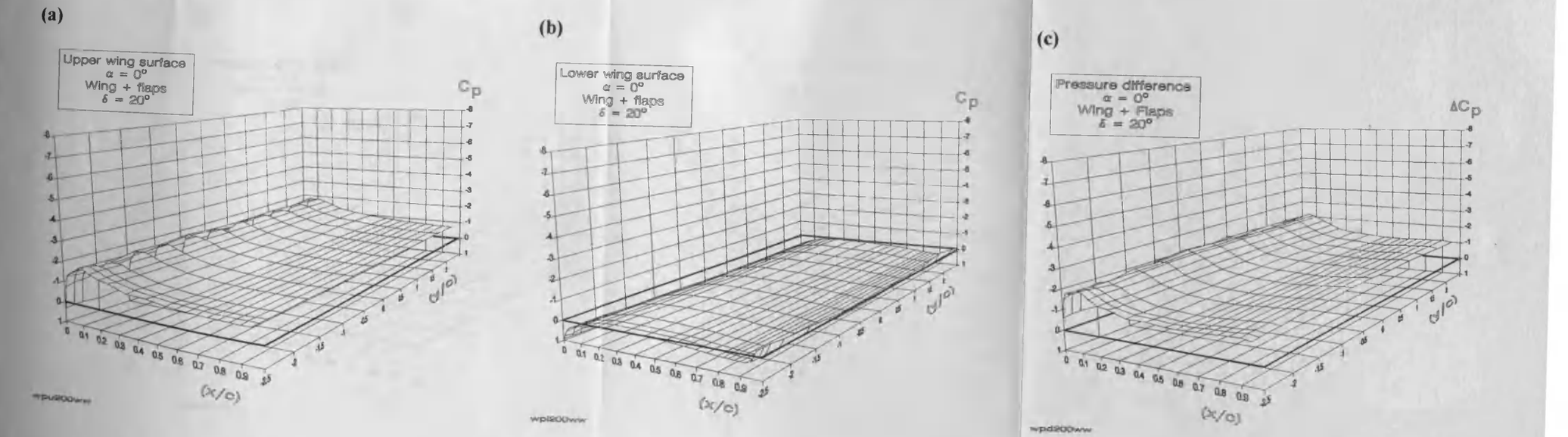

Fig. 4.4 **Wing pressure distribution for wing & flaps, $\alpha = 0^o$,$\delta = 20^o$**

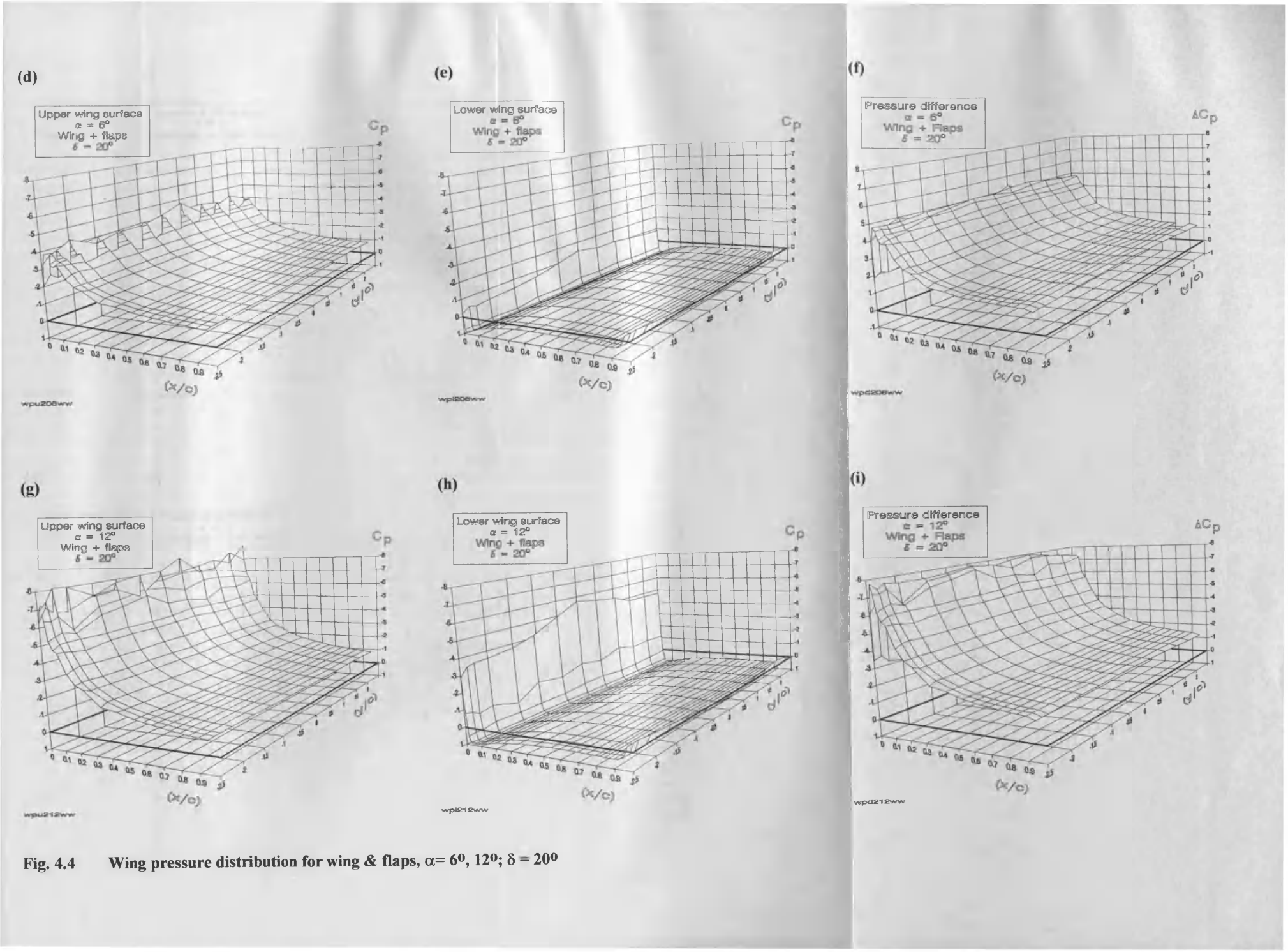

Fig. 4.4 Wing pressure distribution for wing & flaps, $\alpha = 6^0, 12^0$; $\delta = 20^0$

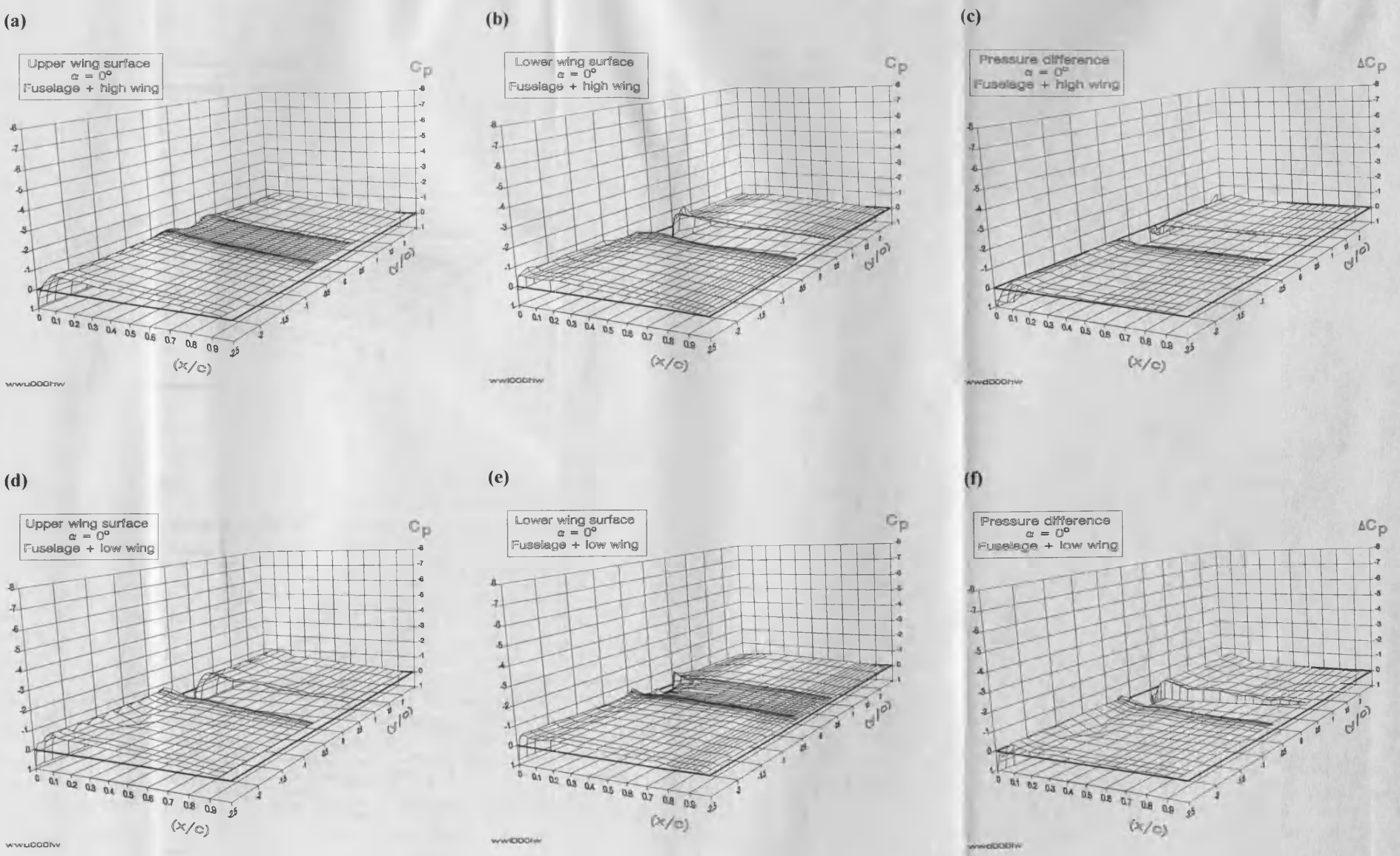

Fig. 4.5 Wing pressure distribution for fuselage & wing, $\alpha = 0^0$

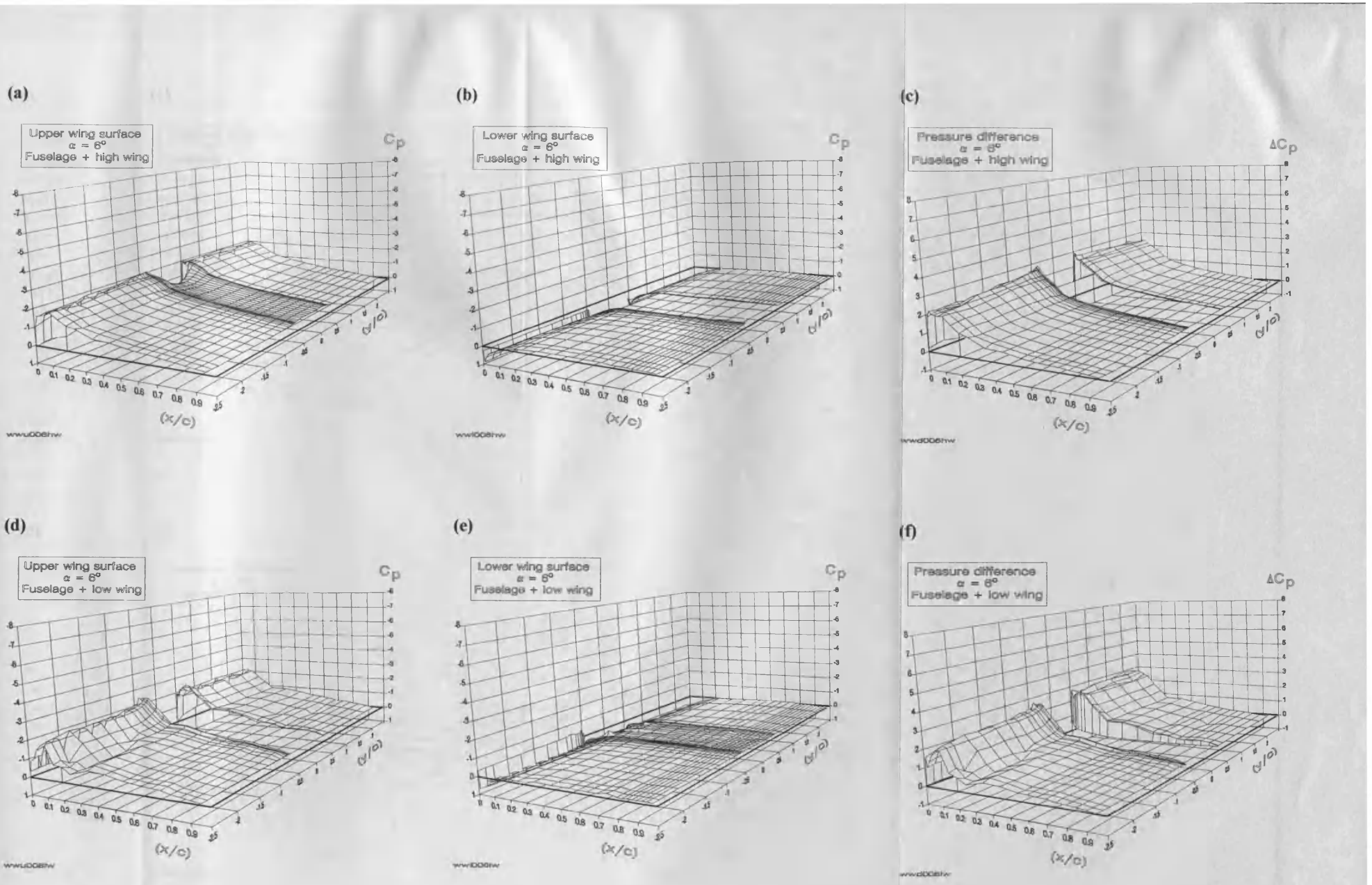

Fig. 4.6 **Wing pressure distribution for fuselage & wing, $\alpha = 6^0$**

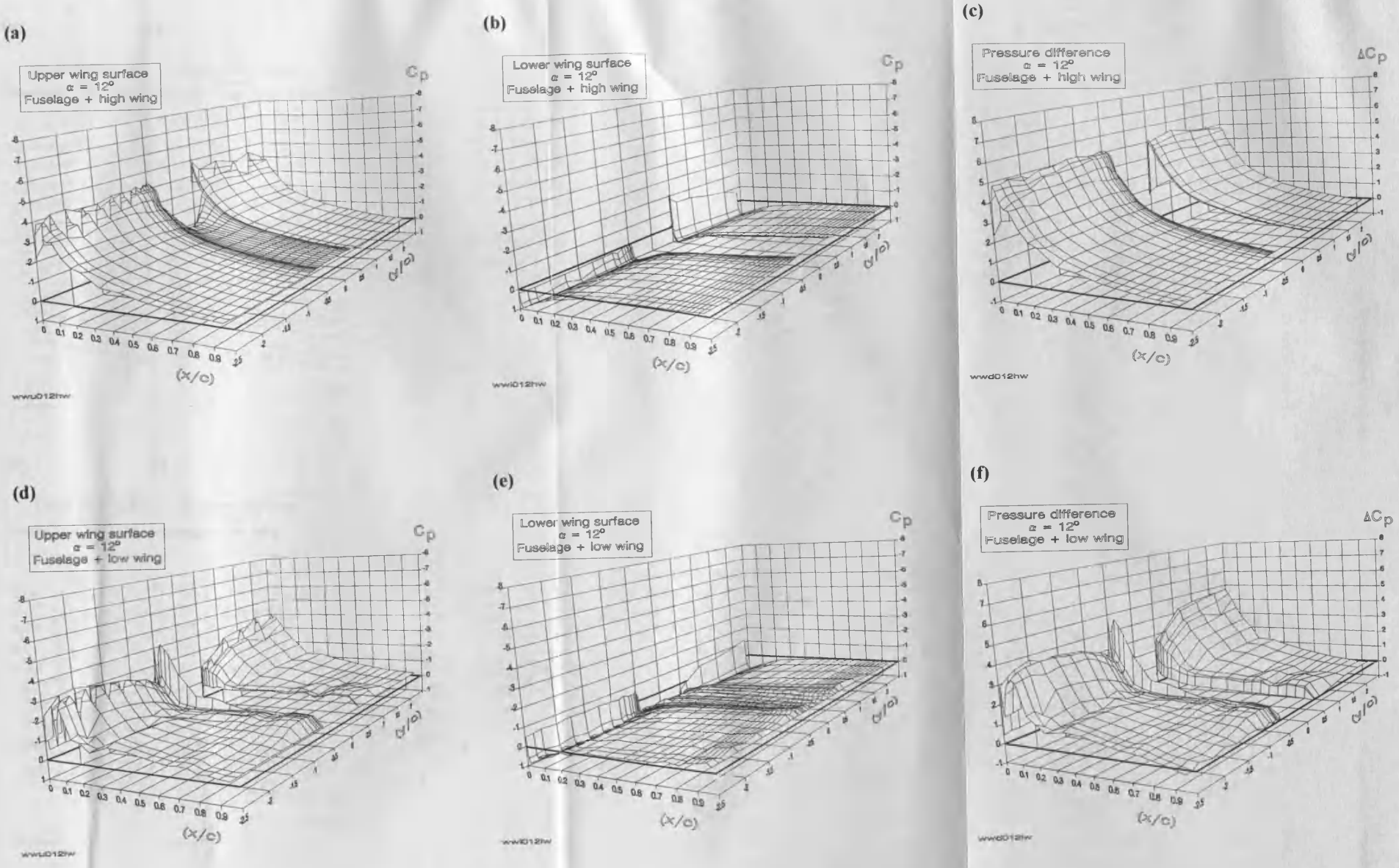

Fig. 4.7 **Wing pressure distribution for fuselage & wing, $\alpha = 12^o$**

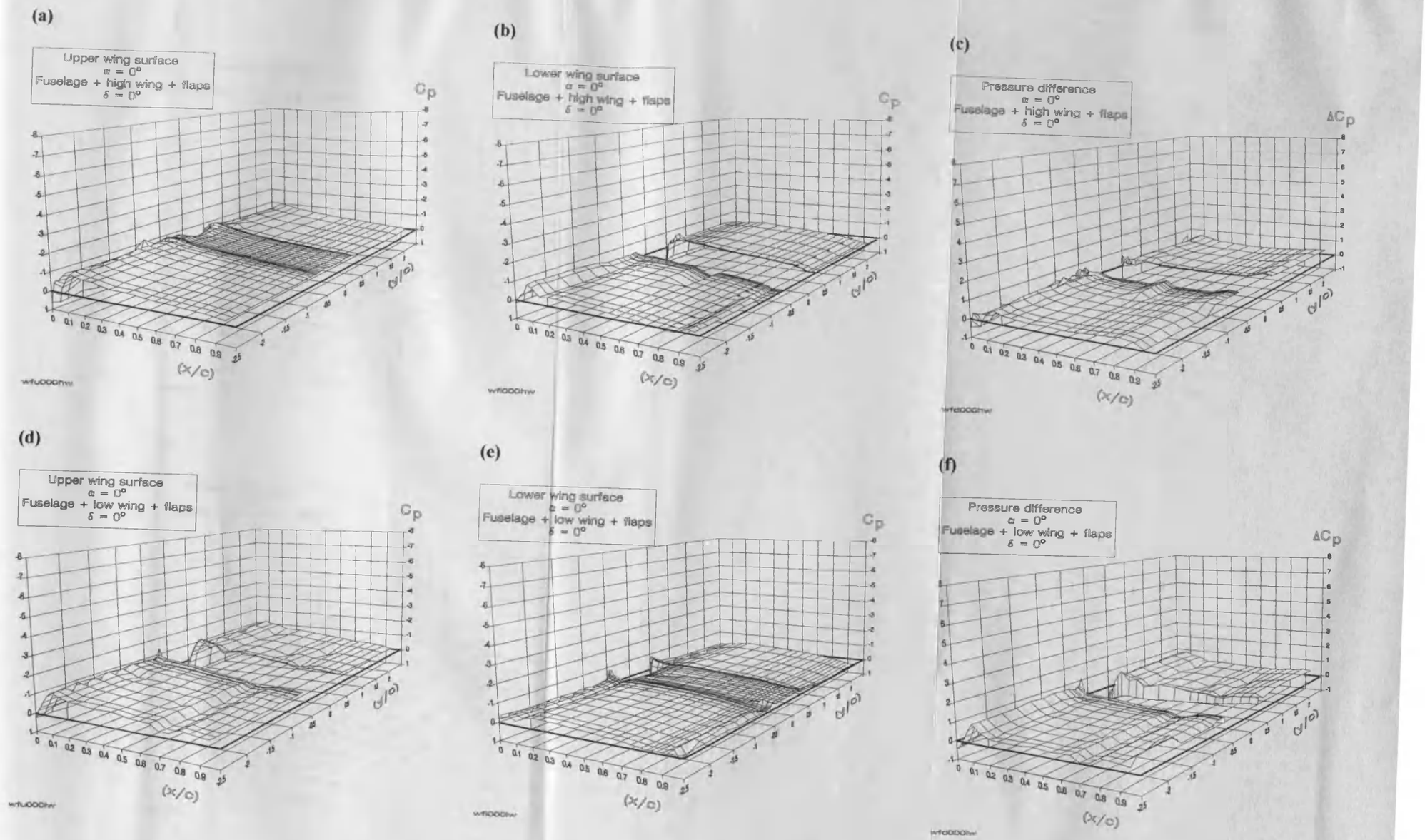

Fig. 4.8 **Wing pressure distribution for fuselage & wing & flaps, $\alpha = 0^o$, $\delta = 0^o$**

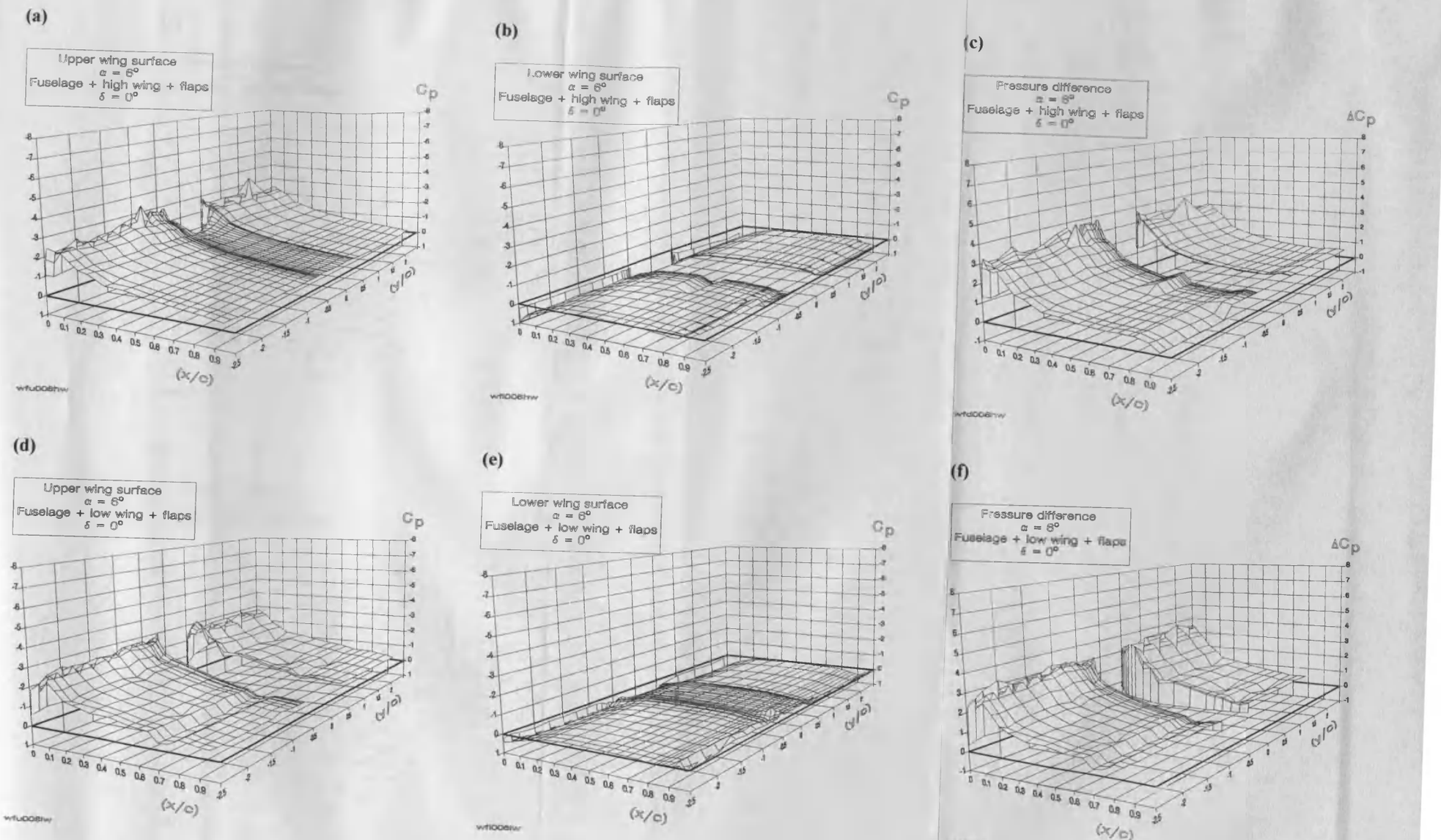

Fig. 4.9 **Wing pressure distribution for fuselage & wing & flaps, $\alpha = 6^0$, $\delta = 0^0$**

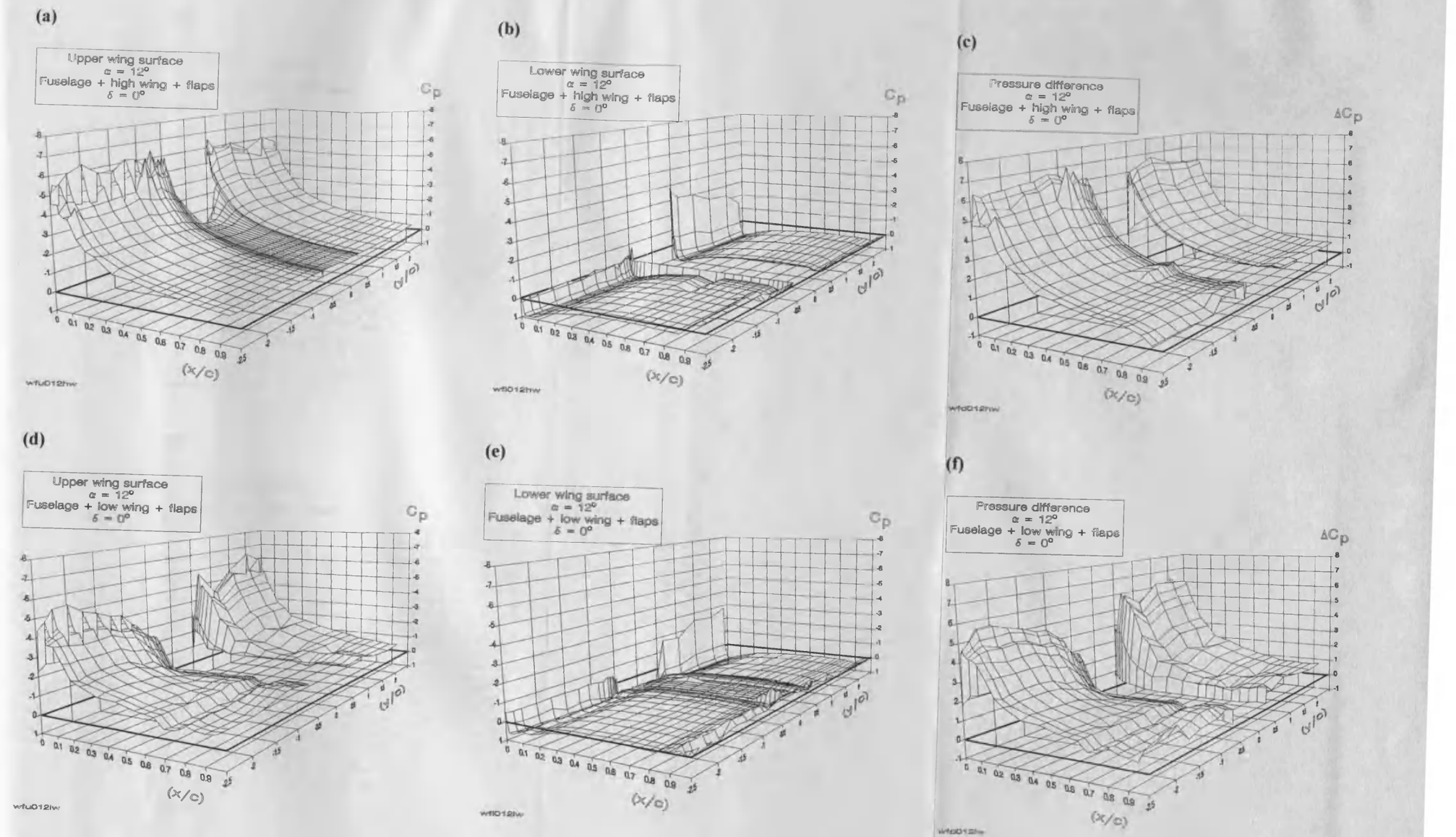

Fig. 4.10 **Wing pressure distribution for fuselage & wing & flaps, $\alpha = 12^0$, $\delta = 0^0$**

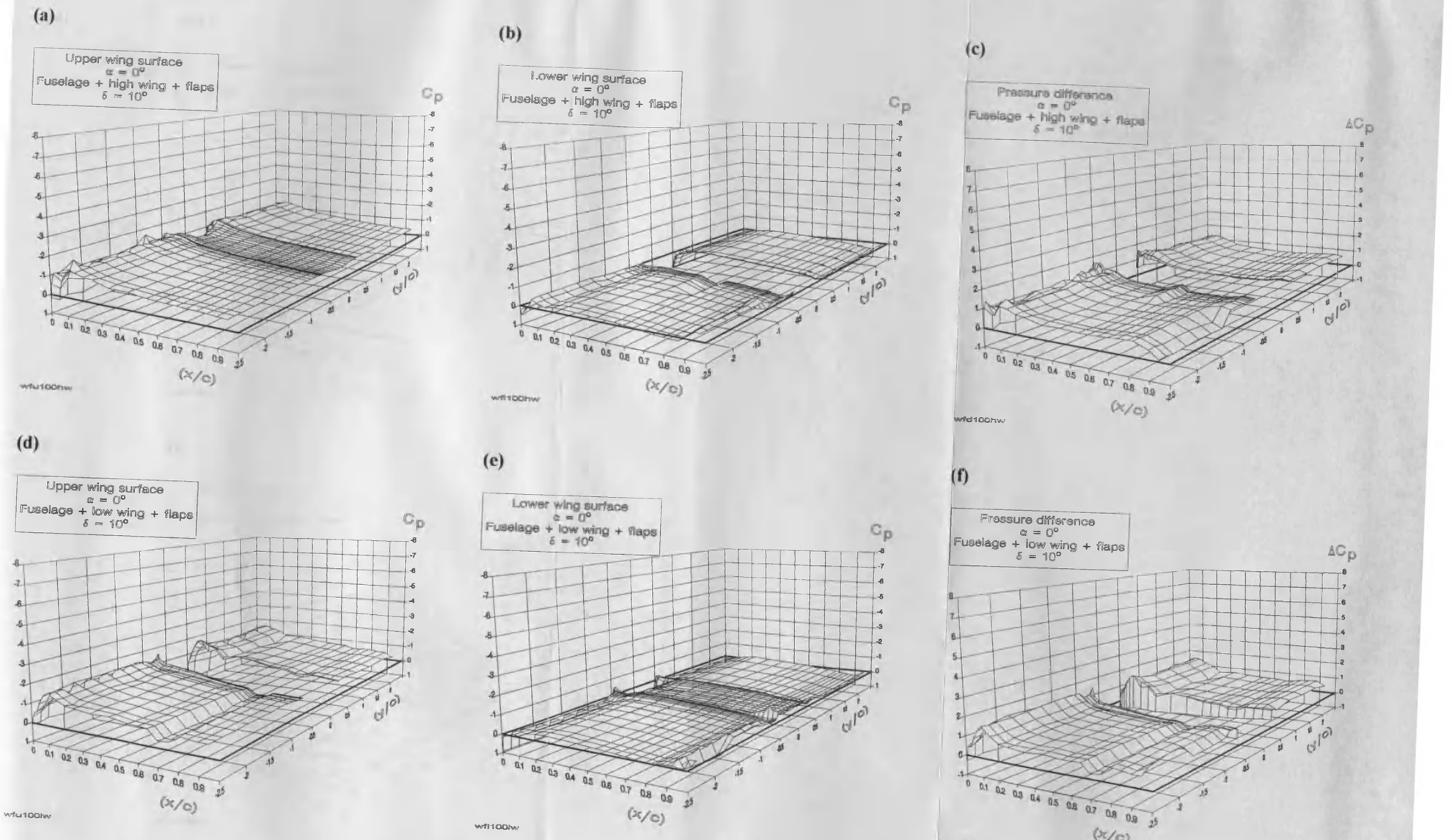

Fig. 4.11 **Wing pressure distribution for fuselage & wing & flaps, $\alpha = 0^o$, $\delta = 10^o$**

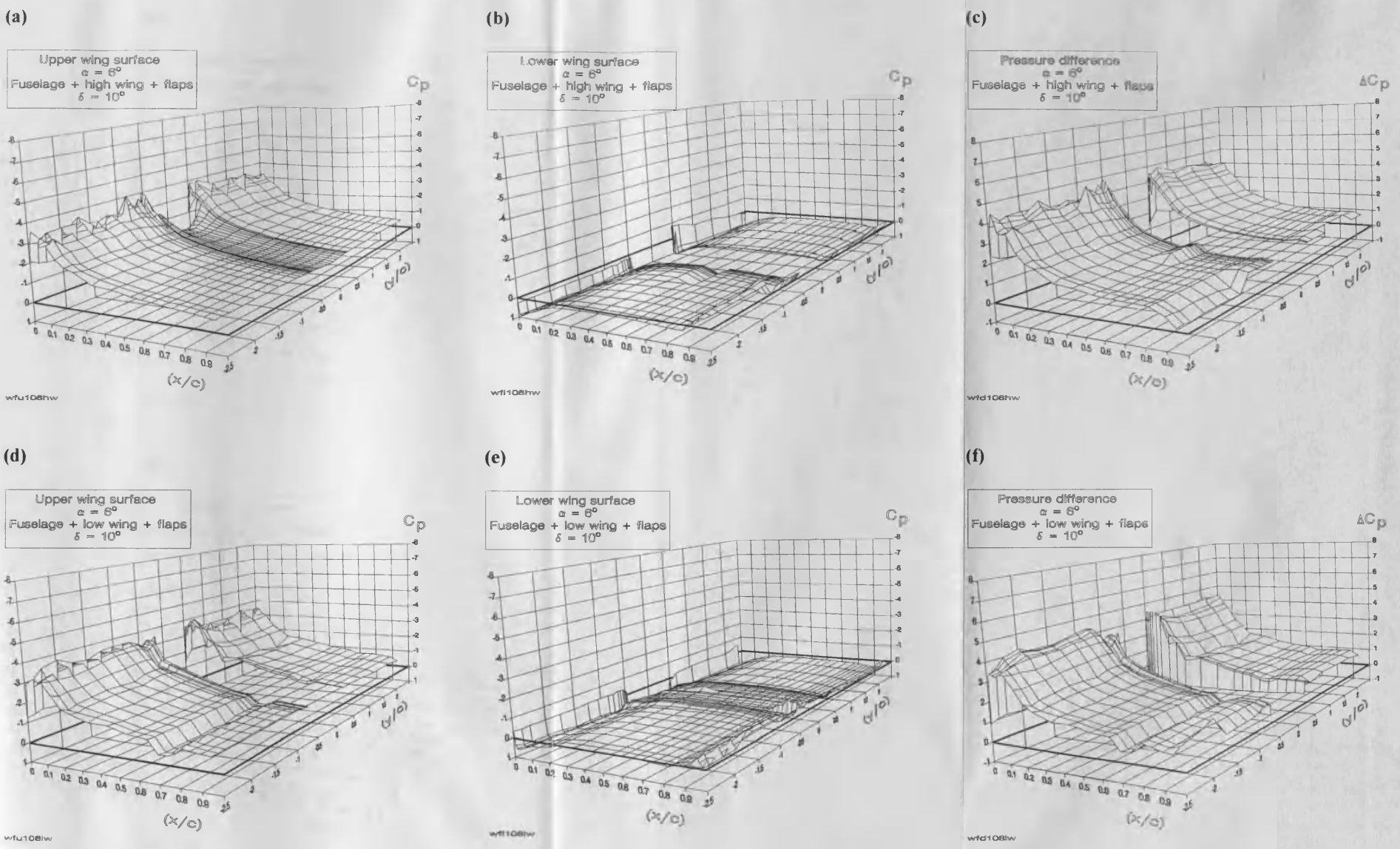

Fig 4.12 **Wing pressure distribution for fuselage & wing & flaps, $\alpha = 6^0$, $\delta = 10^0$**

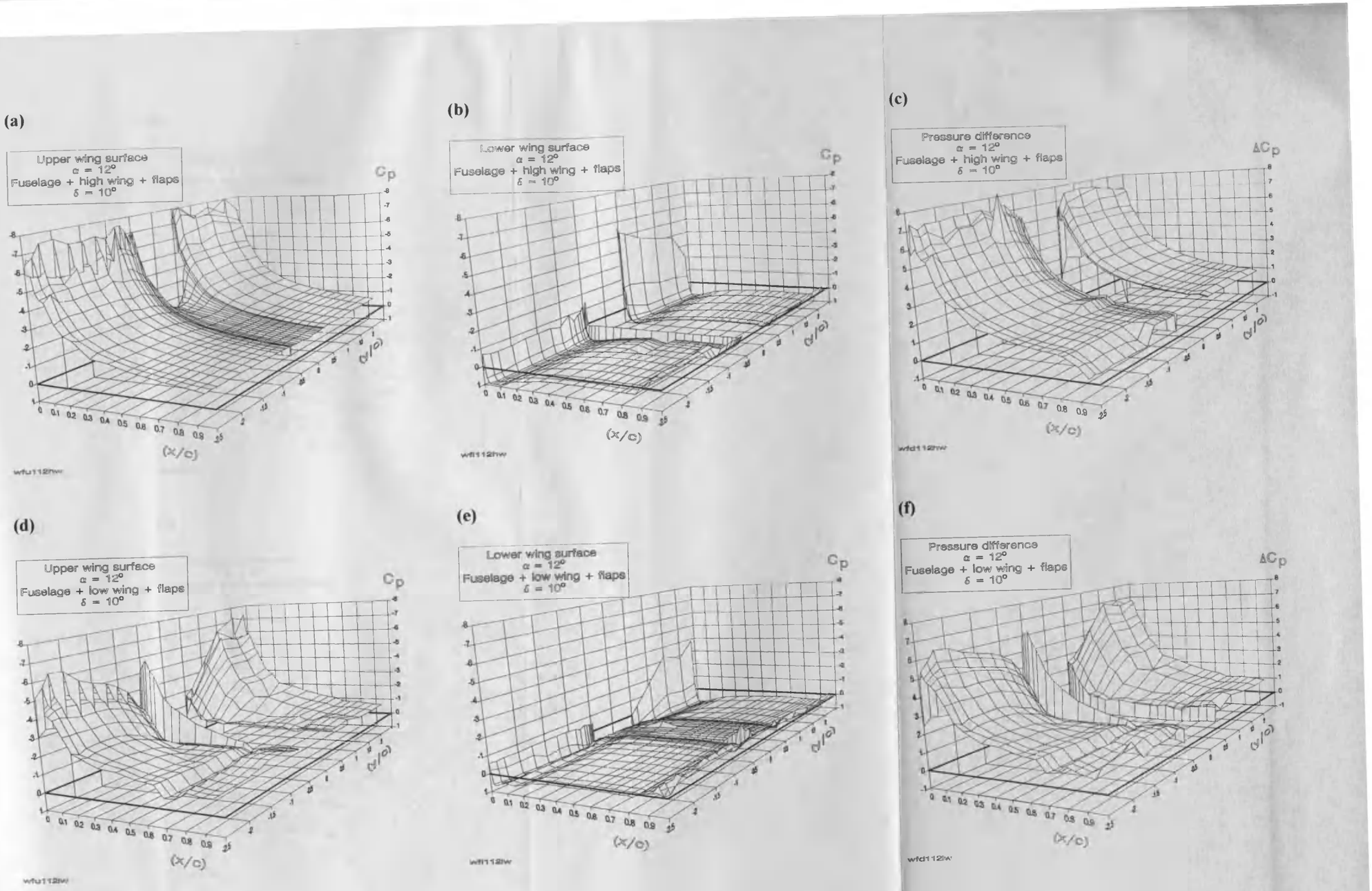

Fig. 4.13 **Wing pressure distribution for fuselage & wing & flaps, $\alpha = 12^o$, $\delta = 10^o$**

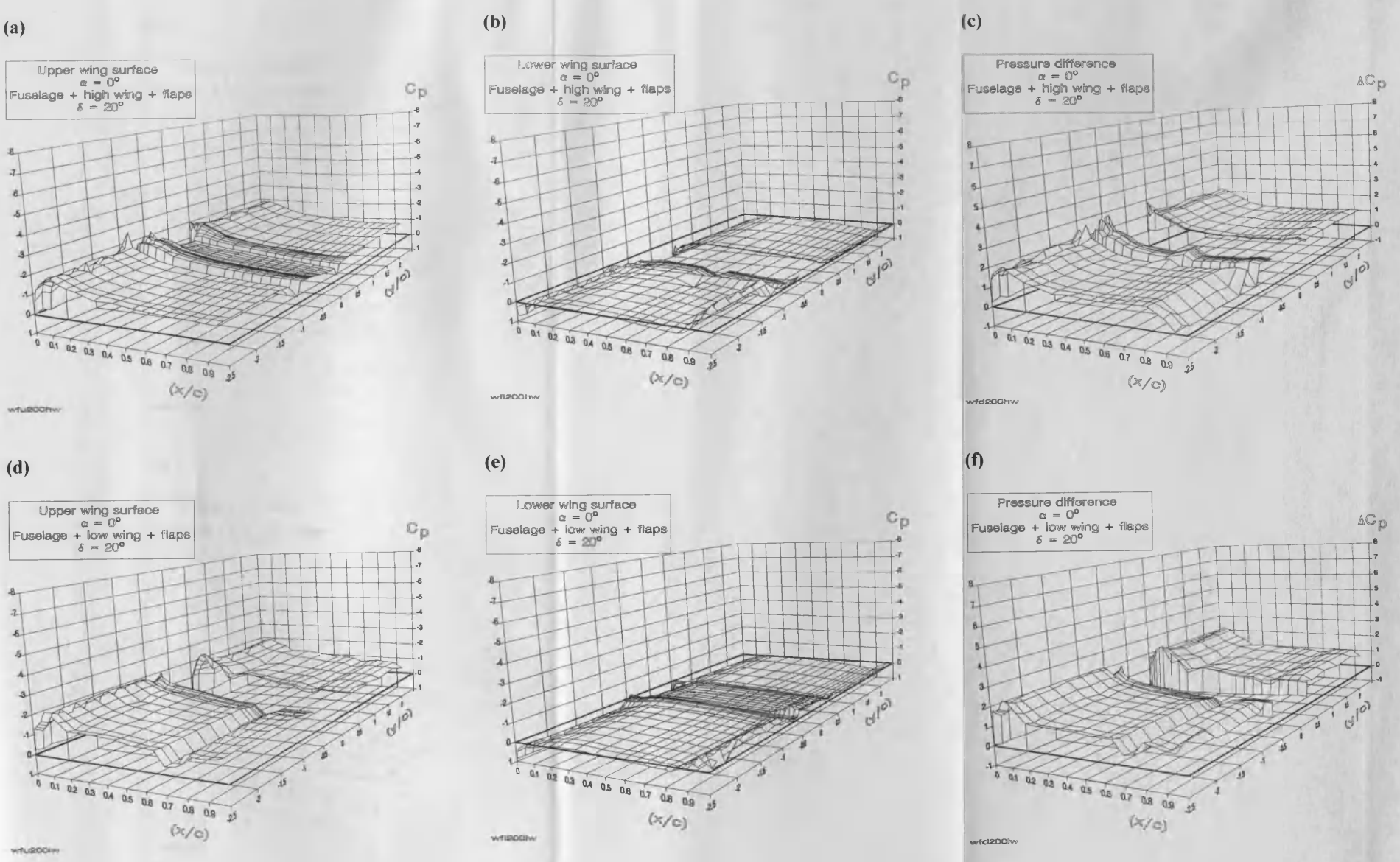

Fig. 4.14 **Wing pressure distribution for fuselage & wing & flaps, $\alpha = 0^0$, $\delta = 20^0$**

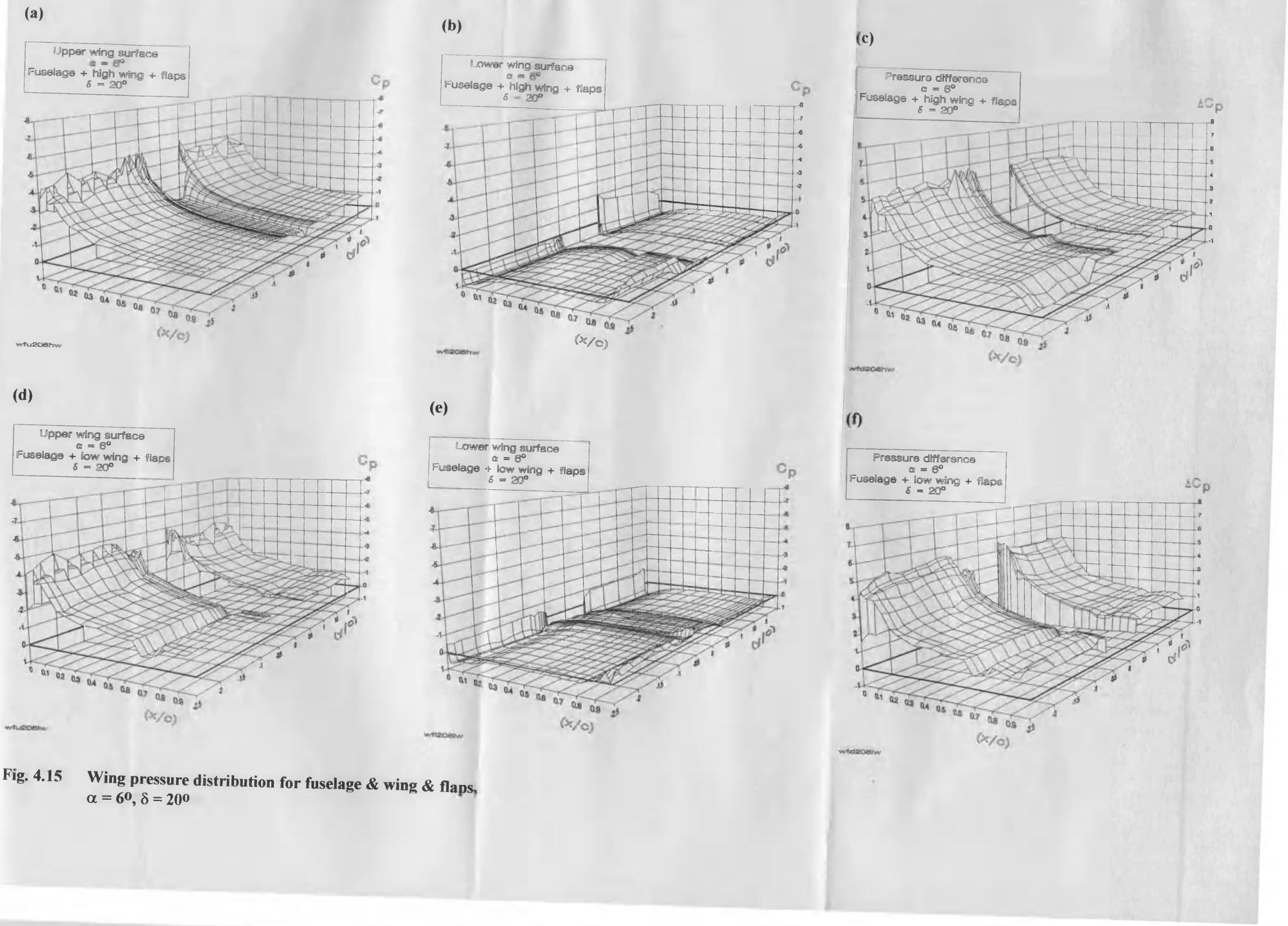

Fig. 4.15 **Wing pressure distribution for fuselage & wing & flaps, $\alpha = 6^0$, $\delta = 20^0$**

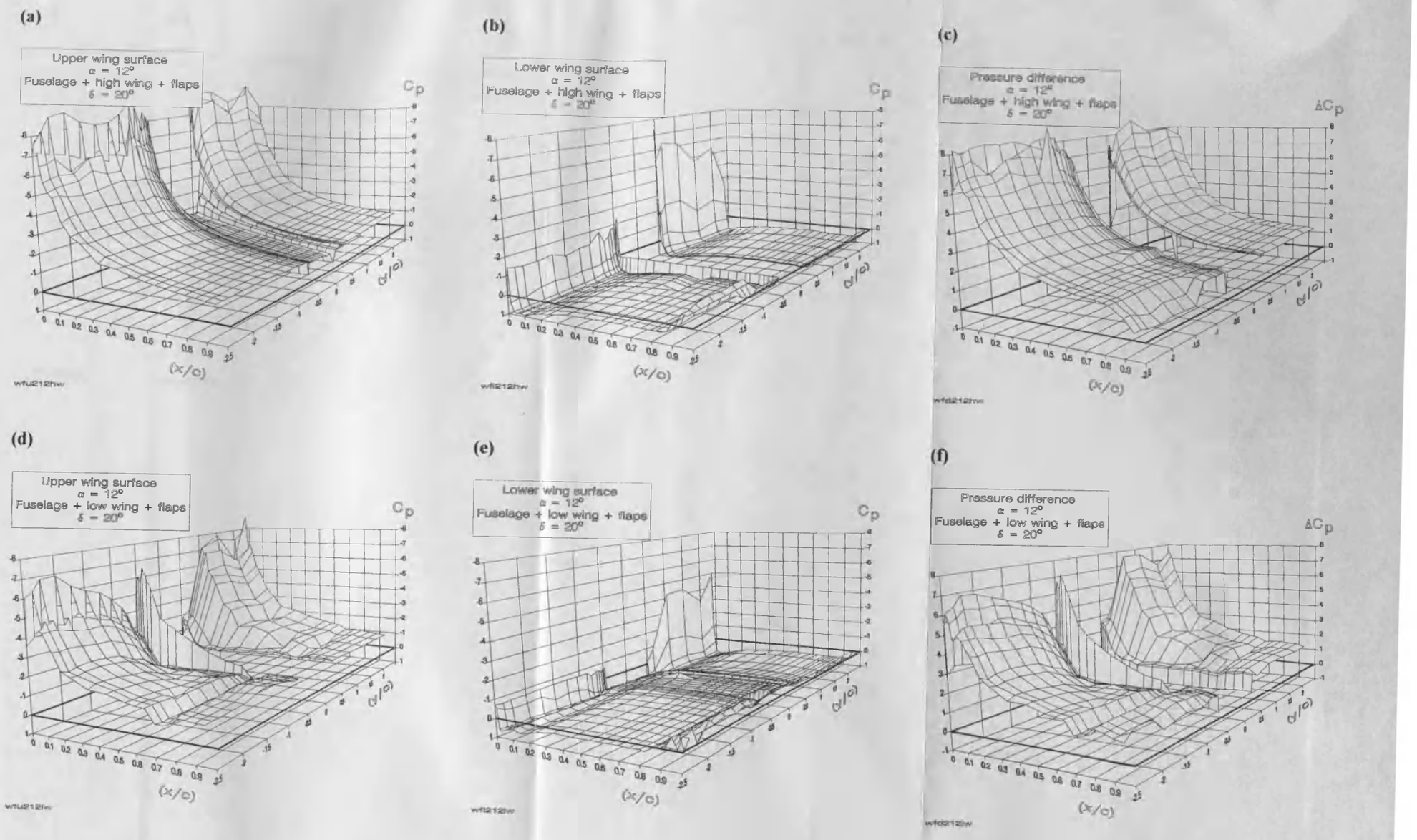

Fig. 4.16 **Wing pressure distribution for fuselage & wing & flaps, $\alpha = 12^o$, $\delta = 20^o$**

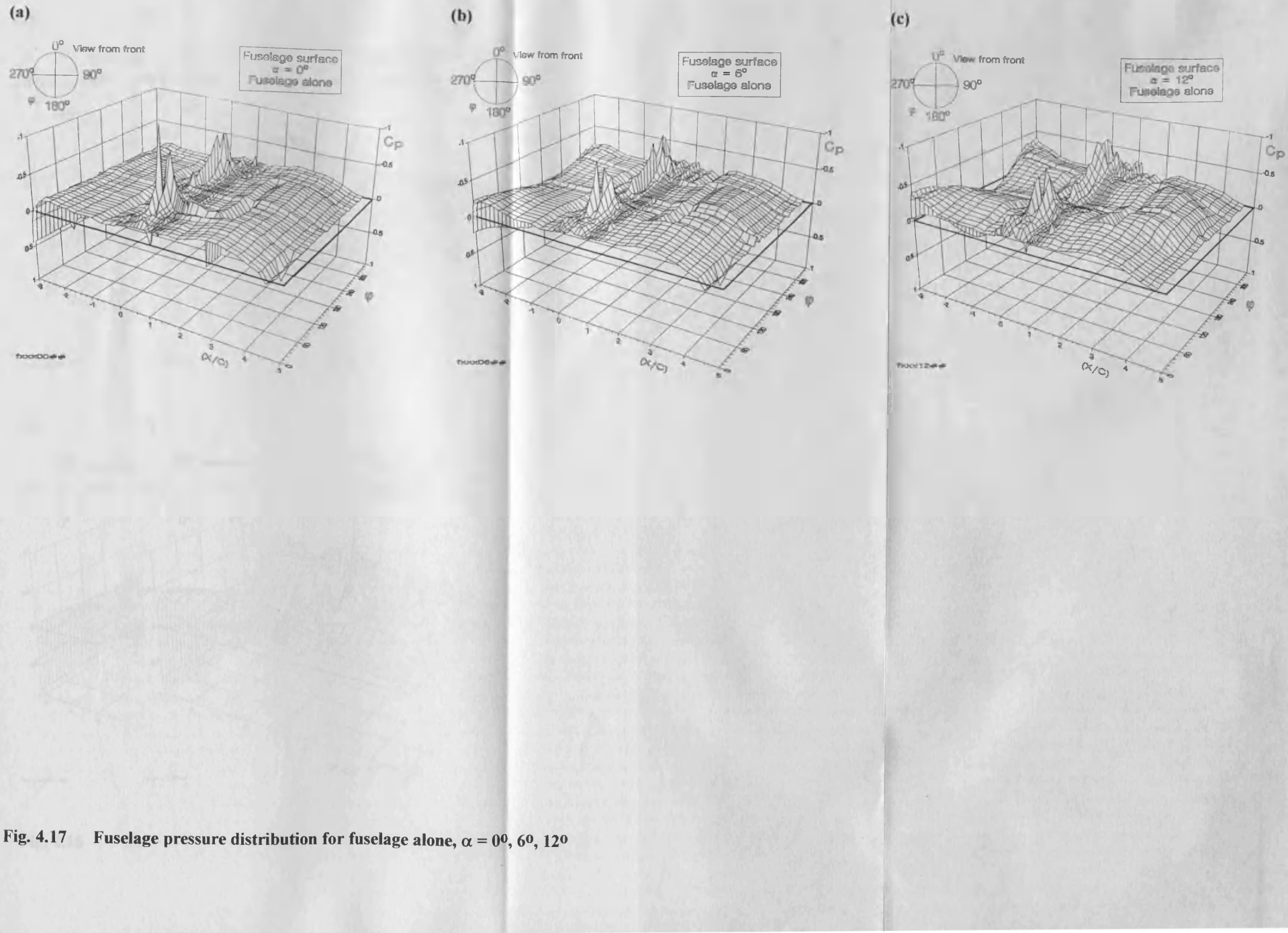

Fig. 4.17 Fuselage pressure distribution for fuselage alone, $\alpha = 0^0, 6^0, 12^0$

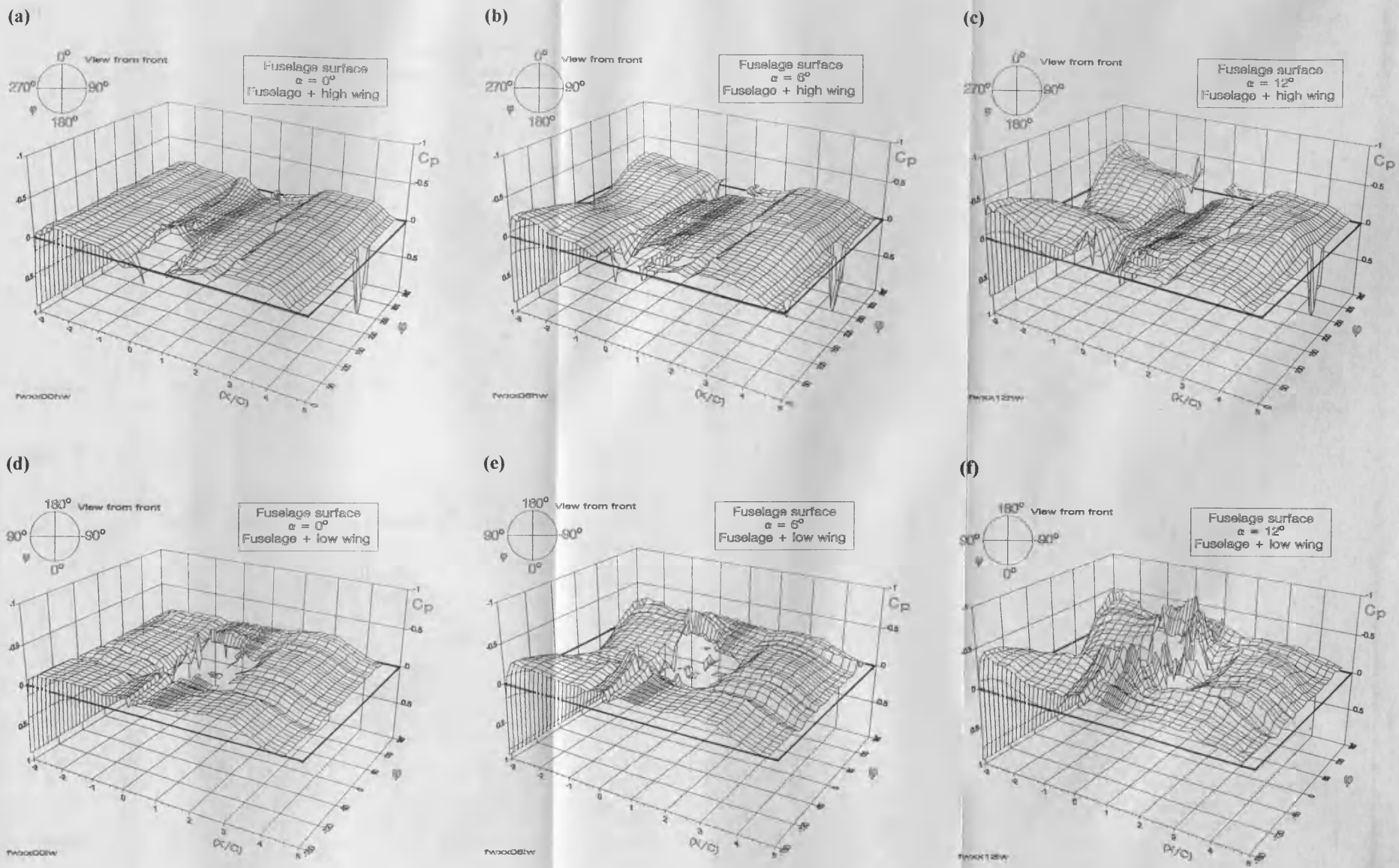

Fig. 4.18 Fuselage pressure distribution for fuselage & wing, $\alpha = 0^o, 6^o, 12^o$

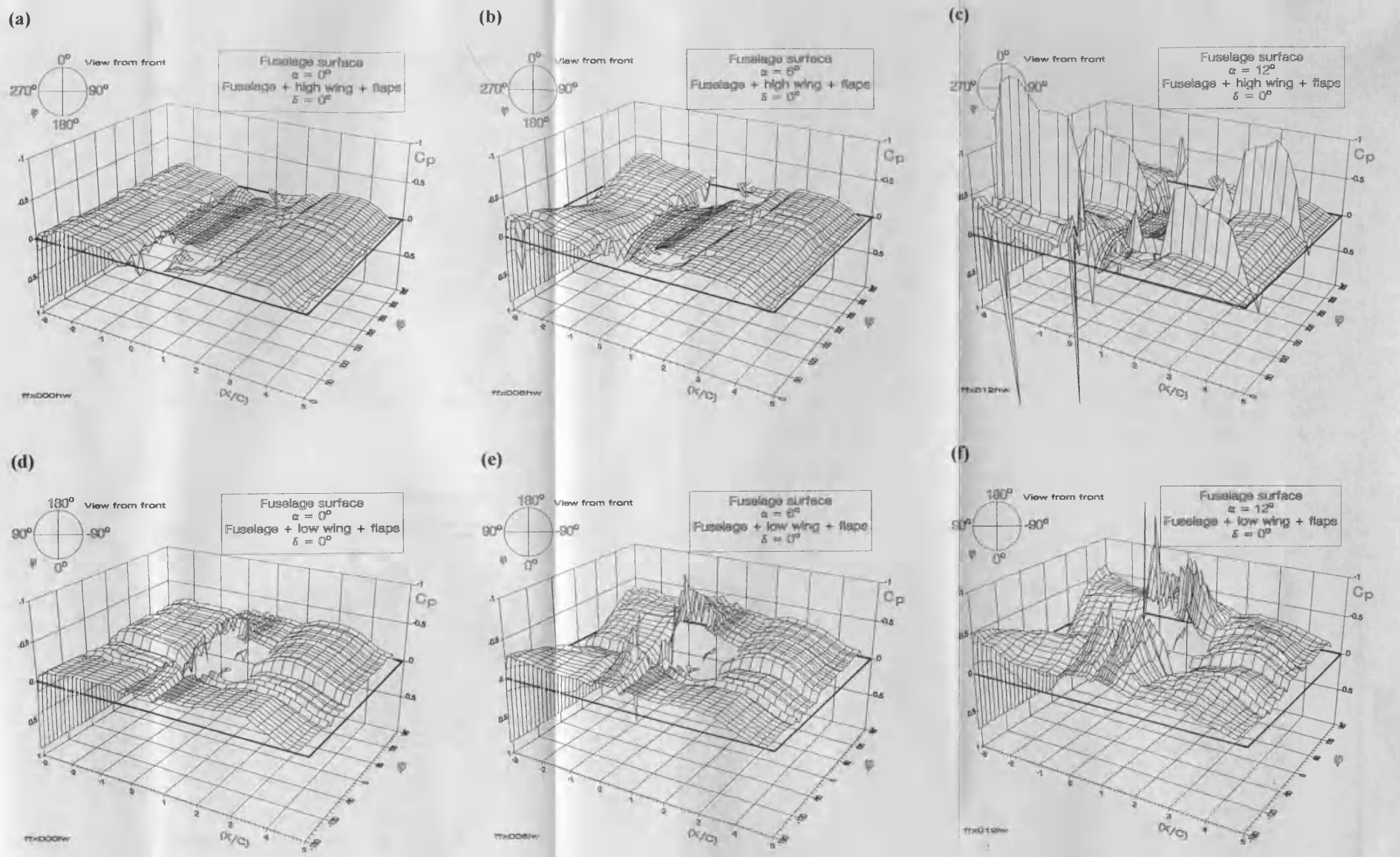

Fig. 4.19 Fuselage pressure distribution for fuselage & wing & flaps, $\alpha = 0^o, 6^o, 12^o; \delta = 0^o$

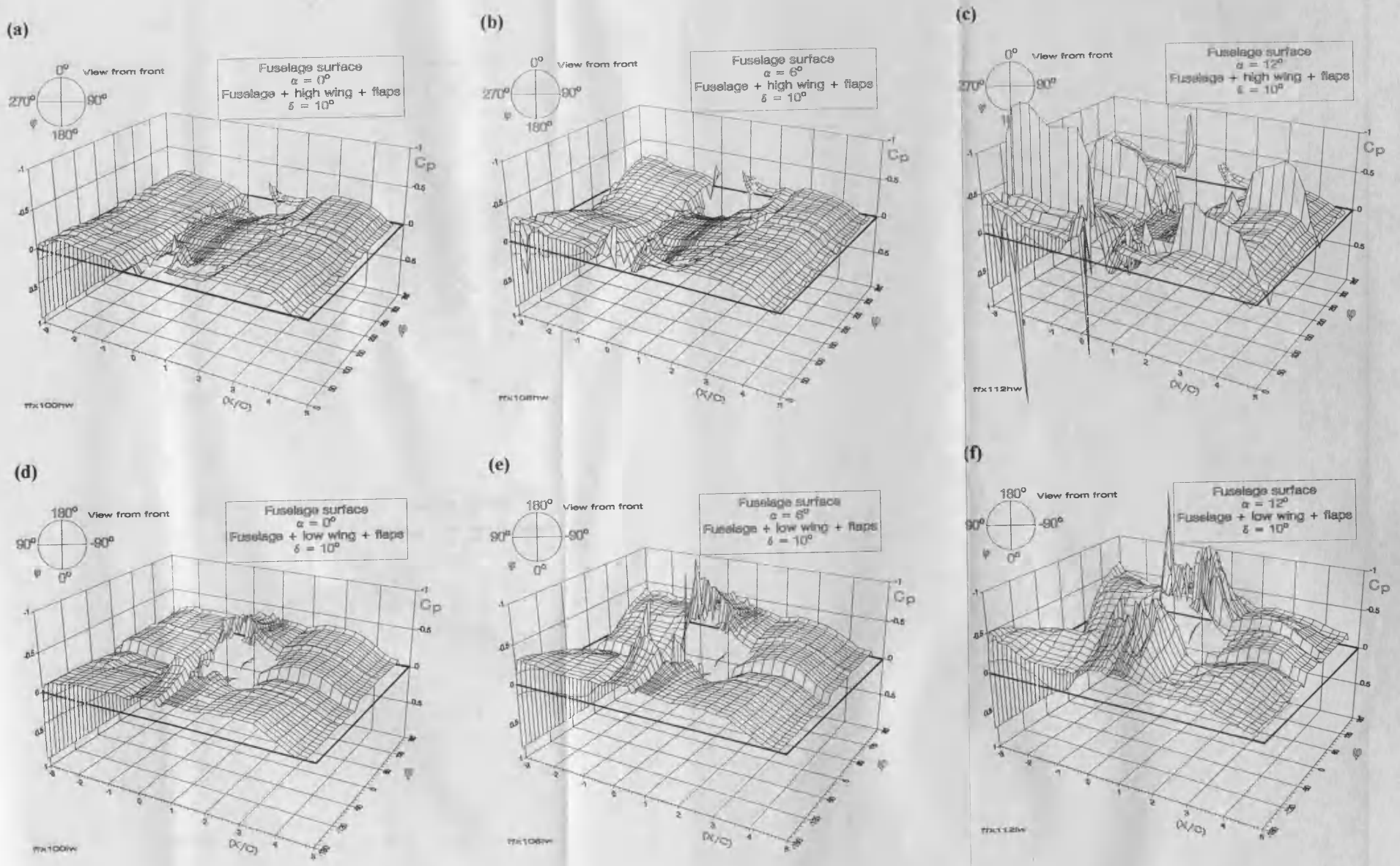

Fig. 4.20 Fuselage pressure distribution for fuselage & wing & flaps, $\alpha = 0^0, 6^0, 12^0; \delta = 10^0$

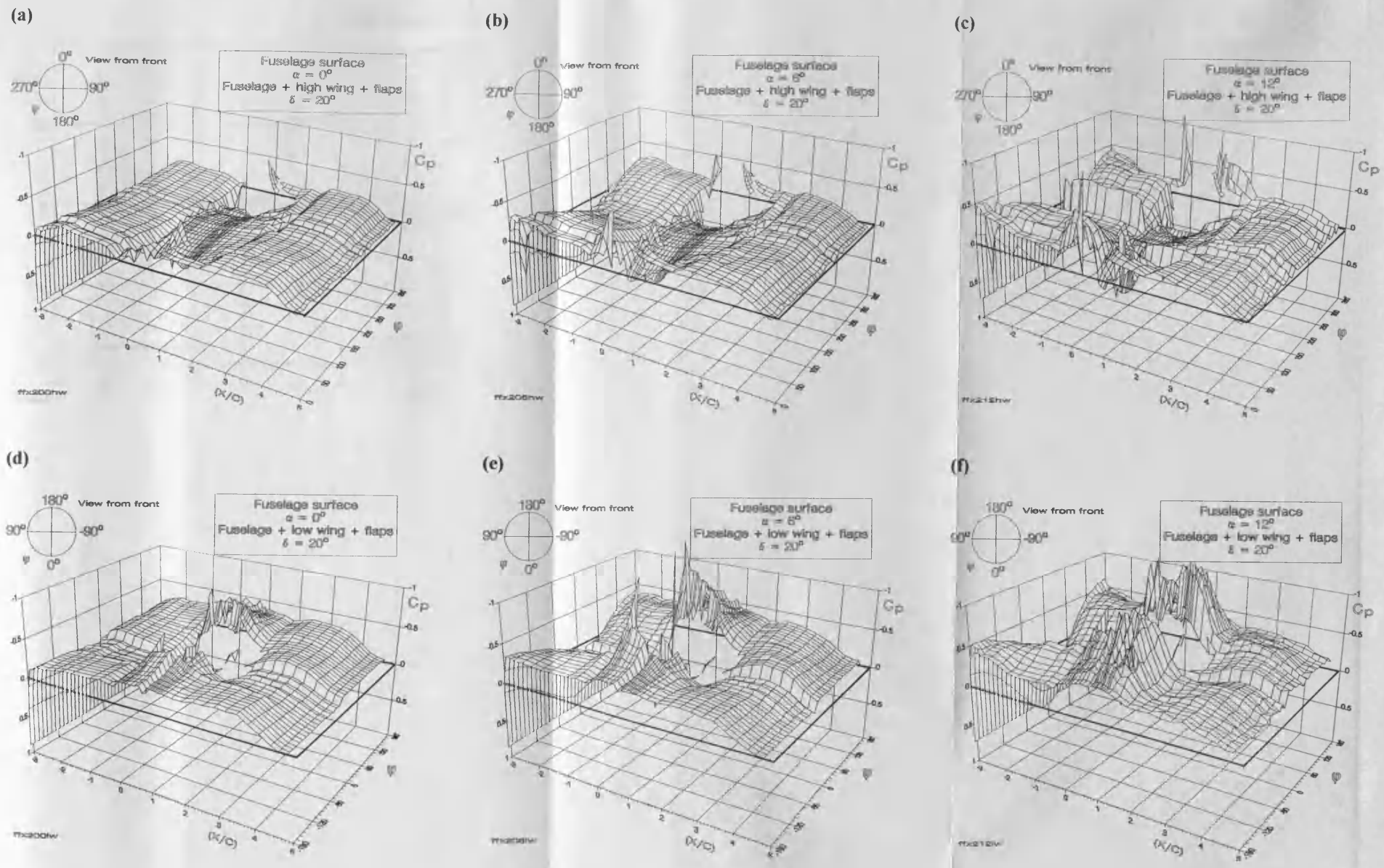

Fig. 4.21 Fuselage pressure distribution for fuselage & wing & flaps, $\alpha = 0^0, 6^0, 12^0$; $\delta = 20^0$

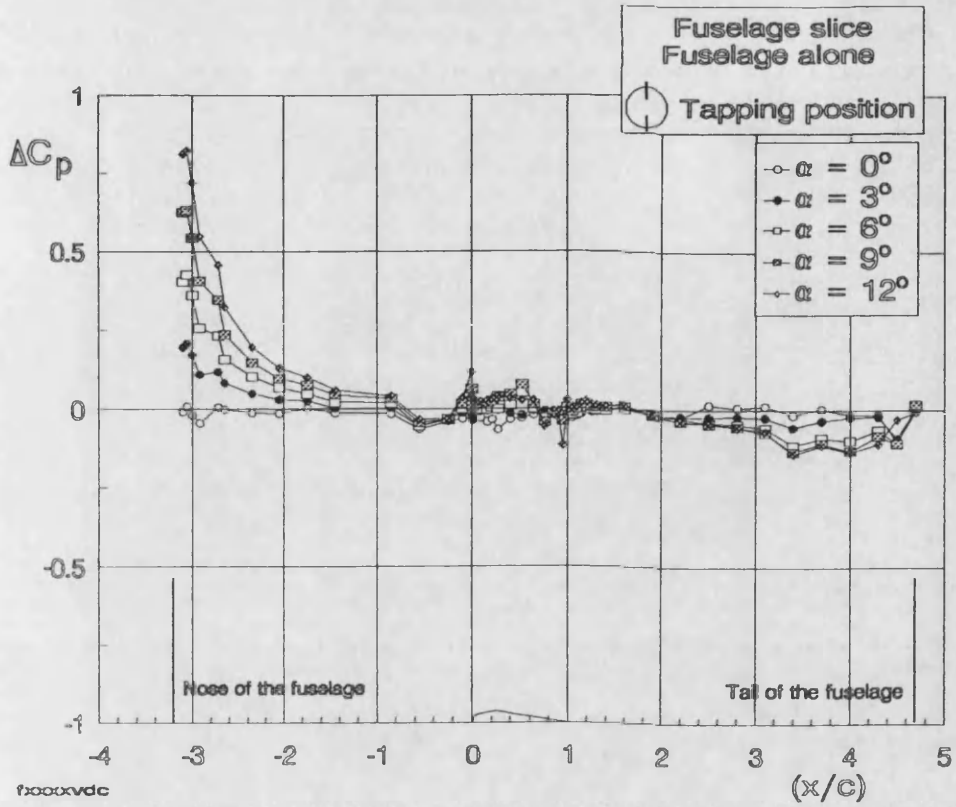

Fig. 4.22 Centreline pressure difference for fuselage alone, ($\varphi = 0°, 180°$)

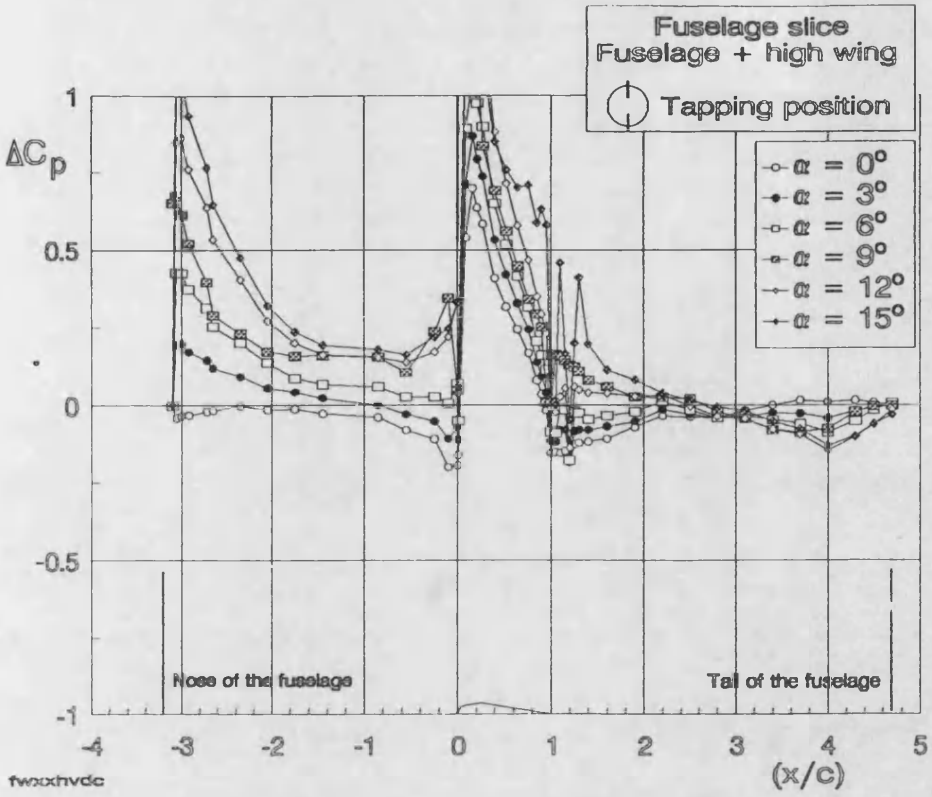

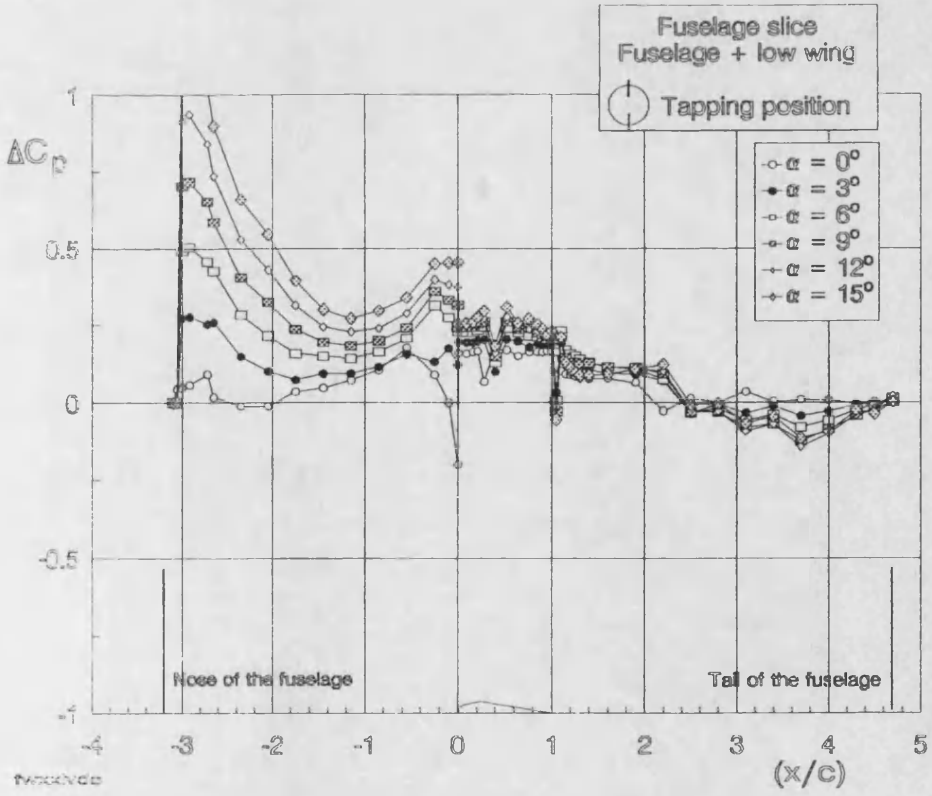

Fig. 4.23 Centreline pressure difference for fuselage & wing ($\varphi = 0°, 180°$), high wing/low wing

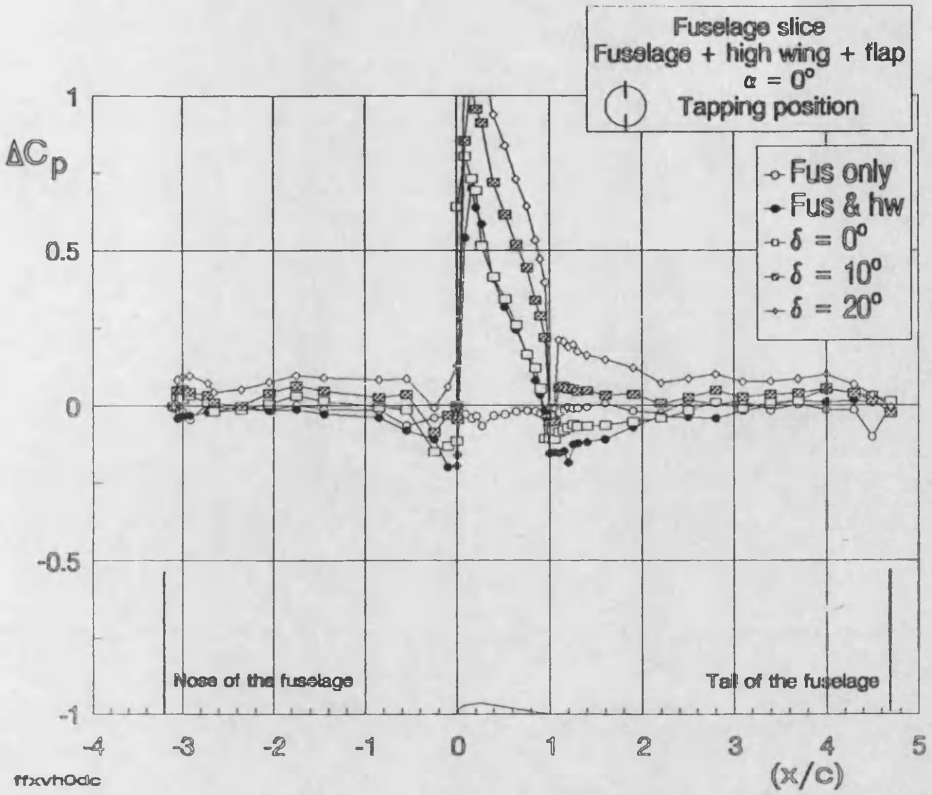

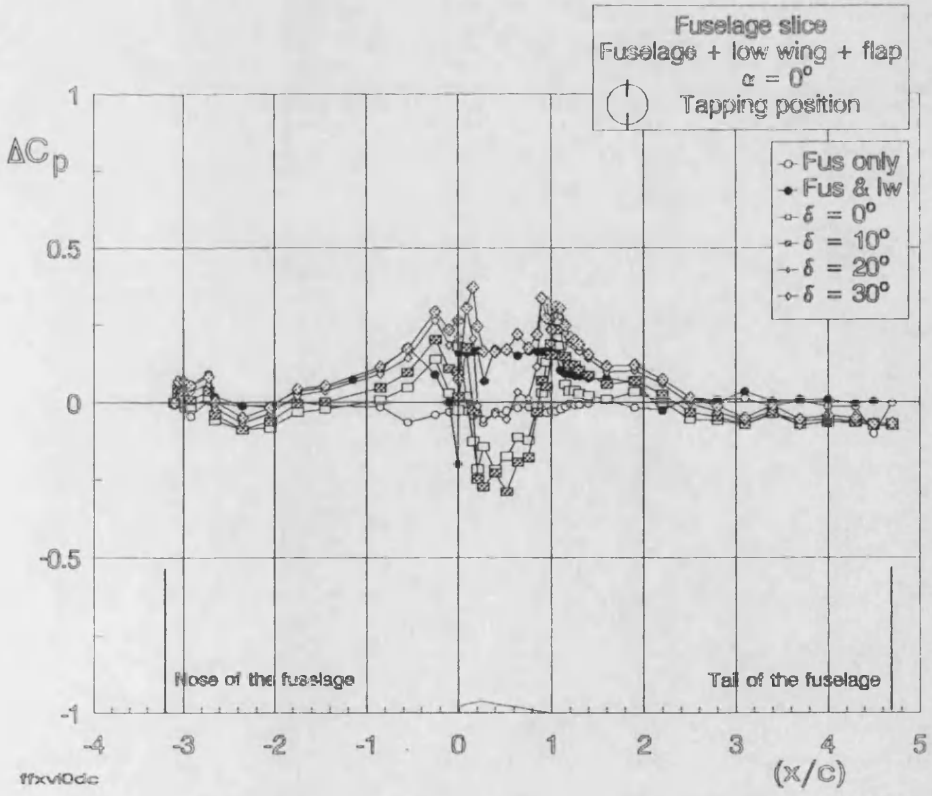

Fig. 4.24 Centreline pressure difference for fuselage & wing & flaps, ($\varphi = 0°, 180°$), high wing/low wing, $\alpha = 0^o$

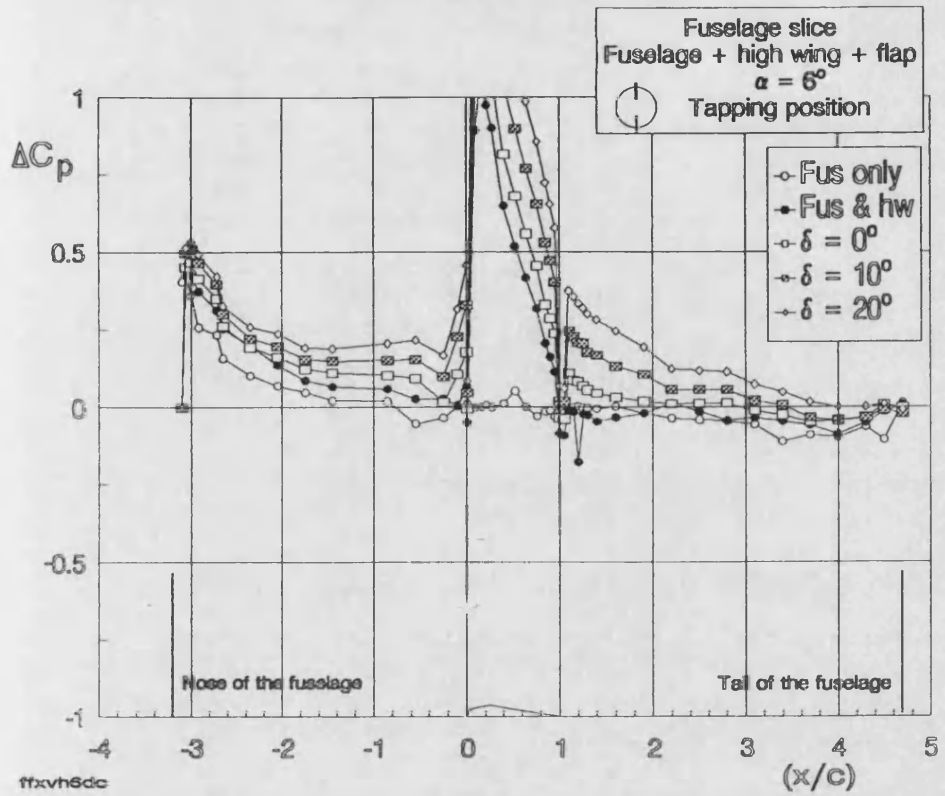

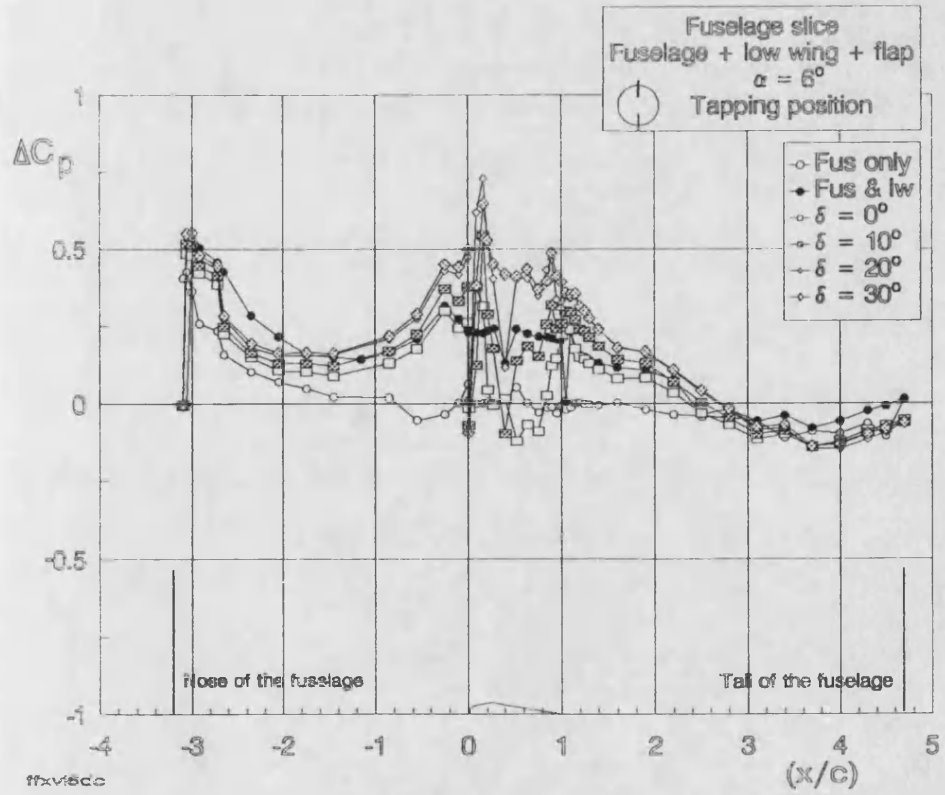

Fig. 4.25 Centreline pressure difference for fuselage & wing & flaps, ($\varphi = 0°, 180°$), high wing/low wing, $\alpha = 6^0$

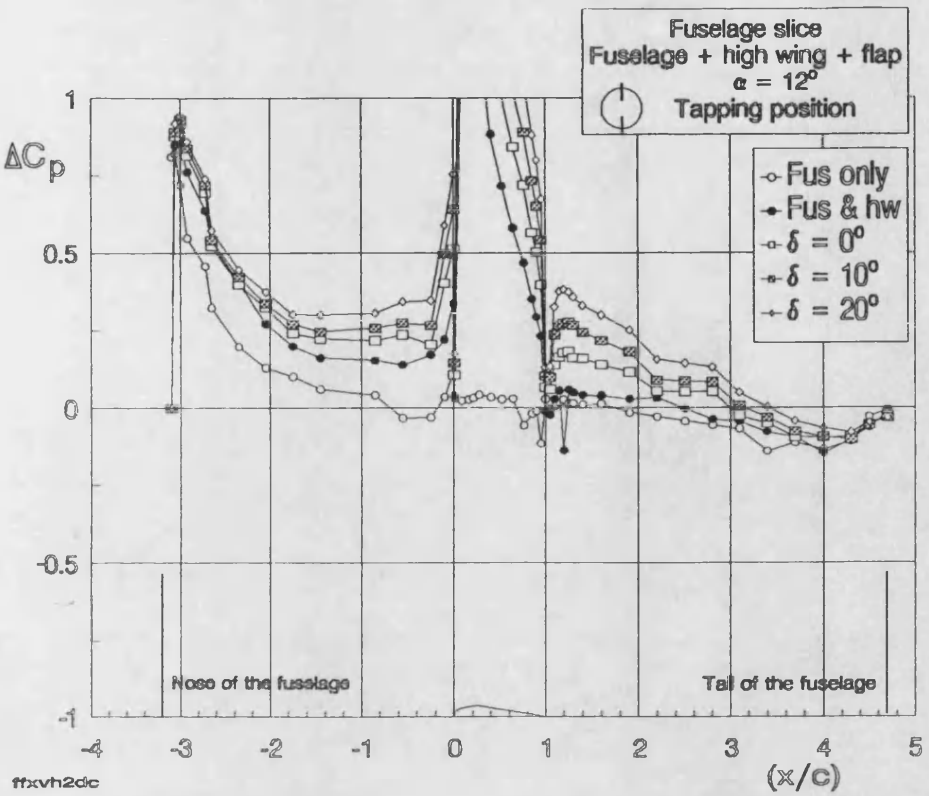

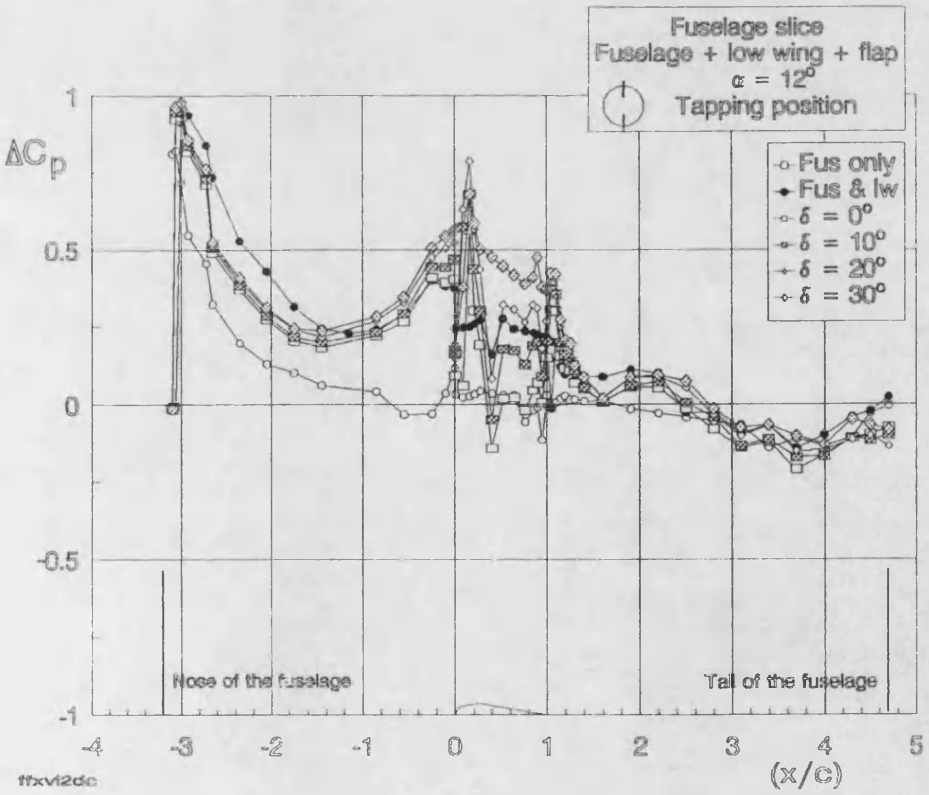

Fig. 4.26 Centreline pressure difference for fuselage & wing & flaps, ($\varphi = 0°, 180°$), high wing/low wing, $\alpha = 12^o$

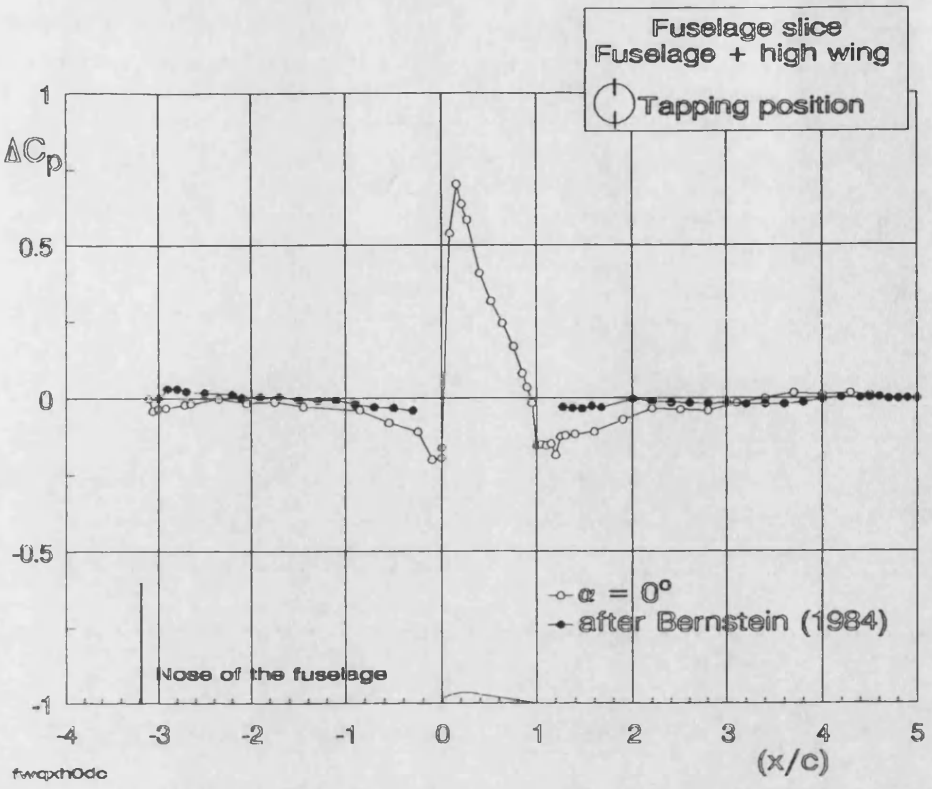

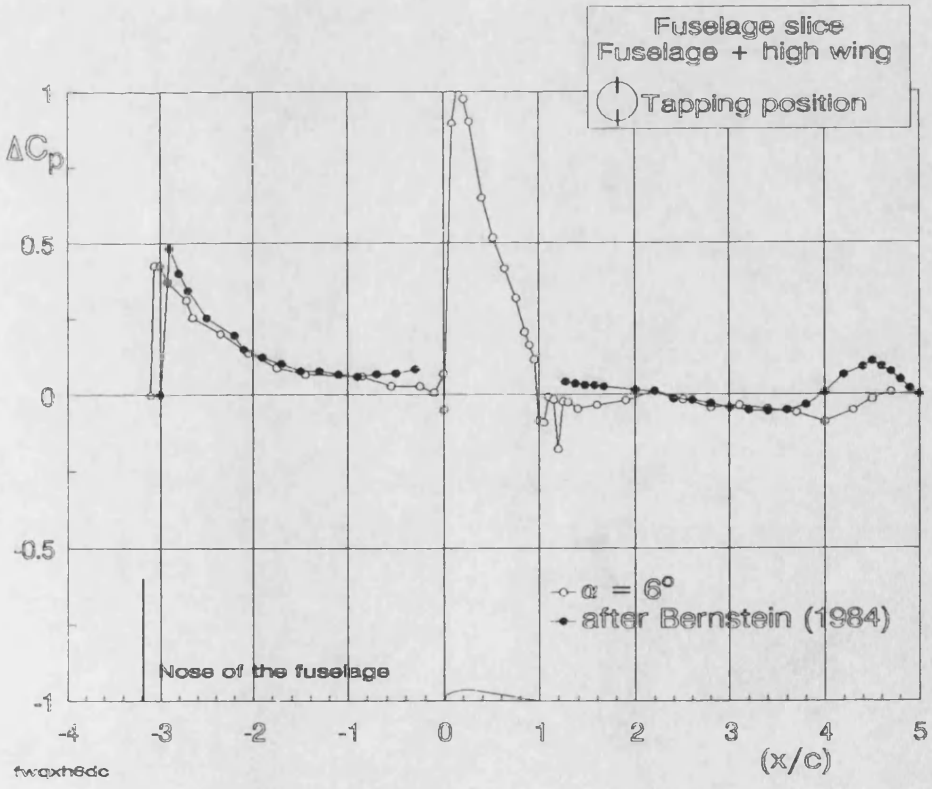

Fig. 4.27 Centreline pressure difference for fuselage & high wing, ($\varphi = 0°, 180°$), incl. data from Bernstein (1984)

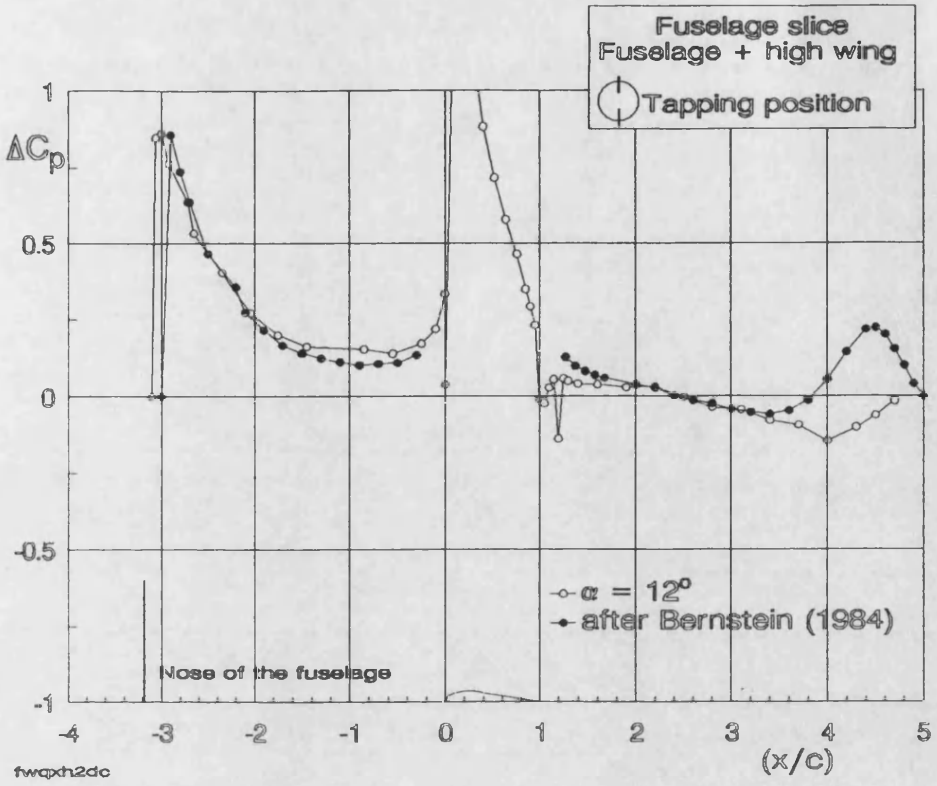

Fig. 4.28 Centreline pressure difference for fuselage & high wing, ($\varphi = 0°, 180°$), incl. data from Bernstein (1984)

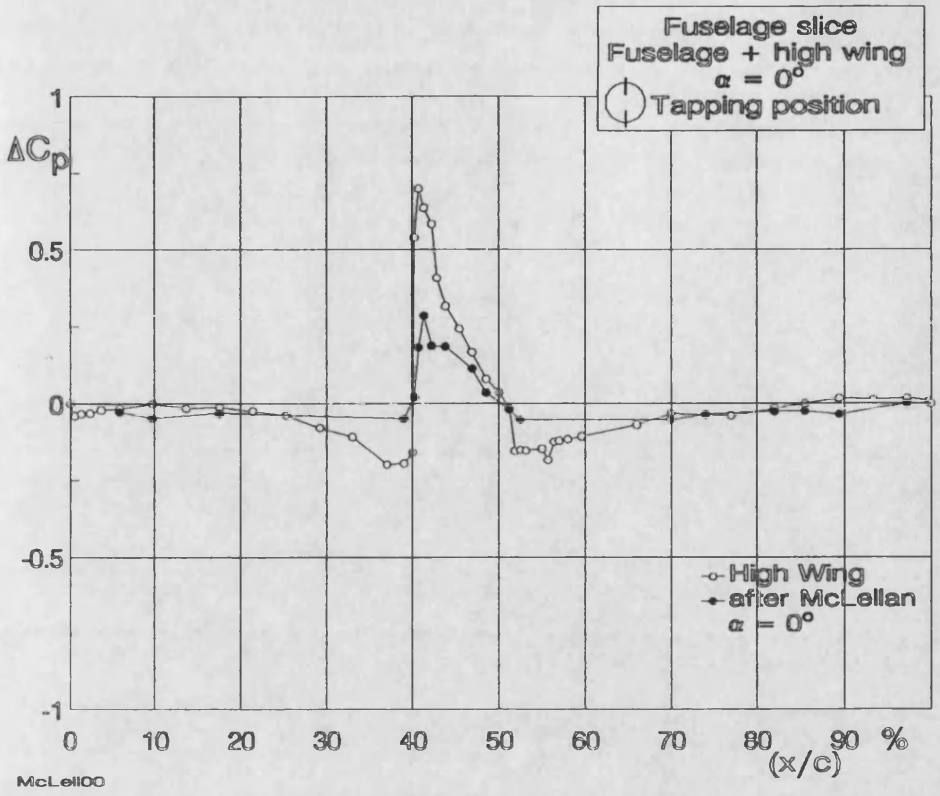

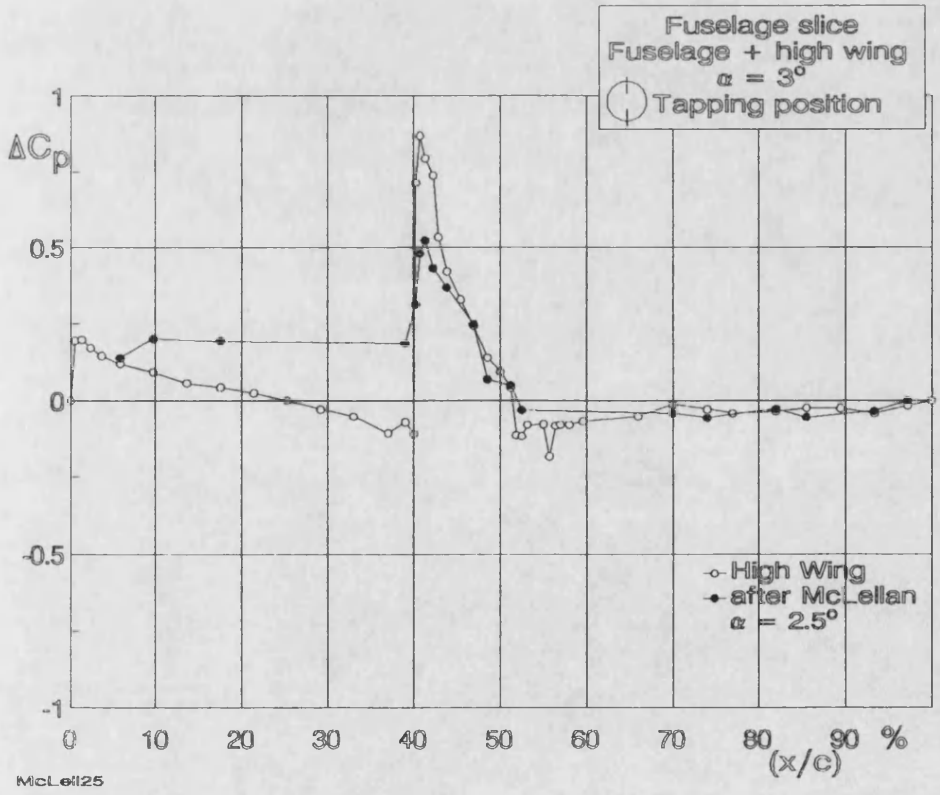

Fig. 4.29 Centreline pressure difference fuselage/nacelle & high wing, ($\varphi = 0°, 180°$), incl. data from McLellan (1948)

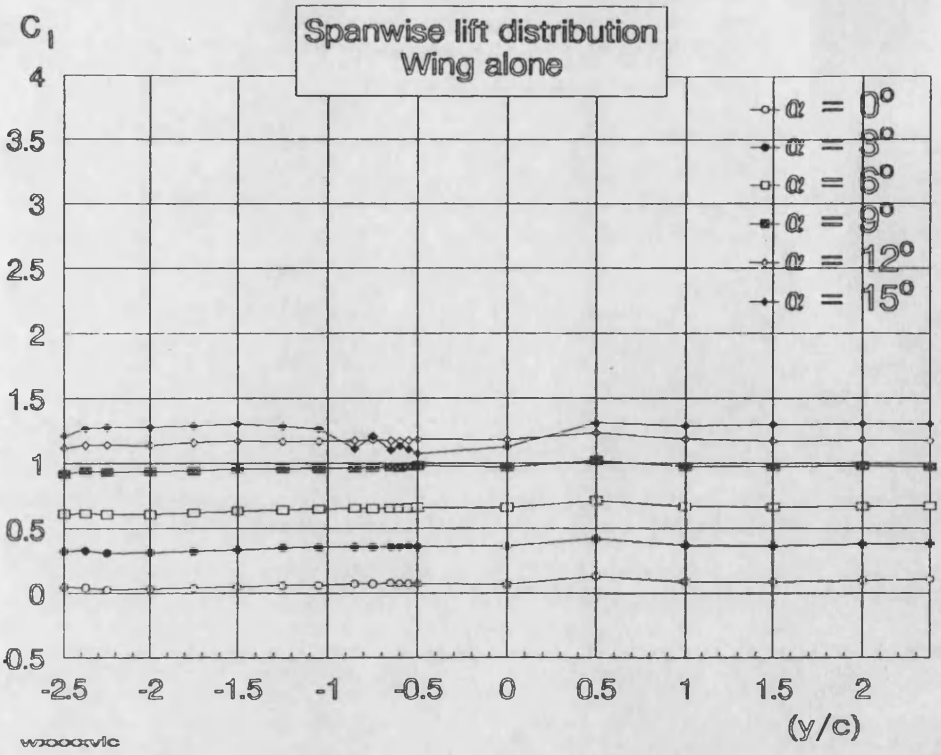

Fig. 4.30 Spanwise lift distribution for wing alone

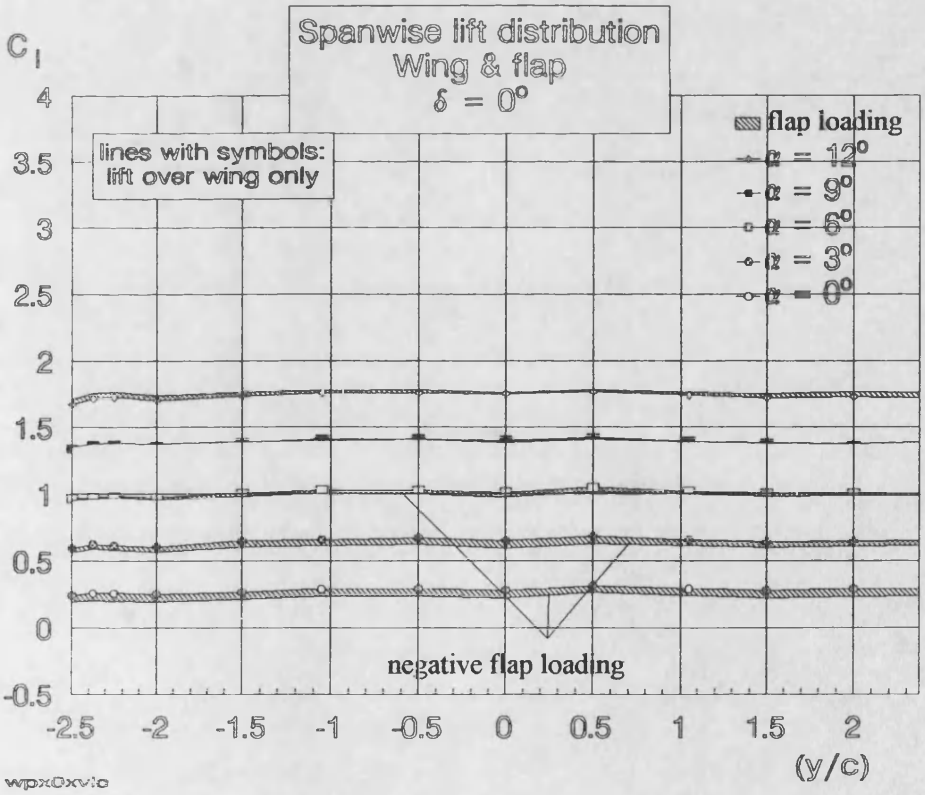

Fig. 4.31 Spanwise lift distribution for wing & flap, $\delta = 0^o$

continued -->

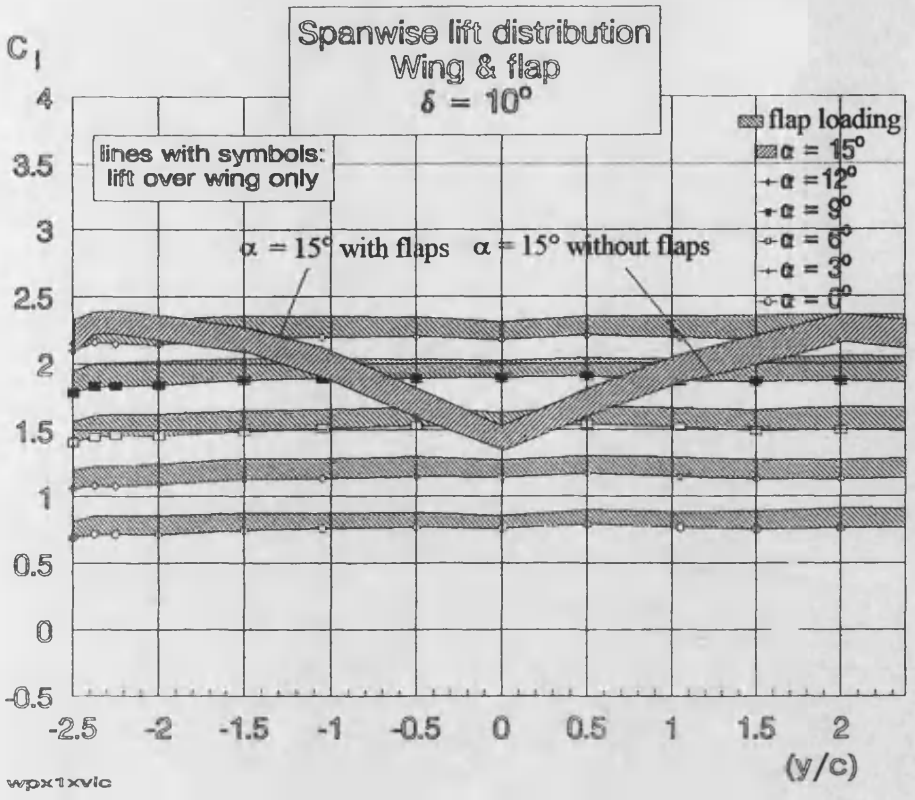

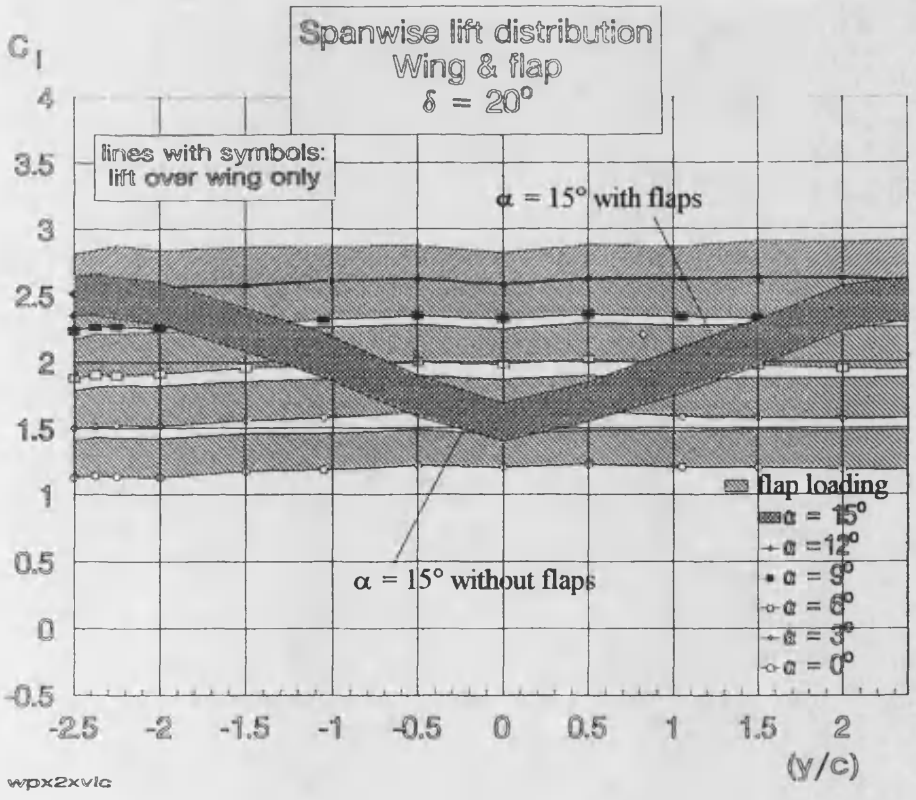

Fig. 4.31 cont. Spanwise lift distribution for wing & flap, $\delta = 10^o, 20^o$

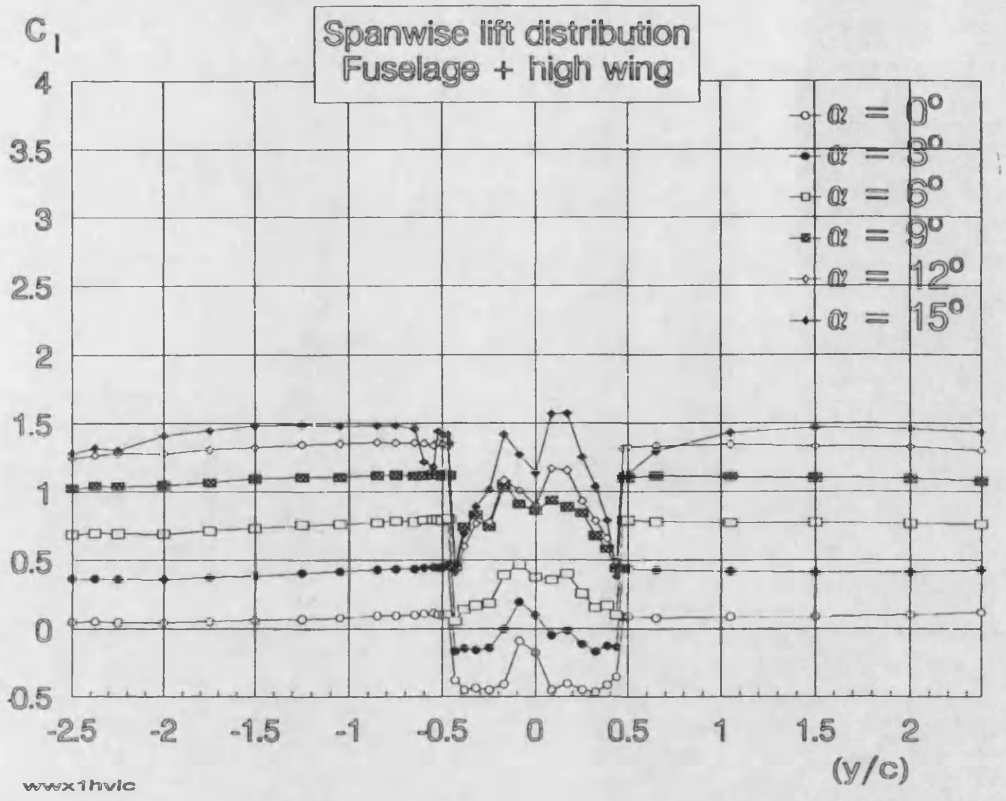

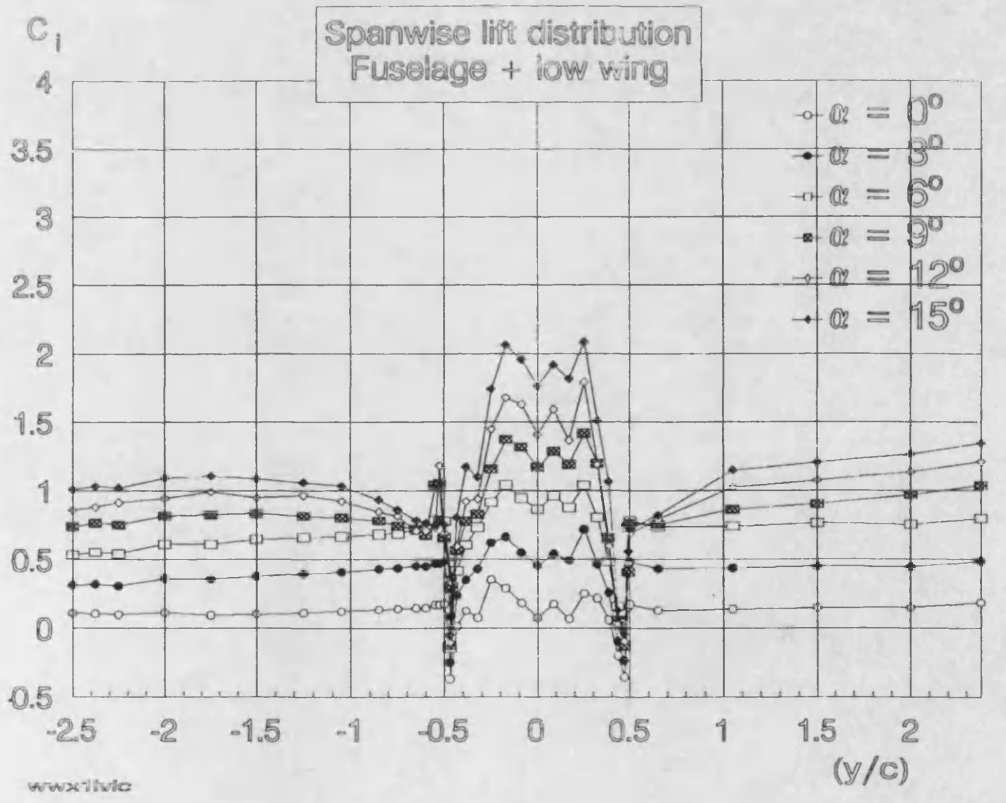

Fig. 4.32 Spanwise lift distribution for fuselage & wing high/low mounted wings

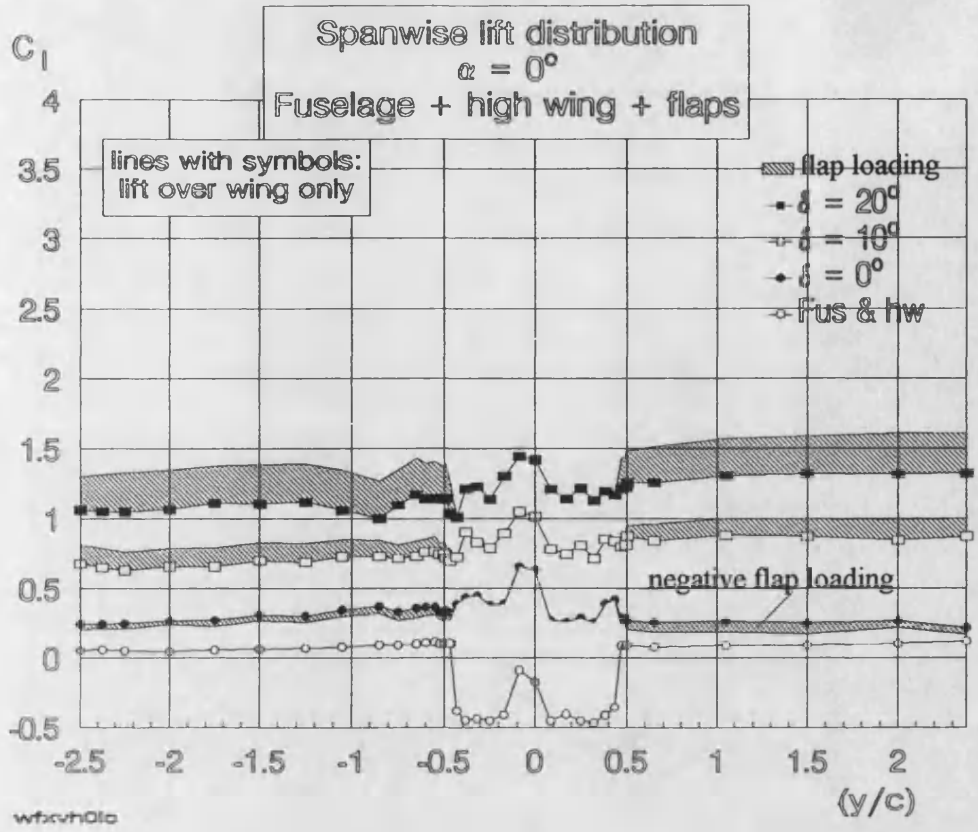

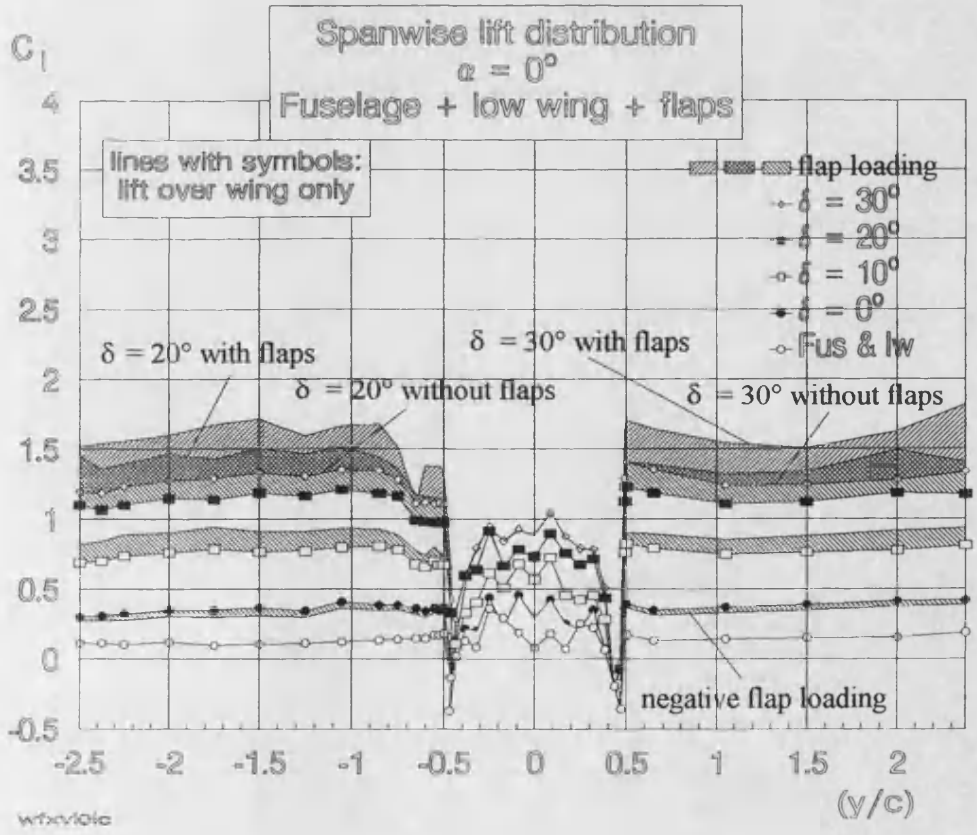

Fig. 4.33 Spanwise lift for fuselage & wing & flaps, $\alpha = 0^o$ high/low mounted wings

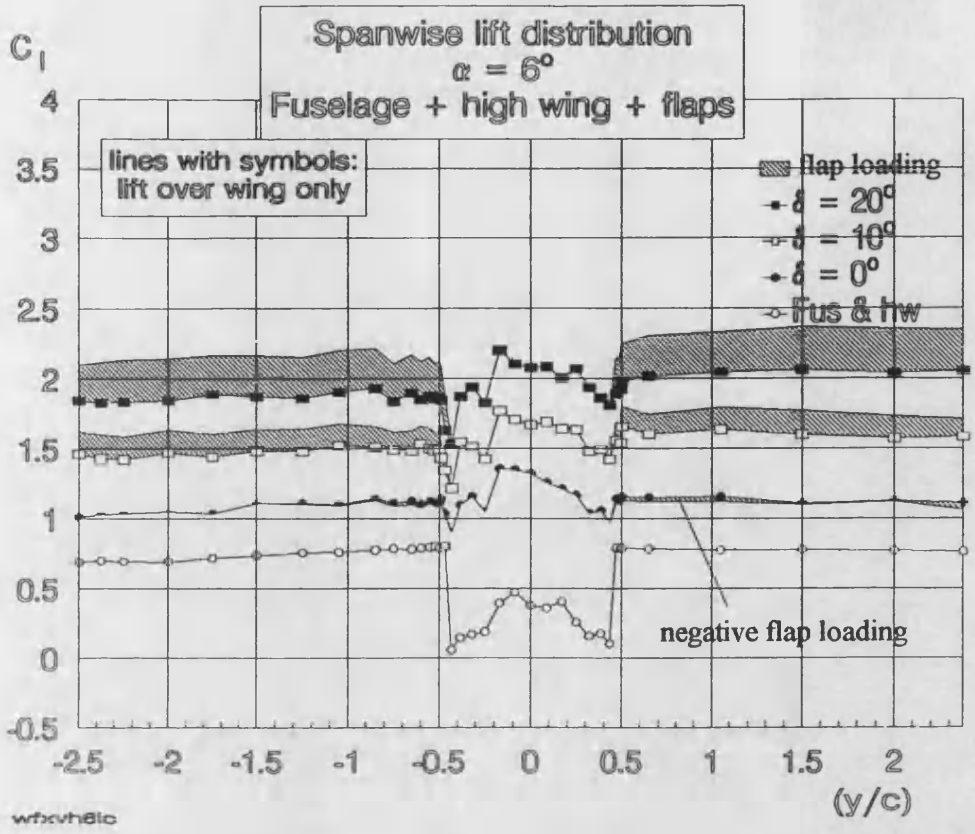

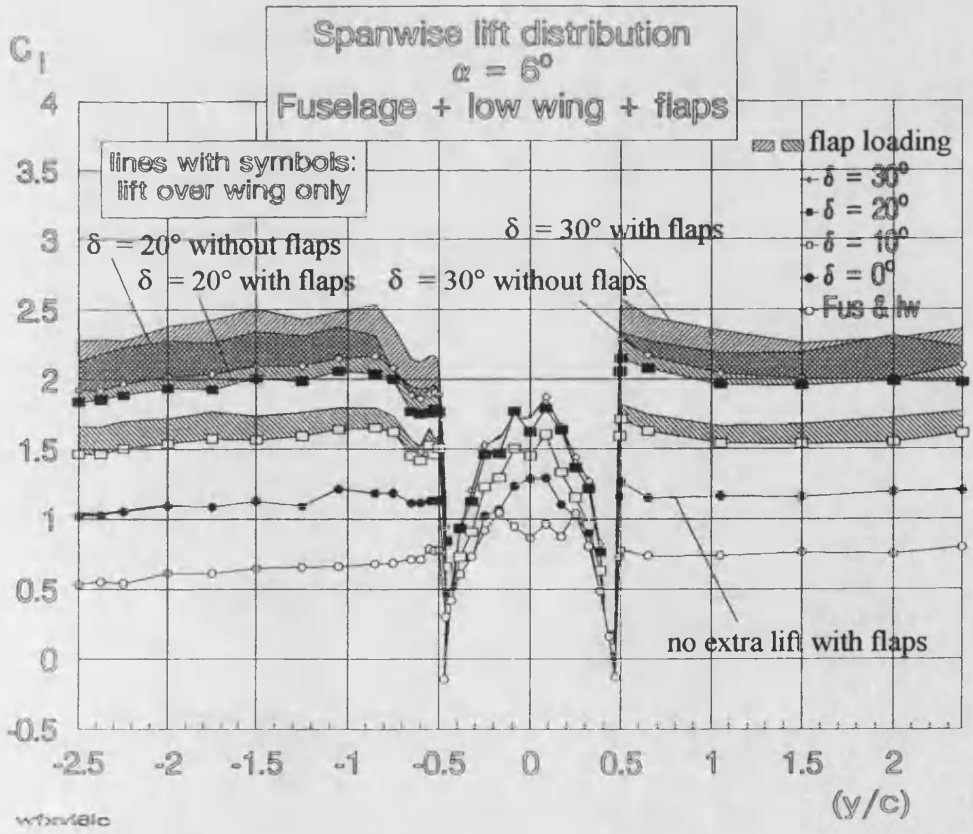

Fig. 4.34 Spanwise lift distribution for fuselage & wing & flaps, $\alpha = 6^0$ high/low mounted wings

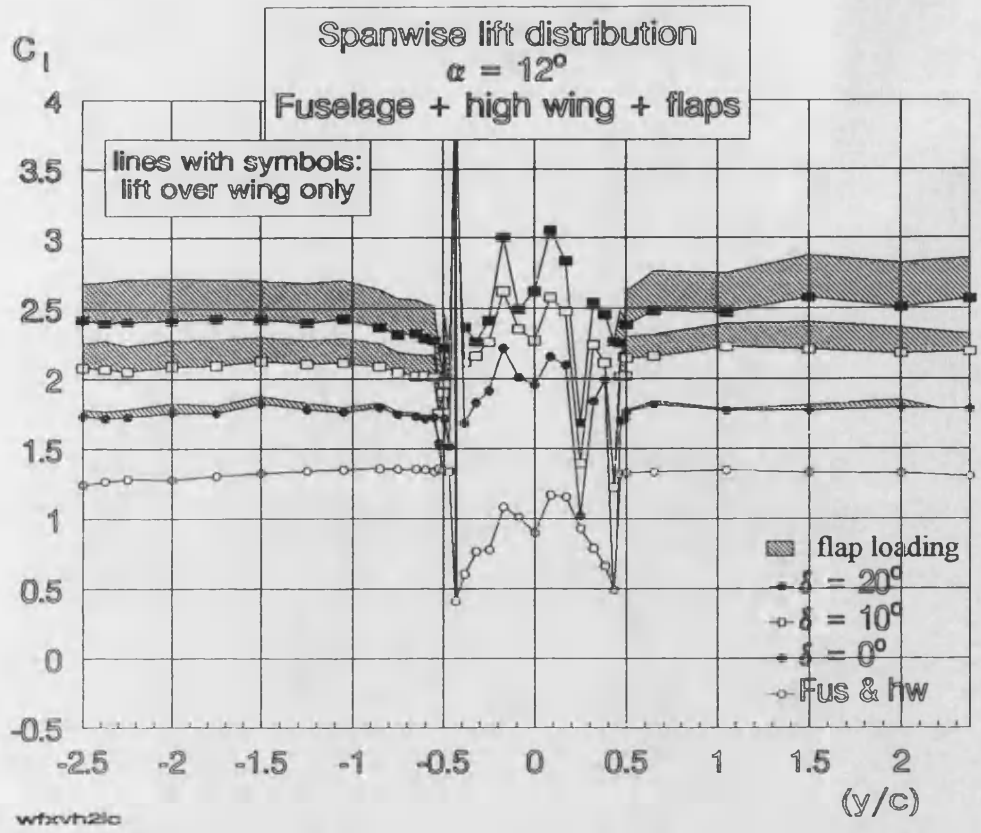

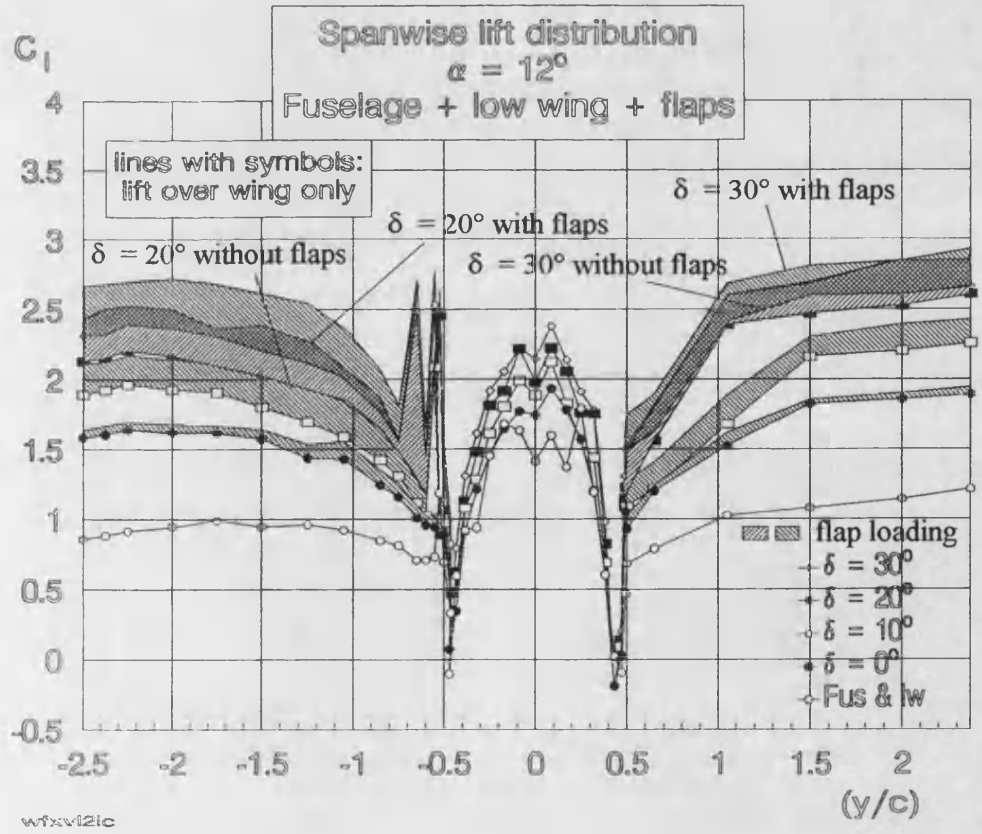

Fig. 4.35 Spanwise lift distribution for fuselage & wing & flaps, $\alpha = 12^o$ high/low mounted wings

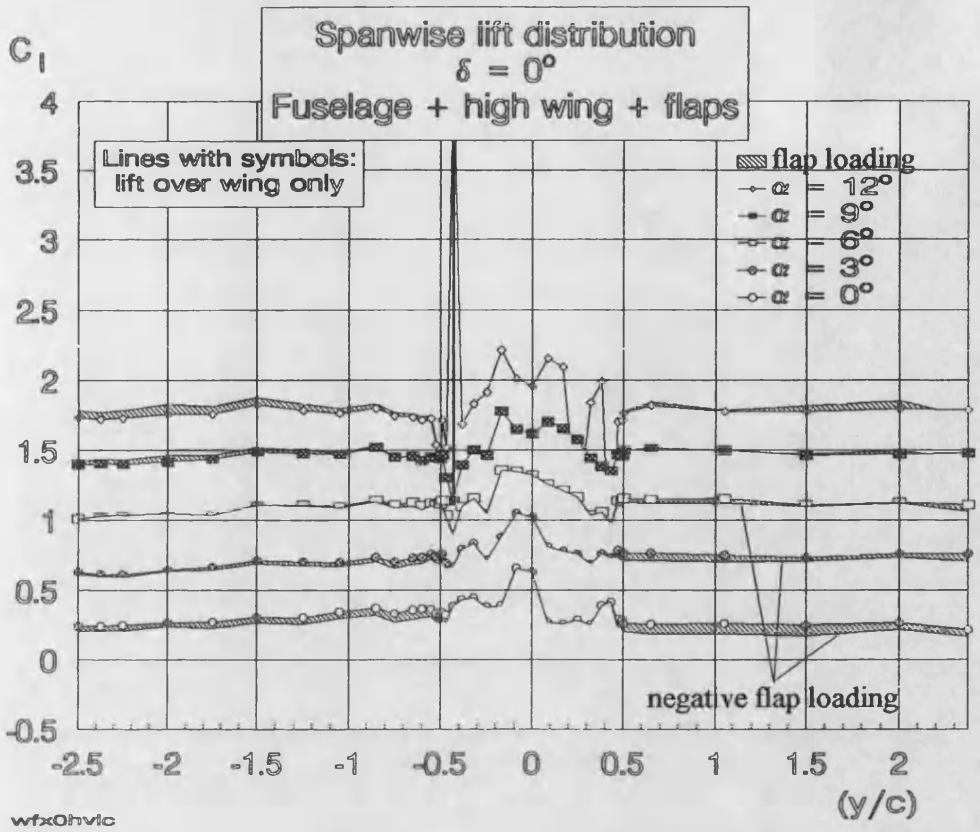

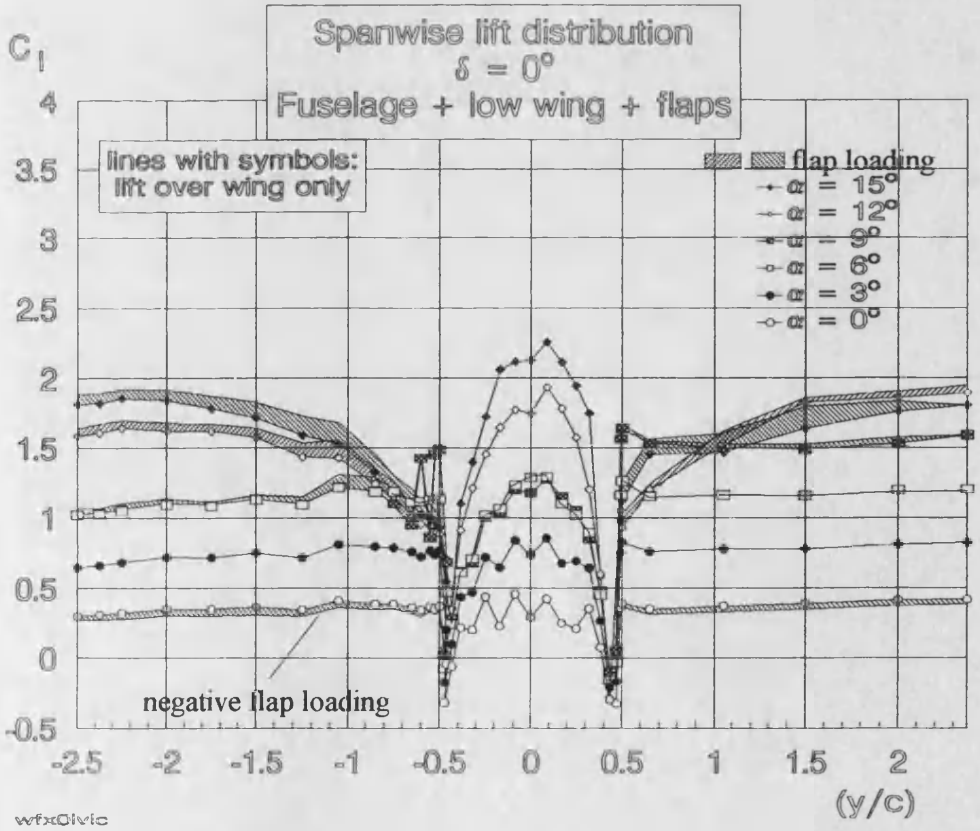

Fig. 4.36 Spanwise lift distribution for fuselage & wing & flaps, $\delta = 0^o$ high/low mounted wings

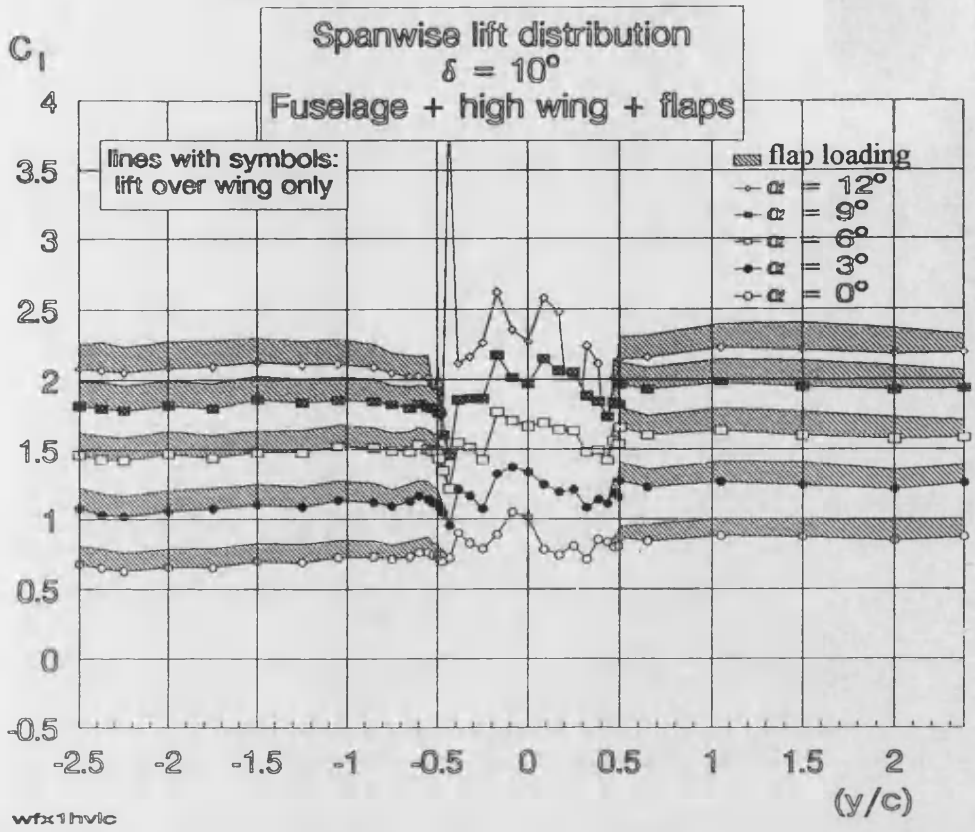

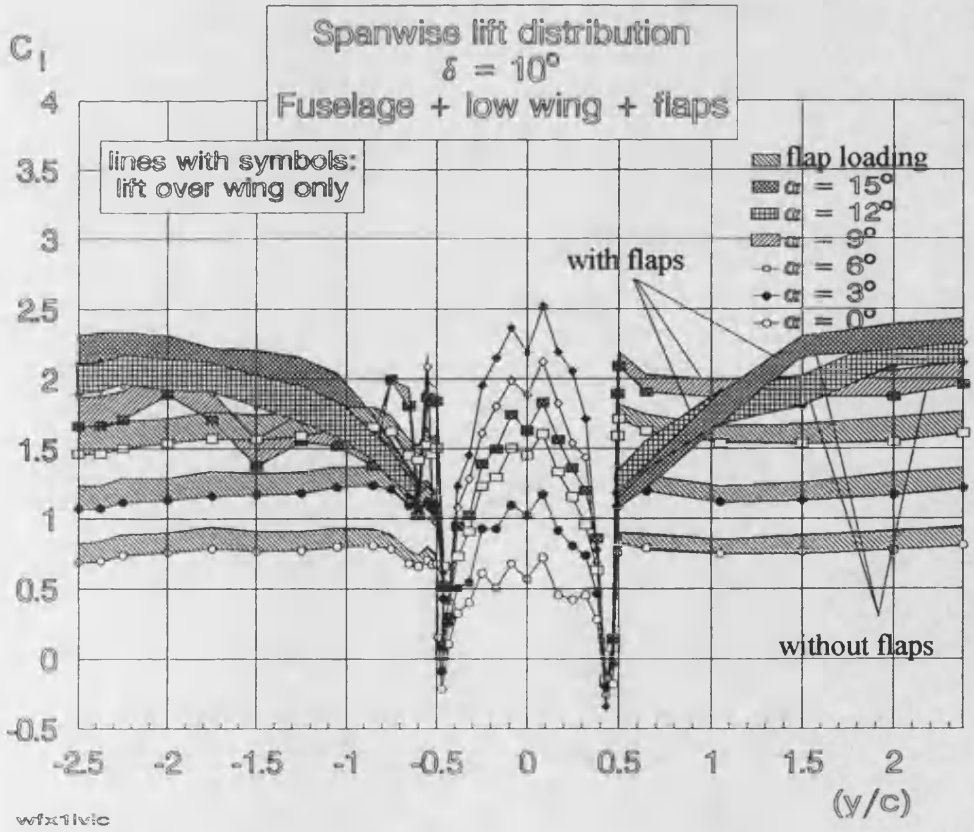

Fig. 4.37 Spanwise lift distribution for fuselage & wing & flaps, $\delta = 10^{o}$ high/low mounted wings

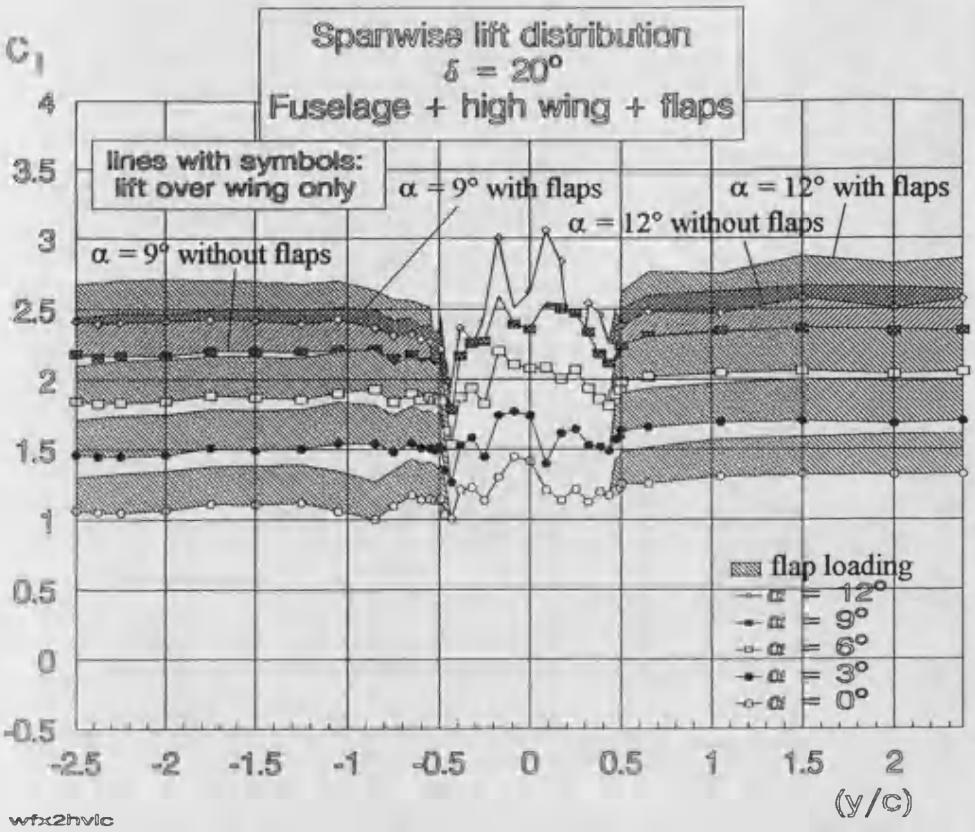

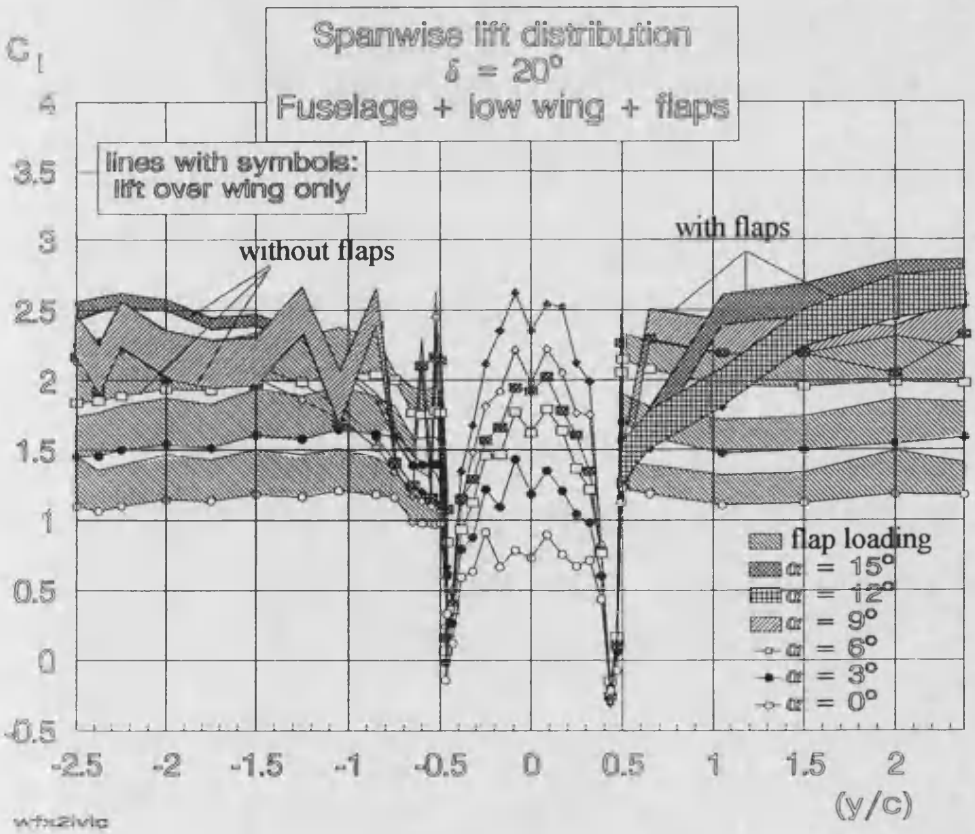

Fig. 4.38 Spanwise lift distribution for fuselage & wing & flaps, $\delta = 20^o$ high/low mounted wings

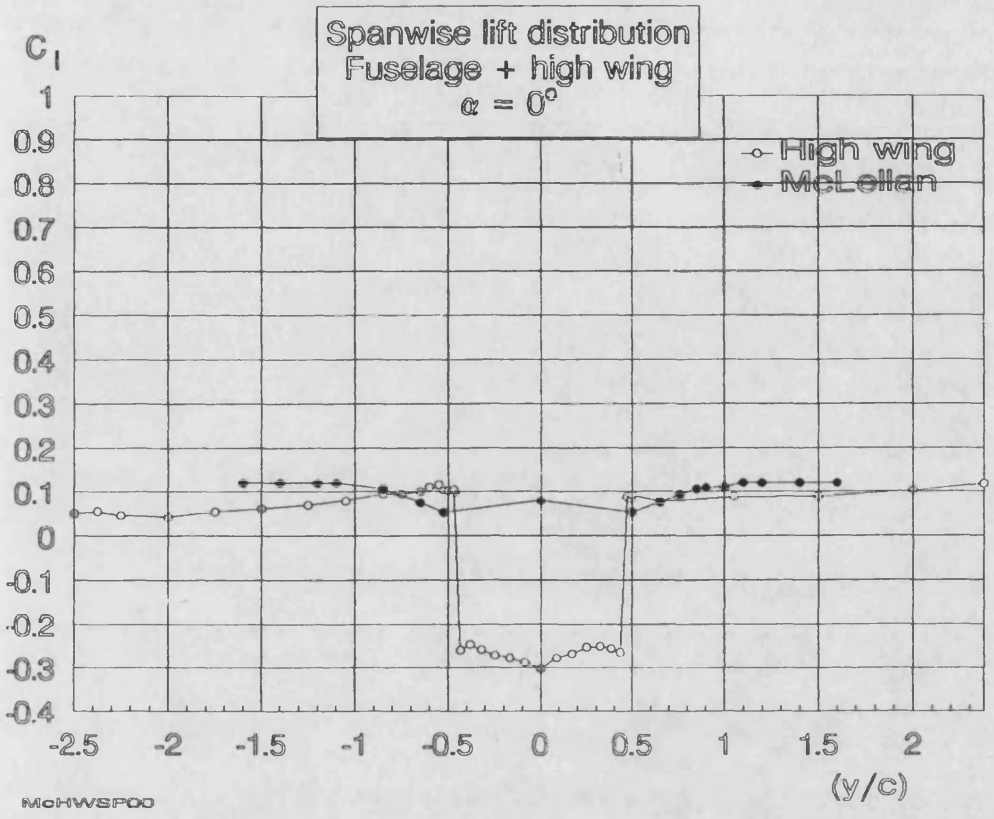

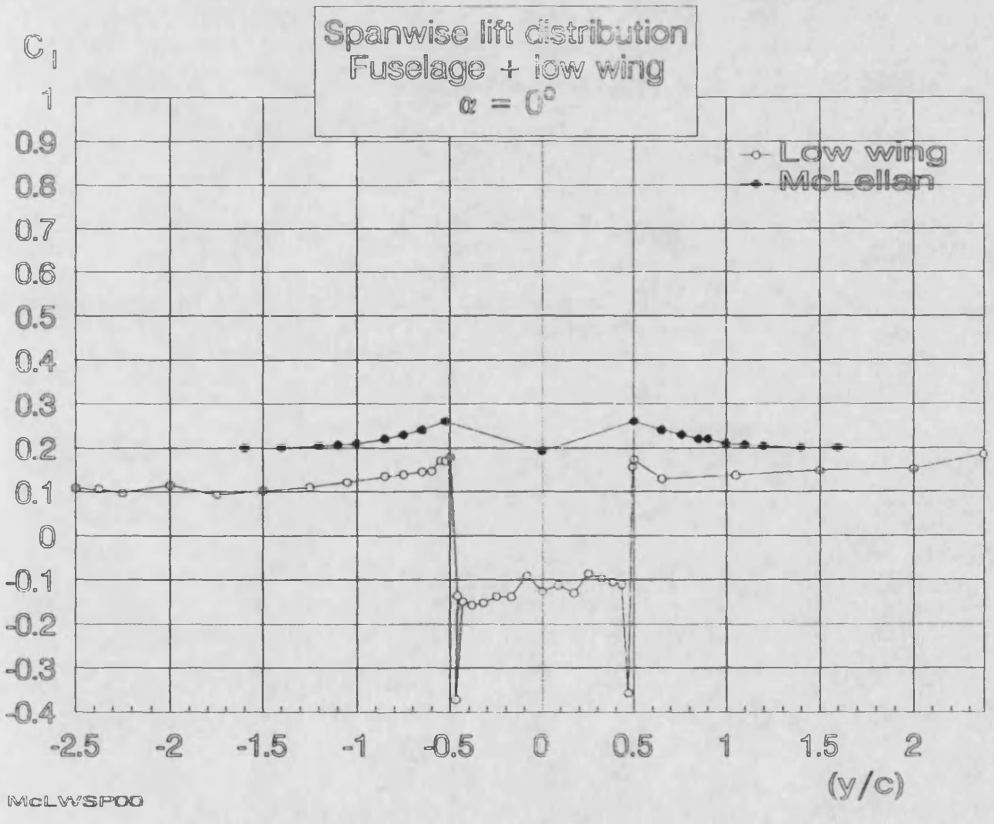

Fig. 4.39 **Spanwise lift distribution, incl. data from McLellan (1948), $\alpha = 0^o$** (wing chord zone only, across the fuselage)

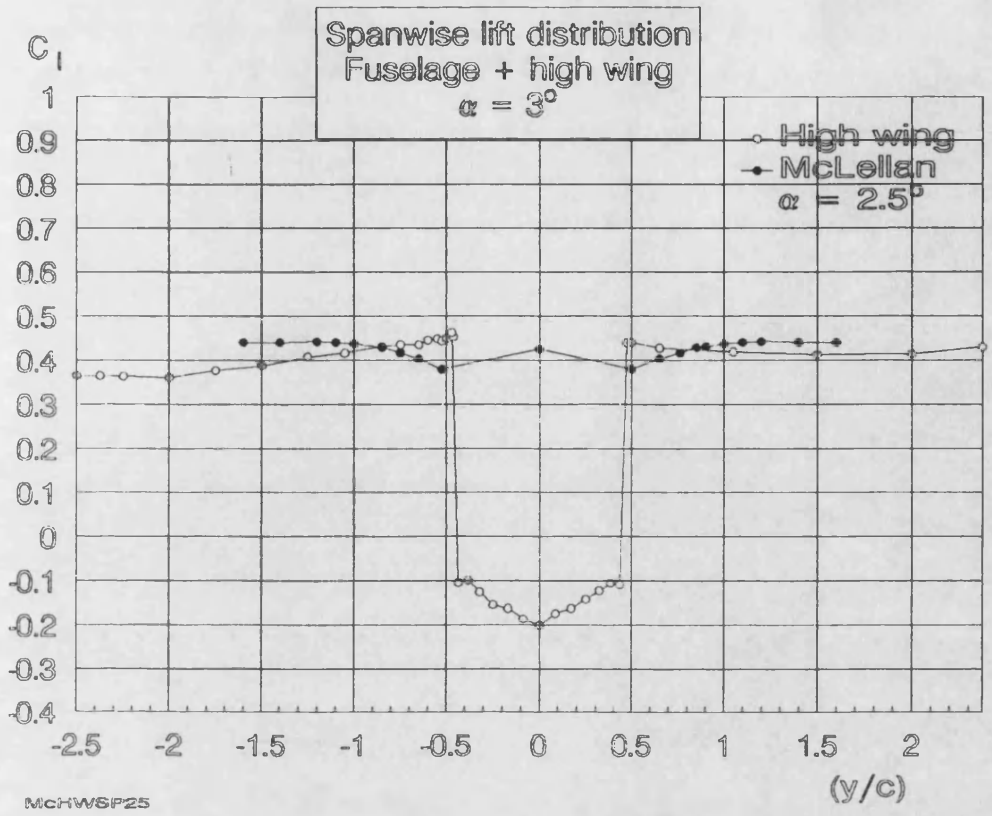

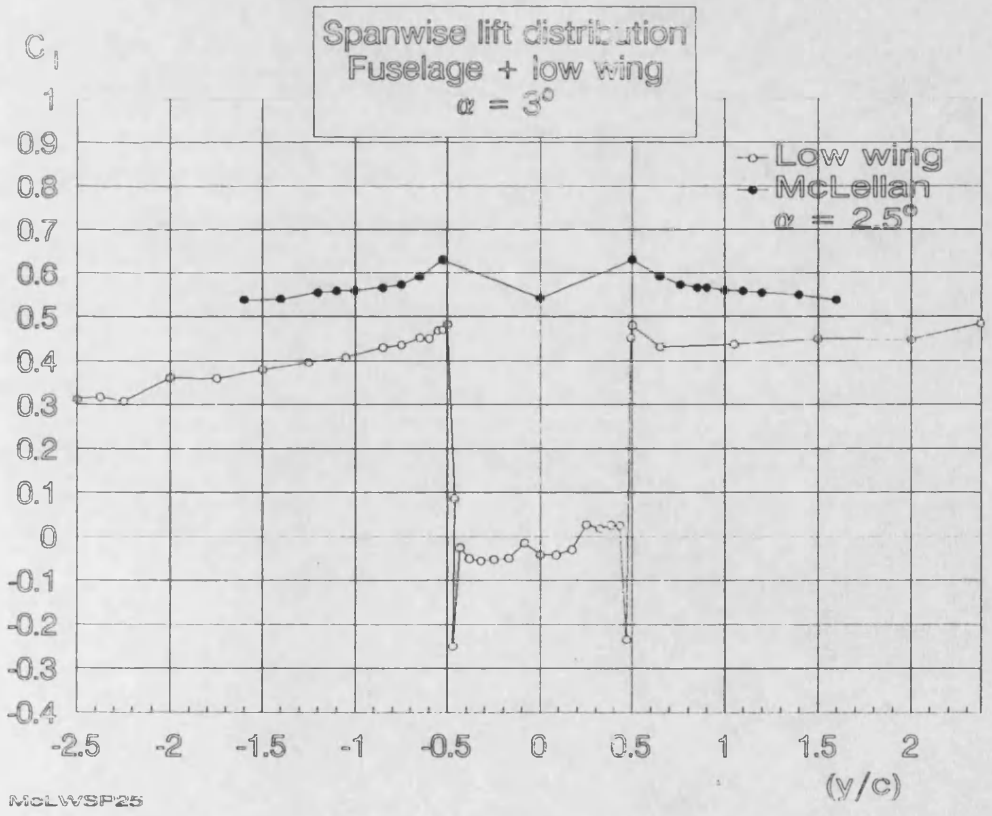

Fig. 4.40 **Spanwise lift distribution, incl. data from McLellan (1948)**
$\alpha = 2.5^o / 3^o$ (wing chord zone only, across the fuselage)

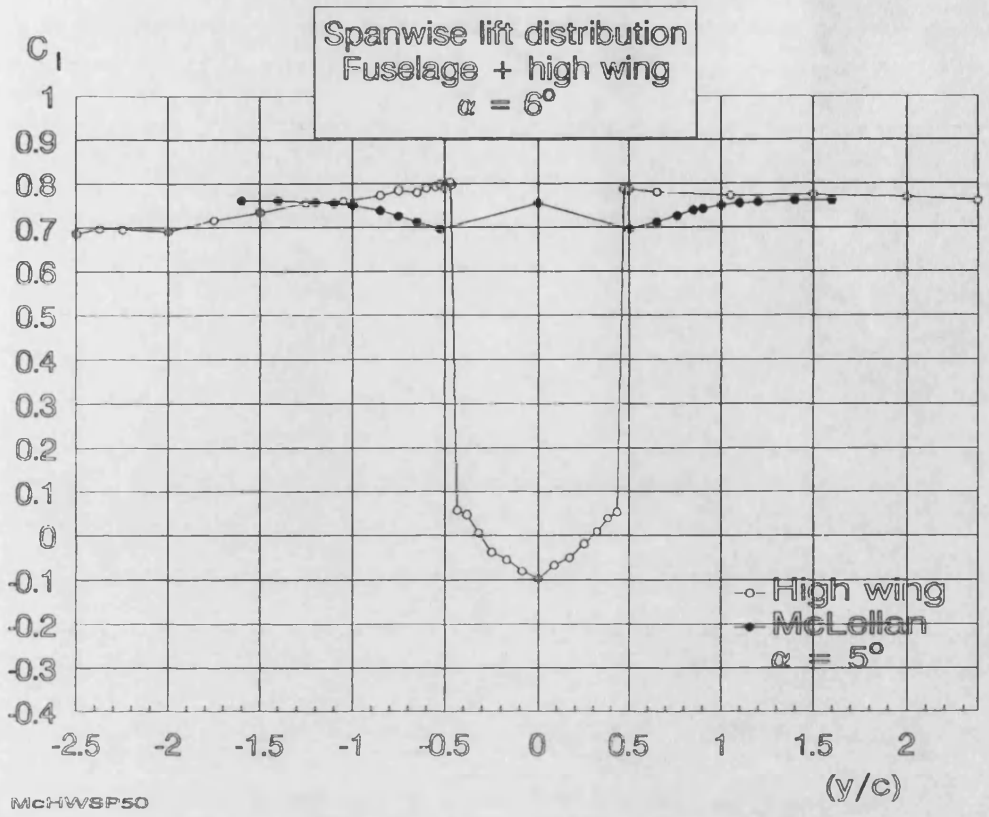

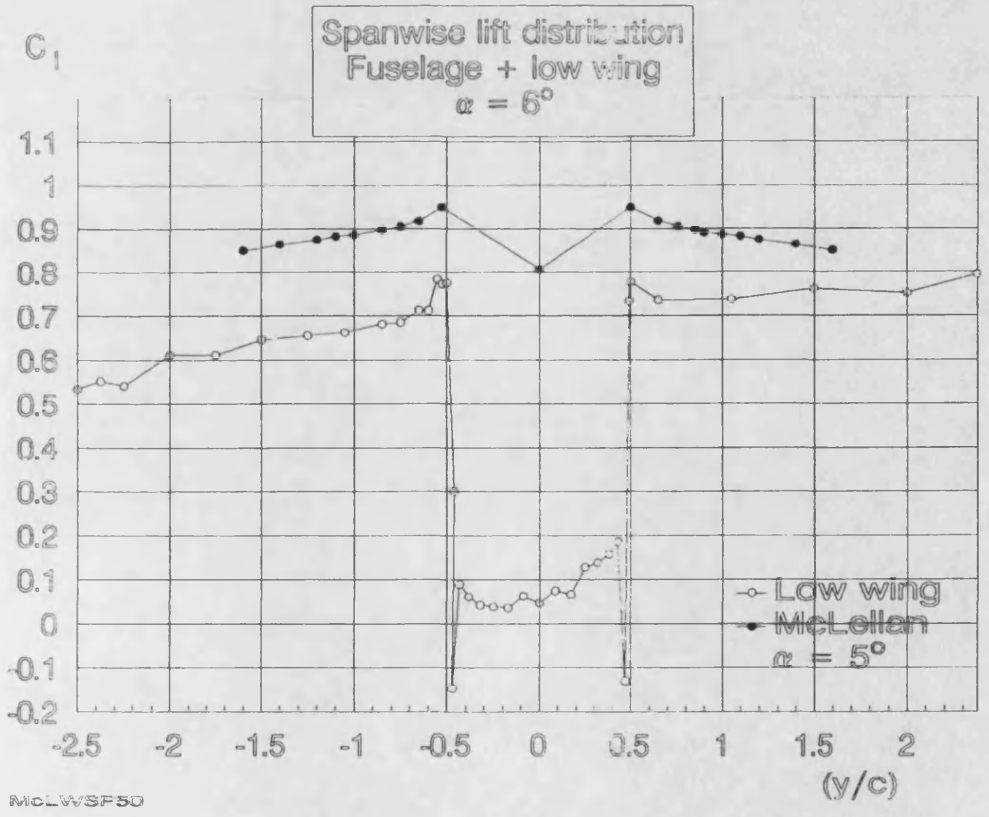

Fig. 4.41 **Spanwise lift distribution, incl. data from McLellan (1948)**
$\alpha = 5^0 / 6^0$ (wing chord zone only, across the fuselage)

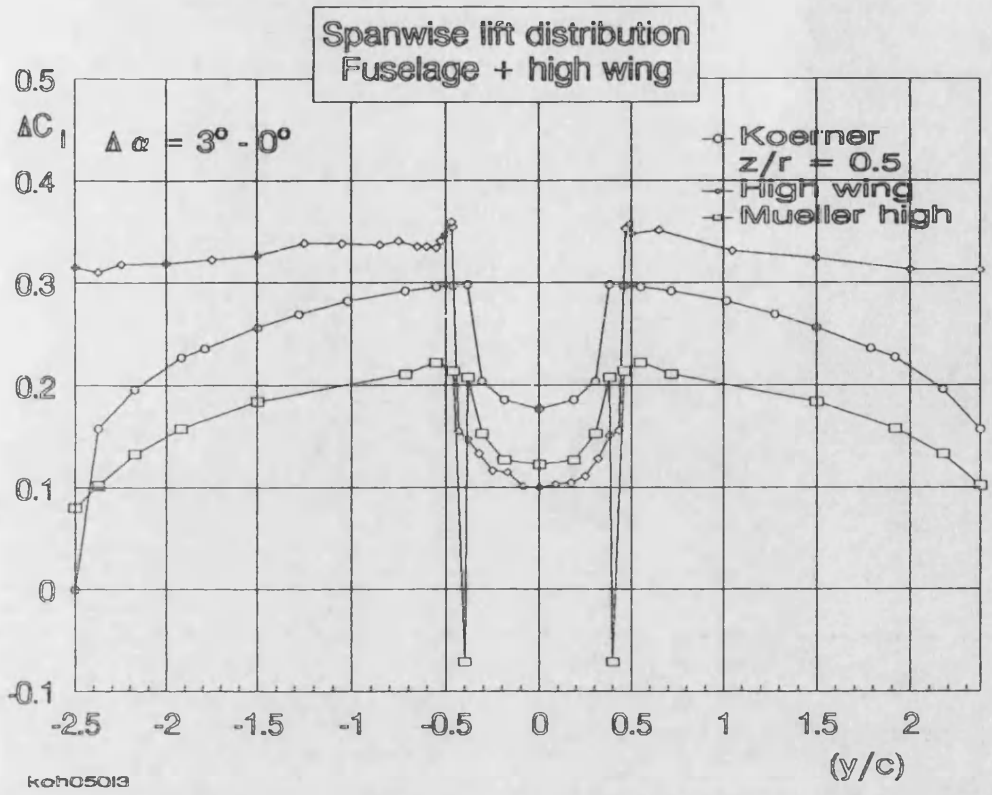

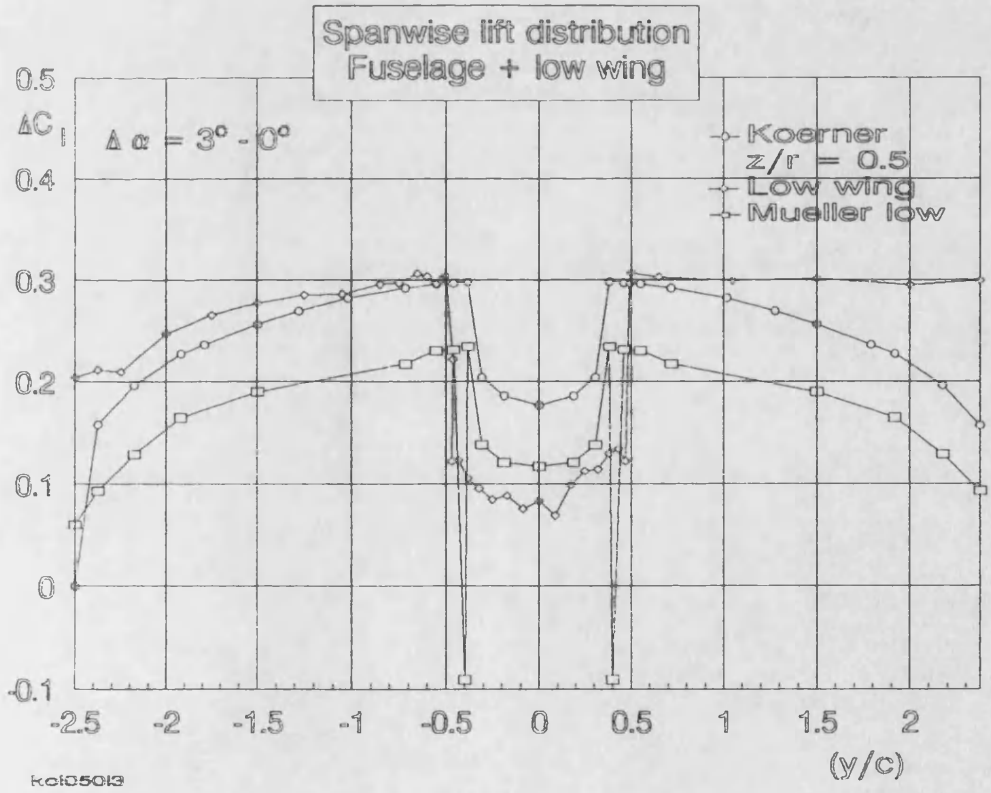

Fig. 4.42 Spanwise lift distribution, incl. data from Körner (1972) and Müller (1970), $^{z}/_{r} = \pm 0.5$
(wing chord zone only, across the fuselage)

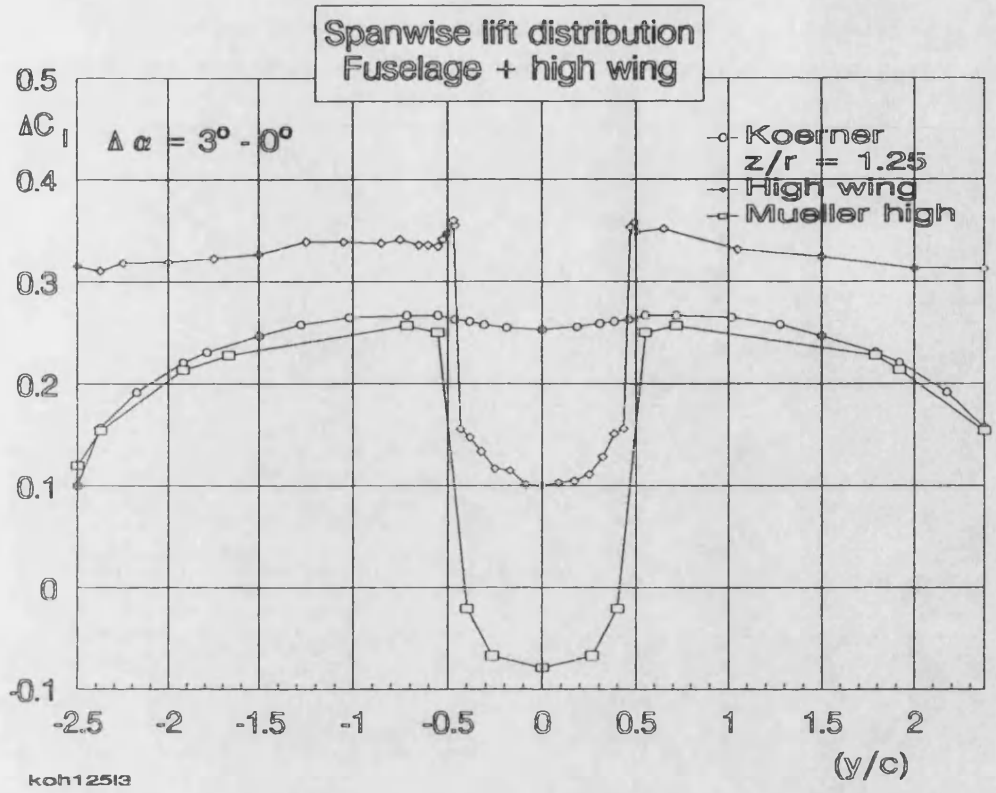

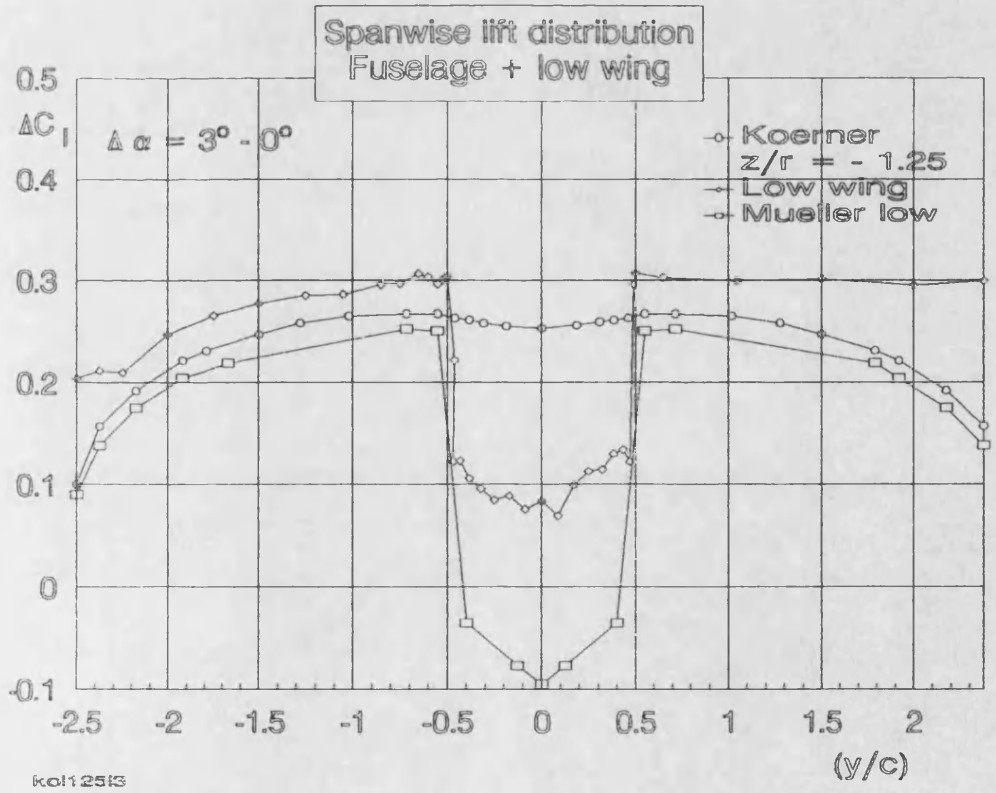

Fig. 4.43 **Spanwise lift distribution, incl. data from Körner (1972) and Müller (1970), $^{z}/_{r} = \pm 1.25$**
(wing chord zone only, across the fuselage)

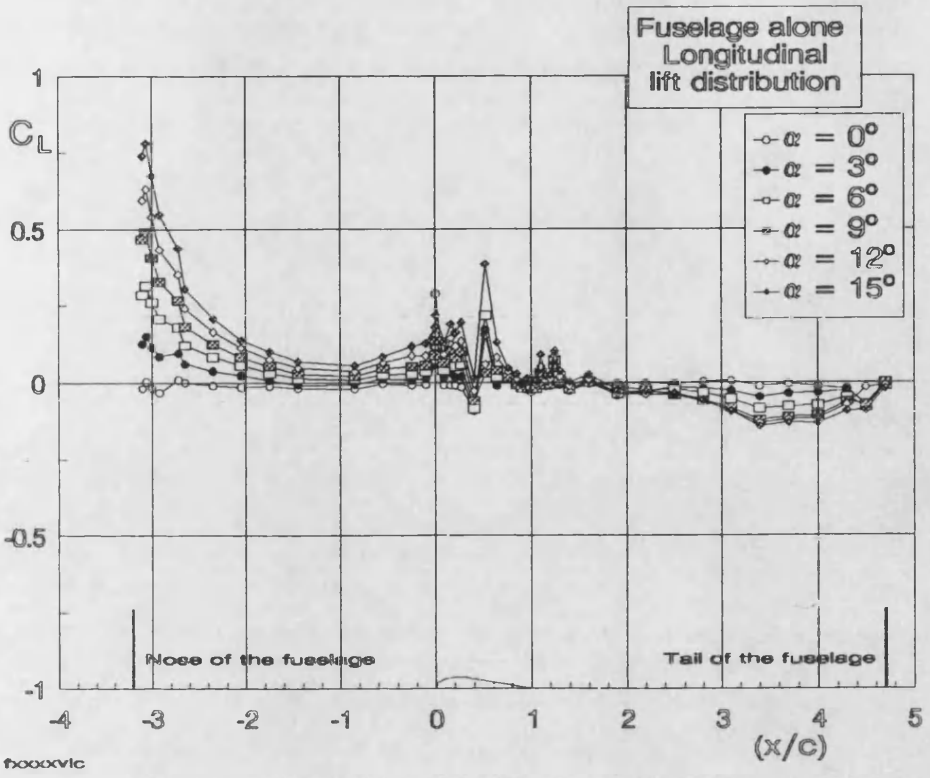

Fig. 4.44 Fuselage lift distribution for fuselage alone

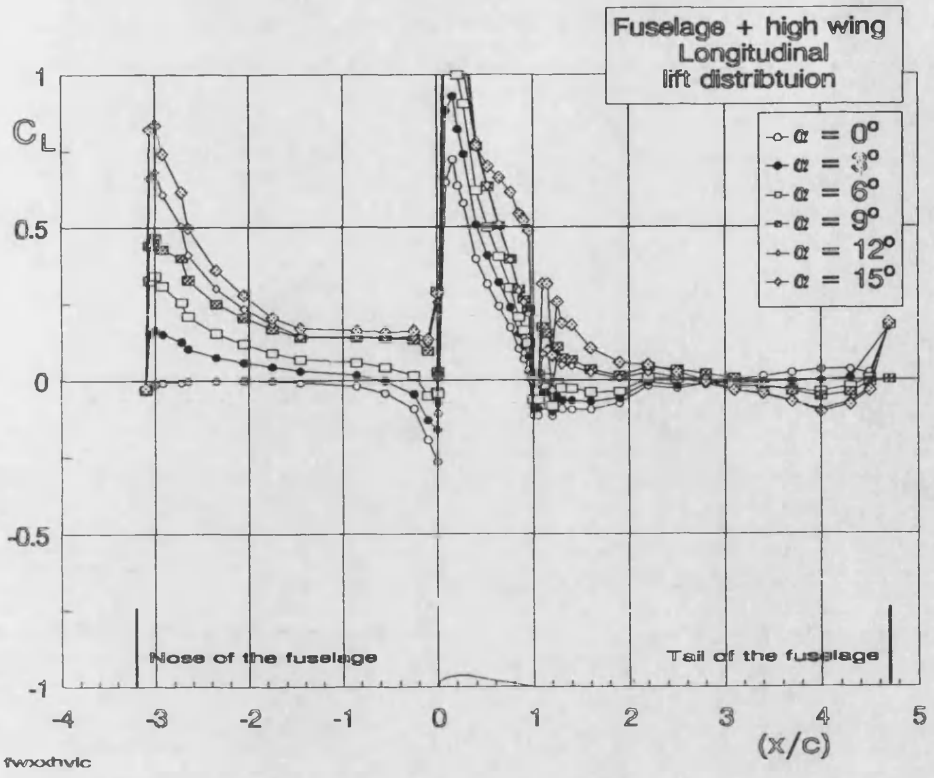

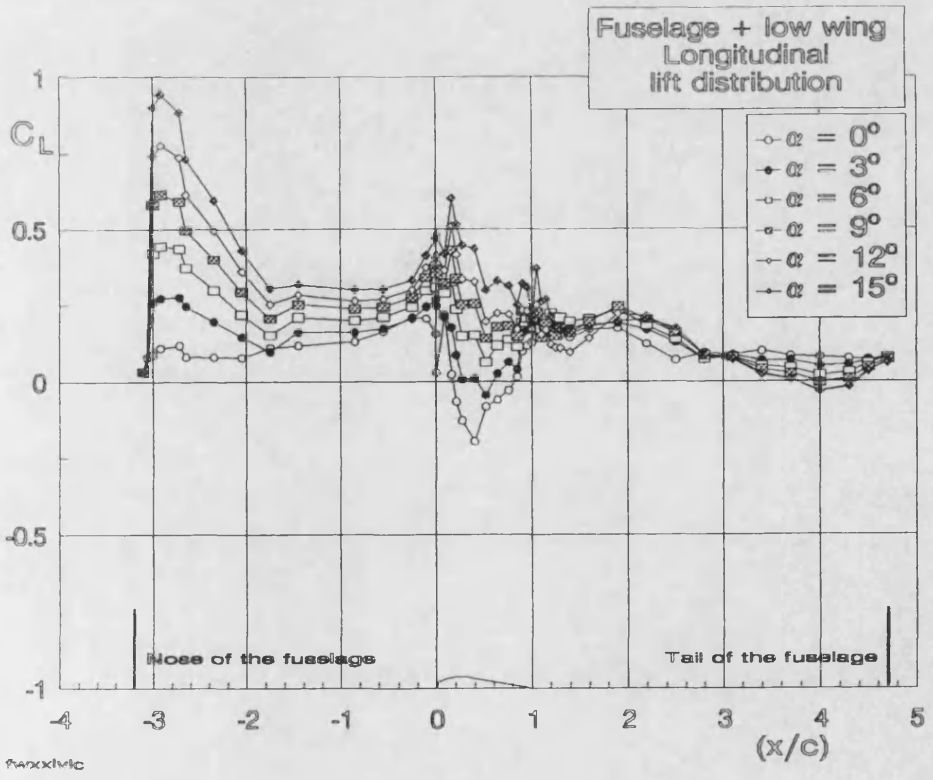

Fig. 4.45 Fuselage lift distribution for fuselage & wing

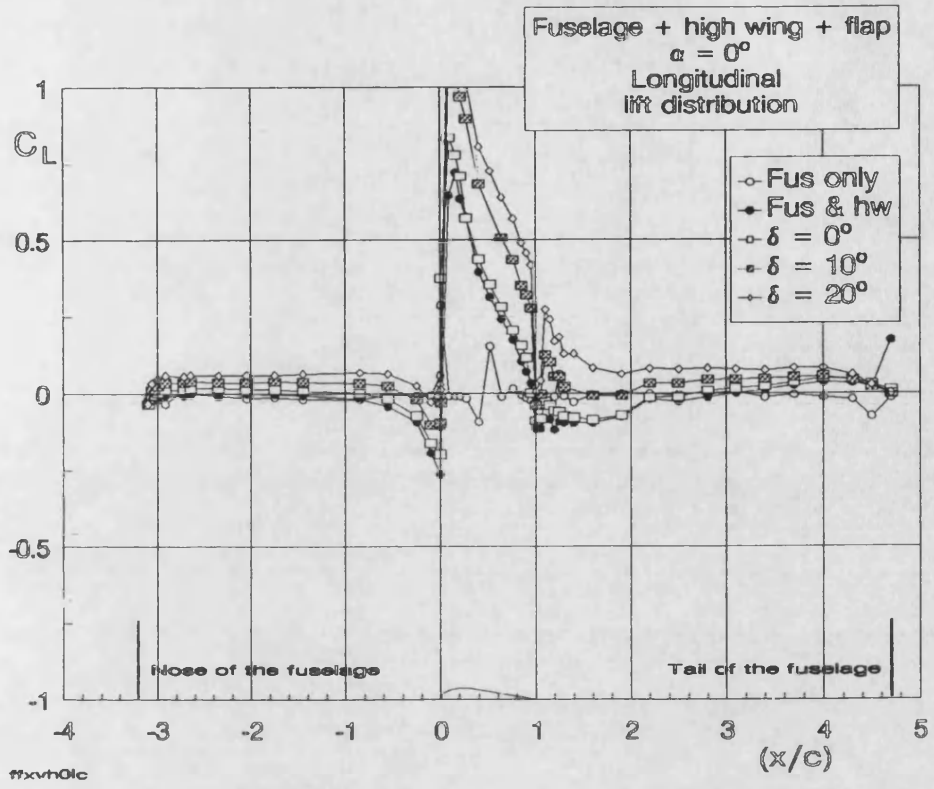

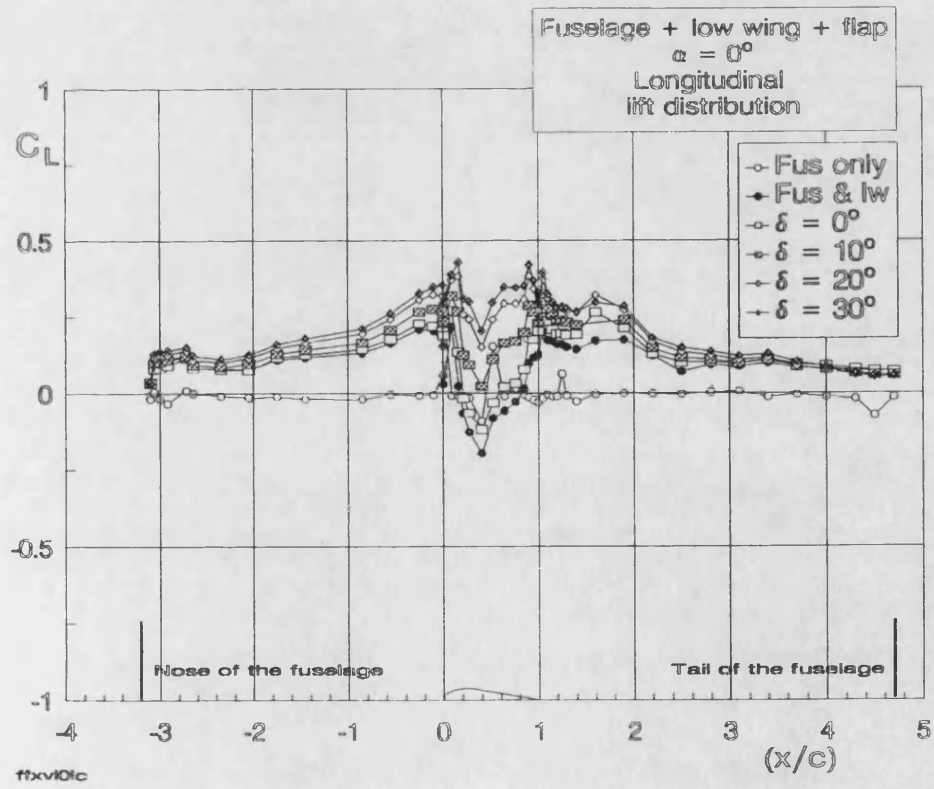

Fig. 4.46 Fuselage lift distribution for fuselage & wing & flaps, $\alpha = 0^o$

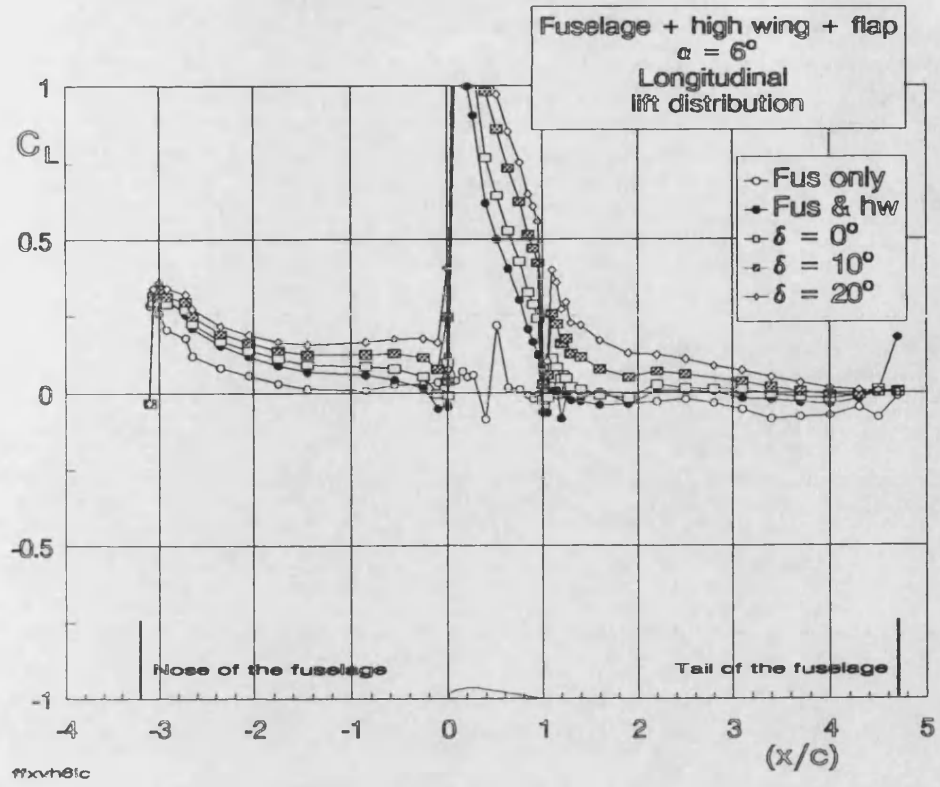

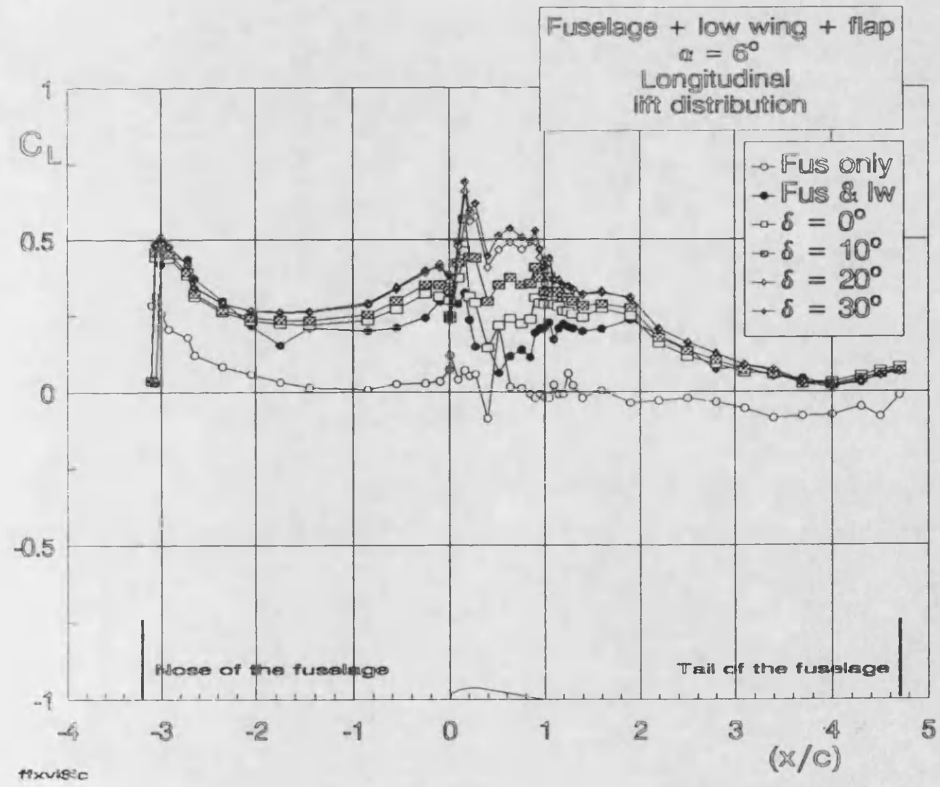

Fig. 4.47 Fuselage lift distribution for fuselage & wing & flaps, $\alpha = 6^o$

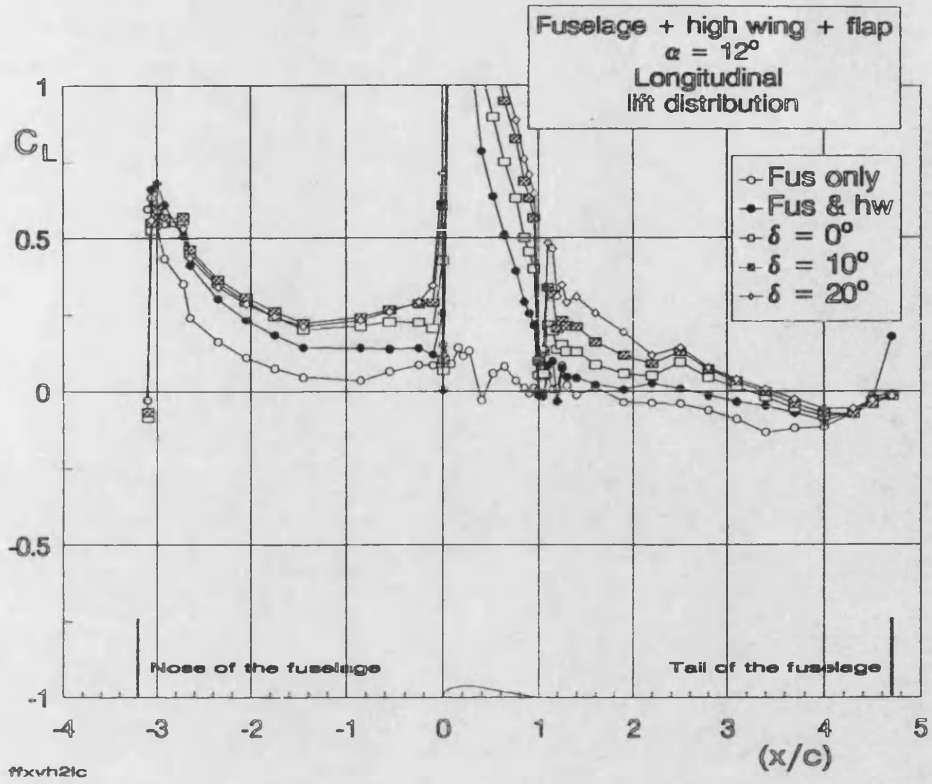

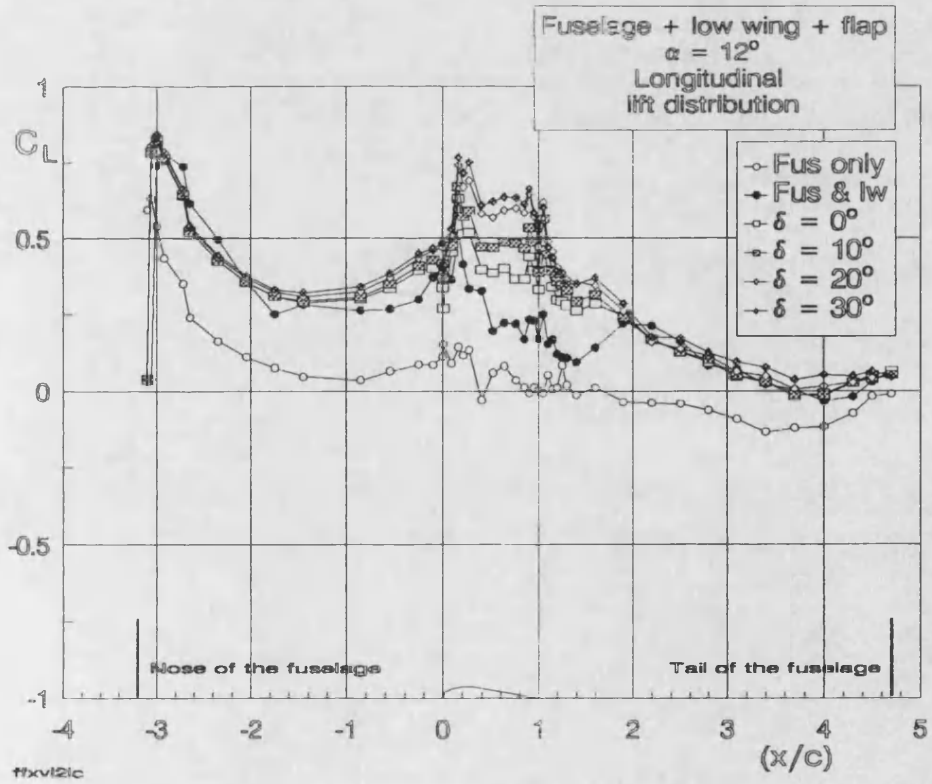

Fig. 4.48 Fuselage lift distribution for fuselage & wing & flap, $\alpha = 12^o$

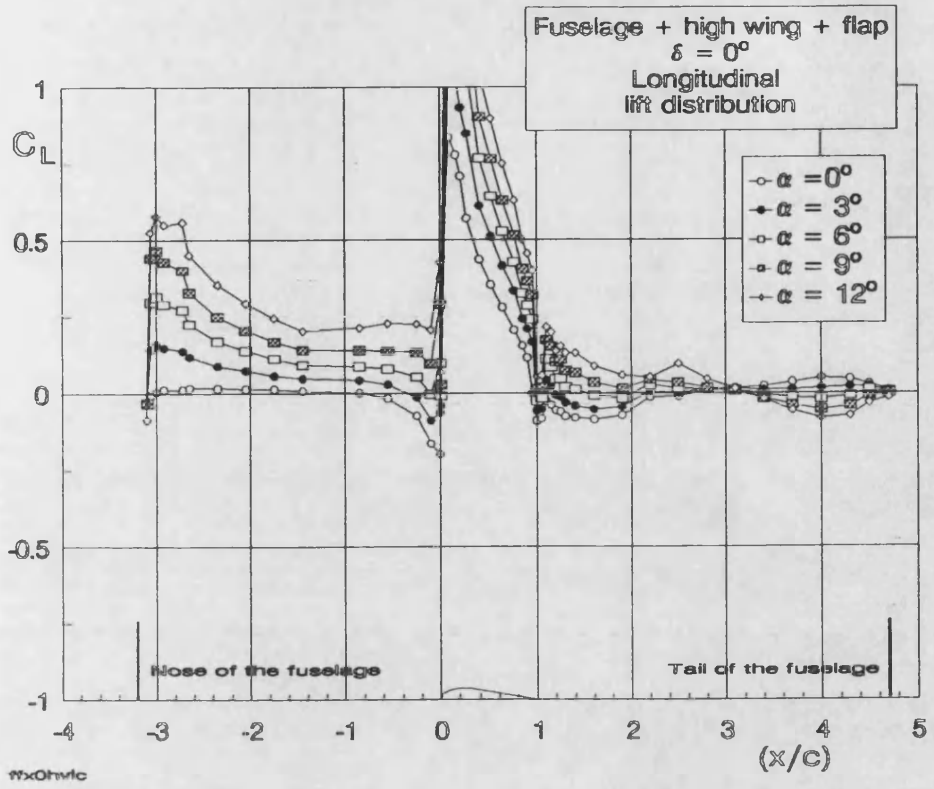

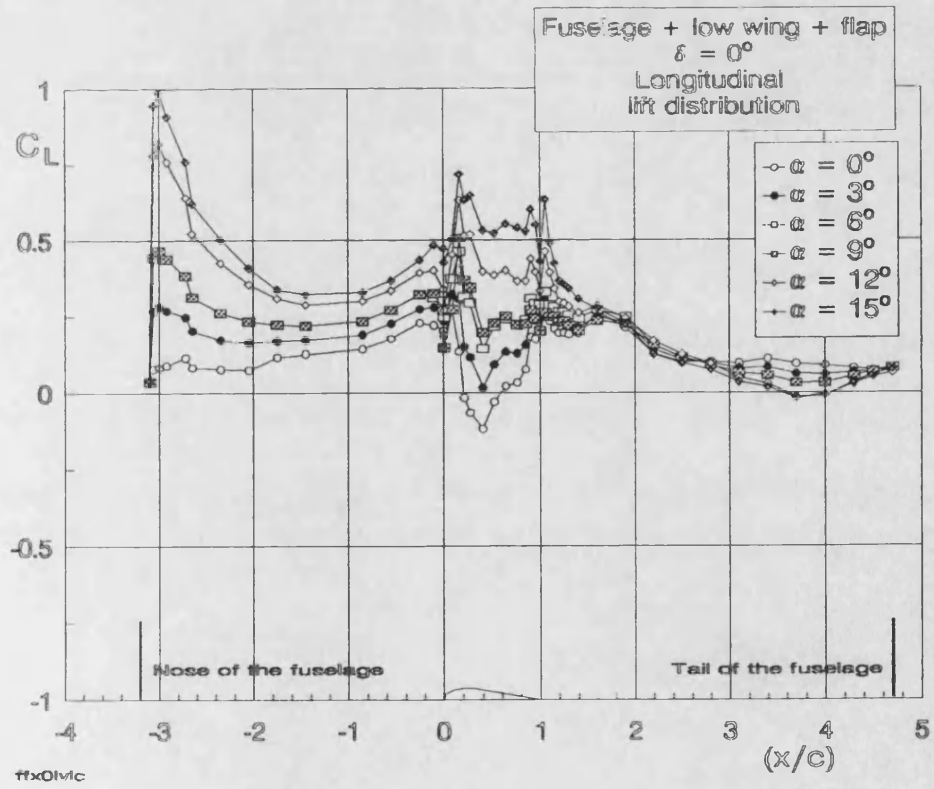

Fig. 4.49 Fuselage lift distribution for fuselage & wing & flaps, $\delta = 0^o$

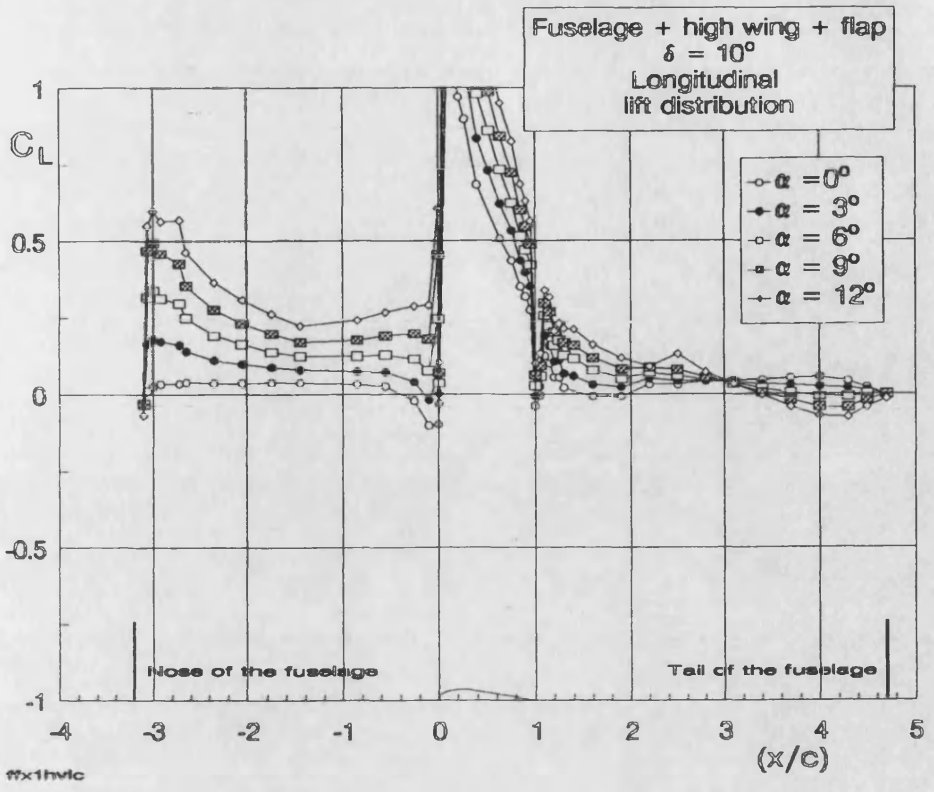

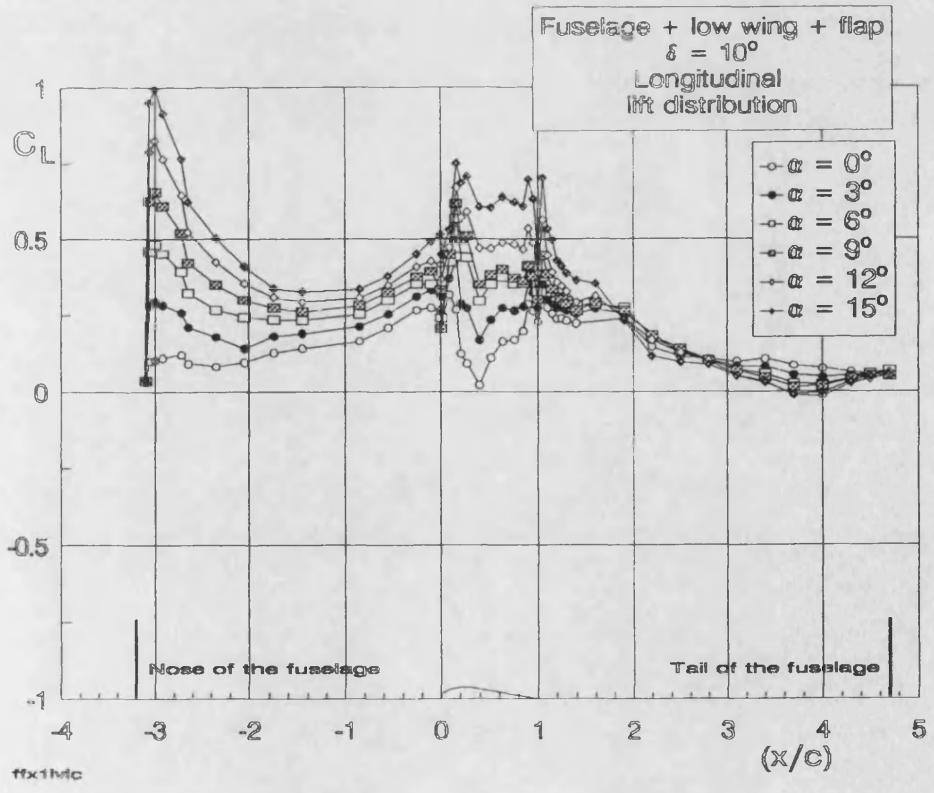

Fig. 4.50 Fuselage lift distribution for fuselage & wing & flaps, $\delta = 10^o$

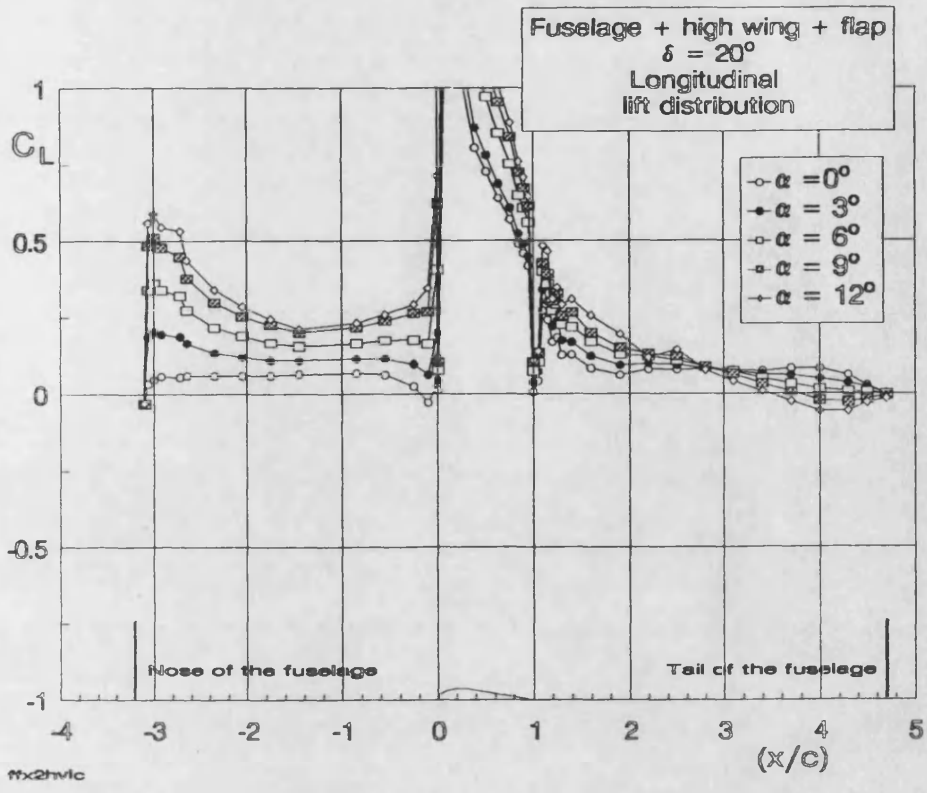

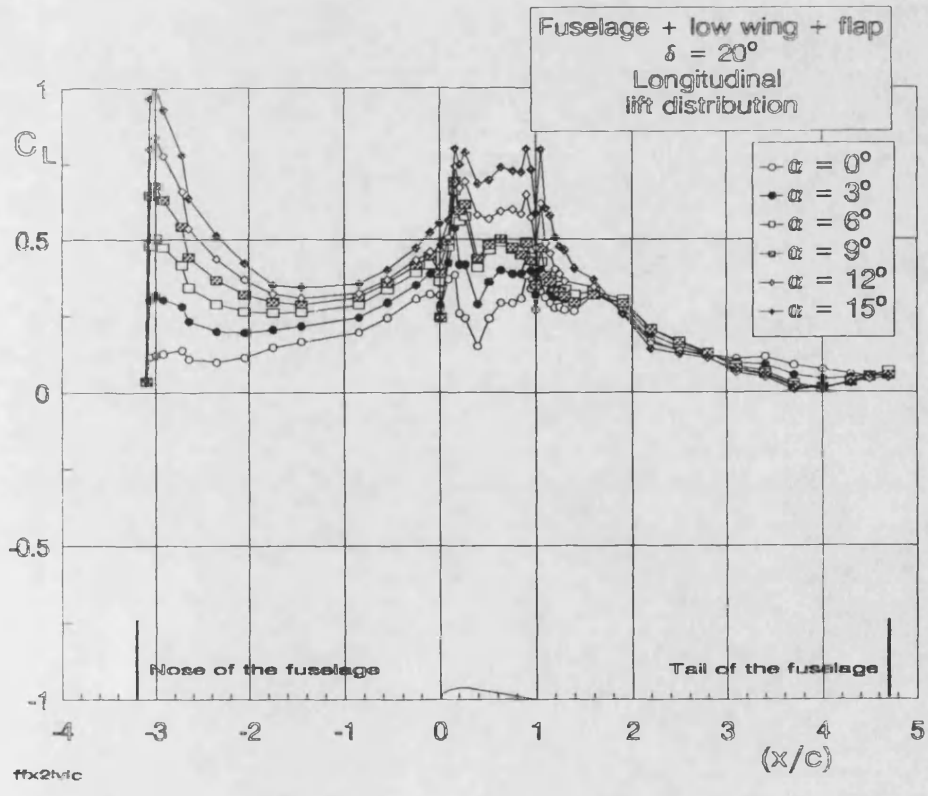

Fig. 4.51 Fuselage lift distribution for fuselage & wing & flaps, $\delta = 20^o$

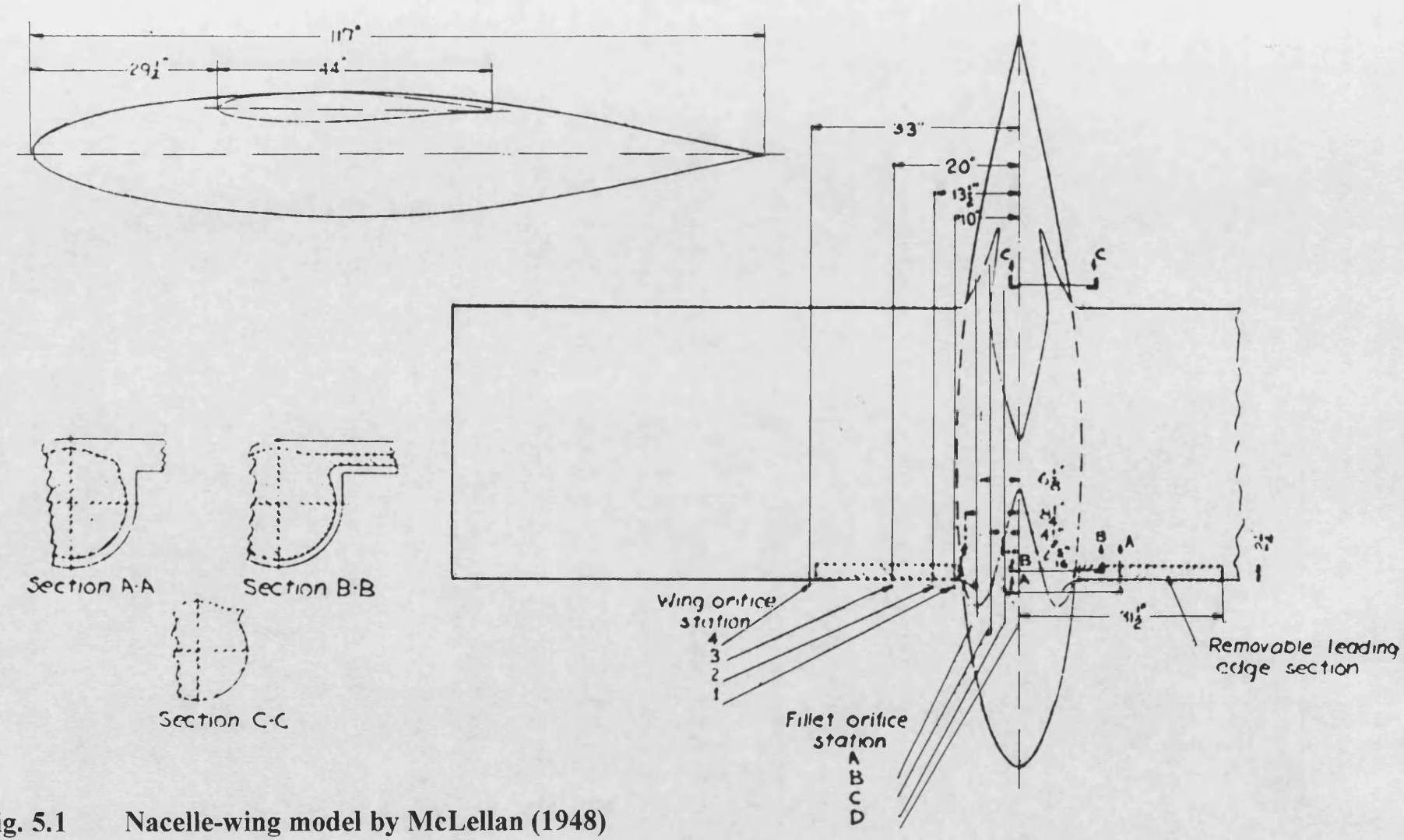

Fig. 5.1 Nacelle-wing model by McLellan (1948)

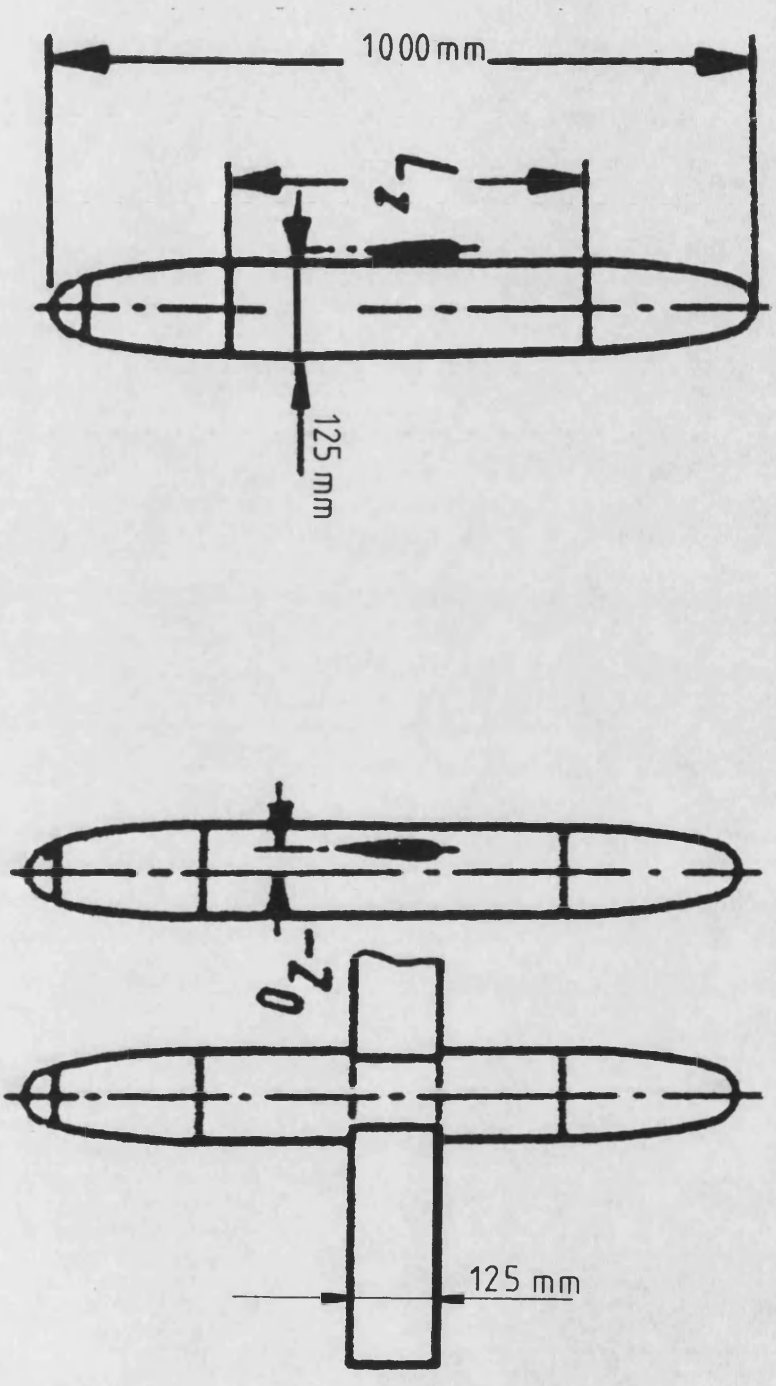

Fig. 5.2 Fuselage-wing model by Körner (1972) and Müller (1970)

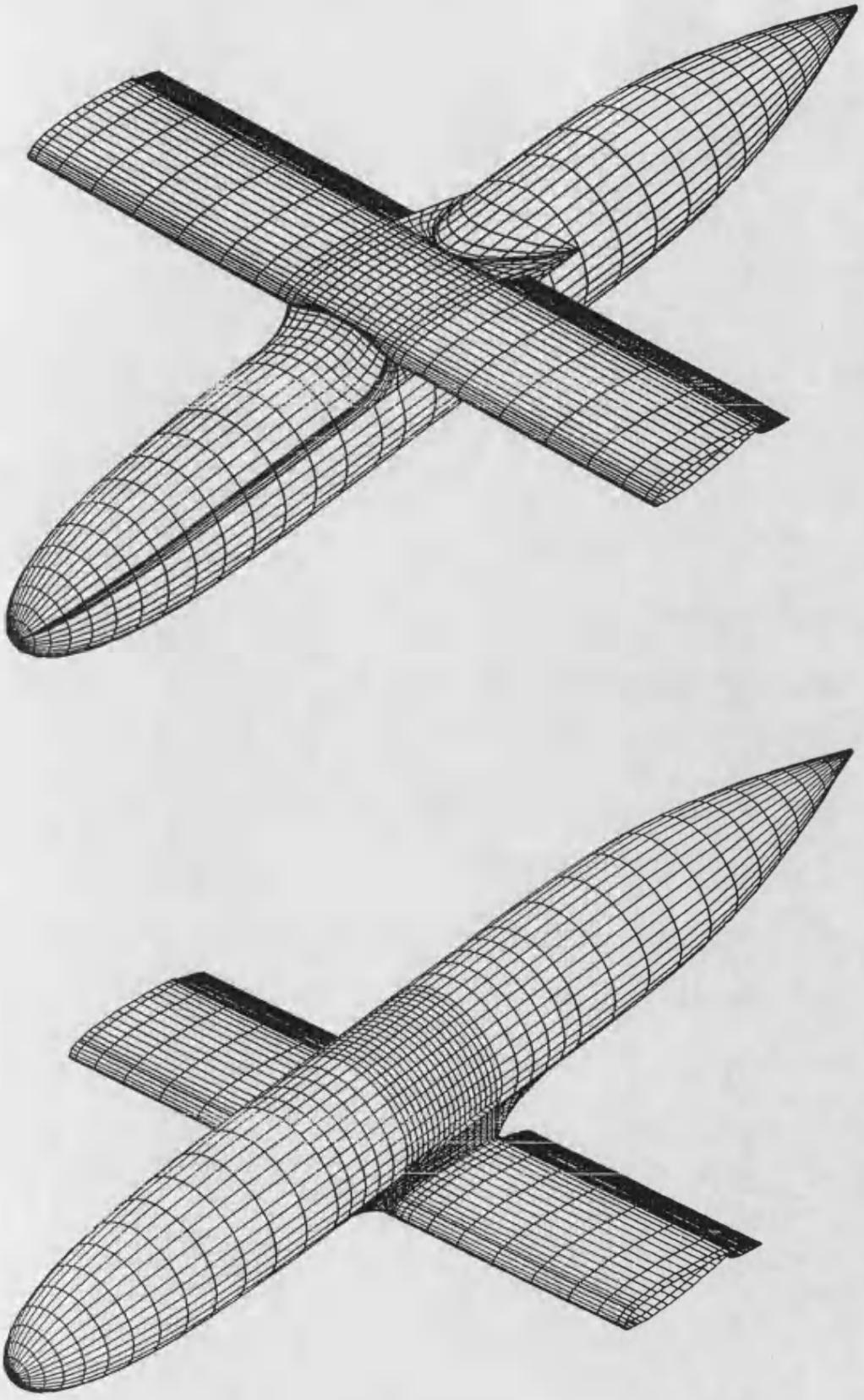

Fig. 7.1 Panel representation of the high and low wing model, using VSAERO

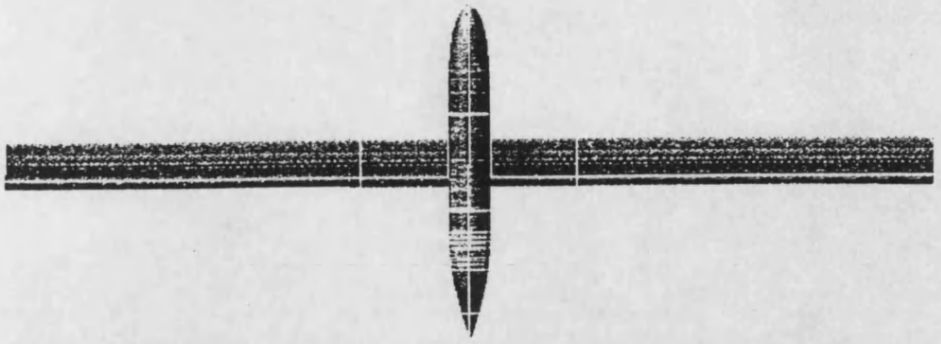

Fig. 7.2 Span modification of the VSAERO model

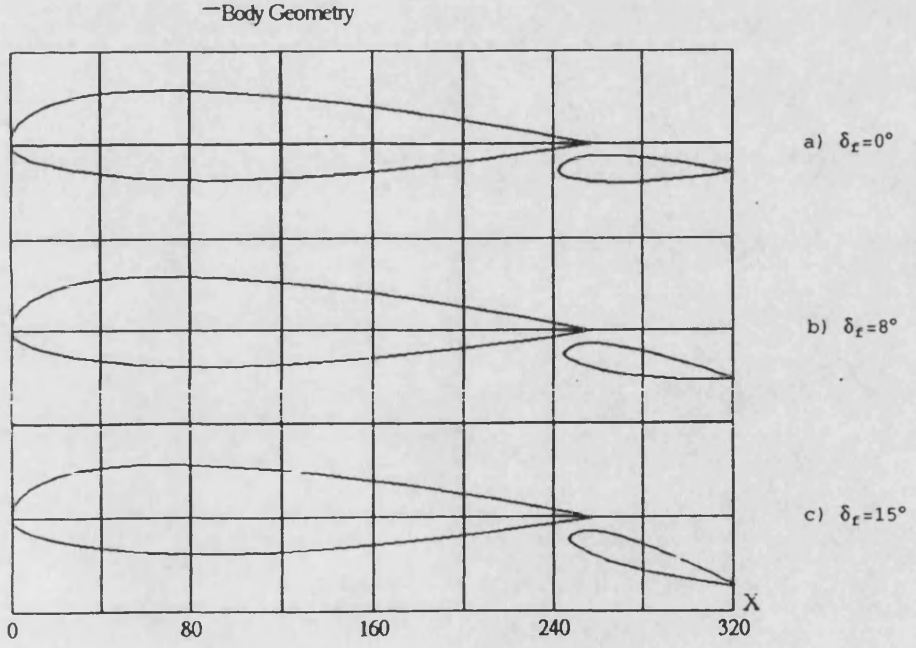

Fig. 7.3 Flap deflection and position relative to the wing

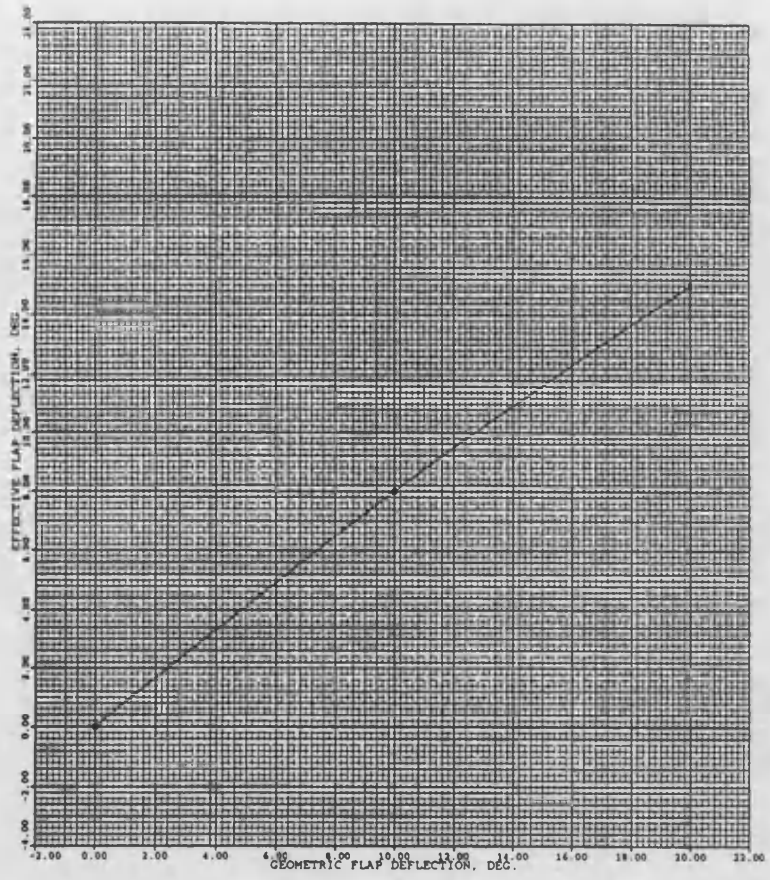

Fig. 7.4 Comparison of the theoretical and experimental flap angle

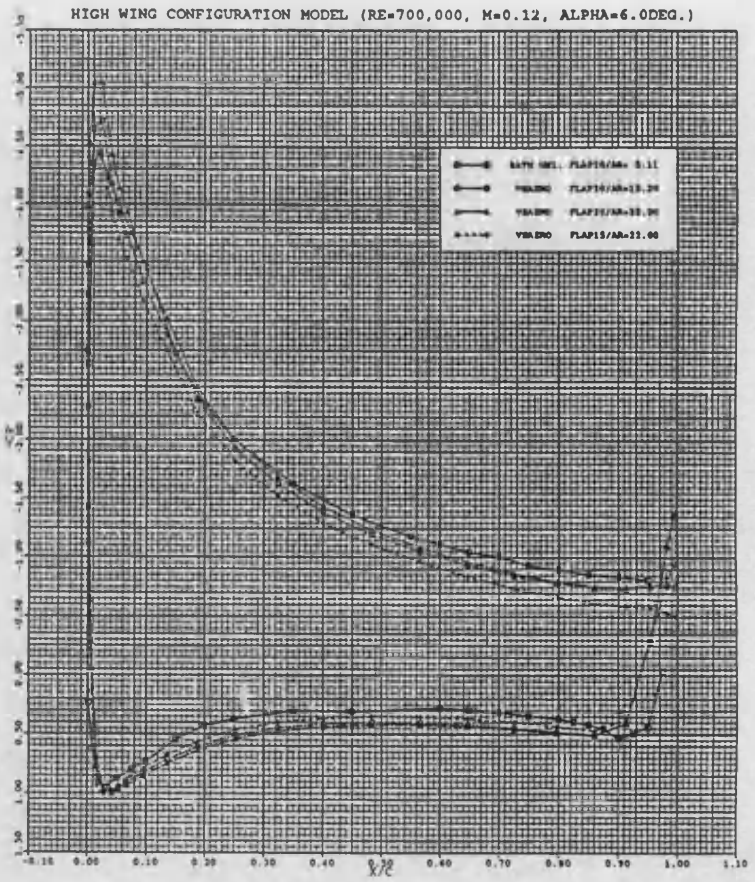

Fig. 7.5 Pressure distribution over wing at quarter span for different aspect ratios and flap angles

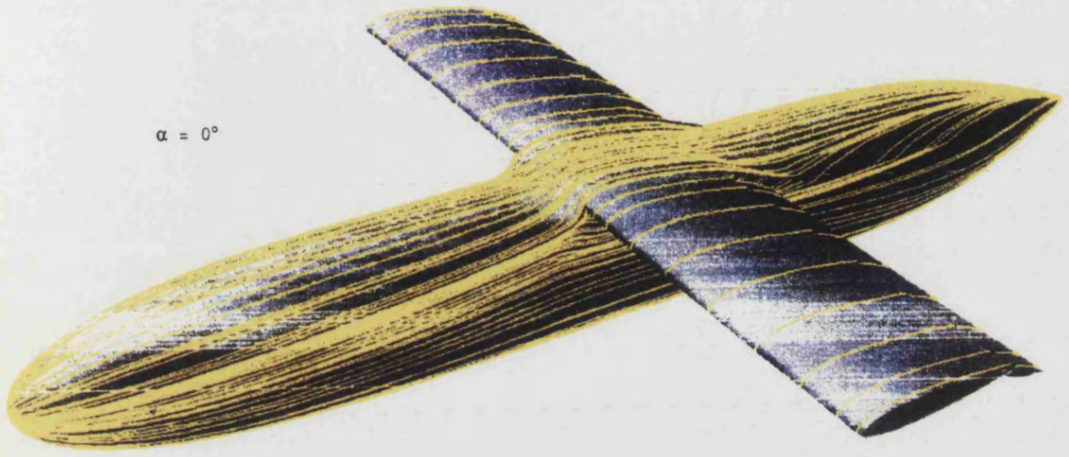

VSAERO streamlines for the high wing configuration

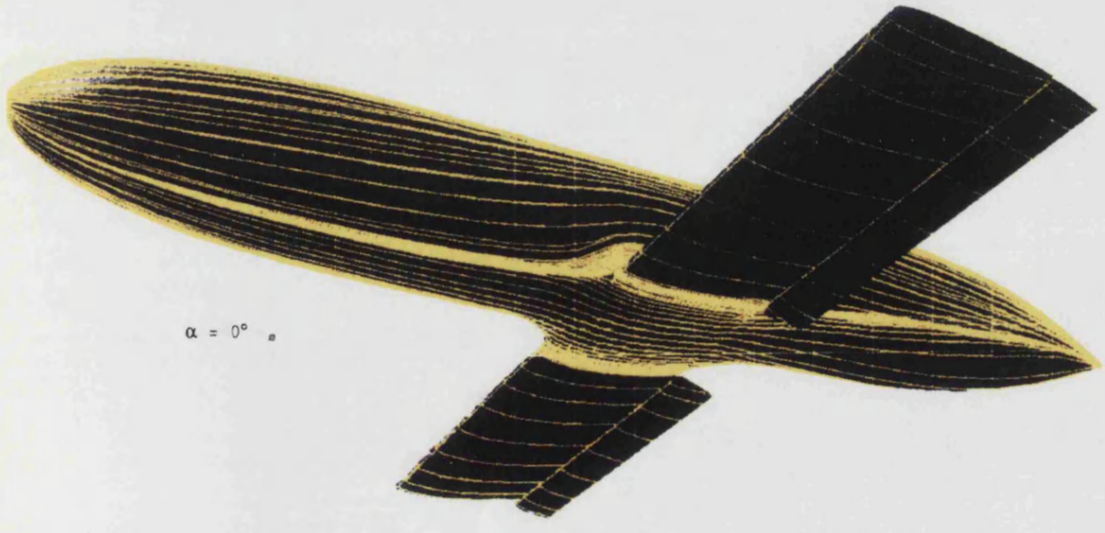

VSAERO streamlines for the low wing configuration

Fig. 8.1 Streamlines over fuselage & wing & flaps, $\alpha = 0°$, $\delta = 15°$

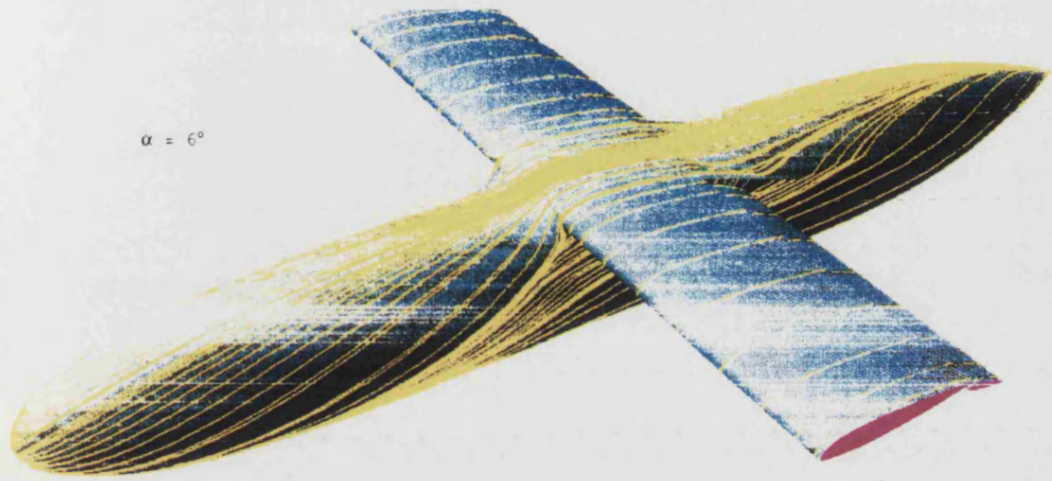

VSAERO streamlines for the high wing configuration

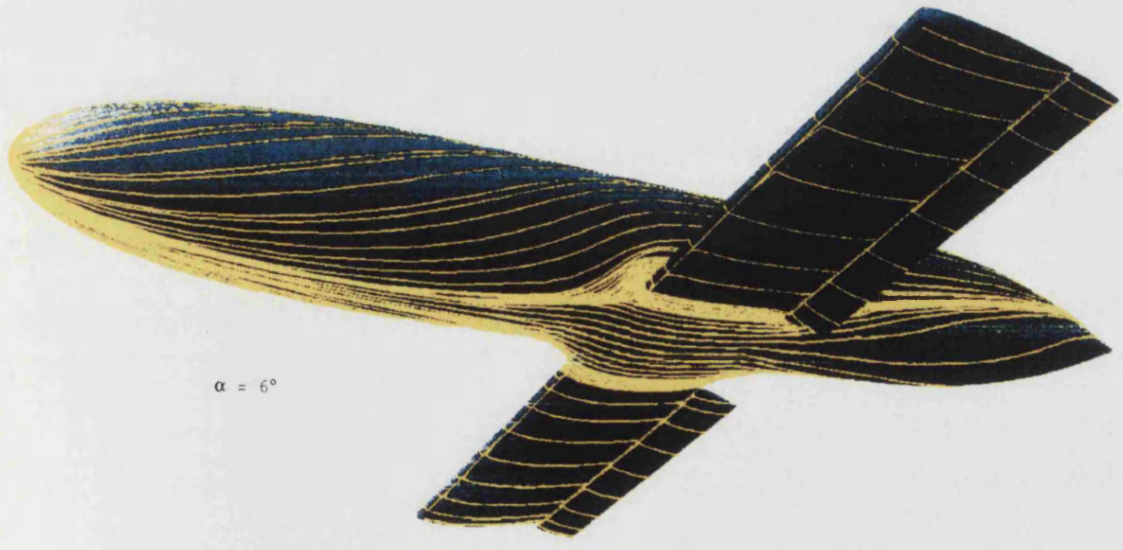

VSAERO streamlines for the low wing configuration

Fig. 8.2 Streamlines over fuselage & wing & flaps, $\alpha = 6°$, $\delta = 15°$

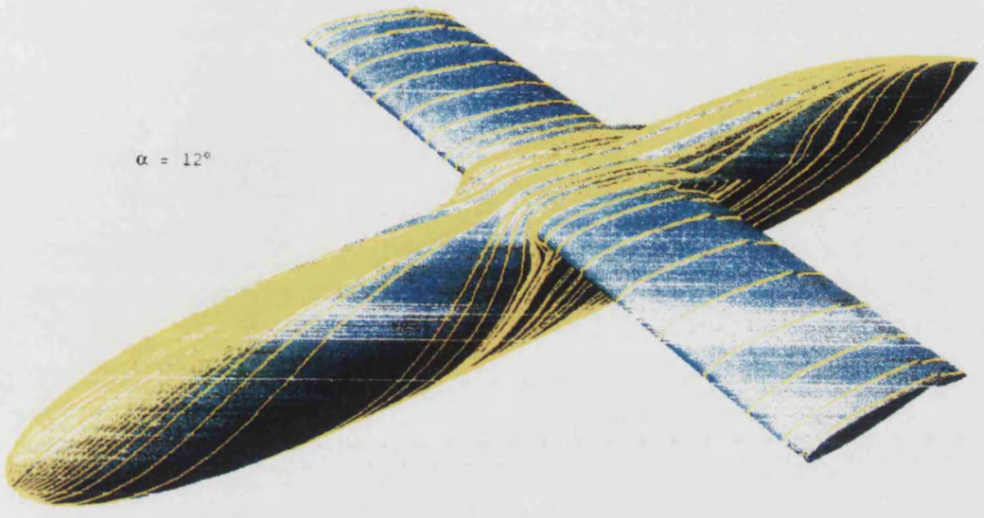

VSAERO streamlines for the high wing configuration

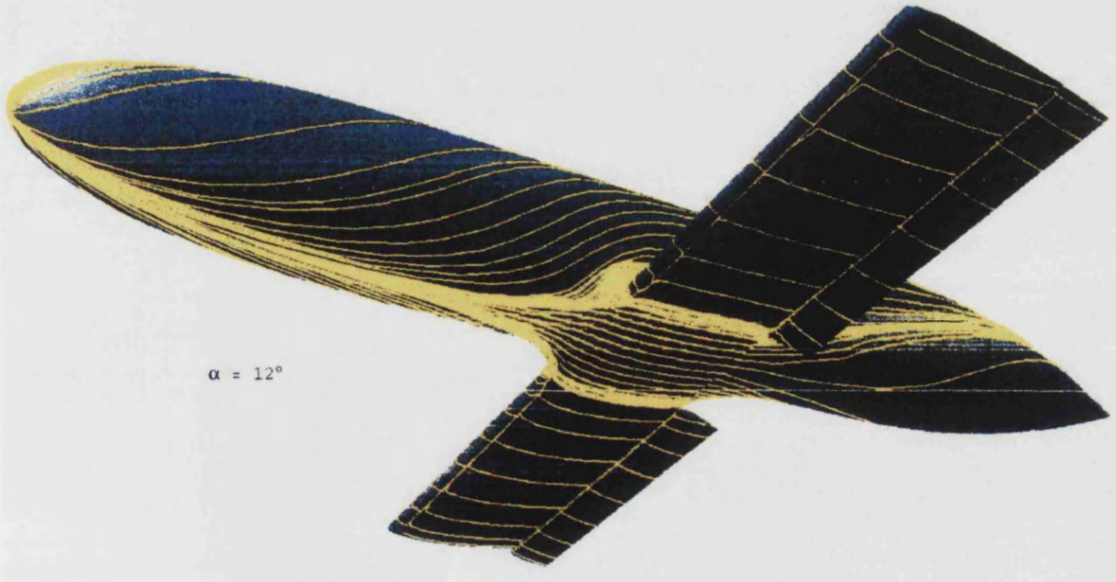

VSAERO streamlines for the low wing configuration

Fig. 8.3 Streamlines over fuselage & wing & flaps, $\alpha = 12°$, $\delta = 15°$

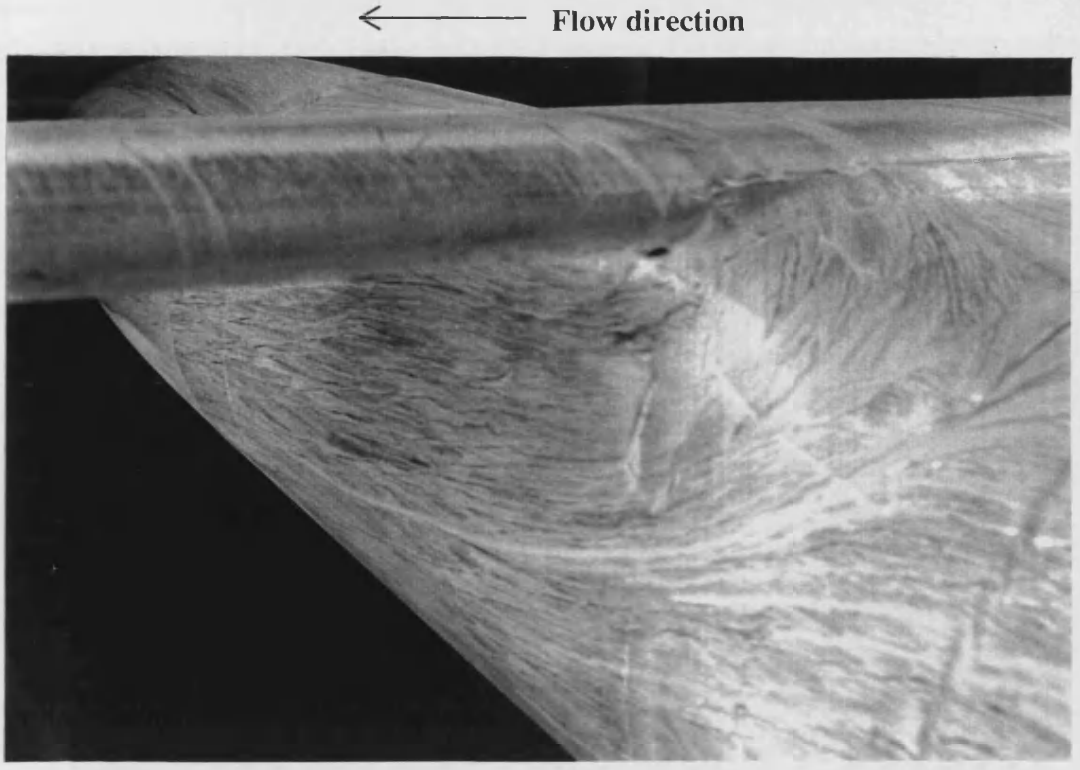

(a) Sideview of the wing-fuselage junction in the high wing configuration

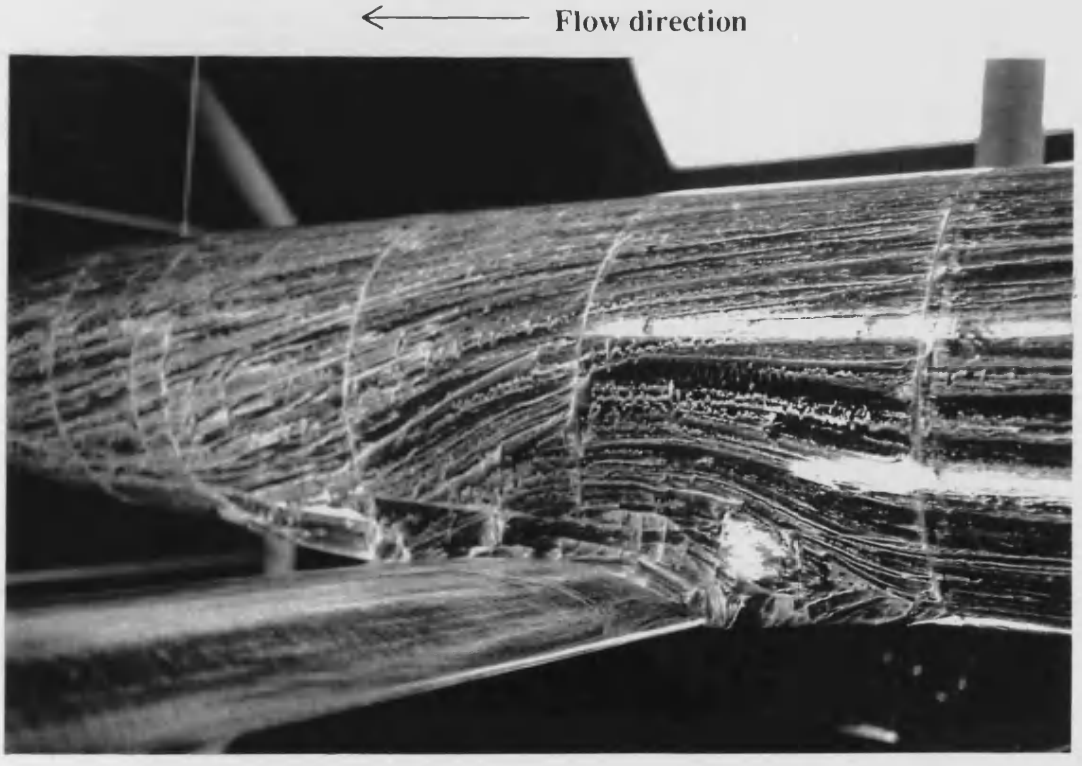

(b) Sideview of the wing-fuselage junction in the low wing configuration

Fig. 8.4 Surface flow over fuselage & wing, $\alpha = 0°$

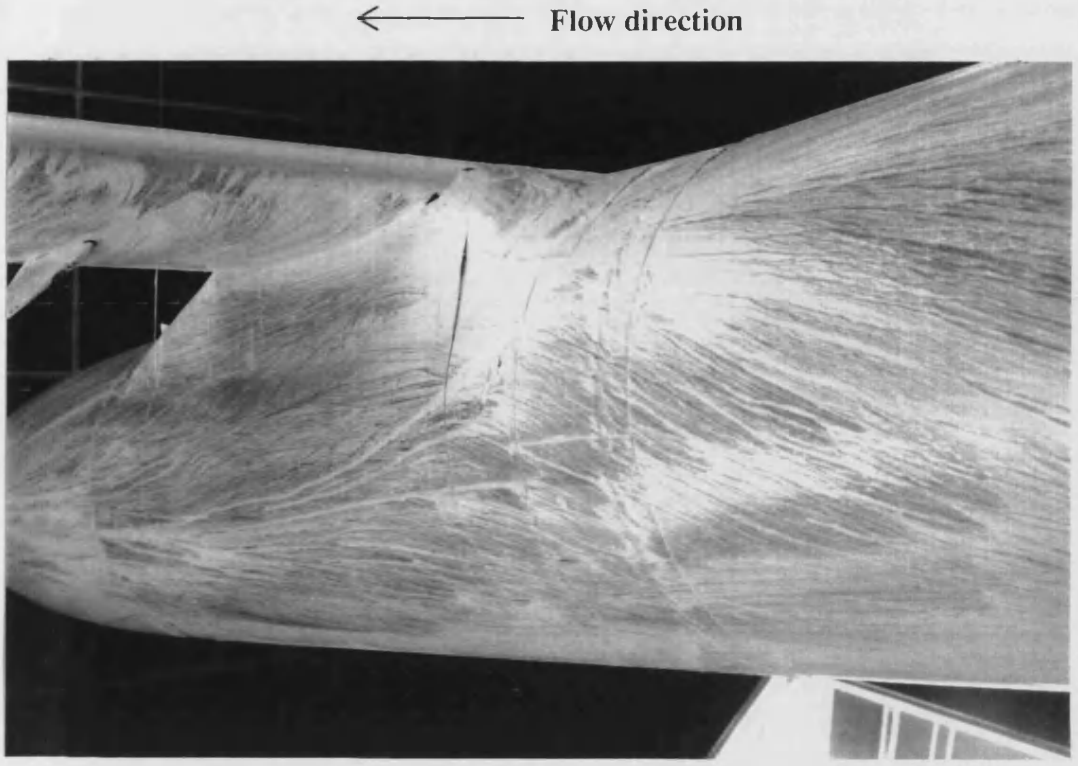

(a) Sideview of the wing-fuselage junction in the high wing configuration

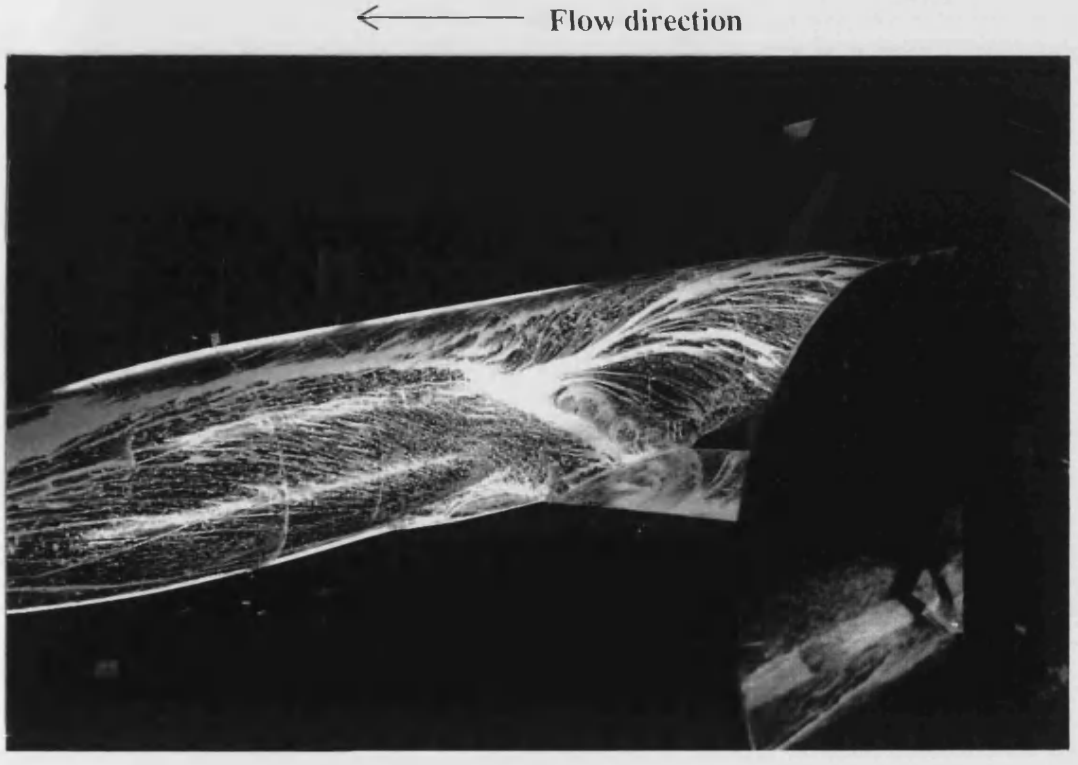

(b) Sideview of the wing-fuselage junction in the low wing configuration

Fig. 8.5 Surface flow over fuselage & wing, $\alpha = 12°$

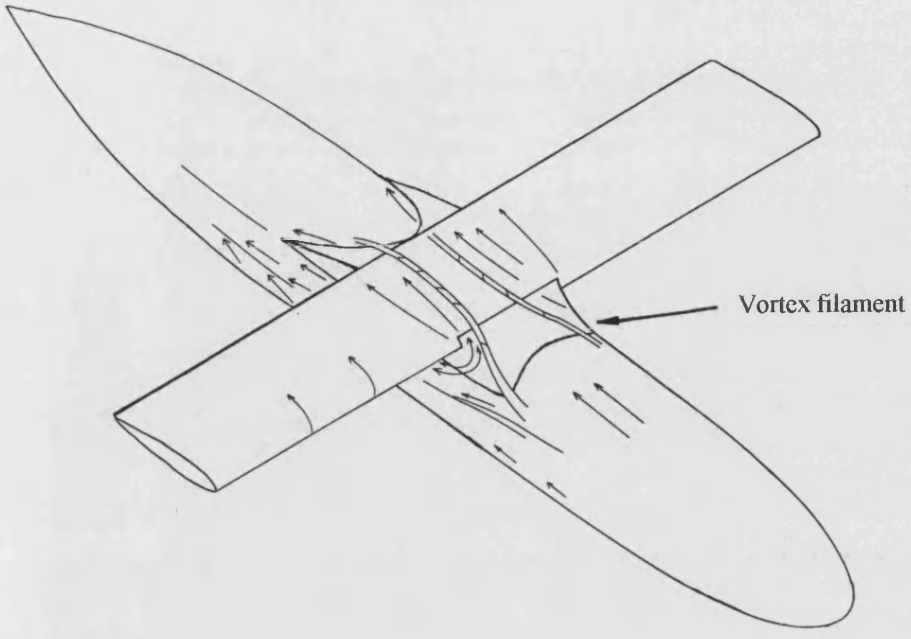

Sideview of the wing-fuselage junction in the high wing configuration

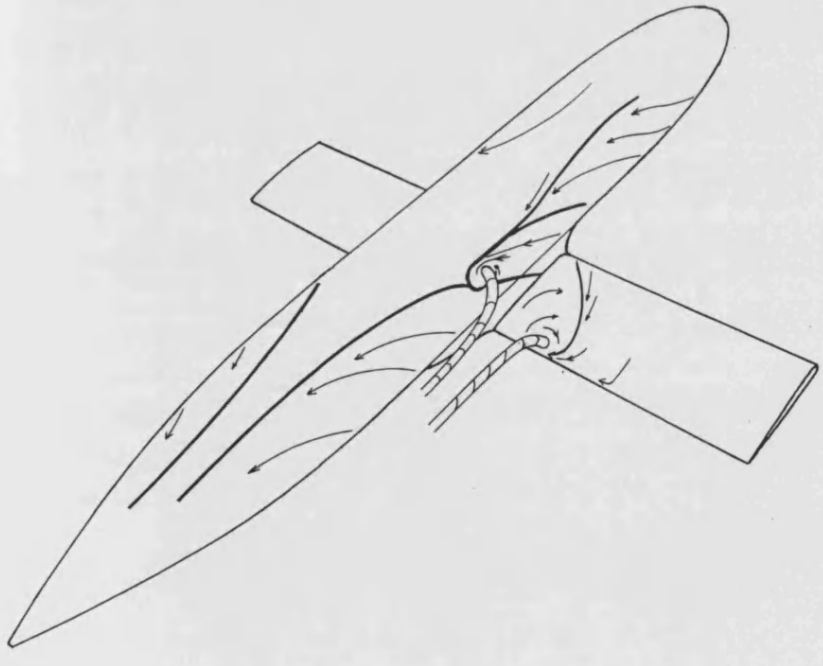

Sideview of the wing-fuselage junction in the low wing configuration

Fig. 8.6 Suggested flow over fuselage & wing, $\alpha = 12°$

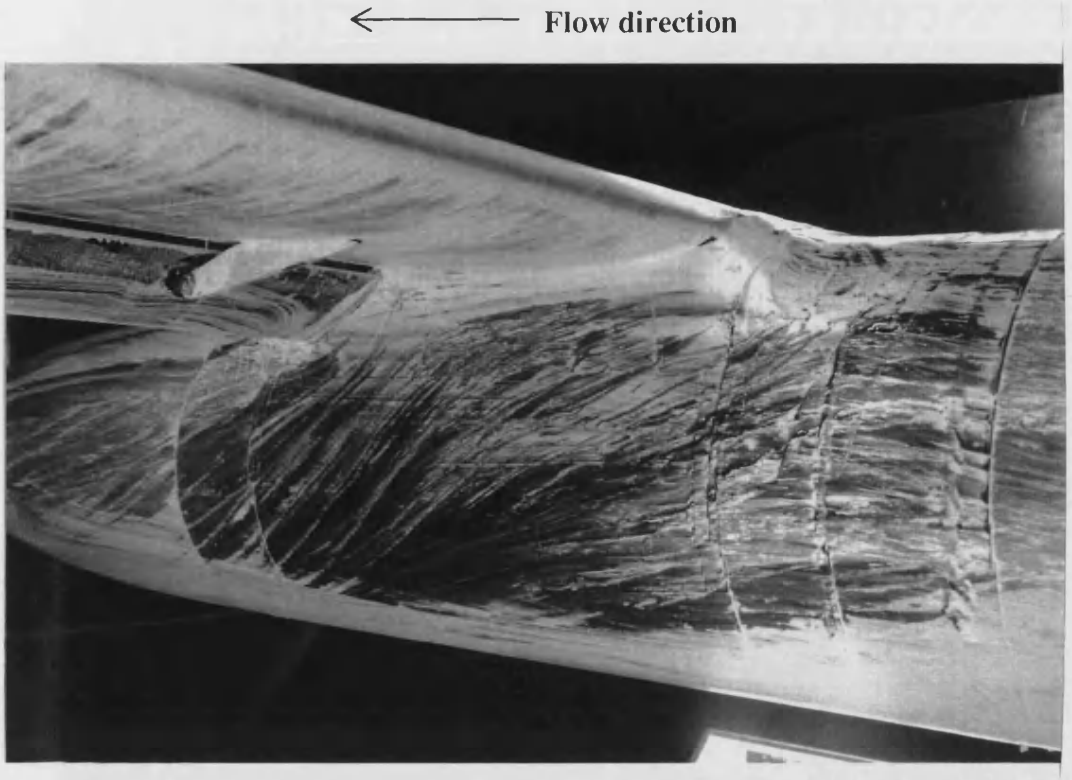

(a) Sideview of the wing-fuselage junction in the high wing configuration, $\delta = 30°$

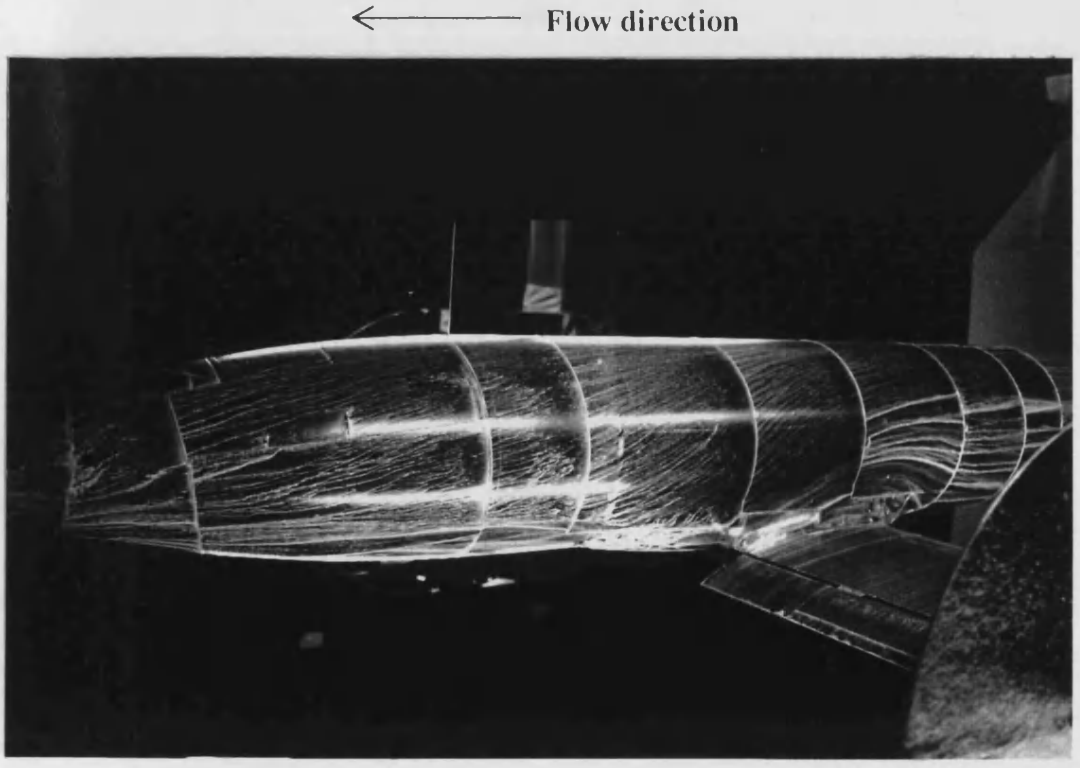

(b) Sideview of the wing-fuselage junction in the low wing configuration, $\delta = 20°$

Fig. 8.7 Surface flow over fuselage & wing & flaps, $\alpha = 0°$

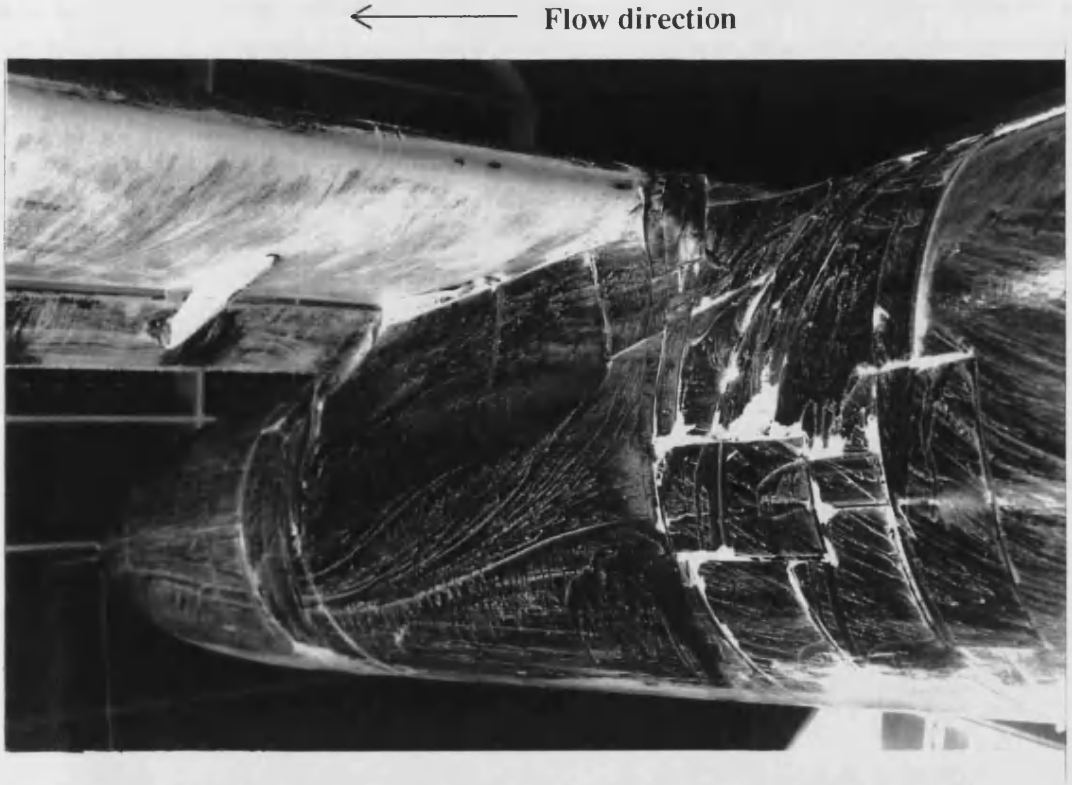

(a) Sideview of the wing-fuselage junction in the high wing configuration

(b) Sideview of the wing-fuselage junction in the low wing configuration

Fig. 8.8 Surface flow over fuselage & wing & flaps, $\alpha = 12°$; $\delta = 20°$

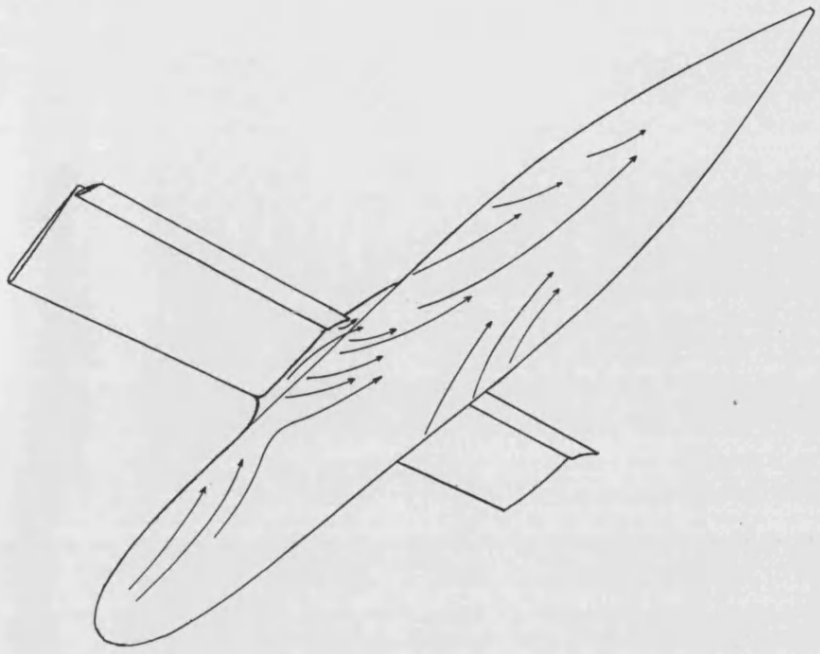

Sideview of the wing-fuselage junction in the high wing configuration

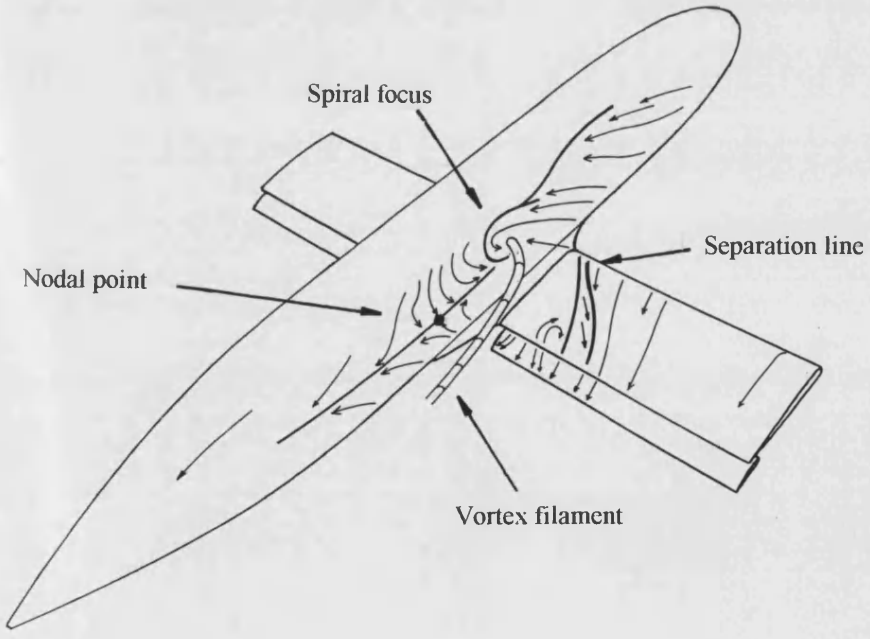

Sideview of the wing-fuselage junction in the low wing configuration

Fig. 8.9 Suggested flow over fuselage & wing & flaps, $\alpha = 12°$; $\delta = 20°$

Flow direction ⟶

Wingview of the wing-fuselage junction, high wing configuration, $\alpha = 6°$, $\delta = 20°$

Flow direction ⟶

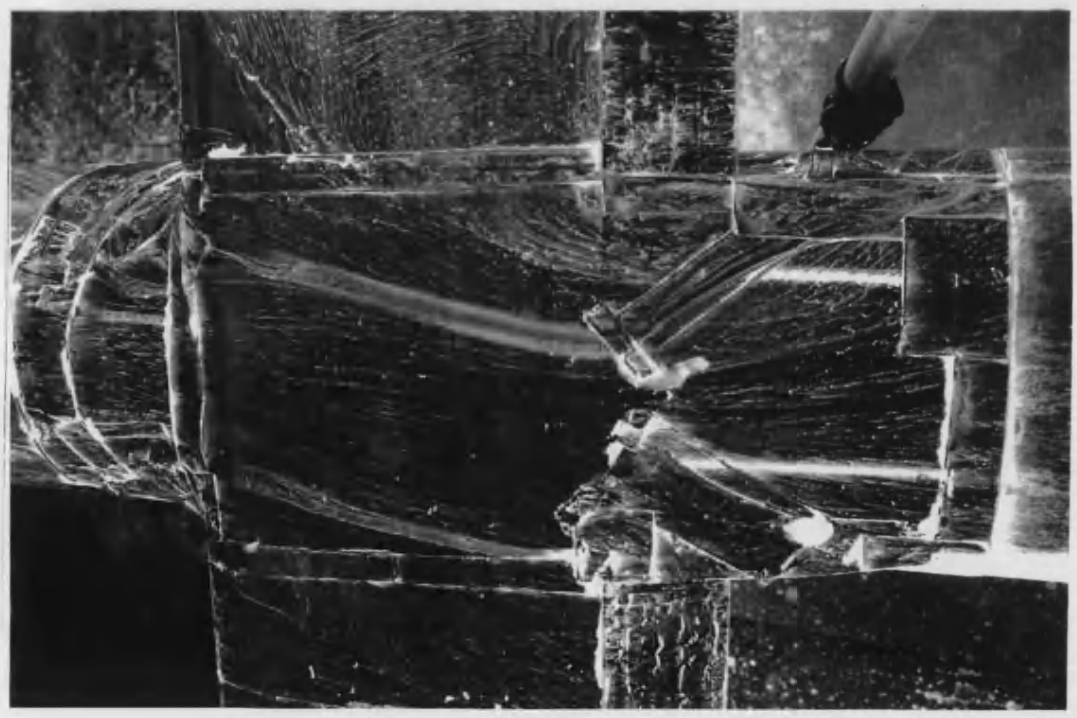

Wingview of the wing-fuselage junction, high wing configuration, $\alpha = 12°$, $\delta = 30°$

Fig. 8.10 Surface flow over fuselage & wing & flaps

Leading edge

Wingview of the wing-fuselage junction, low wing configuration, $\alpha = 6°$

Leading edge

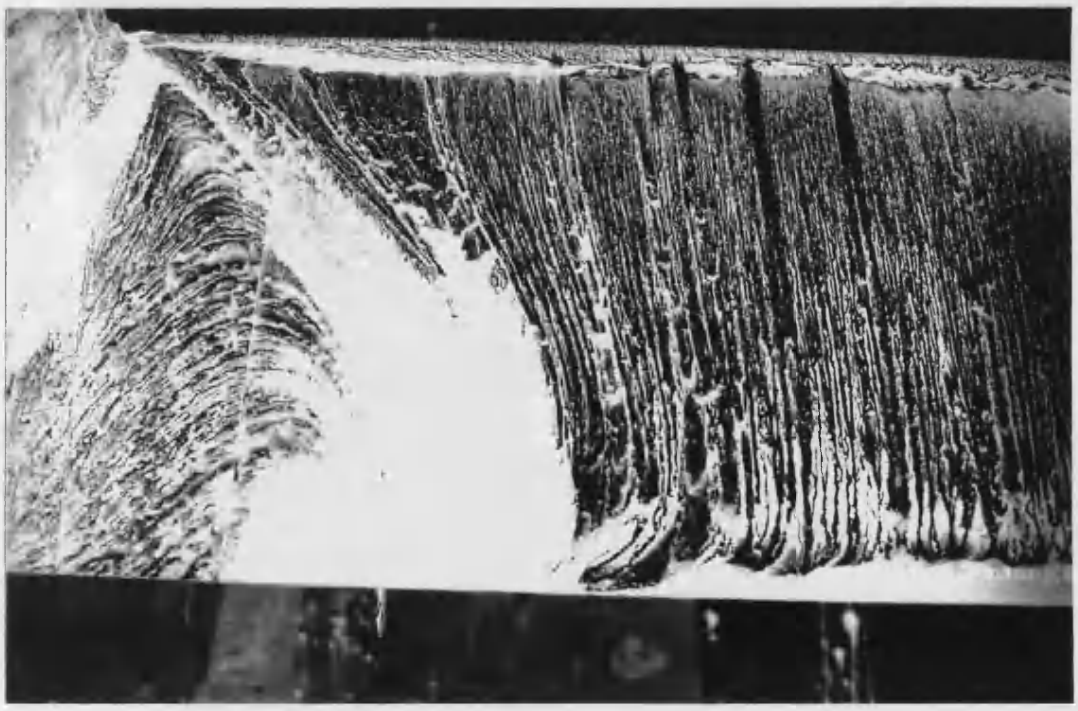

Wingview of the wing-fuselage junction, low wing configuration, $\alpha = 12°$

Fig. 8.11 Surface flow over fuselage & wing

Flow direction ⟶

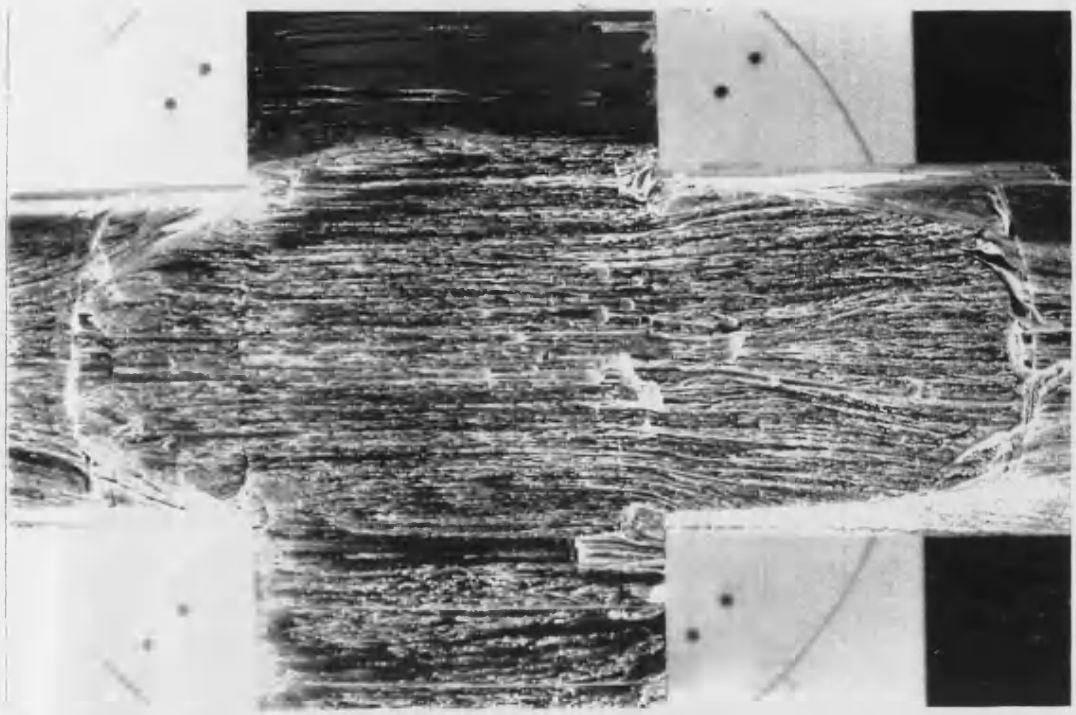

Lower wing surface, low wing configuration, $\alpha = 6°$

Flow direction ⟶

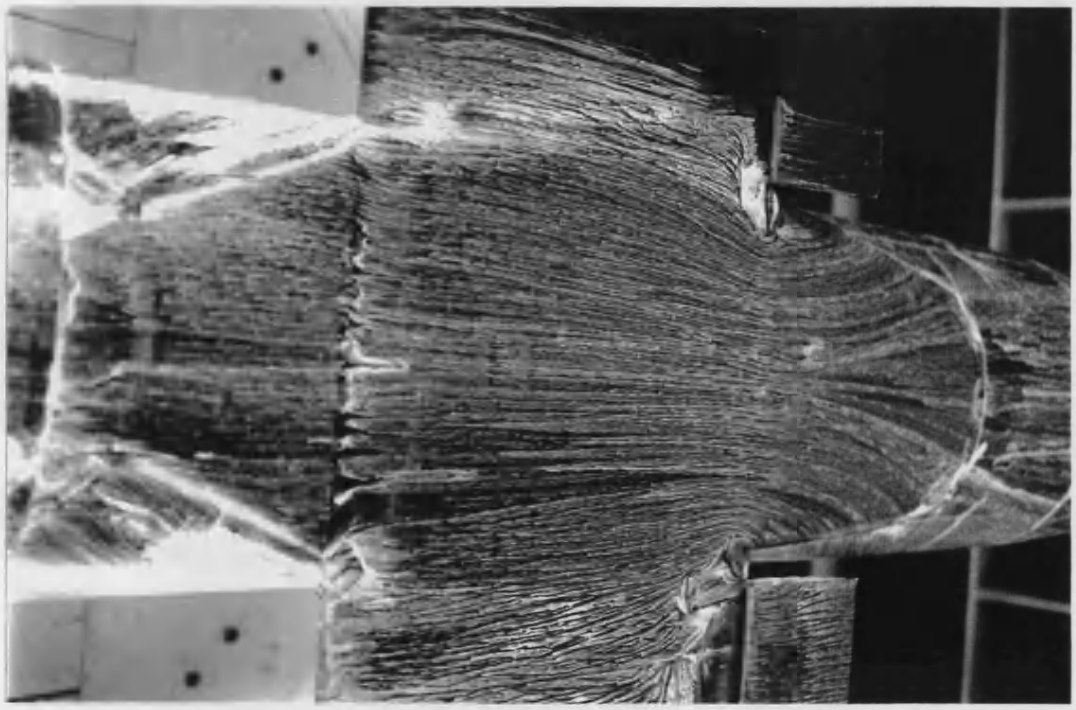

Lower wing surface, low wing configuration, $\alpha = 12°$, $\delta = 10°$

Fig. 8.12 Surface flow over fuselage & wing